

Entrainment Processes during Plume Ascent

Dissertation
zur Erlangung des Doktorgrades
der Mathematisch-Naturwissenschaftlichen Fakultät
der Christian-Albrechts-Universität zu Kiel

vorgelegt von

Frank Cord Lohmann

Kiel, Dezember 2005

Referent/in:
Korreferent/in:
Tag der mündlichen Prüfung:
Zum Druck genehmigt:

Prof. Dr. J. Phipps Morgan
Prof. Dr. K. Hoernle
03.02.2006
03.02.2006

Der Dekan

for Claudia

in a way, this is all your fault.

Abstract

Basalts from intraplate or hotspot ocean islands are found to have distinct geochemical signatures. In particular, at strong plumes like Hawaii, Iceland or Galápagos, there is evidence for at least three geochemically distinct components. This diversity in composition is generally believed to result from the upwelling plume entraining shallow mantle material during ascent, while potentially also entraining other deep regions of the mantle.

In order to understand the geochemical message brought to the surface by plumes, this thesis presents a comprehensive study on the dynamics of plume entrainment using analogue laboratory experiments and 3D numerical modelling, with the focus on the following three questions:

- Which regions of the mantle are most efficiently sampled by mantle plumes?
- Is the heterogeneous nature of mantle plumes inherited at the source, or does it develop through entrainment during plume ascent?
- How are the plume and plume entrainment affected by mantle discontinuities?

The analogue laboratory experiments are conducted using glucose syrup contaminated with glass beads to visualize fluid flow and origin. The plume is initiated by heating from below or by injecting hot uncontaminated syrup. Results from the laboratory experiments indicate the presence of a sheath of mostly unheated material enveloping the core thermal plume structure and rising along with the plume. This 'plume sheath' is chiefly made up from material of the lowermost plume source region. All entrainment into the plume head has its origin in the plume sheath, and all entrainment of ambient material happens between plume sheath and surrounding material. The plume sheath itself is too viscous and too cold to rise under its own thermal buoyancy, which suggests that it owes its rise to drag/pull of the fast ascending plume core material.

Investigating the plume sheath model inferred from the laboratory experiments via numerical modelling, it is found that the numerical models readily reproduce plume sheath behaviour in the ascending plume. Furthermore, it is observed that there is little to no vorticity within the ascending plume core, and hence no lateral transport of material found within.

Numerical models for mantle conditions introduce depth-dependent viscosity, which dramatically changes the dynamics of plume ascent and plume dynamics. Most notably, the passage of an ascending plume through sharp viscosity interfaces (attributed to mineral phase changes) lead to massive distortion and deformation of the plume head. This results in a remarkably complex compositional structure of the plume, and in increased sampling of specific regions in the mantle through entrainment. Still, despite the massive disturbance of plume shape and structure, there is little to no indication of lateral transport in either plume sheath or plume core.

Applying a simple melting model to the numerical calculations, it is seen that deformation of the plume head during plume ascent may result in deep source and mid-source material being entrained into the plume head and ending up in the melting portion of the plume head, thus adding to the heterogeneity of the plume head melts.

Lastly, the effects of plume deflection by a moving plate is investigated. It is found that a plume rising from a zoned source region exhibits characteristic patterns in the plume swell,

thus potentially allowing for the drawing of conclusions on the composition and layout of the source region from the zonation of the plume track.

Zusammenfassung

Basalte aus Intraplatten- oder Hotspot-Vulkanismus weisen eine eindeutige geochemische Zusammensetzung auf. Besonders an starken Mantelplumes wie Hawaii, Island oder Galápagos findet man Spuren von mindestens drei unterschiedlichen geochemischen Quellen. Diese Vielfalt der Zusammensetzung wird üblicherweise darauf zurückgeführt, dass Mantle Plumes während ihres Aufstiegs Material aus dem oberen Mantel ebenso wie Material aus tieferen Regionen „mitreißen“ und bis unter die Lithosphäre tragen.

Diese Arbeit präsentiert die Ergebnisse von ausgiebigen Untersuchungen der Dynamik dieses „Mitreißens“, dem sogenannten „Plume Entrainment“, mittels analoger Laborexperimente und numerischer Simulationsrechnungen. Dabei liegt das Hauptaugenmerk auf folgenden Fragen:

- Aus welchen Regionen des Mantels speisen sich Plumes hauptsächlich?
- Ist die heterogene Zusammensetzung von Plumes Zeichen einer inhärent heterogenen Quellregion, oder entsteht sie durch Entrainment während des Plumeaufstiegs?
- Wie werden Plume und Plume Entrainment durch Phasenübergänge im Mantel beeinflusst?

Für die analogen Laborexperimente wird Glukosesirup mit Glaspartikeln verunreinigt, um Flussverhalten und Geschwindigkeiten zu visualisieren. Der Laborplume wird entweder durch ein Heizelement am Boden des Versuchstanks oder durch das Injizieren von unkontaminiertem, heißen Sirup erzeugt. Die Laborexperimente deuten darauf hin, dass ein eine Hülle aus größtenteils kaltem Material den aufsteigenden Plume umgibt. Dieses „Plumefutteral“ besteht vornehmlich aus Material aus der tiefsten Quellregion. Das Plumefutteral schirmt den Plume-kern regelrecht vor Entrainment von Material aus der Umgebung ab. Alles Entrainment in den Plume-kern hat seinen Ursprung im Plumefutteral, und umgebendes Material wird ausschließlich in das Plumefutteral entrained. Das Plumefutteral selbst ist zu viskos und zu kalt, um eigenständig aufzusteigen - vielmehr wird es vom schnell aufsteigenden Plume-kern geradezu mitgeschleift.

Das Plumefutteral lässt sich auch in numerischen Simulationsrechnungen von Laborbedingungen nachweisen. Die oben aufgezählten Eigenschaften, die das Plumefutteral im Labor aufweist, werden in den Simulationen mühelos reproduziert. Ferner zeigt sich, dass es zu keinem lateralen Transport von Material innerhalb des Plumes kommt.

Die numerischen Simulationsrechnungen von Erdmantelbedingungen berücksichtigen den Einfluss der Tiefe auf die Viskosität des Mantels, was zur Folge hat, dass sich die Dynamik des Plumeaufstiegs dramatisch ändert. Vor allem wird beobachtet, dass steile Übergänge und Unstetigkeiten in der Viskosität (die mit Phasenübergängen im Mantel in Verbindung gebracht werden) ein starkes Verformen von Plume und Plume-kopf zur Folge haben, was zu einer komplexen Zonierung von Material im Plume sowie zum verstärkten Einbeziehen bestimmter Mantelreservoirs in den Plume führt. Trotz allem ist aber weiterhin kein lateraler Transport in Plume oder Plumefutteral zu erkennen.

Wendet man ein einfaches Schmelzmodell auf die numerischen Rechnungen an, so zeigt sich, dass Verformungen des Plume-kopfes während des Aufstiegs durch den Mantel zur Folge haben, dass Material aus unterschiedlichen Tiefen des Mantels in die Schmelzregion des Plume-kopfes gefördert wird und so zur Heterogenität der Plumeschmelze beiträgt.

Zu guter Letzt werden die Folgen der Ablenkung des aufsteigenden Plumes durch eine sich bewegende Lithosphärenplatte untersucht. Es zeigt sich, dass ein Plume, der sich aus einer zonierten Quellregion speist, auch in der Plumespur ein charakteristisches Muster aufweist, so dass sich aus der Zonierung eines solchen Plumes an der Oberfläche Rückschlüsse auf die Zusammensetzung seiner Quellregion ziehen lassen.

Contents

1	The Great Plume Debate	1
1.1	The Great Paradigm Change	1
1.2	Hotspots and Mantle Plumes	3
1.3	The Plume Controversy	4
1.4	Motivation & Aim	7
2	An Introduction to Analogue Experiments	13
2.1	Previous Laboratory Studies of Plumes	13
2.2	Scaling Laws and Theory	15
2.3	Instabilities	17
2.3.1	Rayleigh-Taylor-Instability	18
2.3.2	Kelvin-Helmholtz-Instability	18
2.3.3	Rayleigh-Bénard-Instability	19
3	Laboratory Methodology	21
3.1	The Experimental Tank	21
3.2	Specifics of the Measurement Methods	22
3.2.1	Temperature measurements	22
3.2.2	Particle Tracking Velocimetry	23
3.2.3	Plume Height	25
3.2.4	Entrainment Rates	25
3.3	Experiment Preparation	26
4	Laboratory Experiments	29
4.1	Point Source thermally driven Plume	29
4.1.1	Setup	29
4.1.2	Experiments	30
4.2	Injection Source thermally driven Plume	43
4.2.1	Setup	43
4.2.2	Experiments	44
4.3	Assessment, Summary and Proceedings	50

5	An Introduction to Numerical Modelling	53
5.1	Previous Analytical and Numerical Studies of Plumes	53
6	Numerical Methodology	57
6.1	Mathematical Treatment	57
6.2	Hydrodynamic Equations	58
6.3	Numerical Methods	60
6.3.1	Discretisation	60
6.3.2	Solving of the equations and Multigrid	61
6.3.3	Advection scheme	64
6.3.4	Limiting of the timestep	65
6.3.5	Tracer Particle implementation	66
7	Numerical Modelling of Lab Conditions	69
7.1	Initial Setup and Boundary Conditions	69
7.2	Point Source Runs	70
7.3	Pressure Runs	76
7.4	Sampling of the source layer	81
7.5	Assessment & Summary	84
8	Application to the Earth's Mantle	85
8.1	The Earth's Mantle	85
8.2	Numerical Modelling of Mantle Conditions	86
8.2.1	Initial Setup and Boundary Conditions	86
8.2.2	The Constant Mantle Viscosity Model	88
8.2.3	The Mitrovica / Forte Viscosity Model	94
8.2.4	The Steinberger Viscosity Model	102
8.2.5	The Walzer et al. Viscosity Model	109
8.3	Sampling of the Source Layer	116
8.4	Assessment and Summary	118
9	Summary, Discussion and Outlook	121
9.1	Summary of the Experimental and Numerical Work	121
9.2	Implications for Plume Ascent and Plume Entrainment	123
9.3	Outlook	126
A	Properties of the Glucose Syrup used in the laboratory experiments	127
B	Laboratory Inventory	131

List of Figures

1.1	Plates, ridges and plumes	3
1.2	Humoring the plume controversy	5
1.3	Zonation of the Galápagos plume	8
2.1	The <i>Griffiths & Campbell</i> [1990] plume model	15
2.2	Convective flow regimes	16
2.3	Rayleigh-Taylor instability	18
2.4	Kelvin-Helmholtz instability	18
2.5	Rayleigh-Bénard instability	20
3.1	Sketch of the fundamental experimental setup, and experimental tank cross-section	22
3.2	The particle tracking method	24
3.3	The particle tracking calibration tank	27
4.1	Picture and schematic sketch of the Heating Element	29
4.2	Experimental setup for the point source experiments	30
4.3	Plume height vs. time for the high plume temperature point source experiments	31
4.4	Evolution of a sample low plume temperature point source experiment	32
4.5	Temperature profiles of the low plume temperature point source experiments . .	33
4.6	Evolution of a sample high plume temperature point source experiment	35
4.7	A closer look at plume head evolution	37
4.8	Horizontal slices through the plume head	38
4.9	Plume height vs. time for the high plume temperature point source experiments	39
4.10	Temperature profiles of the high plume temperature point source experiments . .	40
4.11	Plume head volume vs. time for the high plume temperature point source exper- iments	41
4.12	Entrainment in the high plume temperature point source experiments	42
4.13	Experimental setup for the injection source experiments	43
4.14	Pictures of the piston and injection tank	44
4.15	Evolution of a sample injection source experiment	46
4.16	Plume sheath velocities in a sample injection source experiment	47
4.17	Plume height vs. time for the injection source experiments	48

4.18	Temperature profiles of the injection source experiments	48
4.19	Plume head volume vs. time for the injection source experiments	49
6.1	Staggered Grid	60
6.2	Example of the dampening of high-frequency error modes	61
6.3	Prolongation	62
6.4	Relaxation	63
6.5	Fourth-order Runge Kutta method	66
7.1	Temperature profile and ascent rate of the point source numerical lab model . . .	71
7.2	Thermal evolution of the point source numerical lab model	72
7.3	Material starting height of the point source numerical lab model	73
7.4	Inner and outer sheath in the point source numerical lab model	74
7.5	Flow rates of the point source numerical lab model	75
7.6	Temperature profile and ascent rate of the point source numerical lab model . . .	77
7.7	Thermal evolution of the injection source numerical lab model	78
7.8	Material starting height of the injection source numerical lab model	79
7.9	Inner and outer sheath in the injection source numerical lab model	80
7.10	Flow rates of the injection source numerical lab model	81
7.11	Sampling of the source layer for the point source numerical lab model	82
7.12	3D plume evolution of the point source numerical lab model	83
8.1	Mantle model temperature profile and ascent rate of the constant viscosity model	88
8.2	Thermal evolution of the constant viscosity model	89
8.3	Material starting depth of the constant viscosity model	90
8.4	Flow rates of the constant viscosity model	91
8.5	Sampling of the source layer for the constant viscosity model	92
8.6	3D plume evolution of the constant viscosity model	93
8.7	The constant viscosity model melting region	94
8.8	Mitrovica / Forte viscosity profile and ascent rate	95
8.9	Thermal evolution of the Mitrovica / Forte viscosity model	96
8.10	Material starting depth of the Mitrovica / Forte viscosity model	97
8.11	Flow rates of the Mitrovica / Forte viscosity model	98
8.12	Sampling of the source layer for the Mitrovica / Forte viscosity model	99
8.13	3D plume evolution of the Mitrovica / Forte viscosity model	100
8.14	The Mitrovica / Forte viscosity model melting region	101
8.15	Steinberger viscosity profile and ascent rate	102
8.16	Thermal evolution of the Steinberger viscosity model	103
8.17	Material starting depth of the Steinberger viscosity model	104
8.18	Flow rates of the Steinberger viscosity model	105

8.19	Sampling of the source layer for the Steinberger viscosity model	106
8.20	3D plume evolution of the Steinberger viscosity model	107
8.21	The Steinberger viscosity model melting region	108
8.22	Walzer et al. viscosity profile and ascent rate	109
8.23	Thermal evolution of the Walzer et al. viscosity model	110
8.24	Material starting depth of the Walzer et al. viscosity model	111
8.25	Flow rates of the Walzer et al. viscosity model	112
8.26	Sampling of the source layer for the Walzer et al. viscosity model	113
8.27	3D plume evolution of the Walzer et al. viscosity model	114
8.28	The Walzer et al. viscosity model melting region	115
8.29	Sampling of distinct source region reservoirs	117
A.1	Syrup viscosity	128
A.2	Syrup density	129
B.1	Experimental tank	131
B.2	Injection tank	132

List of Tables

4.1	Overview of the laboratory experiments set A.	31
4.2	Nominal and effective viscosity contrast of the laboratory experiments set A. . .	34
4.3	Overview of the laboratory experiments set B.	36
4.4	Nominal and effective viscosity contrast of the laboratory experiments set B. . .	40
4.5	Overview of laboratory experiments set C.	45
7.1	Overview of the point source laboratory condition numerical models.	71
7.2	Overview of the injection source laboratory condition numerical models.	76
8.1	Physical parameters of the mantle models.	86
A.1	Datacard Cerestar C*Sweet 01444	127
A.2	Further syrup data	129
B.1	Datacard Thermal Bath Haake C35 with Thermostat Haake F6.	132
B.2	Datacard Haake SIL180 silicone oil.	133
B.3	Datacard Progressive Scan CV-M10 camera.	133
B.4	Datacard Sony DCR-PC2E video camera.	134

Chapter 1

The Great Plume Debate

1.1 The Great Paradigm Change

In the middle of the last century, particularly in the 1960s, a series of discoveries in Geosciences dramatically changed the way scientists viewed the Earth's history and evolution. Using instruments originally developed for military purposes in World War Two and in the budding cold war, and oftentimes being funded by the military of their home country, scientist were able to study the earth, and in particular the ocean floor, in unprecedented detail (e.g. *Hamblin [2002]*). Four major scientific developments in particular brought about what is these days considered a 'paradigm change' in Geosciences. These developments were:

- Demonstration of the ruggedness and youth of the ocean floor:
While the first instances of ocean floor imaging date back to the middle of the 19th. century, when survey ships laying the trans-Atlantic telegraph cable used deep-sea line soundings to measure ocean depths, it wasn't until the first World War and the advent of early, primitive sonar systems that a clear picture of the ocean floor emerged. It soon became apparent that the ocean floor was much rougher than previously imagined. Further work during the 1940s, particularly by Maurice Ewing and the U.S. research vessel 'Atlantis' (*Schlee [1978]*) proved that the sediment layer on the floor of the Atlantic was much thinner than expected, hinting at a sea floor that was much younger than the 4 billion years estimated back then. In the 1950s, joint oceanographic surveys by scientists from many nations revealed a great mountain range on the ocean floor that virtually encircled the Earth. Dubbed the 'Global Mid-Ocean Ridge', this immense chain of mountains proved to be the most prominent topographic feature on the planet.
- Confirmation of repeated reversals of the Earth magnetic field in the geologic past:
Using instruments initially built for hunting submarines during World War Two, scientists began to find odd magnetic variations across the ocean floor. Further study revealed that these variations were not isolated or random occurances, but combined to form patterns of magnetic variations between normal polarity and reversed polarity reminiscent of zebra stripes. This strongly indicated periodic phases of reversed polarity in Earth's history, something that had been theorised about as early as the late 17th. century, and that had been concluded from the studies of Bernard Brunhes in France, Paul Mercanton in Australia and Motonori Matuyama in Japan in the first quarter of the 20th. century (*Backus et al. [1996]*).

- Precise documentation that the world's earthquake and volcanic activity is concentrated along oceanic trenches and submarine mountain ranges:
The early 20th. century saw the rapid development of a string of seismometer designs, each more sensitive and more precise than its predecessors (e.g. the work of Wiechert and La Coste). This enabled scientists worldwide to precisely pin down the locations of sources of earthquakes. It was *Wadati* [1935] and Benioff who first identified a number of prominent earthquake zones that were lying parallel to prominent trenches, and that were dipping downward at degrees between 40° and 60°, with earthquake sources situated several hundred kilometers deep in the Earth - the so-called Wadati-Benioff-zones. With the advent of global seismic networks to control adherence to the 1963 treaty banning above-ground nuclear testing, the accurate determination of earthquake locations took another big step forward, leading to identifying the world's oceanic ridges and trenches as the most seismologically active regions.
- Emergence of the seafloor-spreading hypothesis and associated recycling of oceanic crust:
The surprisingly young seafloor and its peculiar magnetic striping challenged the predominant theories about the buildup and evolution of the Earth. Scientists began to speculate on the mid-ocean ridges marking zones on the ocean floor that were structurally weak, and that were ripped apart along the length of the ridge. *Hess* [1962] and *Dietz* [1961] coined this process 'seafloor spreading' and suggested that Earth's crust must be destroyed at the same rate that it was produced at the mid-ocean ridges. Hess named the known oceanic trenches as the most likely places where crust was being 'destroyed', using the analogy of conveyor-belt motion. Extensive research and drilling programs in the late 1960s proved that the youngest rocks on the seafloor could be found at the crests of mid-ocean ridges, that these rocks consistently displayed present-day polarity, and that the oldest oceanic crust found did not exceed 200 million years in age - and in fact that much of the ocean floor was no older than 65 million years.

In light of these discoveries, scientists turned for explanation to an old theory that had previously received little acceptance: The theory of continental drift, as proposed by *Wegener* [1915]. While Wegener had hardly been the first to notice the remarkable fit of the South American and African coastlines (notable observers of this fact preceding Wegener include the Flemish mapmaker Abraham Ortelius, Francis Bacon, Benjamin Franklin, Alexander von Humboldt and Eduard Suess), his work had been the first to form this into a full-fledged theory of continental motion including extensive geologic and paleontologic evidence. Essentially, he postulated that all continents had once been joined into a supercontinent called Pangaea, and had subsequently drifted apart. Wegener, however, was nebulous on the driving force behind continental drift, suggesting tidal friction, precession forces or the Earth's rotation as the motor for continental drift. All of these forces were proven to be insufficient to propel continents by Harold Jeffries in 1928, relegating the theory of continental drift to the fringes of geoscience.

Incorporating Wegener's ideas and scientific proof with the newly found sea-floor spreading 'conveyor belt' of mid-ocean ridges and subduction zones as the mechanism behind continental drift, scientists were now able to formulate the theory of plate tectonics. In his talk at the AGU spring meeting in April 1967, W.J. Morgan proposed a plate tectonics model consisting of 12 rigid plates moving relative to one another¹. This model was later refined in *Morgan* [1968], and

¹An extended handout/abstract that was distributed to the audience of this talk has been published in *Tectonophysics* by Xavier Le Pichon, one of the scientists in attendance then, as a historical document. It was published along with a foreword by Le Pichon, and can be found as *Le Pichon* [1991] and *Morgan* [1991],

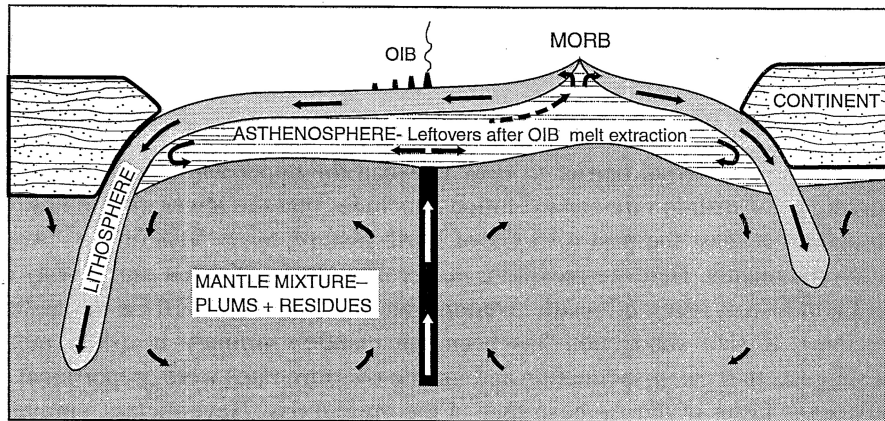


Figure 1.1: Figure from *Phipps Morgan [1998]* illustrating some of the major features of the plate tectonics model. Plates are created at mid-ocean ridges and recycled into the mantle at subduction zones. Mantle plumes bringing up deep mantle material cause intraplate volcanism and the formation of ocean island basalts (OIB). Whether the mantle is compositionally layered or intrinsically heterogeneous (as displayed) is still very much subject of discussion (see chapter 8, chapter 9 and the sections below).

along with *McKenzie & Parker [1967]* and *Le Pichon [1968]* formed the foundation of the plate tectonics model. This new theory could all of a sudden provide simple explanations for many of the geological and geophysical phenomena that pre-tectonic theories struggled to find answers to. Consequently, the theory of plate tectonics was eagerly accepted, probably being embraced by the earth sciences community faster than any prior scientific theory. This theory has been refined and extended over the following years, and while some points, like the driving force behind plate motion, are still contested, it is universally accepted as the mechanism behind a majority of geological and geophysical phenomena.

1.2 Hotspots and Mantle Plumes

Along with the phenomenon of seafloor spreading and of subduction, a number of other geological and geophysical phenomena were also critically reexamined and reevaluated for inclusion in the greater theory of plate tectonics. However, midplate volcanism leading to the formation of seamount chains such as the Hawaiian Islands, and excessive volcanism at segments of the mid-ocean ridge, such as evidenced on Iceland, could not obviously be linked with plate tectonics (figure 1.1).

Explanations of Hawaii and other Pacific seamount chains in terms of surface expressions of mantle plumes were presented as early as the early 1960s (*Wilson [1963a,b, 1965]*), in a time where plate tectonics had not been fully understood or generally accepted. Hawaii had been the object of extensive geological and geophysical research since the early 19th. century. In fact, *Dana [1849]* can be considered the first geologist to conclude that the order of extinction of Hawaiian volcanoes was approximately from west to east². Dana also recognized that the

respectively.

²This is also reflected in the Hawaiian myth of the goddess Pele, who was said to have first inhabited Kauai. After she had seduced the husband of her older sister Na-maka-o-kaha'i, she was chased by her vengeful sister eastwards island by island to Kilauea volcano, where she is said to reside to this day. For further reading, see e.g. *Nimmo [1987]*.

Hawaiian chain included the islets, atolls and banks that stretch for some distance to the west of Kauai. He saw, however, no reason to think that the volcanoes of the Hawaiian chain did not originate simultaneously. This idea was first proposed by *Cross* [1904], but received little attention.

The idea of *Wilson* [1963a,b, 1965] was that the long-lasting periods of volcanism as evidenced at locations like Hawaii and other parallel volcanic chains could only happen if relatively small, persistent and exceptionally hot regions - regions he called 'hotspots' - existed below the plates to provide localised sources of high heat. More specifically, Wilson suggested that the distinctive linear shape of the Hawaiian island chain resulted from movement of the Pacific plate over a stationary hotspot in the mantle that would produce a constant source of magma by partially melting the Pacific plate. This in turn would lead to a continuing sequence of volcanic eruptions which would, eventually, form an island volcano. Continuing plate motion would, over time, move the island away from its magma source.

These ideas were picked up by *Morgan* [1971, 1972a,b], who proposed that hotspots are manifestations of convection in the lower mantle. Morgan outlined the idea of a mantle plume, a comparatively hot and narrow upwelling of deep mantle material that would partially melt when reaching the base of the lithosphere, thus serving as the hotspot source for volcanic chains. These melts would, on account of their origin, be compositionally different to the melts produced at mid-ocean ridges, thus providing an explanation for the differences observed between OIBs and MORBs (e.g. *Engel et al.* [1965]). In his initial 1971 paper, Morgan further identified about twenty mantle plumes on earth, ranging from the intraplate Hawaiian plume to the triple-junction Galápagos and Réunion plumes. Later he noted how closely spaced hotspots on the same plate had not moved significantly relative to each other, which he offered as evidence for the relative fixity and deep mantle origin of plumes. Morgan also pointed out that some hotspot tracks are traceable to flood basalts, and suggested that flood basalts are caused by the melting of a voluminous plume head at the onset of a hot spot.

1.3 The Plume Controversy

The mantle plume model did not receive the general acceptance with which the rest of the plate tectonics model was received. The reason for this might lie in the peculiarities of the plume theory: in general, the physics and kinematics of plumes are complicated and comparatively hard to observe, when observable at all. Adding to this, the observations relevant to mantle plumes span a wide range of fields, running from geochemistry to paleontologic dating, from sedimentological studies to seismic observations, from monitoring uplift and subsidence to measuring geoid and heat flow anomalies - and all of these processes would presumably interact on a global level. Also, it must be conceded that both Wilson and Morgan were proposing mechanisms responsible for plume formation that were, at the time, inherently not testable, thus giving rise to scepticism. Much of the early criticism leveled at the plume model is summarised in *Tozer* [1973], while *Holden & Vogt* [1977] presented a very humorous overview on the points and counterpoints of the plume debate (figure 1.2).

Over the following decades, both the plume model (e.g. *Yuen & Peltier* [1980], *Stacey & Loper* [1983], *Sleep* [1990], *Davies* [1990], *Loper* [1991], *Sleep* [1992b], *Steinberger* [2000]) and alternative models (e.g. *Sleep* [1984], *King & Anderson* [1995], *Anderson* [1996], *Anderson* [2000]) have been elaborated and specified. The following will briefly summarise the arguments and counter-arguments of the great plume debate:

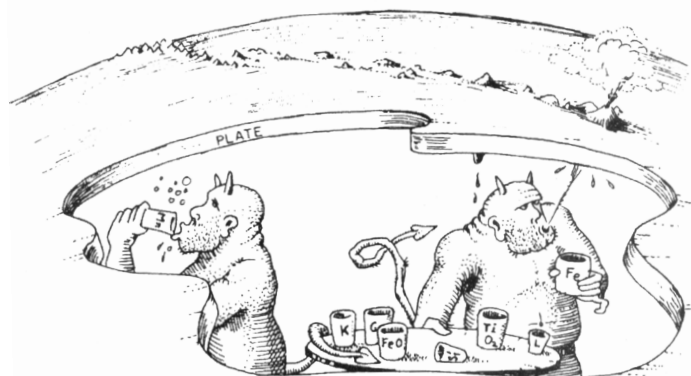


Fig. 7. Strange chemistry of ocean island tholeiites, hawaiites, balonites, and similar hot spot generated rocks, attributed to the culinary habits of X. Vulcan et al. (regurgitated material, in preparation, 1977).

Figure 1.2: *Figure and original caption from Holden & Vogt [1977].*

- Link between mantle plumes and flood basalts / large igneous provinces:
 The link between flood basalts and many prominent hotspots is well documented (e.g. *White & McKenzie [1989]*, *Richards et al. [1989]*, *White & McKenzie [1995]*, *Takahashi et al. [1998]*, *Courtillot et al. [1999]*, *Ernst et al. [2005]*). Essentially, flood basalts are seen as the result of the voluminous plume head thinning and uplifting the lithosphere and inciting a short-lived voluminous eruption of volcanic material, as e.g. demonstrated for the Deccan Traps by *Duncan & Richards [1991]*. Subsequent volcanism is less voluminous and is restricted to the long-lived hotspot track of the plume tail. However, some prominent hot spots exhibit no geological evidence for a plume head and associated voluminous volcanism - it seems likely, though, that these missing plume heads can be explained by the subduction of crust carrying the signs of plume head impact. Still, this has raised doubts among plume sceptics, who argue that the observed phenomena of rapid eruption of very large volumes and the formation of volcanic chains can be explained through propagating cracks in the lithosphere and resulting stress- and pressure-release melting, through lithospheric delamination, or through giant bolide impact (*Elkins-Tanton & Hager [2005]*). However, it is very much contested whether these processes can actually produce melting and voluminous volcanism on the scale that e.g. flood basalts seem to require.
- Distinct geochemical characteristics in Ocean Island Basalts:
 Ocean Island Basalts (OIBs), such as found at many prominent hotspots, display geochemical signatures that are distinct from those produced at mid-ocean ridges or subduction zones. In particular, the enrichment in incompatible elements in OIBs hint at a melt source that is different from the upper mantle source of MORBs. This conclusion, however, has become contested through the discovery of many small MOR seamounts and some continental rifts that also share these peculiar characteristics, leading to the conclusion that such enrichment as e.g. characterised by a positive ΔNb can be the result of processes solely confined to the upper mantle and asthenosphere, like edge-driven convection (*King & Anderson [1998]*). However, these alternate models cannot explain the isotopic ratios of noble gases found in many hotspot basalts, which still point towards a 'primitive', undegassed melt source that must be attributed to material from the lower mantle. For more on the geochemical signatures found at hotspots, see section 1.4 below.

- **Interaction of Plumes and Ridges:**
 One of the key elements of the early plume models is that hotspot tracks cross ridge axes, implying that an off-axis hotspot can evolve into an on-axis hotspot and back into an off-axis hotspot. This is evidenced e.g. in the Kerguelen hotspot and resulting track, whose age progression switches polarity after ridge-crossing. The alternative models mentioned under the previous points, like lithospheric cracks, would not be expected to cross the free edge of a ridge axis (*Sleep [2002]*).
- **Numerical convection modelling readily reproduces mantle plumes:**
 The numerical study of convection processes in the mantle is a relatively new scientific field, only made possible through the tremendous increase in computational power and resources in the last two decades. Numerical convection models of the mantle readily produce mantle plumes, and serve as a valuable tool to constrain characteristics and behaviour of plumes that are not observable through seismic observations or other geophysical and geochemical techniques. However, numerical models always depict a simplified model of the mantle, for reasons of limited computational resources, the lack of adequate mathematical models to explain the physical processes in the mantle in their full complexity, and the physical properties of the deep mantle not being tightly constrained. This has given plume sceptics reason to question the validity and applicability of these numerical models. Still, the capabilities of numerical models are increasing almost as fast as the computer platforms they run on, with today's models incorporating a broad range of physical effects (like the visco-elasto-plastic behaviour of subducting slabs - see e.g. *Toussaint et al. [2004]* and *Stein et al. [2004]*) that was inconceivable even ten years ago. This continually increasing complexity of numerical mantle models suggest that, within time, models will be able to address many of the concerns that are voiced today. For more on numerical modelling, see chapter 5.
- **Replenishing of the Asthenosphere:**
 According to *Phipps Morgan et al. [1995b]* and *Phipps Morgan & Morgan [1999]*, up to 250 km³ per year of asthenosphere is destroyed by accreting to the bottom of lithospheric plates, or by entrainment at subduction zones. Obviously, this material has to be replenished somehow, and mass transport into the asthenosphere through mantle plumes obviously lends itself to being the dominant mechanism by which this replenishment takes place. Currently, there is no alternative process suggested through which adequate replenishing rates could be achieved.
- **Seismic observations hint at structures underneath many prominent hotspots that go down to the core-mantle boundary:**
 Regional seismic studies of oceanic hotspots have been conducted as early as the late 70s (e.g. *Ellsworth & Koyanagi [1977]*). With the advent of powerful advanced data acquisition and data processing techniques, these regional studies have been able to achieve investigation depths of up to 400km and more, confirming evidence of plume-like slow structures in the upper mantle beneath several hotspots (e.g. *Wolfe et al. [1997]*, *Laske et al. [1999]*). Typical diameters range between 100km and 300km, with the data indicative of temperature anomalies on the order of 300K. This is further supported by regional receiver function studies of the prominent 660km and 410km seismic discontinuities - significant thinning of the transition zone between these two instabilities has been observed e.g. for Hawaii (*Li et al [2000]*) and Iceland (*Shen et al. [1998]*), hinting at a deep mantle origin for either plume. Recently, *Montelli et al. [2004a,b]* presented arguably the best seismic

evidence for mantle plumes to date. Using the finite-frequency tomography method championed by *Dahlen et al. [2000]* and *Hung et al. [2000]*, they found that small-scale velocity heterogeneities (such as plume tails) are underestimated by "classic" tomography by up to 60%. The 'banana-doughnut' kernels of their study were able to resolve the seismic structures of at least nine plumes originating in the core-mantle boundary layer, as well as a number of other plumes whose structure could only be tracked to shallower depths, or that seem to exhibit 'gaps' in their plume tail. Lastly, analysis of SP_dKS and ScP waveforms hint at ultra-low velocity zones at the core-mantle boundary that may well be plume roots (e.g. *Garnero [2000]*, *Rost et al. [2005]*). While there is still concern about the reliability and resolution of the techniques involved as well as about the correspondence between seismic velocity and physical parameters, an alternative theory explaining the common observations of low-velocity anomalies under many hotspots has yet to be brought forth.

In summary, the plume theory has, by virtue of providing a comparatively simple and plausible mechanism to explain many of the phenomena observed in connection with intraplate magmatism and hotspots, become widely recognised today. The main problem with the plume theory lies with the lack of a linked tail and head at some localities and the absence of an identified seismic anomaly beneath some volcanic chains, as well as with the lack of firm definition and the resulting vagueness of the term 'mantle plume'. This lack of definition has paved the way for a plume population growth that seems, on close examination, somewhat excessive (e.g. the 5200 plumes that *Malamud & Turcotte [1999]* propose). Recent efforts to categorize and classify the plume model (e.g. *Courtillot et al. [2003]*) have curbed this number somewhat, with a vast number of scientists today assuming the existence of ~ 10 plumes or less.

Additionally, the subject of the driving mechanism behind the formation of plumes is still very much discussed. Suggestions range from subducting plates overlying the core-mantle boundary layer causing thermal instabilities or trapping hot D" material under slab material (e.g. *Tan et al. [2002]*) to extraterrestrial causes (e.g. *Abbott & Isley [2002]*, *Hagstrum [2005]*).

1.4 Motivation & Aim

As mentioned above, basalts from intraplate or hotspot ocean islands are found to have distinct geochemical signatures. In particular, at strong plumes like Hawaii, Iceland or Galápagos, there is evidence for at least three distinct components:

- A depleted component different from the depleted upper mantle source of MORB: For the Iceland plume, e.g. *Kempton et al. [2000]* find the depleted component present in Iceland basalts to be disparate to the depleted upper mantle sampled by the North Atlantic mid-ocean ridge. The high hafnium isotope ratio of the depleted component, being a long-lived and intrinsic feature in the Iceland basalts, presumably has its origin in ancient melting events. This is also evident in the Hawaiian basalts, for which *Hauri et al. [1996]* and *Lassiter & Hauri [1998]* preclude an asthenospheric or lower crust origin for the depleted component. Where in the mantle exactly the source region for this component resides is still a matter of ongoing discussion (e.g. *Hofmann [1997]*, *Hanan et al. [2000]*, *Fitton et al. [2003]*).
- An enriched component most likely associated to the presence of ancient recycled oceanic crust or to deep portions of recycled oceanic lithosphere:

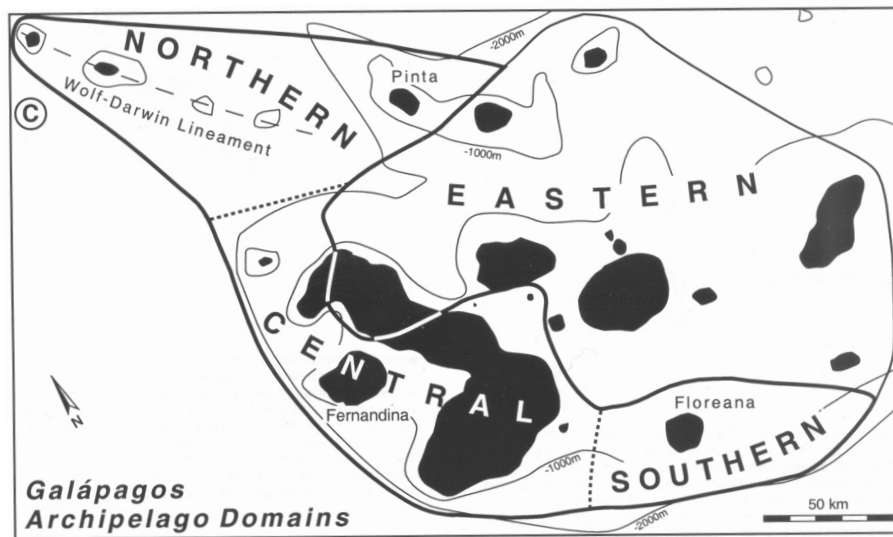


Figure 1.3: Figure from *Hoernle et al. [2000]* outlining the zonation of the Galápagos plume. Southern, Western and Northern domains form a horseshoe-shaped region of enriched material (denoted by the thick black line) that encloses the depleted Eastern domain.

The former had originally been suggested by *Hofmann & White [1982]*, and is widely documented in e.g. *Hart et al. [1992]*, *Christensen & Hofmann [1994]* and *Lassiter & Hauri [1998]*. The presence of such a component for the Iceland basalts has been suggested e.g by *Hanan & Schilling [1997]*. *Hauri et al. [1996]* allege that the Os-O isotope correlations of Hawaiian lavas serve as a strong indicator for crustal recycling, while *Niu & O'Hara [1991]* argue that oceanic crusts are isotopically too depleted to produce e.g. high-magnesian OIB melts, and suggest recycled deep portions of oceanic peridotitic lithosphere as a more likely candidate for the origin of this component.

- A primitive, 'undegassed' component associated with deep mantle origin:
This component is chiefly identified by Sr- and Nd-isotope values that approach those inferred for the bulk silicate earth. Also, the identification of near-solar neon isotopic ratios in Hawaiian and Iceland basalts suggests the presence of an 'undegassed' mantle component with high $[Ne_{solar}] / [U + Th]$ (e.g. *Dixon et al. [2000]*, *Moreira et al. [2001]*). It is further characterised by high $^3He/^4He$ ratios (e.g. *Graham et al. [1992, 1993, 1998]*), although this has recently been contested (*Class & Goldstein [2005]*; *Class et al. [2005]*).

This diversity in composition is generally believed to result from the upwelling plume entraining shallow mantle material during ascent, while potentially also entraining other deep regions of the mantle (e.g. the 'FOZO' region, *Hart et al. [1992]*). Geochemically, entrainment-induced mixing of mantle reservoirs has been invoked to explain the systematics of arrays of basalts from a given Hotspot (*Hart et al. [1992]*, *Farley & Craig [1992]*). In addition to this, the distinct spacial distribution of isotope characteristics, as evidenced e.g. in the 'Kea' and 'Loa' chains of Hawaiian volcanoes (e.g. *Hauri et al. [1996]*, *Abouchami et al. [2005]*) or in the 'horseshoe' pattern of enriched northern, central and southern domains encircling a depleted eastern domain found on the Galápagos islands (e.g. *Hoernle et al. [2000]*, *Werner et al. [2003]*, figure 1.3) have been attributed to the partial entrainment of distinct mantle reservoirs by the ascending plume. Apparently, plume entrainment has become an accepted 'base assumption' in geochemical thinking, even though it has been the focus of comparatively little geodynamic

investigation.

In order to understand the geochemical message brought to the surface by plumes, this thesis presents a comprehensive study on the dynamics of plume entrainment using analogue laboratory experiments and 3D numerical modelling, with the focus on the following three questions:

- Which regions of the mantle are most efficiently sampled by mantle plumes?
- Is the heterogeneous nature of mantle plumes inherited at the source, or does it develop through entrainment during plume ascent?
- How are the plume and plume entrainment affected by mantle discontinuities?

This thesis is subdivided into two parts.

Part one encompasses the analogue laboratory experiments:

Chapter 2 introduces the rationale behind analogue laboratory experiments, and elaborates on questions such as comparability, applicability and scaling. Chapter 3 presents the specifics of the laboratory experiment and measurement methods. Chapter 4 presents the laboratory experiments conducted as part of this study and discusses their results and implications.

Part two contains the numerical modelling work:

Chapter 5 gives a brief introduction to numerical modelling. Chapter 6 introduces the constitutive equations of the numerical model, and discusses approaches to discretisation, advection etc. Chapter 7 presents the numerical modelling of laboratory conditions, and discusses the exactness of laboratory result reproduction as well as the results and implications of these models. Chapter 8 propounds the results and implications of numerical modelling of mantle conditions, and discusses differences and similarities to the lab experiments and lab condition modelling.

Lastly, chapter 9 presents a summary and conclusions to this study, as well as providing an outlook for future laboratory and numerical investigations of plume entrainment processes.

Part One

Laboratory Experiments



Picture of a sample experimental setup. In the centre, the main experimental tank is connected to both heating baths (background left and background far right). Left of the center, in the foreground, is the CCD camera recording the experiments. Right of the center, in the foreground, the indicator for the thermoprobes can be seen. See chapter 3 for more on the laboratory setup.

Chapter 2

An Introduction to Analogue Experiments

Analogue laboratory experiments have long since been a very effective and useful tool for researchers to get a better understanding of physical processes. Compared to numerical simulations, analogue laboratory experiments are inherently well-resolved, can handle situations in which numerical methods prove inadequate (e.g. sharp interfaces, or multi-scale dynamics), and can be applied to phenomena for which equations do not exist today. Furthermore, laboratory experiments can be set up in 3D effortlessly, and all equations relevant to the experiment are precisely chosen, and solved, by Nature itself. Lastly, laboratory experiments provide a useful benchmarking tool for numerical codes simulating well-studied problems.

Analogue laboratory experiments do have limits, though. Most importantly, many of the physical phenomena we observe in Earth's interior (e.g. phase transitions, heterogeneous internal heating, or the simple fact that the Earth has a spherical geometry with centered gravity) cannot be adequately represented or studied in the laboratory, or cannot be studied at all. In addition to this, in situ measurements of many physical properties (like velocity, temperature or pressure) are complicated, costly, or flat-out impossible, especially in 3D. Lastly, boundary conditions in general are difficult to control, while certain boundary conditions (like free-slip boundaries) are almost impossible to implement at all.

This chapter will give a brief overview of previous works in laboratory plume modelling and the appendant theory and scaling laws. The chapter will close with a brief discussion of hydrodynamic instabilities.

2.1 Previous Laboratory Studies of Plumes

A number of studies have used analogue experiments to explore plume dynamics and entrainment processes. In most early studies, chemically buoyant material was used to initiate plume instabilities and to study the dynamics of plume rise. Some of the first experiments of this kind were carried out by *Whitehead & Luther* [1975], who filled a tank with glycerin and added a thin layer of silicone oil at the top. The tank was then turned 180°, and the lower density silicone oil started to rise through the onset of a Rayleigh-Taylor instability (see section 2.3.1). The onset phase of these experiments was found to agree well with the results derived from linear stability analysis (e.g. *Selig* [1965]). Additionally, *Whitehead & Luther* [1975] injected

fluids of different densities and viscosities into an experimental tank through its bottom. A ball of injected fluid formed on the spout of the injector and the lifted off the spout to form the plume head. A thin feeder conduit extended from the spout to the head, and newly injected fluid rose up this conduit. It was found that the shape and ascent velocity of a plume vary considerably for different viscosity ratios.

Since then several experiments with chemically buoyant material have been carried out, most notably *Olson & Singer* [1985], *Olson & Nam* [1986], *Whitehead & Helfrich* [1988], *Bercovici & Kelly* [1997], *Davaille* [1999], *Jellinek & Manga* [2002] and *Le Bars & Davaille* [2004]. As pointed out by *Richards & Griffiths* [1989], there is a significant difference between experiments carried out with chemically buoyant or thermally buoyant material. In the case of chemically buoyant material, diffusional growth of the rising plume head and especially the plume tail is unimportant, as chemical diffusion is very slow. Therefore, entrainment by diffusion of material into the plume head in this kind of experiment is rather unimportant.

Most experiments with thermally buoyant material have used a reservoir of a viscous fluid and have injected from below hot fluid of the same composition. The experimental work of *Griffiths* [1986a,b,c,d, 1991] explored the slowing effects of buoyancy diffusion first hinted at by *Olson & Singer* [1985]. In contrast to the continuously injected plumes of previous studies, Griffiths injected a fixed volume of warm glycerol into a larger container of the same material at a lower temperature. These solitary waves, or 'thermals', grew in size owing to entrainment of the ambient fluid, and their ascent speed decreased with time, demonstrating that buoyancy diffusion with subsequent entrainment slows plume ascent. This work was later expanded into continuous injection experiments: *Griffiths & Richards* [1989] and *Richards & Griffiths* [1989] explored the dynamics of deflected mantle plumes. They were able to show that in the case of deflection, most of the entrained material can become concentrated at the centre of the plume tail, whereas in vertically rising plumes the entrained material does not penetrate the tail's interior (*Griffiths & Campbell* [1990]). The work of *Griffiths & Campbell* [1990] focused on entrainment in the growing head of a mantle plume and showed how stirring of ambient mantle in the plume head could lead to effective entrainment during plume ascent. A general observation in these earlier studies is that in the case of injection of hot fluid from below, both the plume head and especially the plume tail are found to grow significantly through entrainment aided by thermal diffusion. In fact, it can be said that the work of *Griffiths & Campbell* [1990] shaped the perception of plume anatomy and interaction with the surrounding medium (see figure 2.1).

Neavel & Johnson [1991] studied entrainment under different injection rates and found that entrainment only occurred within a certain range of viscosity ratios. *Bercovici & Mahoney* [1994] and *Kumagai & Kurita* [2000] injected hot fluid into a tank holding two fluids of distinct density to examine the more realistic case of a non-homogeneous system. They categorised different behaviours of plumes hitting a density- and viscosity interface, and concluded that this interaction could explain cases of successive events in flood basalt volcanic history, as observed e.g. on the Ontong Java Plateau. Recently, *Kumagai* [2002] demonstrated that for certain high viscosity ratios, the vortex ring type structure of the plume head, as seen in *Griffiths & Campbell* [1990], is replaced by chaotic stirring within the plume head, and tried to connect the different anatomies of mantle plume heads with distinct isotopic signatures.

Comparatively little research has been dedicated to the entrainment rates of purely thermally driven plumes in the laboratory. The work of *Singer* [1986] already applied some of the

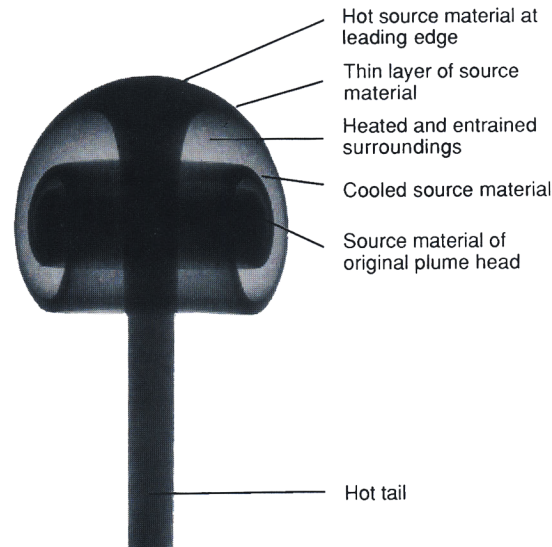


Figure 2.1: *Anatomy of an ascending plume, as presented by Campbell & Griffiths [1990]. Dark areas represent dyed material from the plume source, while light areas represent ambient material. The plume is differentiated into plume head and plume tail. While the tail acts chiefly as a conduit transporting material from the source to the plume head, the plume head entrains and envelopes ambient material within a thin outer layer of source material. Entrained material is wound up in spiral structures around a doughnut-shaped center region made up chiefly of source material.*

methods used for the laboratory experiments presented in this thesis, but received relatively little attention save for a mention in *Olson [1990]*. *Moses et al. [1993]* used thermochromatic liquid crystals to mark plumes rising from a cylindrical heater, but focused more on the interaction between multiple rising plumes and how plumes interact with a turbulent matrix fluid. The work of *Coulliette & Loper [1995]* mirrored the work of *Griffiths & Campbell [1990]*, but used a purely thermal input without corresponding mass input to generate plumes. They discovered a significant heat loss in the plume head during plume ascent, and concluded that estimates of mantle plume size, internal temperature and amount of entrainment must be reevaluated to reflect the importance of the observed heat loss from the plume head. This heat loss in the plume head was also observed by *Kincaid et al. [1995]*, even though their study focused less on the physics of plume ascent, but rather on the interaction between a spreading centre and an off-axis stationary plume. *Kaminski & Jaupart [2003]* focused on the dependence of plume ascent velocity and behaviour on the geometry of the experiment and the dependence on the Prandtl number, but paid little attention to the entrainment rates of their experiments. *Kerr & Mériaux [2004]* use entrained material to mark their laboratory plumes, but don't address the process of entrainment further, instead focusing on lateral transport (or the lack thereof) in ascending and stationary plumes and their interaction with an overlying moving boundary. Lastly, the pictures in *Davaille & Vatteville [2005]* show obvious entrainment and even signs of what will be, over the course of this thesis, be referred to as a 'plume sheath', but the accompanying text focuses mostly on the evolution of a thermal boundary layer as a source for plumes in the mantle.

2.2 Scaling Laws and Theory

Chief consideration in determining if an analogue laboratory experiment can provide useful insight into more complex physical processes, like those we find in the Earth's interior, is the question of proper scaling. It is common knowledge that the Earth's mantle can be considered to exhibit fluid-like behaviour if investigated over significantly long periods of time, and that the mantle is generally viewed as a thermally convecting system. For the analogue laboratory experiments to be comparable to mantle-like conditions, it must be assured that the fluid used in the laboratory experiments shows flow characteristics and behaviour similar to those of the mantle.

Thermal convection, also called Rayleigh-Benard convection, is the transfer of heat through fluid motion. The properties of thermal convection are determined by a number of dimensionless parameters: the Prandtl number, the Grashof number, the Rayleigh number, and the Reynolds number.

The regime of convection of a convecting system is determined by the dimensionless Prandtl number:

$$Pr \equiv \frac{\nu}{\kappa}, \quad (2.1)$$

where ν is the kinematic viscosity and κ is the thermal diffusivity of the fluid. The Prandtl number of the mantle is generally estimated to be $Pr_{mantle} \approx 10^{23}$ and more, and is generally set as $Pr_{mantle} \rightarrow \infty$ in numerical simulations. For the laboratory experiments, the Prandtl number is found to be $Pr_{lab} \gg 10^6$, which, while being noticeably smaller than the mantle values, does put the tank experiments in the same convective regime (*Grossmann & Lohse [2000]*). Thus, judging from the Prandtl number, lab experiments and mantle processes are comparable in their behaviour.

The ratio of buoyancy force to viscous force acting on a fluid is approximated by the dimensionless Grashof number:

$$Gr \equiv \frac{g\alpha\Delta TL^3}{\nu^2}, \quad (2.2)$$

where g is the gravity, α is the thermal expansion coefficient, ΔT is the temperature perturbation causing buoyant uplift, and L is the typical length scale. For both mantle and laboratory conditions, we find $Gr \ll 1$, thus showing that the mantle and the laboratory experiment can be considered as dynamically similar.

Prandtl number and Grashof number can be combined into one expression associated with the mode of heat transfer within a fluid:

$$Ra \equiv GrPr = \frac{g\alpha\Delta TL^3}{\nu\kappa}. \quad (2.3)$$

This is the Rayleigh number. With increasing Rayleigh number, the modes of convection change from simple two-dimensional structures to full convection (figure 2.2). When the Rayleigh number of a given fluid is below the critical value for that fluid (see also section 2.3.3 below), heat is transferred primarily through conduction. When the Rayleigh number exceeds that value, heat is transferred primarily through convection. The critical value Ra_{crit}

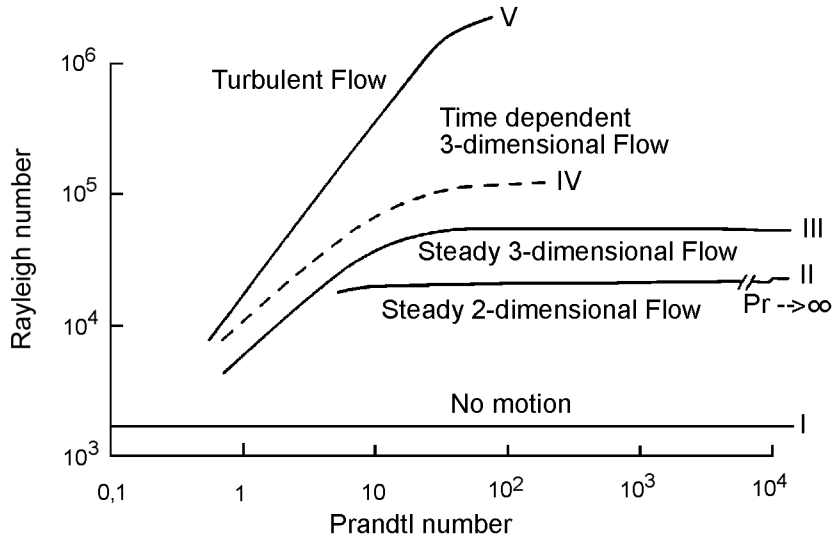


Figure 2.2: The influence of Prandtl number and Rayleigh number on the convective flow regime. Figure taken from [Krishnamurti \[1970\]](#).

for the onset of convective motion is on the order of 1000 (the exact value of Ra_{crit} depends on the mechanical and thermal boundary conditions - see e.g. [Chandrasekhar \[1961\]](#)). The actual Rayleigh number of the mantle is assumed to be $Ra_{mantle} \geq 10^7$, while the actual Rayleigh number in the experiments varies between approximately 5×10^5 and 5×10^6 in each experiment. Obviously, both laboratory and mantle conditions are well in the region of convective heat transfer, thus making both systems comparable in their behaviour (e.g. [Somatov \[1995\]](#)).

Finally, the Reynolds number gives the ratio of inertial forces to viscous forces:

$$Re = \frac{\rho v L}{\eta}, \quad (2.4)$$

where v is the mean fluid velocity, L is the typical length scale and η is the dynamic viscosity of the fluid. The Reynolds number determines whether flow in a given system is laminar or turbulent: Laminar flow occurs at low Reynolds number, meaning that viscous forces are dominant and fluid motion is relatively smooth and constant, while turbulent flow occurs at high Reynolds number and is dominated by inertial forces, producing vortices, eddies and other random fluctuation phenomena. The Reynolds number of the mantle is generally given as $Re \sim 10^{-17}$, while the Reynolds number in the experiments is on the order of $Re \leq 10^{-3}$. Thus, both mantle and laboratory conditions are placed firmly in the regime of laminar flow, making both systems dynamically similar ([Grossmann & Lohse \[2000\]](#)).

Taking these considerations into account, it can be safely said that the laboratory plume model can be considered to adequately reflect the physics during mantle plume ascent. More on the scaling of laboratory conditions, including a detailed scaling analysis for a number of laboratory setups, can be found in [Davaille & Jaupart \[1993\]](#) and [Davaille & Jaupart \[1994\]](#), as

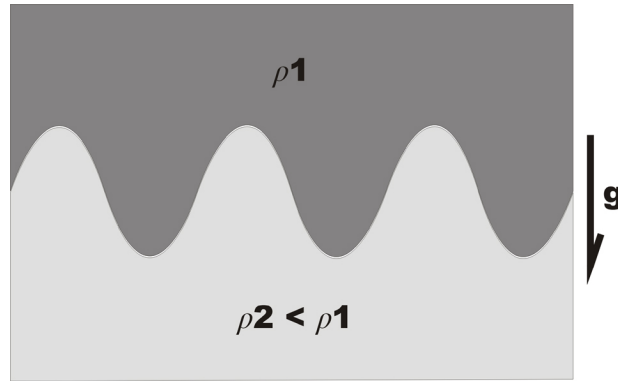


Figure 2.3: Schematic example of a Rayleigh-Taylor instability

well as [Gonnermann et al. \[2004\]](#).

2.3 Instabilities

If two fluids of varying physical properties (e.g. composition, density, temperature) meet at a common boundary layer, instabilities may form along this boundary layer. These take the form of a gradual defibration of the formerly smooth boundary between the two fluids. The most common hydrodynamic instabilities are the Rayleigh-Taylor instability, the Kelvin Helmholtz instability and the Rayleigh-Bénard instability. For the model problem at hand, only the Rayleigh-Taylor and Rayleigh-Bénard instabilities are relevant, but all three types shall be briefly discussed here. For an in-depth treatment of hydrodynamical instabilities, see e.g. [Chandrasekhar \[1961\]](#).

2.3.1 Rayleigh-Taylor-Instability

This kind of instability forms in an effective gravitational field \vec{g} when a heavy fluid overlays a lighter fluid (figure 2.3). This is also the case for a lighter fluid that is being flown against a heavier fluid, as is the case for the injection experiments presented in chapter 4.2. In that specific case, the effective gravitational field is given by the sum of the acceleration \vec{a} of the lighter fluid and the gravitational acceleration \vec{g} . The boundary layer between the two fluids in this case is unstable: instead of forming a slow-rising spherical bubble, the lighter fluid forms bulges that turn into into diapir-like structures that are brought up through the heavier fluid by buoyant force.

The growth rate ω for the Rayleigh-Taylor instability is given by e.g. [Shu \[1992\]](#) as:

$$\omega^2 = gk \frac{\rho_2 - \rho_1}{\rho_2 + \rho_1}, \quad (2.5)$$

where k is the wave number of the instability. Thus as long as $\rho_1 > \rho_2$, the instability will grow.

2.3.2 Kelvin-Helmholtz-Instability

This kind of instability forms whenever two fluids are moving tangential to one another, or a tangential discontinuity exists between the two fluids (figure 2.4). Given are two fluids, one overlying the other, in an effective gravitational field \vec{g} with a common boundary layer of surface

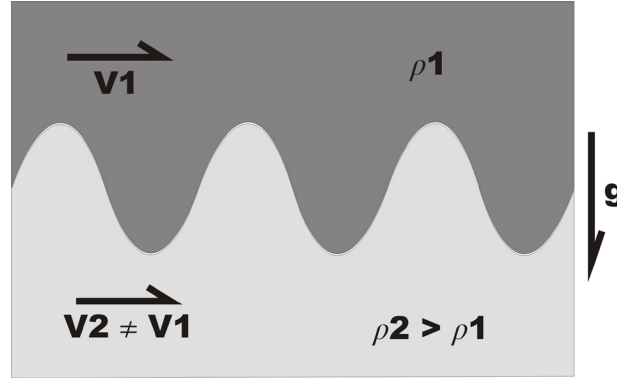


Figure 2.4: Schematic example of a Kelvin-Helmholtz instability

tension T . As long as the upper fluid is lighter than the lower, so $\rho_2 > \rho_1$, this system is stable towards Rayleigh-Taylor instabilities. Once the fluids start to move at speeds $v_1 \neq v_2$, they become prone to Kelvin-Helmholtz instabilities. The critical relative velocity is given by e.g. [Shu \[1992\]](#) as:

$$(v_1 - v_2)^2 \geq \frac{2(\rho_1 + \rho_2)}{\rho_1 \rho_2} \sqrt{Tg(\rho_2 - \rho_1)}. \quad (2.6)$$

The growth rate ω for the Kelvin-Helmholtz instability is given as:

$$\omega^2 = k^2 v_{rel}^2 \frac{\rho_1 \rho_2}{(\rho_1 + \rho_2)^2}. \quad (2.7)$$

This instability is dampened by the gravity field. A perturbation of wave number k is completely cushioned if

$$g > k \frac{\rho_1 \rho_2}{(\rho_2^2 - \rho_1^2)} v_{rel}^2. \quad (2.8)$$

2.3.3 Rayleigh-Bénard-Instability

This kind of instability forms in a fluid that is enclosed by two horizontal plates kept at different temperatures, with the temperature of the upper plate being lower than the temperature of the lower plate (figure 2.5). This system is unstable - small perturbations in the temperature field initiate instabilities that result in buoyant upwelling and the onset of a local convective flow. This, in turn, strengthens the temperature perturbation, resulting in a self-sustained process if diffusion of temperature and the viscosity of the fluid don't cancel out the fluid flow.

The velocity with which a parcel of fluid will rise as a result of thermal convection is given by the Stokes equation for velocity:

$$\vec{v} = \frac{1}{3} \frac{g \alpha \Delta T L^2}{\nu}, \quad (2.9)$$

where g is the gravity, α is the thermal expansion coefficient, ν is the kinematic viscosity, ΔT is the temperature perturbation, and L is the length scale. For convection to prevail, the transport time across the perturbation must be smaller than or equal to the diffusion time to the surface. Thus, putting 2.9 into

$$\frac{2L}{\vec{v}} \leq \frac{\left(\frac{1}{2}L\right)^2}{\kappa}, \quad (2.10)$$

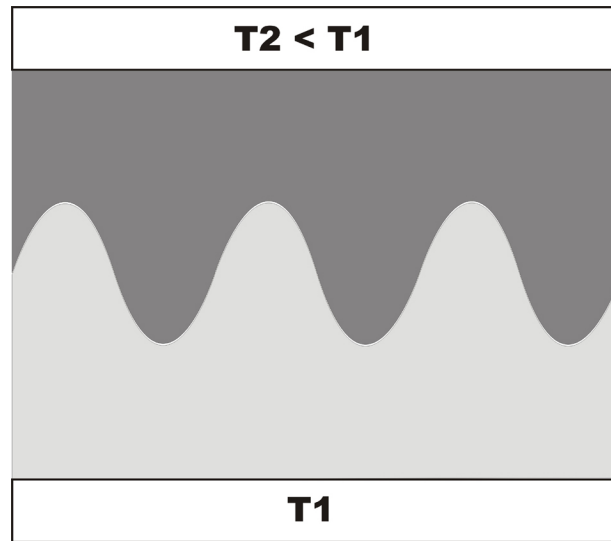


Figure 2.5: *Schematic example of a Rayleigh-Bénard instability*

with κ being the thermal conductivity of the fluid, we get a minimum criteria in the form:

$$Ra_c \leq \frac{g\alpha\Delta TL^3}{\nu\kappa}. \quad (2.11)$$

Here, Ra_c is the critical Rayleigh number defined along the lines of equation 2.3. It is a dimensionless number marking the onset of convection. As long as $Ra \geq Ra_c$, heat transfer through convection will prevail in the system.

Chapter 3

Laboratory Methodology

This chapter introduces the basic equipment, setup, preparation and measurement methods universal to the set of analogue experiments conducted for this study. Specifics of the different experimental setups will be discussed along with the experimental results in the next chapter.

3.1 The Experimental Tank

The main feature of the laboratory experiments is a plexiglass tank with a base of 20cm x 20cm and a height of 50cm, a sketch of which can be seen in figure 3.1. This inner tank is encased in a second outer plexiglass tank. This outer tank is connected to a thermal bath that is circulating water kept at a specific temperature during the experiments. Hot water is being pumped into the outer tank through a special, multi-punctured hose hanging just below the lid of the outer tank that distributes the fresh hot water equally over the outer tank. The water drains off through a valve and back into the heating bath, where it is reheated. This way, stable boundary conditions are achieved, with a negligible temperature gradient between the top and the bottom of the tank, and the experiments are relatively unaffected by changes in room temperature.

This experimental tank can be used for both point source thermal-driven plume, whole-bottom heated thermal layer plume and injection plume experiments due to interchangeable bottom plates. The tank features a small, easily sealable inlet for placing probes and other measuring instruments directly into the tank (see section 3.2.1 below), and another larger opening for quickly emptying the tank to change the experimental setup.

For the experiments, the inner tank is filled with a viscous fluid, in this case glucose syrup. The physical properties and other specific data of this syrup can be found in appendix A. The viscosity of the syrup is determined in advance using a tube viscosimeter. Since the syrup viscosity is very sensitive to changes in the temperature and water content of the syrup, the tank lid is heavily isolated with styrofoam and foam rubber to prevent dewatering¹, heat loss and temperature fluctuations at the surface of the syrup.

To further prevent heat loss and heat fluctuations, the areas of the experimental tank not surrounded by the outer heating tank (notably, the top and bottom of the tank), as well as

¹While a thin layer of oil covering the syrup has proven to be more effective in preventing dewatering, it has also proven to be impractical in conjunction with the experimental preparation procedure. See section 3.3 for details.

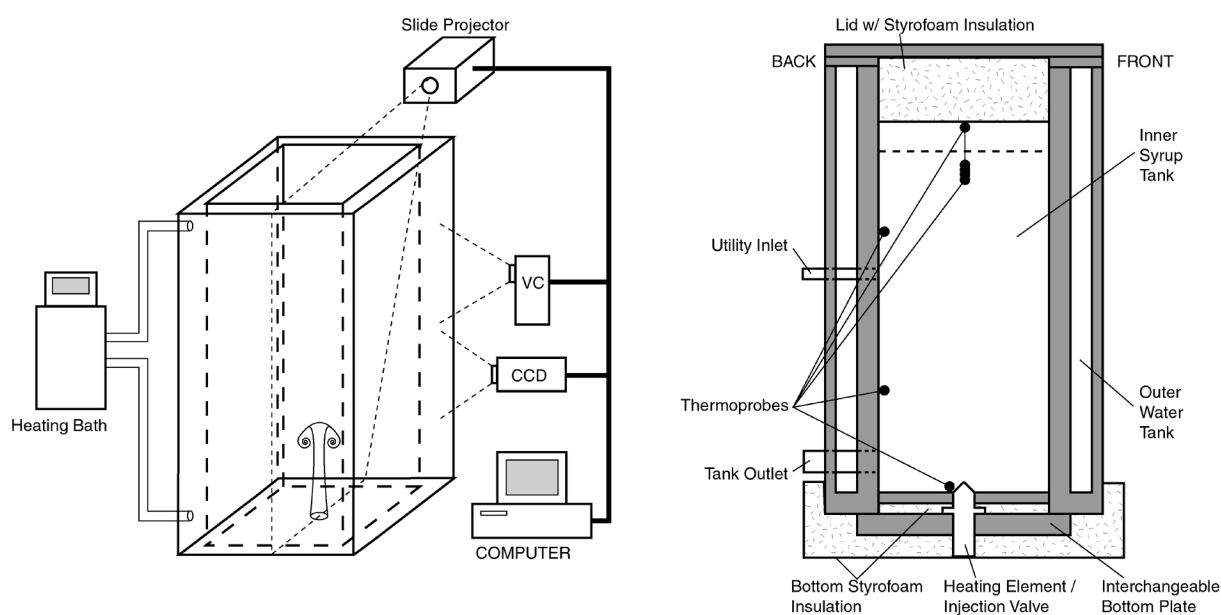


Figure 3.1: *Left: fundamental experimental setup, showing experimental tank and relative position of light source and recording equipment. Right: Cross-section of the experimental tank showing general layout and placement of thermoprobes.*

any feed pipes, are extensively insulated with styrofoam and insulation foam to prevent heat loss and heat fluctuations. The bottom insulation is particularly important for the injection plume experiments presented in section 4.2 to prevent unwanted heating of the bottom due to the hot injection tank situated beneath the experimental tank. The temperature of the water filling the outer heating tank is constantly monitored both through temperature sensors in the heating bath and through sensors in the inlet and outlet of the heating tank.

The sides and back of the experimental tank are covered with black cardboard to prevent ambient light entering the tank. The front side of the tank remains uncovered, providing an ample window for the CCD and Video recording instruments.

3.2 Specifics of the Measurement Methods

3.2.1 Temperature measurements

There are generally two ways of measuring temperature in a laboratory experiment - invasively and non-invasively. The former method uses direct measurements through thermoprobes to get temperature data. However, in the case of a flow experiment, no matter how small the thermoprobe, it is always affecting and disturbing the flow patterns - sometimes up to the point that the measurements themselves become unreliable, or that the continuation of the experiment after the measurement makes little sense. The latter method uses non-contact methods, like taking and processing an optical image of the experiment, to get measurements of the temperature fields. These methods are often very complicated or costly to implement, in addition to usually only being able to sample the temperature field of planar cross-sections of the experiment.

For the laboratory setup presented here, a non-invasive measurement technique as presented

by *Laudenbach & Christensen* [2001] was initially considered. This technique uses an advanced Schlieren photography method to sample the thermally-induced changes in the refractive index of the tank fluid. This is done by reflecting the beam of a He Ne laser at varying angles towards the tank, and measuring the time lapse between the initial signal and the arrival of the laser beam, as well as the offset of the laser beam from the focal point at its arrival at a CCD line array. However, besides being rather complicated to set up and calibrate, this method is very susceptible to the presence of tracer particles in the experimental fluid (*Laudenbach* [2001]), which makes it impractical to implement for the entrainment experiments of this study. While this problem can be circumvented by using fluorescent dye (e.g. *Coolen et al.* [1999], *Sakakibara & Adrian* [1999], *Seuntjens et al* [2001] and their application in *Kumagai et al* [2003]) or thermochromatic liquid crystals (*Davaille* [2005]), both approaches were deemed too costly within the budgetary scope of this work.

Therefore, it was resolved upon using an invasive temperature measurement method using fixed thermoprobes and a small handheld temperature indicator with two probes. The placement of the thermoprobes in the tank is illustrated in figure 3.1: two thermoprobes are fixed equidistant on the back wall of the experimental tank - these serve mainly to control and constrain the experimental boundary conditions. One thermoprobe is placed directly at the plume source, one thermoprobe is placed directly below the upper syrup boundary, and one thermoprobe is placed at the bottom of the tank lid to derive the upper boundary condition. The measurements of these thermoprobes are continually monitored and recorded during the experiments. In addition to this, in a number of experiments temperature measurements of the ascending plume head, plume tail, and plume surroundings were obtained through the use of the handheld temperature indicator. These measurements involve sticking the temperature feelers directly into the plume head and/or plume tail, thereby massively disturbing the ascending plume - thus, experiments are usually discontinued after these measurements. From these measurements, a reasonably accurate approximation of the plume temperature profile can be derived.

3.2.2 Particle Tracking Velocimetry

Since a comprehensive measurement of the temperature in the experimental tank over the whole duration of an experiment is not possible with the experimental setup presented here, the chief indicator on whether a given parcel of fluid in the experimental tank is to be attributed to the plume or to the ambient material around the plume is the velocity of that parcel of fluid.

There are a number of approaches for non-intrusive measurement of velocity in a given fluid available to scientists today. For systems in which the characteristics of flow can be adequately described by measuring at one single characteristic point in the flow, methods like Laser Doppler Velocimetry (e.g. *Lyn et al.* [1995]) or Acoustic Doppler Velocimetry (e.g. *Voulgaris & Trowbridge* [1998]) are suitable. For the experimental setup at hand, however, two approaches are most appropriate: Particle Image Velocimetry, where a specific display window in one image is scanned for in subsequent images through cross-correlation (e.g. *Adrian* [1991]), and Particle Tracking Velocimetry, where individual tracer particles are followed, and the global velocity field is formed from the resulting particle trajectories. This method, which has been extensively covered in *Hering* [1996], *Hering et al.* [1997] and *Hering et al.* [1998] is the method that is used in the experimental work presented here.

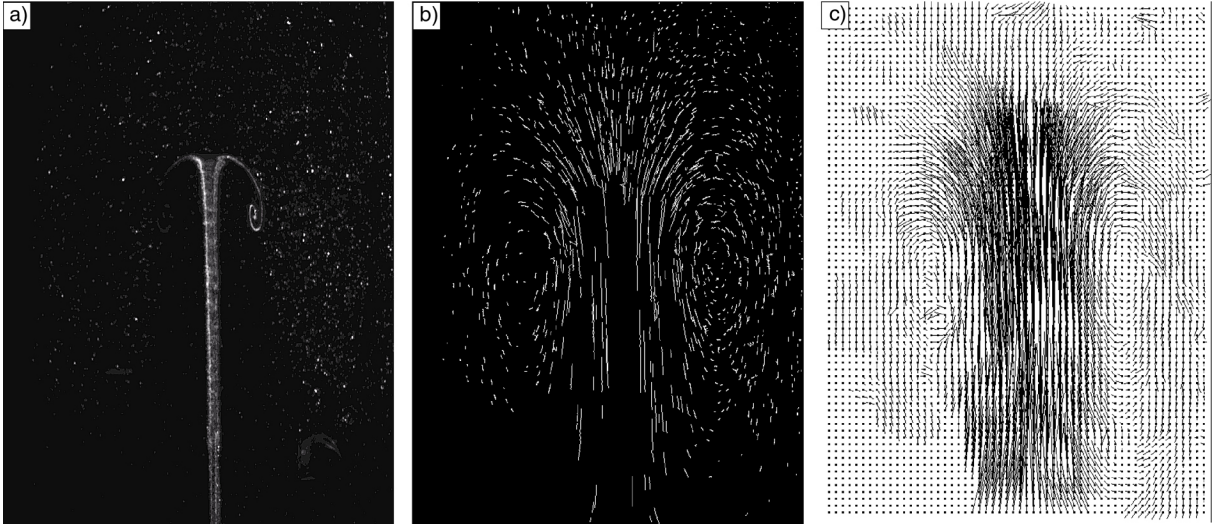


Figure 3.2: A sequence of pictures illustrating the particle tracking velocimetry method used in this work. a) a sample CCD image. Objects are determined through segmentation by greyscale value. b) Objects in successive images are then combined into trajectories. c) From these trajectories, the velocity field is interpolated. Typical speeds range from 0,02mm/sec (slow convective background flow) to 2mm/sec (fast plume core ascent).

The tracer particles necessary for the velocity measurement have to fit two demands: they have to be small enough so that the overall flow field would not be disturbed by the tracer particle, and they have to be visible enough for the recording instrument. In addition to this, the particles should ideally be stationary in the unperturbed fluid, so that any movement of the particle can be attributed to the effect of the flow and not on collateral effects like gravity. Assuming the particles to be spherical and neglecting the interaction between individual particles, the buoyancy term of a single particle can be derived. A density contrast between the fluid (ρ_f) and the tracer particle (ρ_p) results in a vertical drift velocity v_d :

$$v_d = \frac{(\rho_p - \rho_f) d_p^2}{18\mu} \cdot g, \quad (3.1)$$

with d_p being the particle diameter and μ being the dynamic viscosity of the fluid. To minimize this vertical drift, tracer particles should ideally be neutrally buoyant in relation to the fluid. The size of the tracer particles is also important in regard to the precision with which they follow the fluid flow: an ideal tracer particle has to be small enough so that changes in the flow field would instantaneously transfer onto the tracer particle. Assuming fluctuations in the flow field of a given frequency ω , the error of a tracer particle in following fluid flow fluctuations is given by [Hinze \[1995\]](#)

$$\epsilon_f(\omega) = k\omega^2 d_p^4, \quad (3.2)$$

where d_p is the particle diameter, and k is a proportionality constant that is discussed at length in [Hinze \[1995\]](#). To fit these criteria, small hollow glass beads ranging in diameter between 10 μm and 100 μm were chosen. They are small enough not to disturb fluid flow, and at temperatures and viscosity ratios typical for the experiments they are all but trapped in the viscous syrup, neither sinking nor noticeably rising². When illuminated, these tracer particles

²More on finding the right kind of tracer particles suitable for a given experimental setup, as well as a general introduction to fluid visualization, can be found in [Merzkirch \[1987\]](#).

brightly reflect light, showing up prominently on video and CCD recording while being small and light enough to not noticeably effect fluid flow³.

Illumination is realized using a slide projector with a slit aperture that provides a parallel sheet of light. This way, vertical or horizontal 2D slices of the flow field could be illuminated to be picked up by the CCD camera. Images are taken every four seconds in sequences of up to 41 images per sequence. The particle tracking procedure is illustrated in figure 3.2: Individual images are scanned for objects using segmentation by grey value (details on the segmentation methods used can be found in *Hering [1996]*, *Hering et al. [1997]* and *Hering et al. [1998]*), with the focal point of the grey value distribution marking the physical position of the object. The correspondence between two objects in succeeding images is then determined by a two-step algorithm: First, images are tested for direct overlap between objects in succeeding images. Then, objects in the first picture are enlarged through dilation and again checked for overlap with succeeding images. For more details see *Jähne [2005]*. To prevent merging of objects through dilation, this step is done for each object individually. From this, more than 80% of the objects on one image can be correlated with objects in succeeding images. Extrapolating particle positions from preceding images onto the current image can further serve to minimize erroneous correspondences. The succeeding particle positions are then combined into trajectories that, along with the corresponding velocity and time interval information, serve as the base for iterative interpolations of the object velocities using a recursive Kalman-filtering method for the velocity approximation and Adaptive Gaussian Windowing to filter erroneous correspondences. This results in a very accurate (standard error $e_{st} \ll 3\%$) approximation to the observed velocity field.

3.2.3 Plume Height

The height of the plume during the experiments is determined through bearing over a number of vertical scales that were fixed to the front and rear of the experimental tank. This provided a set of reference points from which the actual height of the plume can be approximated both during the experiment and from studying the video recordings of the experiment.

3.2.4 Entrainment Rates

In most of the experiments, the rising plume is marked by an absence of tracer particles. Entrainment is thus registered when a tracer particle enters the otherwise particle-free region of the plume. This simple criteria, however, is relatively complicated to implement into an automatic analysis algorithm because of the fuzzyness of the boundary between plume and ambient material, and because the particle tracking algorithm is unable to derive plume ascent velocities from an absence of particles. Even the very tiny, tightly spaced gas bubbles used to mark the plume that are introduced in section 4.1 are not sufficient for this. Consequently, the evaluation of the entrainment rates is done manually.

The video recording of the experiment is examined through an overlain sector grid serving as a reference frame for identifying specific particles. The plume ascent rate is derived from plume height measurements and the temporal progression of the experiment. Particles situated

³The visibility of the tracer particles could be improved upon by using silver-coated hollow glass spheres. However, these proved to not exhibit the buoyant behavior necessary for the experimental preparation presented in section 3.3.

in the transition area between the rapidly ascending particle-free plume source material and the mostly unmoving particle-filled ambient material that are moving in the same direction as the ascending plume are identified. Using the precise velocity information derived from the CCD recording, it is checked whether the identified particle is consistently moving at a speed of at least 10% of the plume ascent rate. If this is the case, the particle is considered to be entrained by the upward plume flow. If this is not the case, the particle is considered to be agitated and displaced by the passing plume, but not fully entrained. The comparatively high cutoff value was chosen because at the boundary layer between the plume and ambient material, it becomes exceedingly difficult especially at low ascent speeds to distinguish between plume-triggered flow and background fluid movement.

Furthermore, entrainment into the plume head and enrainment into the trailing plume conduit is considered separately. While there is little entrainment into the plume tail expected to be found, there should be some significant entrainment into the plume head, especially late in the experiment when the plume head is spreading out in reaction to the fluid surface boundary. These are two distinct entrainment processes, and shall be evaluated separately.

3.3 Experiment Preparation

Prior to conducting an experiment, a few preparations have to be made: The CCD camera has to be brought in focus for the main sample area of the tank and has to be calibrated, the experimental fluid has to be prepared, its viscosity needs to be checked, and the tracer particles have to be initialized.

To calibrate the CCD camera and particle tracking algorithm, a special calibration tank is being used that mirrors the conditions (wall strength, interfaces, etc.) of the proper experimental tank. A picture of the calibration tank can be seen in figure 3.3. The CCD camera is placed in front of the calibration tank at the same distance that it would later be placed towards the experimental tank. A calibration target holding four dots set in a cross-pattern on the target is placed into the tank. The exact distance between these dots is known, and is thus used to calibrate the field of vision of the camera, so that the particle tracking algorithm has the correct scaling values for particle displacement. Also, since it is inherently more difficult to focus on a sheet of small particles suspended in fluid than it is to focus on a solid target, this preparatory stage is also used to bring the camera objective in focus.

At room temperature as well as at experimental temperatures, the glucose syrup used, because of its high polysaccharide content, is prone to increase in viscosity over time due to the polysaccharides forming longer and more complex molecules. This is an unavoidable process. But since these long polysaccharides are unstable at higher temperatures, they can be broken up by heating the syrup to a temperature of at least 55°C, the recommended storage temperature for the syrup, and keeping it at this temperature for at least 24h. This ensures that the majority of the long-chained polysaccharides are destroyed and that the viscosity in the tank corresponds to the premeasured viscosity curve presented in appendix A. To further control the syrup viscosity, a small set of in-situ measurements is conducted prior to each experiment by dropping ball bearings with uniform, predetermined properties into the experimental tank and measuring their descent rates. These ball bearings are subsequently removed from the tank interior just prior to the start of the experiment, as not to disturb the bottom fluid flow in the tank.

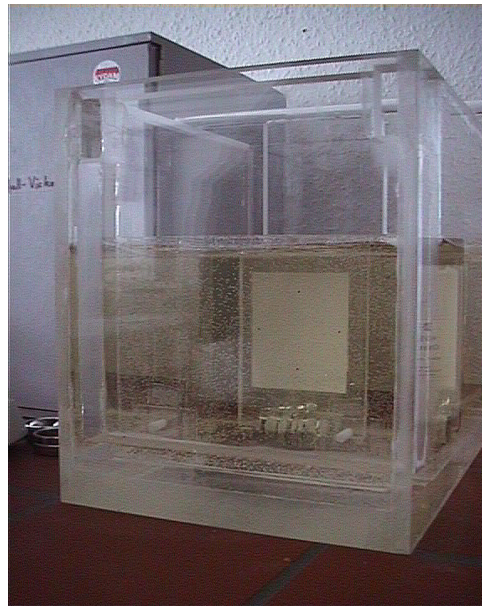


Figure 3.3: *Picture of the small tank used to focus the CCD camera and calibrate the particle tracking field of view. The calibration target can be seen in the center of the tank.*

Heating the syrup up to 55°C and more provides further benefit: At these temperatures, the tracer particles in the syrup begin to slowly float upwards due to their lower density, with ascent speeds being around 10mm/h . Thus, after a full two days heating up of the tank, the syrup will be bereft of almost all the tracer particles, which will by then float on the surface of the syrup. By carefully stirring the tracers back into the syrup after the syrup has been cooled down to experimental temperatures, the syrup can be marked by the tracers in a variety of ways. The most common tracer distribution used in the experiments is that of leaving the lowermost $50\text{mm} - 60\text{mm}$ free of particles, thus making an uncontaminated 'source region' for the plume, but other marking patterns, such as marking a vertical split in the tank reservoir with one side of the split having particles and one side being free of particles, are also used. Obviously, it is exceedingly difficult to produce a sharp, straight boundary through stirring alone, but this method of marking different syrup reservoirs has proven to be adequate for the laboratory experiments at hand.

Chapter 4

Laboratory Experiments

This chapter presents the specific experimental setups for the point source and injection source experiments, and the data derived from working with these setups. Each section starts with a presentation of the specific setup, and then presents experimental data, results and conclusions. The chapter then wraps up with a summary of the experimental work presented here and leads on to the numerical work presented in the next chapters.

4.1 Point Source thermally driven Plume

4.1.1 Setup

In this set of experiments, the plume is induced through a point source heating element fixed at the bottom of the syrup tank. Figure 4.1 shows a schematic sketch and photograph of the heating element used in this set of experiments. This heating element is connected to a thermal bath that pumps distilled water of preset temperature through the influx valve. The bath fluid gets sprayed against the inside of the conical heating tip before flowing downwards along the walls of the heating cone and returning to the heating bath via the outflux valve. Thus, the

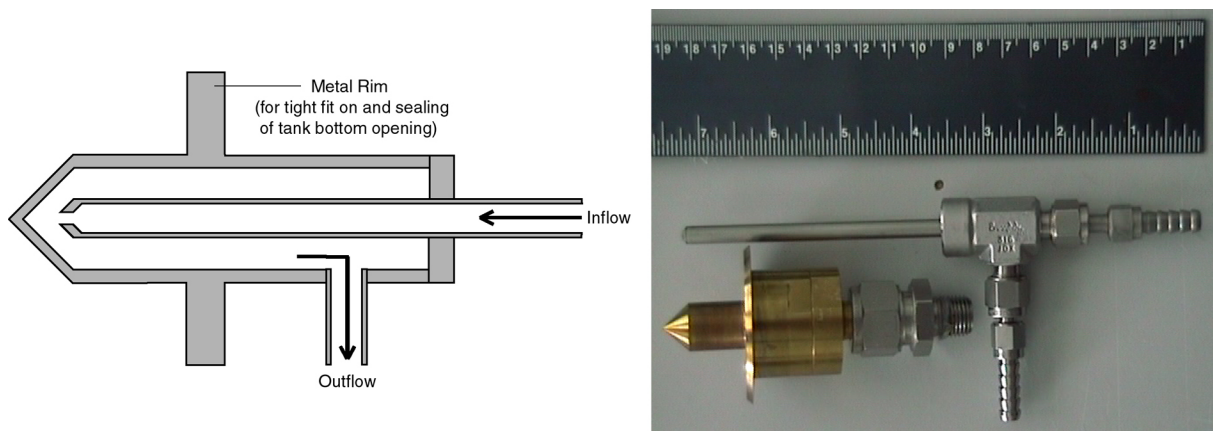


Figure 4.1: *Left: Sketch of the heating element. Hot water is fed to the heating element through the central pipe and drains off through the outlet at the side of the heating element. Right: Photo of the heating element showing conical head, inflow pipe and outlet.*

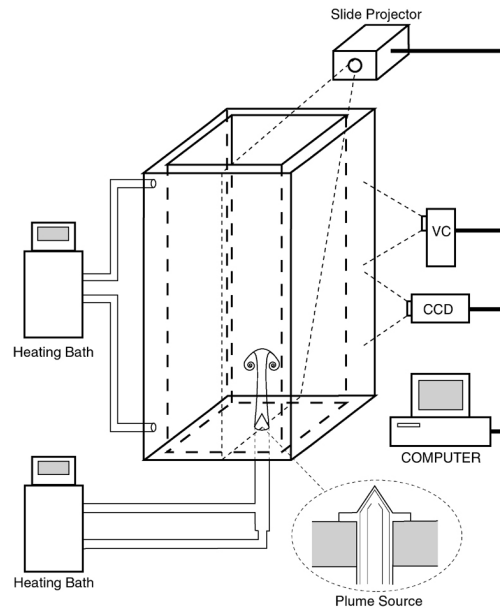


Figure 4.2: *Experimental setup for the point source experiments.*

value of the bottom temperature perturbation is precisely controlled through the heating bath. Heating element temperatures exceeding 100°C are possible through replacing the standard heating bath fluid (distilled water) with silicone oil. The silicone oil used in the experiments can be heated up to 180°C without risk - see appendix B for details. The extended experimental setup can be seen in picture 4.2.

4.1.2 Experiments

49 experiments are conducted in total using the point source thermally driven plume setup. Of these, 11 experiments serve to test and calibrate the experimental setup, and 11 are used to get information on the thermal structure of the ascending plume and are aborted after the flow field of the experiment is disturbed by temperature measurements (see section 3.2.1). The experiments can broadly be divided into two sets: Set A encompasses the experiments conducted at plume source temperatures below 100°C , and Set B encompasses the experiments conducted at plume source temperatures above 100°C . Tables 4.1 and 4.3 give an overview on the various experimental conditions under which experiments were conducted.

4.1.2.1 Set A

For the initial experiments of experimental set A, tank temperature is set at room temperature or slightly above room temperature, while the temperature perturbation is set to a moderate value of either 60°C or 80°C , which nominally results in a viscosity contrast of two orders of magnitude and more. The ascending plume in these experiments shows little resemblance to the 'classic' plume model: instead of the delicate structures seen in the *Griffiths & Campbell [1990]* plume, a very broad, diapiric uprising with no discernable structure is observed. The upwelling diapir shows little disposition to differentiate into the more discernable plume head and plume tail structure, but rises as one single, massive upwelling. Ascent speed for these plumes is on the order of $5\text{mm}/\text{min}$ and less, far below the theoretical prediction. Little to no entrainment can be spotted. Once the plume has crossed about half of the experimental tank, plume ascent

Set	T_T	T_{ps}	# of experiments	source marking	wall effects
A	25°C	60°C	2	no	yes
	25°C	80°C	2	no	yes
	30°C	60°C	2	no	yes
	30°C	80°C	2	no	yes
	40°C	60°C	4	no	no
	40°C	80°C	4	no	no
	45°C	80°C	2	no	no

Table 4.1: Overview of the various point source experiments conducted at low plume source temperature.

stalls considerably, with ascent speeds going as low as 2mm/min. Only the experiments with plume source temperature of 80°C reliably reach the surface boundary of the experimental tank - the experiments with plume source temperature of 60°C consistently failed to traverse the full height of the experimental tank at all.

The reason for this is twofold. First, the width of the upwelling under the conditions outlined above is higher than its distance to the tank walls. Hence, the fluid flow behaviour of the diapir is dominated by wall effects, which results in noticeable decrease in ascent velocity and gradual thwarting of plume ascent. Second, temperature measurements show the plume to be of surprisingly low temperature - little of the initial temperature anomaly remains when the plume reaches the surface.

Considering that the size of the ascending plume directly corresponds to the critical value of

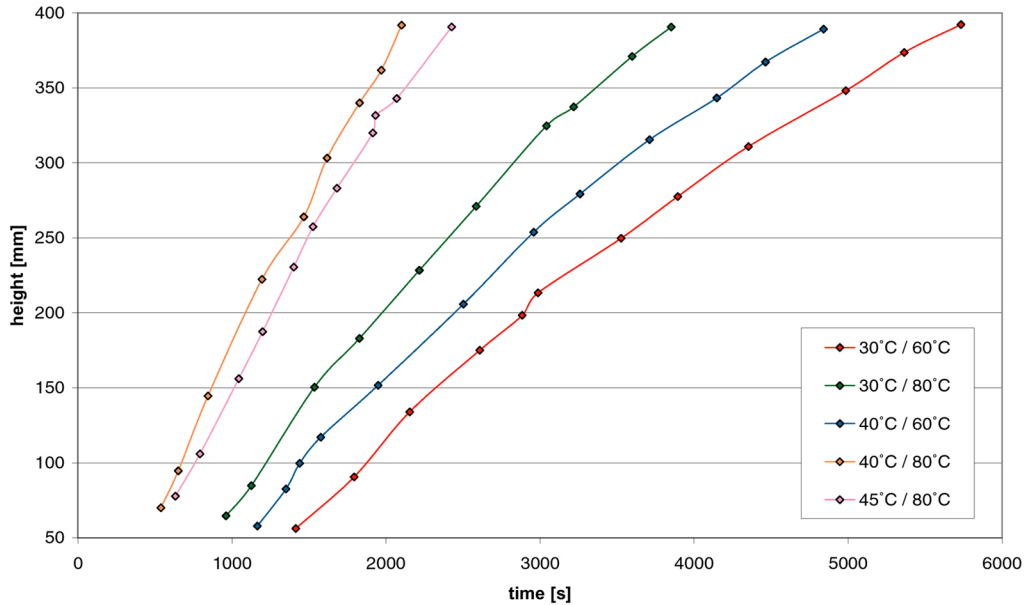


Figure 4.3: Plume ascent rates for the experiments of Set A.

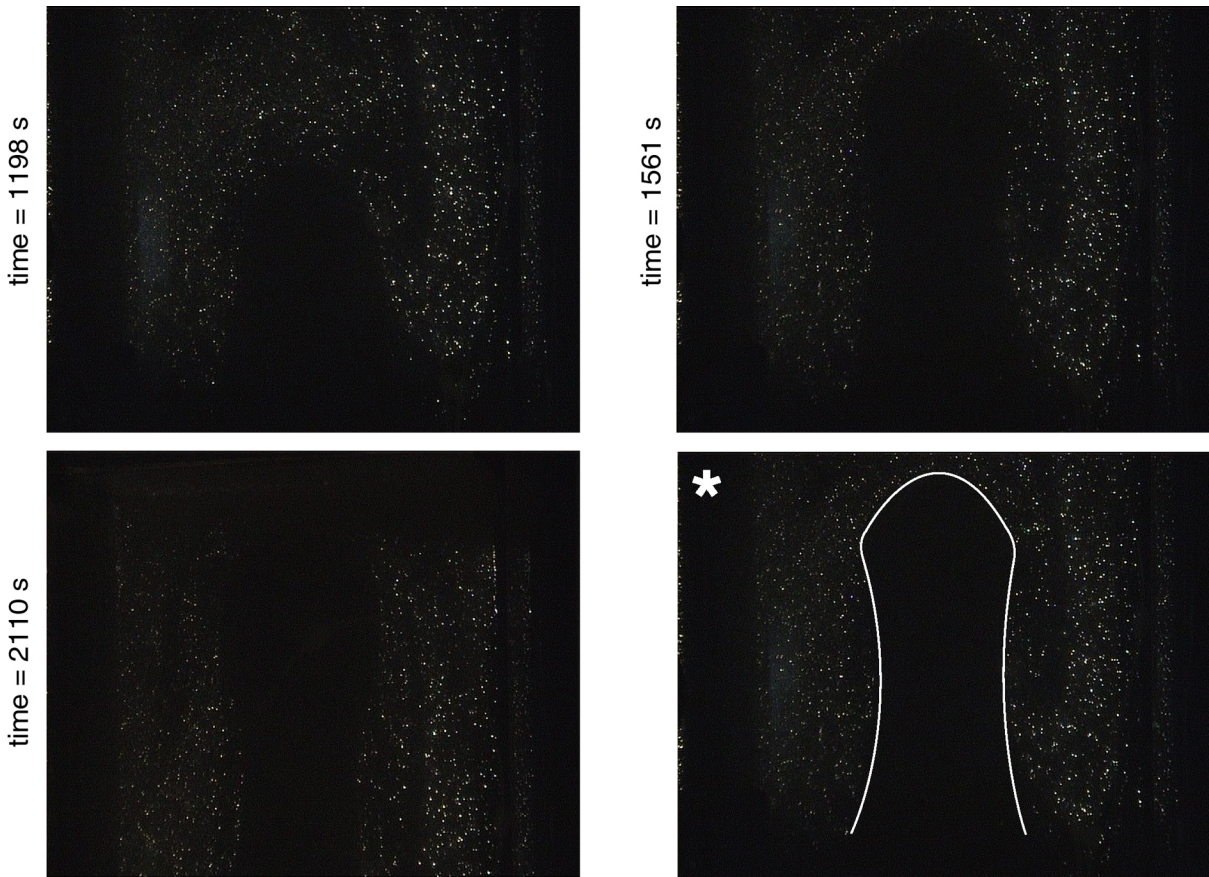


Figure 4.4: *Evolution of an experiment at 40°C tank temperature and 80°C plume source temperature. The bottom-right (asterixed) picture outlines the particle-free region of the experiment at 1561s for clarification.*

the Rayleigh number (see eq. 2.11), and keeping in mind that the viscosity of the syrup decreases exponentially with increased temperature (see appendix A) and/or increased water content of the syrup (Hasenclever [2004]) while the temperature perturbation increases linearly, it becomes obvious that to negate the wall effects and create narrower plumes, the most effective way is to reduce the viscosity of the tank fluid. Weighting the two methods at hand (diluting the syrup with e.g. water, increasing tank temperature), it is deemed more appropriate, more controllable, and more easily reverseable to simply increase the temperature of the tank fluid. A set of long-term measurements finds that the tank can be heated up to 40°C without temperature gradients in the tank (due to the 'water bath' method used for heating, meaning that the center of the tank will be noticeably colder than the continuously heated side wall material at significantly high temperatures) growing so large as to start a slow, global convective motion in the tank that could disturb the experiments.

Consequently, further experiments are conducted at tank temperatures of 30°C, 40°C and 45°C. In the 30°C tank temperature case, the initial plume ascent is narrow enough to avoid wall effects, but with increasing plume height, the plume broadens significantly, and as a result plume ascent is stalled in the upper half of the experimental tank. In the 40°C and 45°C tank temperature cases, the plume is consistently narrow enough as not to be affected by wall effects. The relevant ascent rates are found in figure 4.3. The plumes unaffected by wall effects (40°C / 80°C and 45°C / 80°C) exhibit a comparatively rapid, almost linear ascent that only starts to

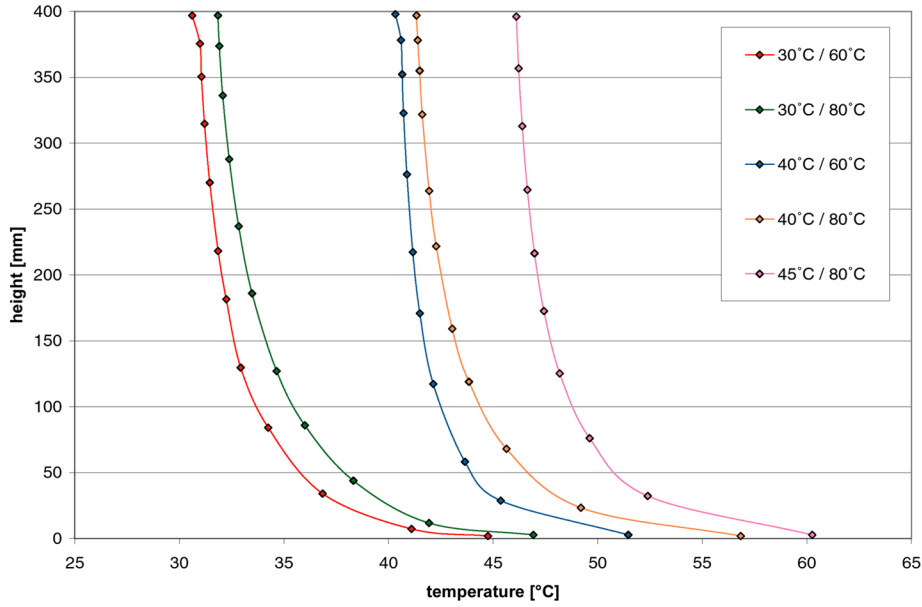


Figure 4.5: *Plume temperature profiles of the experiments of Set A. Displayed is the temperature of the plume core over the depth of the experimental tank, measured after the plume has reached the surface of the tank.*

slow down on the last 50mm, owing to the plume reacting to the upper surface boundary. The plumes that experience notable wall effects (30°C / 60°C and 30°C / 80°C), in contrast, show a gradually decreasing ascent speed over the whole course of the experiment, which in case of the 30°C / 60°C plume, is only increased by the relatively small initial temperature perturbation and subsequent low plume temperature anomaly.

A sample experiment is shown in figure 4.4. Plume ascent is sped up significantly compared to the room temperature experiments, with the plume head reaching the surface boundary in roughly 35 minutes. The upwelling ascending from the particle/no particle interface is distinctively diapir-like, with a broad bulge of particle-free material penetrating into the particle-contaminated region. This bulge extends into a long diapiric 'finger' that slowly but steadily rises to the surface. Again, there is little structure apparent in the ascending plume - while there is a slight inward bend behind the tip of the upwelling that might be seen as a hint for a more complex head-tail structure, overall the plume remains featureless. Entrainment into the plume is very hard to discern because of the low flow speeds at the particle-free plume / particle filled ambient tank material boundary. In fact, while some gradual upward motion can be detected along said boundary, the speed of this upward motion along the boundary is up to a factor 10 smaller than the ascent speed of the plume. There certainly is no evidence of entrainment of ambient tank material into the inner regions of the plume, let alone on the scale proposed by *Griffiths & Campbell [1990]* and others.

Figure 4.5 presents the temperature curves derived from probing along the center axis of the plume after the plume has reached the upper surface of the tank. As these curves show, the temperature difference between the plume and the ambient material is surprisingly low, as is the temperature gradient within the plume itself. This is due to no fault or flaw in the heating element itself - additional tests proved that the heating element reaches and holds the nominal temperature value for each experiment. However, the heating element proves not to be eminently effective in heating the syrup up to the nominal value - rather, the syrup starts to ascend in reaction to even small perturbations in temperature, preventing the heating element

Set	T_T	T_{ps}	nominal visc. contrast $\frac{\eta_0}{\eta(T_n)}$	effective visc. contrast $\frac{\eta_0}{\eta(T_e)}$
A	30°C	60°C	18,36	4,06
	30°C	80°C	70,18	5,06
	40°C	60°C	6,47	2,99
	40°C	80°C	24,75	4,52
	45°C	80°C	16,9	4,42

Table 4.2: Nominal and effective viscosity contrast at low plume source temperature.

from heating up a given parcel of syrup up to maximum temperature before this parcel of syrup moves away and is replaced by fresh, unheated syrup. Consequently the actual viscosity contrast between plume and ambient tank material is much smaller than initially planned for - table 4.2 lists the nominal and effective viscosity contrasts.

In addition to this, off-axis measuring of upwelling temperatures during and at the end of experiments shows that temperatures in the upwelling are surprisingly low even in immediate vicinity of the center plume. Only the innermost 10mm of the upwelling are noticeably effected by the bottom temperature perturbation, the rest of the clear upwelling material is, in general, less than 0.3°C warmer than the ambient particle-filled material, with the clear upwelling syrup at times being thermally indistinguishable from the surrounding syrup. This suggests that it is less thermal buoyancy and more drag from the ascending heated plume source material that causes such a broad uplift of clear material through the experimental tank.

4.1.2.2 Set B

To obtain higher effective viscosity contrasts, the fluid in the heating bath feeding the point source heating element is switched from water to silicone oil. Thus, temperatures exceeding 100°C can be achieved for the heating element. A summary of the experiments of set B can be found in table 4.3.

Increasing the temperature at the plume source above 100° has rather dramatic consequences for the appearance of the experimental plume: The syrup directly in contact with the heating element is heated close to its boiling point, leading to a loss of some of its water content through outgassing, and as a consequence many small bubbles of water vapour form in the syrup. The steam-bubble-riddled syrup is subsequently transported away from the plume source, serving as an excellent marker distinguishing the hottest regions of the ascending plume from the rest of the upwelling. The steam bubbles themselves do not appear to affect the properties or behaviour of the fluid flow: Estimates show that the amount of outgassing is too low to affect fluid viscosity through the loss of water, and the fact that light still penetrates the bubble-filled region hints at the fact that bubbles do not occupy a large enough volume percentage to affect the drag in the fluid which would lead to an increase in the viscosity value (*Ansari & Morris [1985]*).

While light is penetrating the bubble-filled region, the bubbles are still rather effective in dispersing light going through the plume. Thus, in the following photographs of the experiments, the left side of the experiment might appear to be somewhat underexposed because of the light

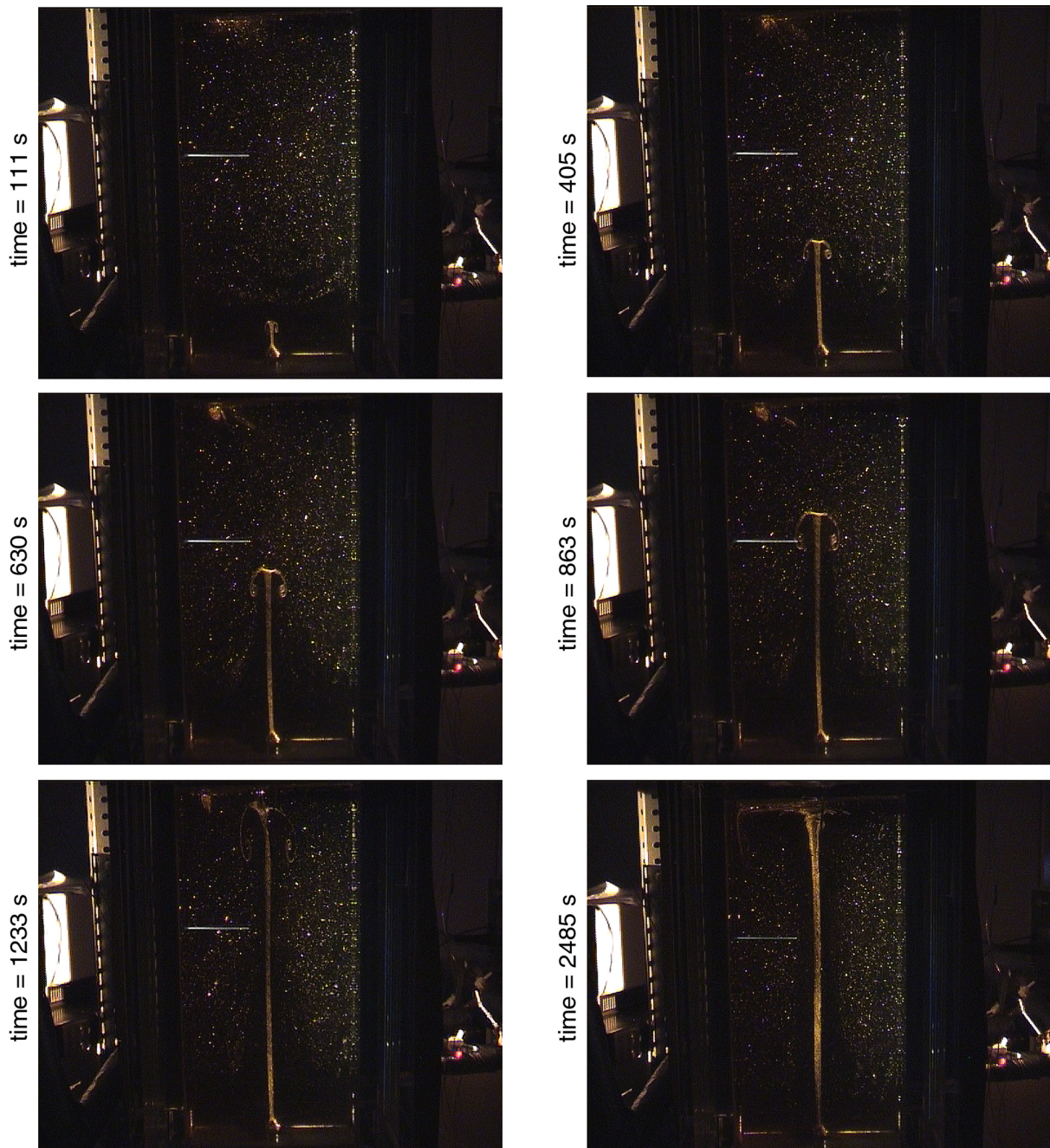


Figure 4.6: *Evolution of an experiment at 40°C tank temperature and 140°C plume source temperature. The plume starts as a small temperature perturbation above the heating element that already exhibits a noticeable plume head and plume tail ($t=111\text{s}$). The plume then ascends and hits the particle/no particle boundary ($t=405\text{s}$). After crossing the boundary, it becomes apparent that there is a considerable upflow of source material following in the wake of the plume - the 'plume sheath' ($t=630\text{s}$). This sheath persists during the entire plume ascent, and even after the plume has completely crossed the experimental tank, establishing a steady conduit ($t=863\text{s} - 2485\text{s}$).*

The horizontal line in the pictures is a reflection from an ill-fitting blind. The bright object on the left is part of one of the heating baths, while other parts of the experimental apparatus can be discerned on the far right of the pictures.

Set	T_T	T_{ps}	# of experiments	source marking	wall effects
B	30°C	120°C	2	yes	yes
	30°C	140°C	2	yes	yes
	40°C	120°C	6	yes	no
	40°C	140°C	6	yes	no
	45°C	120°C	2	yes	no
	45°C	140°C	2	yes	no

Table 4.3: Overview of the various point source experiments conducted at high plume source temperature.

coming from the light source situated on the right side of the experimental tank being scattered.

Figure 4.6 presents a sample experiment of Set B. Comparing the plumes in this set of experiments with figure 2.1, it is evident that the plumes now exhibit all the features of the 'classic' plume structure, like a pronounced plume head and plume tail, and filament-like structures of plume core- and source material being wrapped around a 'doughnut'-shaped region of plume core material. For all but the experiments conducted at 30°C tank temperature, plume ascent again noticeably speeds up compared to the experiments in set A, and the plume itself remains narrow enough over the entire traverse through the experimental tank to remain unaffected by wall effects. While the plume tail remains predominantly constant in diameter, the plume head gradually grows in size during ascent and eventually broadens up and spreads out completely when hitting the surface boundary of the experimental tank.

Even more remarkable, though, is the fact that this 'classic' plume structure, hereafter referred to as the 'plume core', appears to be embedded in a region of particle-free source material that is wrapped around the plume core like a sheath. This sheath is roughly equal in diameter to the plume head, and follows in the wake of the plume head for the entire ascent of the plume. This sheath acts as a sort of protective shell around the plume core, effectively preventing surrounding material from being entrained into the plume head or plume tail. This is especially evident in the plume head, which stays clear and particle-free throughout most of the plume's ascent. There is, however, entrainment of particles into the outer layers of the plume sheath.

It should be noted that when looking at the bigger picture of combined plume core and plume sheath, the plume can still be seen as one large diapiric upwelling comparable to the plumes of set A. It can therefore be safely assumed that the experiments of set A have the same interior plume core + plume sheath structure that the experiments of set B exhibit - only that it has not been marked as it has in this set of experiments.

Figure 4.7 gets into the details of plume head and plume sheath evolution throughout the experiments. The initial plume (figure 4.7-(180s)) starts as a very narrow temperature perturbation - note the size of the plume head in relation to the heating element. Because of the source marking through tiny steam bubbles, details of the interior structure of the plume are visible even at this early stage - already the 'classic' plume shape is well established, and

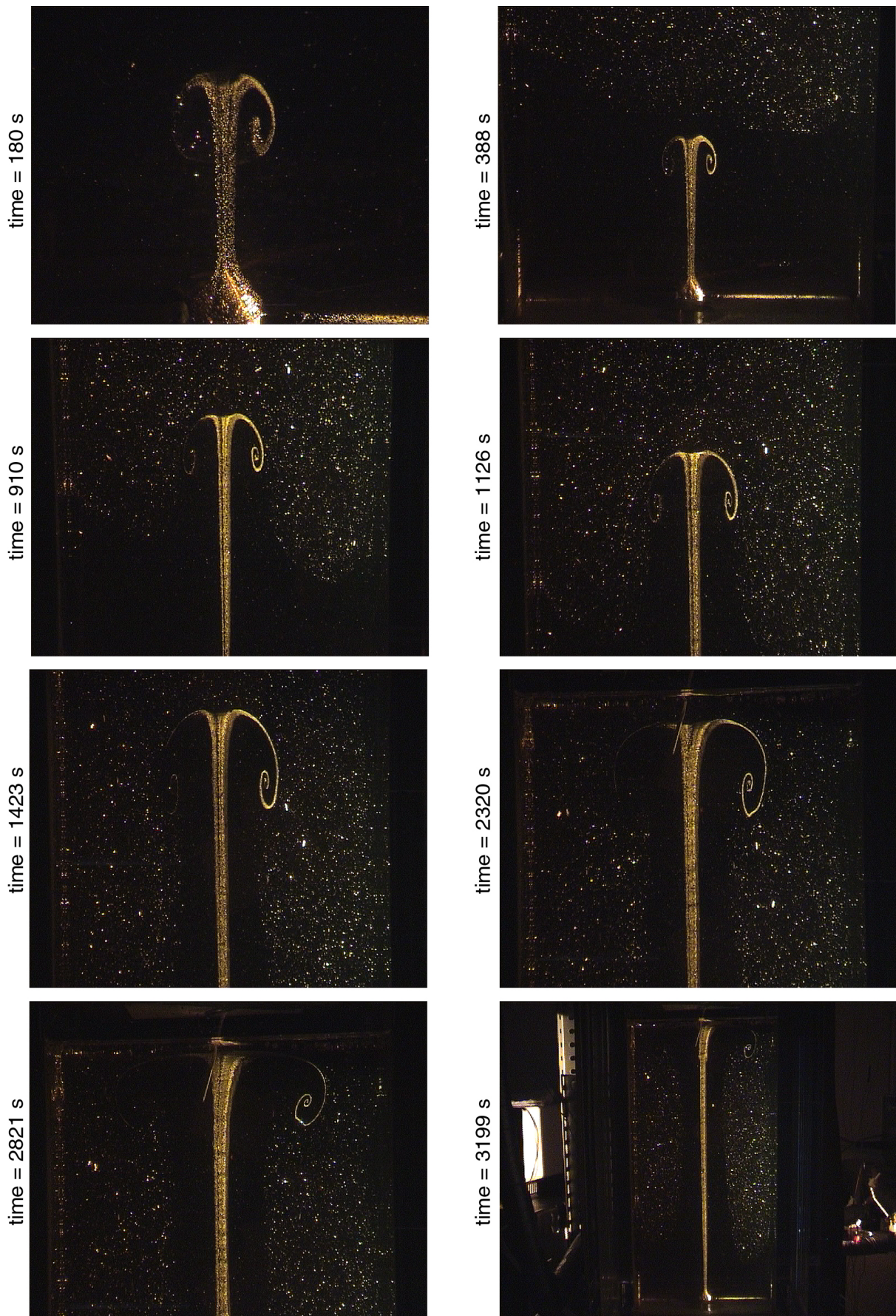


Figure 4.7: Closeups on the plume head and plume sheath during an experiment at 30°C tank temperature and 14°C plume source temperature.

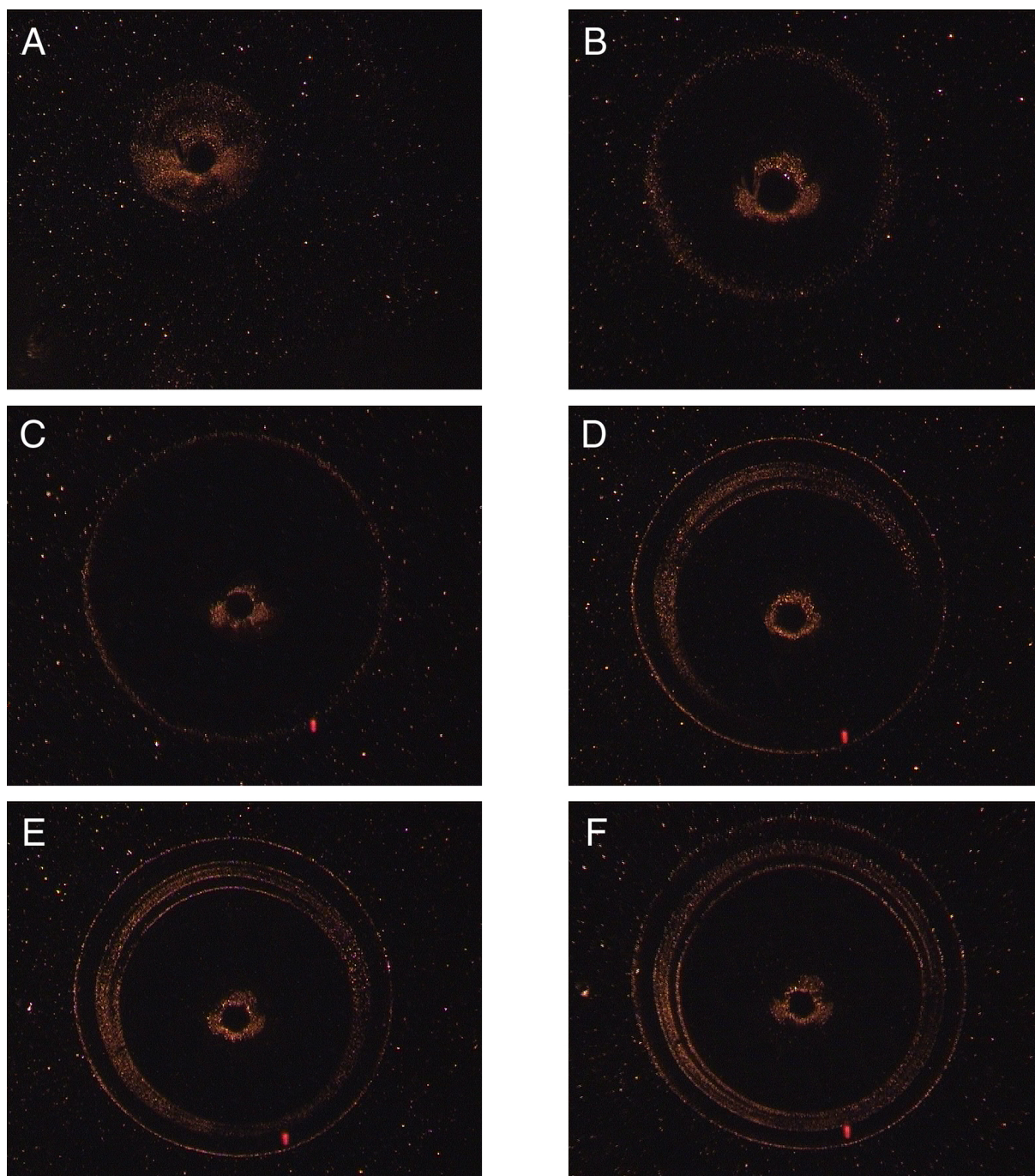


Figure 4.8: A sequence of shots taken as the plume head passes through a horizontal slice at about 240mm height. The red light at the bottom of the pictures is a reflection of the camera on the syrup surface.

the spiralling of source material around colder material in the plume head has already begun. This is even more pronounced when the plume hits the particle/no particle boundary (figure 4.7-(388s)). Subsequent images (figure 4.7-(910s, 1126s)) prominently display the particle-free sheath region broadly trailing behind the plume head. They also show how plume core material is continuously coiled within the plume head, while the plume head itself noticeably grows in

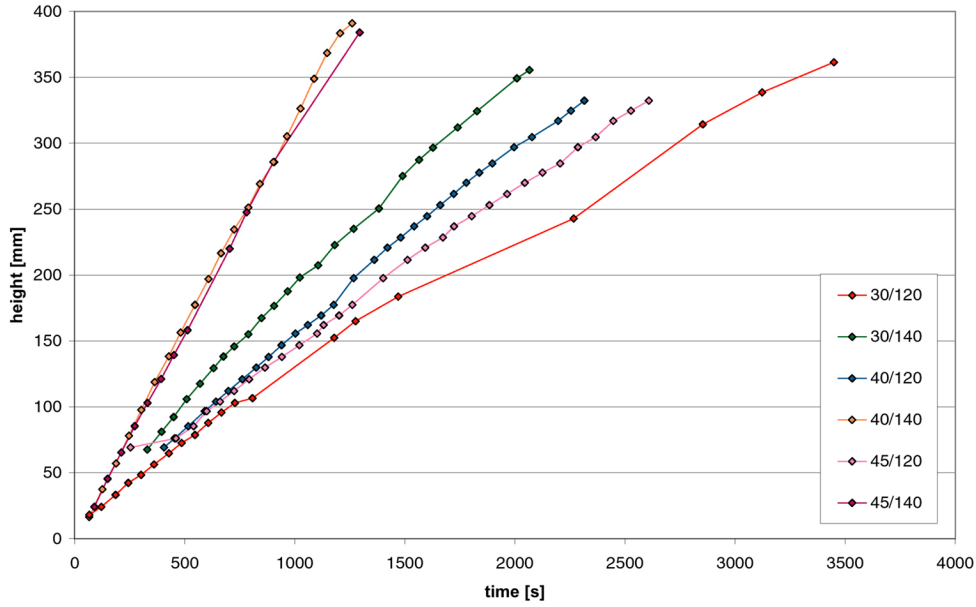


Figure 4.9: *Plume ascent rates for the experiments of Set B.*

size and diameter. Entrainment of particles into the particle-free sheath region subsequently narrows the corridor of clear syrup following the ascending plume head, as seen in figure 4.7-(1423s): the clear region of plume sheath has developed a somewhat conical form, growing narrower the closer it gets to the plume head. The material trailing the plume head, however, still displays a significant upward velocity along a width that corresponds with the total width of the plume head. This can be interpreted as particle-contaminated syrup being entrained into the outer layers of the plume sheath and consequently being transported upwards at the same rate as the rest of the plume sheath. In figure 4.7-(2320s), particles can be observed to have entered the region of the plume head. Note that the plume head has already begun to spread out in reaction to the surface boundary (also note the upper thermoprobe hanging into the syrup, and how it has narrowly missed the center of the plume in this experiment). All the particles now in the plume head region have been entrained into the plume sheath previously - thus what is observed here is less an interaction between the plume head and ambient material, but instead an interaction between the plume head and the plume sheath. In figure 4.7-(2821s), the plume head is in the process of completely spreading out beneath the surface. At this point, due to the rapidly decreasing upward velocities, it becomes increasingly hard to track which particle is still to be attributed to the plume sheath, and which particle can be considered part of the ambient material. Obviously, more and more particles enter the circumference of the plume head, but it is unclear whether this can still be seen as entrainment. Overall, though, as seen in figure 4.7-(3199s), the plume sheath persists through the entire plume ascent and beyond, forming a constant conduit that continues to bring both heated plume core and particle-free plume source material to the surface.

Further proof that the plume head remains free of particles is given in figure 4.8. Here, the passing of the plume head through a horizontal slice of the tank is documented. In figure 4.8A, the top of the plume head has just begun to enter into the illuminated region. Figure 4.8B has the crest of the plume head already well into the illuminated zone. Note the obvious difference between the ambient particle-filled material and the material within the bounds of the plume head. Also note that the slice of light is not perfectly perpendicular to the direction of plume ascent, which explains the ostensible asymmetry of the plume head and its apparent

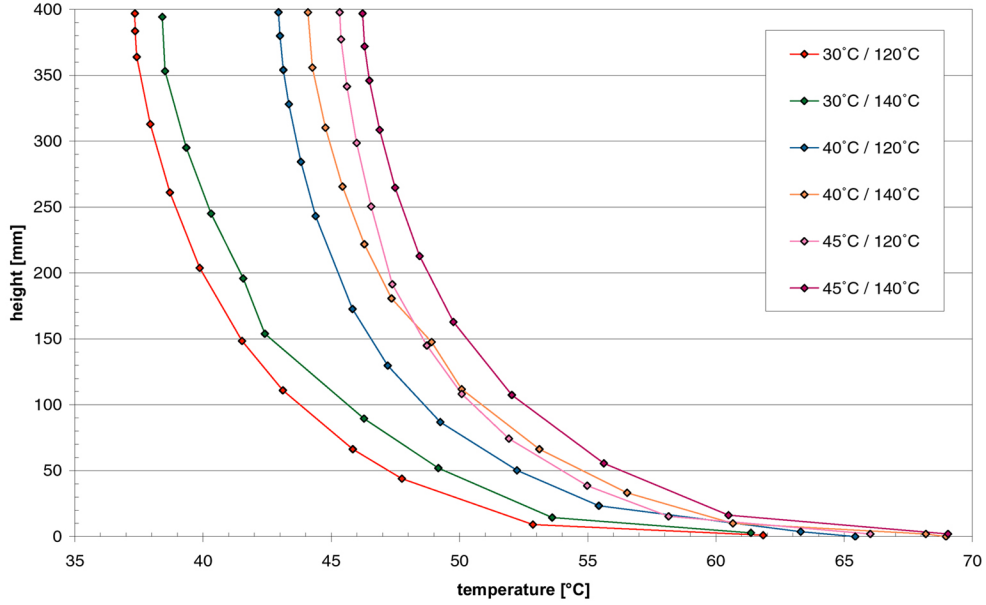


Figure 4.10: *Plume temperature profiles of the experiments of Set B. Displayed is the temperature of the plume core over the depth of the experimental tank, measured after the plume has reached the surface of the tank.*

bulging to the top-left. In figure 4.8C, the slice of the plume head has reached the point of maximum circumference, slightly above the 'doughnut' of coiled plume core material. The filigree structure of the 'doughnut' region is prominently shown in figures 4.8D-F, where the multiple filigree layers of plume core material slowly come into the field of view. Note, again, how the entire region within the bounds of the plume head remains free of particle intrusion.

Figure 4.9 presents the ascent rates for the experiments of set B. Ascent is practically linear, indicating an almost constant ascent velocity, with two exceptions: the experiments conducted at 30°C show a significant slowdown of ascent with increasing height. This, as in set A, corresponds to the onset of wall effects in the upper half of the tank when the plume head, due to the high viscosity of the ambient material, has grown so large that less than the plume head's width remains between the plume head and the walls of the experimental tank. It should

Set	T_T	T_{ps}	nominal viscosity contrast $\frac{\eta_0}{\eta(T_n)}$	effective visc. contrast $\frac{\eta_0}{\eta(T_e)}$
B	30°C	120°C	1050,54	19,32
	30°C	140°C	4038,98	20,38
	40°C	120°C	370,47	8,85
	40°C	140°C	1424,22	11,66
	45°C	120°C	252,95	8,74
	45°C	140°C	972,52	10,22

Table 4.4: Nominal and effective viscosity contrast at high plume source temperature.

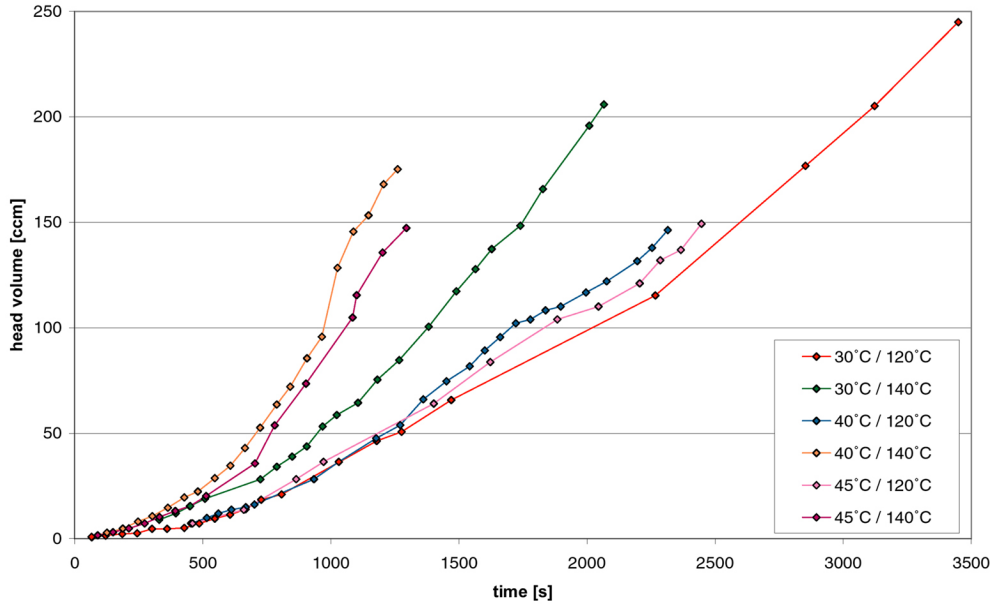


Figure 4.11: *Plume head growth rates for the experiments of Set B.*

also be noted that the experiments conducted at 45°C tank temperature exhibit slower ascent rates than the experiments conducted at 40°C. This indicates that the change in the ambient viscosity between tank temperatures of 40°C and 45°C is not as significant as the change in viscosity contrast for a given source temperature. Furthermore, this indicates that 40°C tank temperature gives the optimal conditions for the experiments at hand.

The temperature curves for set B are shown in figure 4.10. As in set A, these curves are derived from probing the plume after it has reached the upper surface of the tank. Again, the source temperatures measured are far below the nominal temperatures, for the reasons already discussed above. It is evident, however, that more of the original temperature anomaly is retained over the whole height of the plume, and that the plume, in general, is warmer than in the experiments in set B. Table 4.4 lists nominal vs. effective viscosities. For reasons outlined in appendix A, the viscosity values above 90°C are only approximations. As with the experiments of set A, the viscosity contrasts in this set of experiments are far below the nominal values for the aspired source temperatures - a fact that can only be blamed on the low effectiveness of the heating element.

As in set A, off-axis measuring of upwelling temperatures during and at the end of experiments are conducted. In accordance with the findings of set A, the temperatures in the plume sheath are remarkably low. Moving away from the plume core region goes hand in hand with a very sharp decrease in temperature. Effectively, the outer half of the plume sheath can be considered of comparable temperature to the ambient material, with temperature differences between the outer plume sheath and the surrounding material hardly ever rising above 0.1°C. The inner half of the plume sheath, the material directly in contact with the plume core, does exhibit some heating - but even here, temperature rarely rises to more than 1.0°C above tank temperature, leaving even the inner region of the plume sheath distinctively colder than the plume core. This, of course, raises questions on the driving mechanism of plume sheath ascent, since it obviously cannot be attributed to thermal buoyancy. It rather looks like the plume sheath is being affected by the pull of the ascending plume head and plume core material, so that it rises literally in the wake of the plume head, reminiscent of a laminar boundary layer.

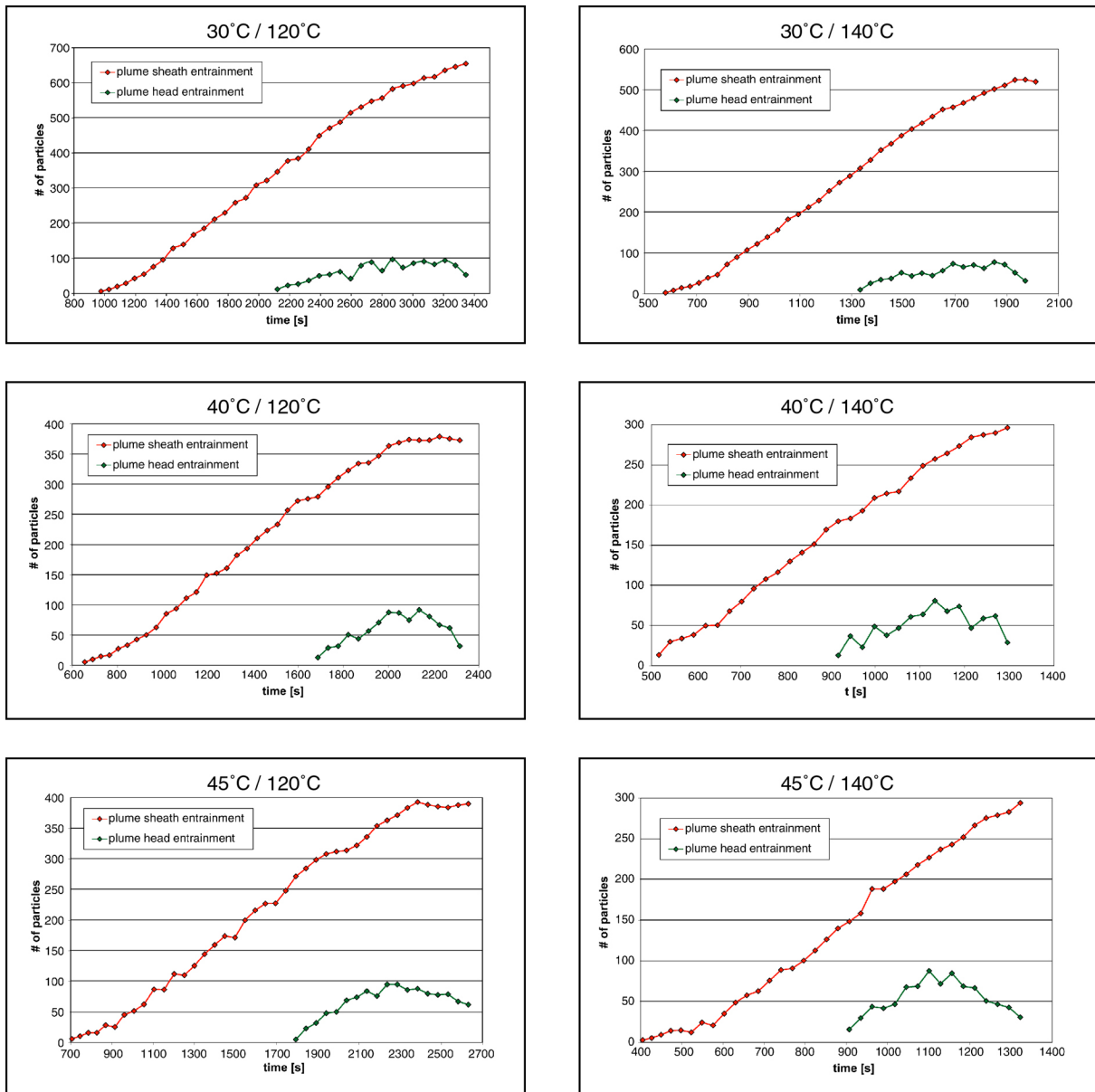


Figure 4.12: *Entrainment rates for the experiments of Set B. Counting of entrained particles begins when the plume leaves the uncontaminated source region at the bottom of the tank and stops with the plume reaching the surface.*

With the plume core marking making a distinction between plume head and plume tail in the broader diapiric upwelling possible, the evolution of plume head volume can be ascertained. This is presented in figure 4.11. Unsurprisingly, the experiments conducted at 30°C exhibit the largest plume head volumes. It should be noted, however, that plume head growth seems to generally experience an initial increase with time in growth rate up to a certain point, from where on plume head growth becomes linear, suggesting a steady growth rate. A good example of this would be the graph for the 40°C/140°C experiment between 600 and 900 seconds, or the graph for the 45°C/120°C experiment between 1000 and 2000 seconds. The subsequent increase in plume head growth can be attributed to spreading out of the plume head in reaction to the surface boundary.

The plume sheath, at the same time, seems to mirror the plume head's increase in diameter, growing somewhat thicker over time as well. Its volume can be estimated in treating the plume sheath as a hollow cylinder, and can be as large as fifteen times the combined volume of plume head and plume tail.

The continually increasing plume head volume hints at constant entrainment of material into the plume head, however, the fact that the plume head remains clear and particle-free throughout most of its ascent hints at the fact that the material entrained into the plume head is, indeed, plume sheath material that has its origins in the particle-free source region of the plume. Yet, some particles penetrate the plume head eventually, and there is also evidence of particle entrainment into the outer regions of the plume sheath. Figure 4.12 presents the amount of particles entrained into the plume sheath and plume head. While there is a general trend visible that more material will be entrained into the plume sheath the slower the plume rises, the amount of entrainment into the plume head remains basically constant. This serves as another indication that entrainment into the plume sheath and entrainment into the plume head are two distinct, decoupled processes.

4.2 Injection Source thermally driven Plume

4.2.1 Setup

This set of experiments mirrors the setup presented by *Laudenbach* [2001]. Here, the plume is induced through injecting hot syrup into the experimental tank through a nozzle at the tank bottom. The nozzle is connected via ball valve to a second tank in which the injected syrup is being heated up to the desired temperatures. During the experiments, a hydraulic piston driven by an actuator presses a light hydraulic oil into the second tank at a preset rate (figure 4.14). This oil displaces the syrup, which is consequently forced through the pipe, valve and nozzle into the experimental tank. The injection rate is precisely adjusted by computer interface prior

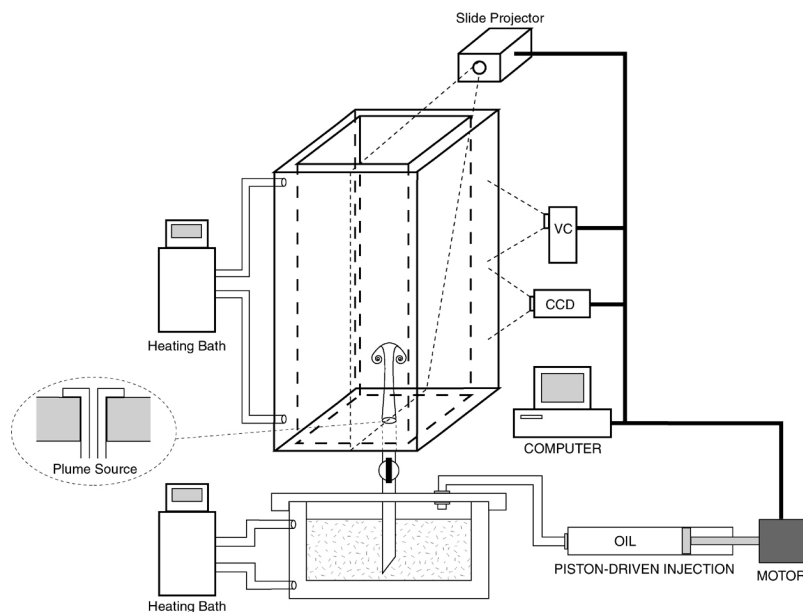


Figure 4.13: *Experimental setup for the injection source experiments.*

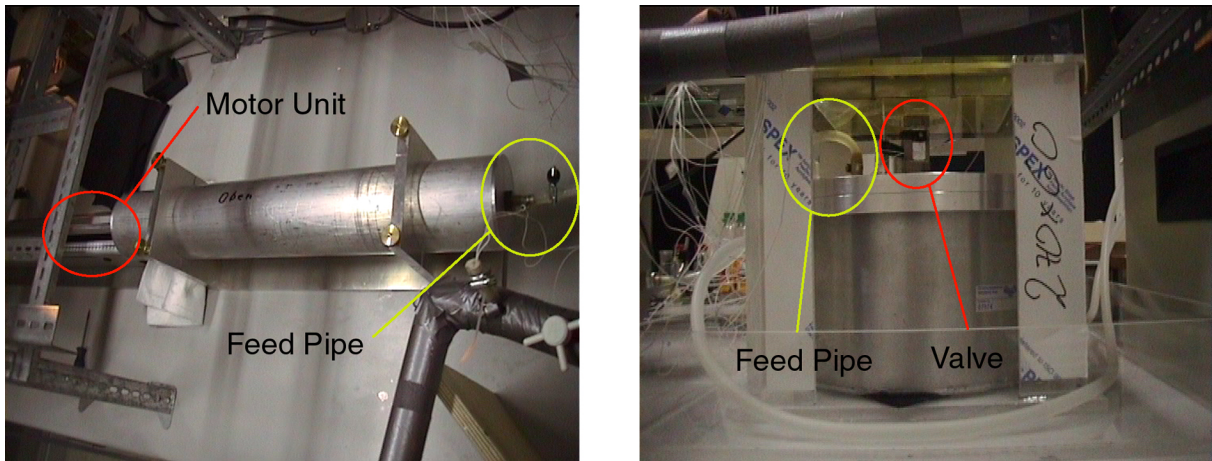


Figure 4.14: *Left: Photo of the hydraulic piston and motor assembly. Right: Photo of the injection tank situated beneath the experimental tank.*

to the experiments. Through this constant injection of hot material, the plume is initiated. The modified experimental setup can be seen in picture 4.13.

The main motivation behind conducting these injection experiments is to show that the plume sheath phenomena observed in experimental sets A and B are valid for experimental setups other than the point source thermally driven plume. Furthermore, injection of preheated material is inherently more effective in inducing a temperature perturbation at set temperature than the heating element used in sets A and B, meaning that the injection experiments will likely exhibit a larger and sharper viscosity gradient between plume core material and ambient material.

4.2.2 Experiments

15 experiments in total are conducted using the pressure driven plume setup. Of these, 3 experiments serve to test and calibrate the experimental setup, and 3 are used to get information on the thermal structure of the ascending plume and are aborted after the intrusive temperature measurement had disturbed the flow field (see section 3.2.1). Table 4.5 gives an overview on the various tank temperature, injected material temperature and injection rate conditions under which experiments were conducted.

For this set of experiments, the injected syrup remains free of particles, while the syrup in the experimental tank is thoroughly contaminated with particles. While this makes the plume core somewhat hard to discern, other methods (like colouring the injected syrup) promised little improvement, considering that experiments are conducted under comparatively low light conditions. The fact that the entire experimental tank reservoir is now contaminated with particles confers the additional benefit that the trailing material of the plume sheath will now also be particle-filled, allowing for a much more precise determination of flow speeds in the plume sheath.

Figure 4.15 presents a sample experiment from set C. The initial plume upwelling (figure 4.15-(1:42)) shows little resemblance to the sophisticated plume structure of the experiments of set B. In figure 4.15-(3:30), however, a marked segmentation into plume tail and plume head has become visible. This trend continues into figures 4.15-(5:39, 7:14), which prominently show

Set	T_T	T_{inj}	inj. rate	# of experiments
C1	40 °C	60 °C	10 $\frac{ml}{min}$	1
	40 °C	70 °C	10 $\frac{ml}{min}$	1
	40 °C	80 °C	10 $\frac{ml}{min}$	1
C2	40 °C	60 °C	15 $\frac{ml}{min}$	1
	40 °C	70 °C	15 $\frac{ml}{min}$	1
	40 °C	80 °C	15 $\frac{ml}{min}$	1
C3	40 °C	60 °C	20 $\frac{ml}{min}$	1
	40 °C	70 °C	20 $\frac{ml}{min}$	1
	40 °C	80 °C	20 $\frac{ml}{min}$	1

Table 4.5: Overview of the various injection plume experiments.

the plume head / plume tail separation, and also hint at the whorl structure and 'doughnut' on the far ends of the plume head. Figure 4.15-(11:02) shows a somewhat flattened plume head that is in the process of spreading out in reaction to the surface, while in figure 4.15-(12:28), the plume has reached the surface and is establishing a steady conduit between the bottom and top of the tank.

The region of high particle density visible in the center of the upper half of figure 4.15-(102s) lends itself to backing up the statement about plume head entrainment made after looking at the experiments of set B: that contrary to previous models presented e.g. by *Griffiths & Campbell [1990]* or *Coulliette & Loper [1995]*, material originating in the ambient region that the plume passes through is not entrained into the plume head. Following the region of high particle density mentioned above through figures 4.15-(210s-662s), it can be seen that the region, upon the plume head hitting it, is deflected sideways by the ascending plume and is literally slipping down the curvature of the plume head. In prior models this material would then be dragged into the plume head after reaching the base of the mushroom-shaped crown - however, it can be clearly seen that this is not the case. On the contrary, while some remains of the dense particle region can be spotted as a roughly triangle-shaped satellite directly at the base of the plume head in figure 4.15-(662s) that has apparently ended up as part of the plume sheath, more of the particles originally from the high particle density region are simply shed by the ascending plume head and remain in the ambient material.

What these pictures do not and cannot convey, save for trying to trace individual packets of tracer particles from picture to picture, is that there is a steady upward flow over the entire width of the plume head trailing the plume head. The plume sheath in these experiments is as prominent and constant as it had been in the experiments of set A and B. Figure 4.16 presents velocity curves of three cross-sections taken at a time where the plume has almost reached the surface boundary. These velocity curves clearly show that there is a significant movement of material upward even outside of the plume core region - that there is, indeed, a plume sheath ascending alongside the plume. Furthermore, the velocities in this plume sheath are about constant at different depth of the plume, leading to the conclusion that, barring changes in

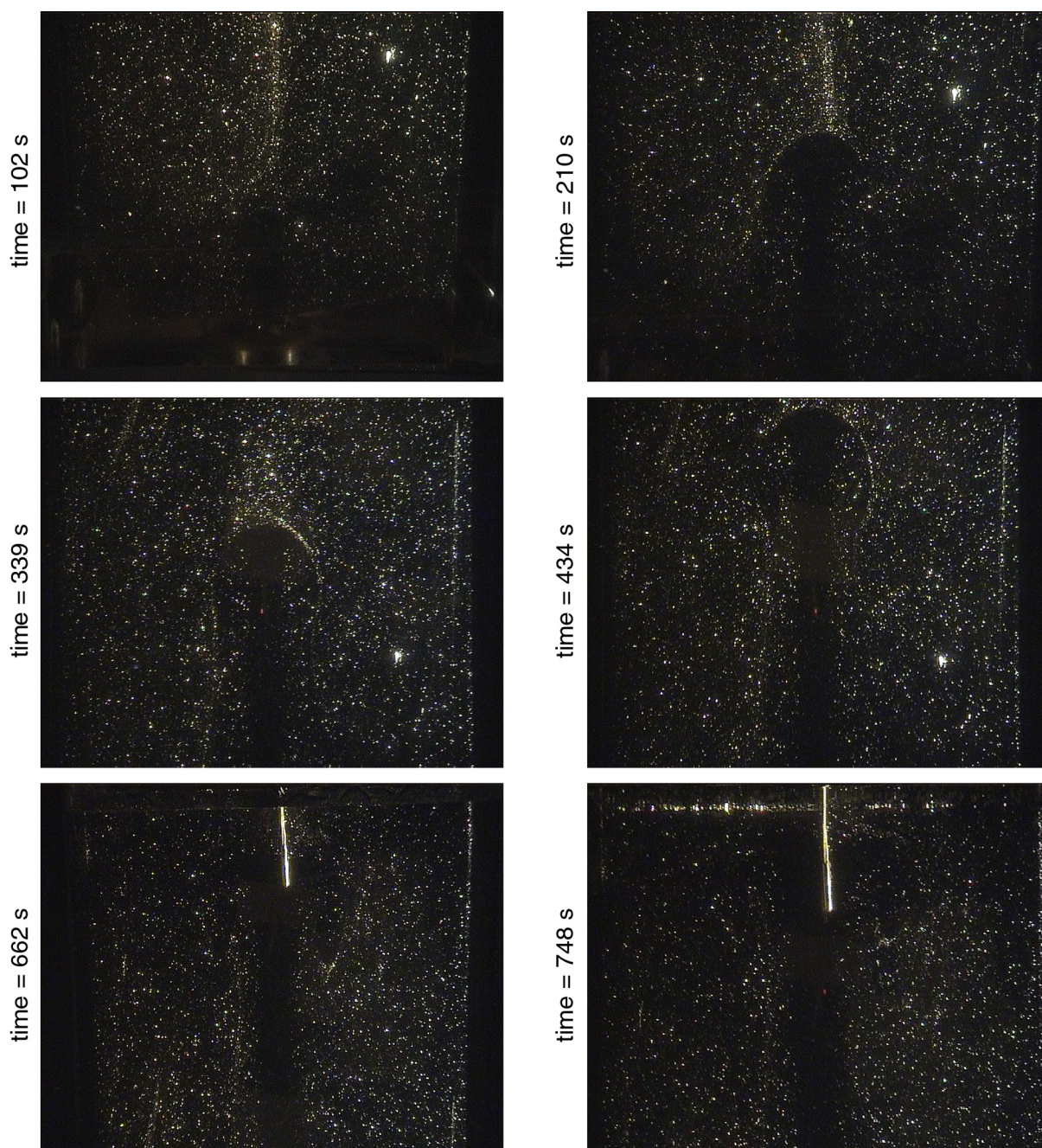


Figure 4.15: *Evolution of an experiment at 40° C tank temperature and 60° C injection material temperature, with an injection rate of 20ml/min. The bright white light on the right side of some of the pictures is a reflection from an ill-fitting blind, while the red dot in the center is a reflection from the camera.*

the physical properties of the plume source region, the plume tail + plume sheath region of the ascending plume can be considered as a fixed perturbation. It should be noted that the maximum velocities presented in figure 4.16 do not represent the actual plume ascent velocity - rather, material in the inner plume sheath and tail region of the plume core moves faster than the plume head ascends, thus causing the observed growth of the plume head.

Figure 4.17 presents the ascent rates for the experiments of set C. For the most part, ascent

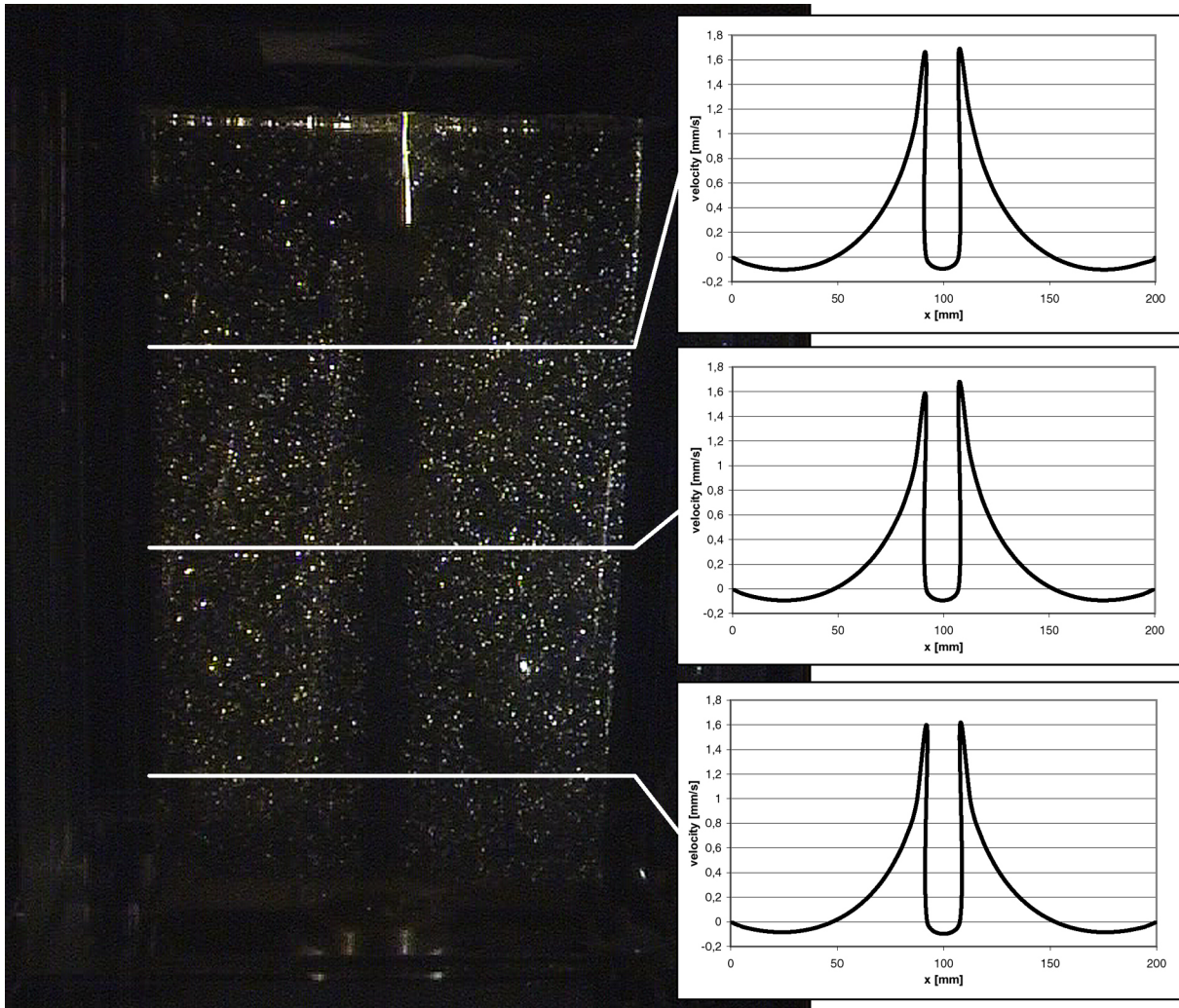


Figure 4.16: *Plume sheath and ambient material velocities, measured at 80mm, 190mm and 280mm, respectively, during an experiment at 40° C tank temperature and 80° C injection material temperature, with an injection rate of 20ml/min. Note that the velocity of the plume core could not be measured because of the absence of particles in the plume core.*

is once again linear for the most part, indicating an almost constant ascent velocity. When nearing the surface boundary, ascent slows down noticeably due to the plume head spreading out. Furthermore, the influence of the injection rate on plume ascent speed becomes obvious: for the low temperature (=60°C) injection experiments in particular, there is a significant increase in ascent speed corresponding to an increase in injection rate.

The temperature curves for set C are shown in figure 4.18. It should be noted that the reason for the unexpectedly low source temperatures in this case lies with the placement of the bottom thermoprobe. Since a disturbance of the inflow right at the source is undesirable, the bottom thermoprobe is not placed directly at the injection opening, but closely beside it. This means that the bottom thermoprobe does not measure the full temperature perturbation of the injected material, but a slightly reduced value due to its additional measuring of unheated ambient material temperature. Actual source temperatures are verified through the heating bath tempering the injection supply. This indicates that temperature losses in the first 10-20mm are as dramatic in the injection experiments as in the bottom heating experiments of set

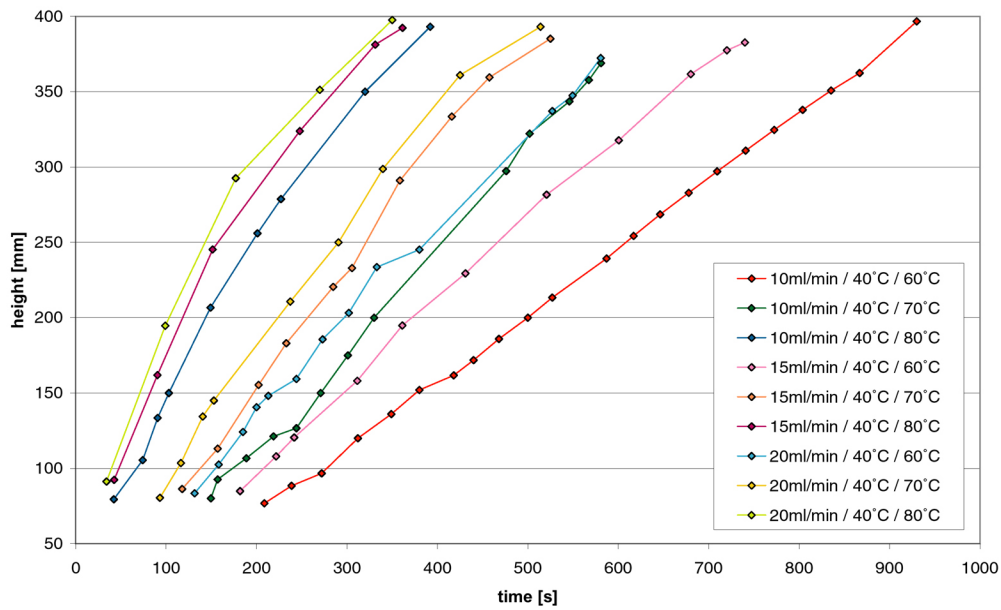


Figure 4.17: *Plume ascent rates for the experiments of Set C.*

B.

Comparing the temperature curves of set B and set C further, it can be seen that the plumes of set C are able to retain much more of the initial temperature perturbation during ascent, resulting in a much more gradual, almost linear temperature loss with height compared to the exponential temperature loss with height of set B. This does not necessarily mean higher temperature perturbations at the surface boundary, though - the low injection rate (=10ml/min) experiments in particular exhibit surface temperatures that are well in the range of surface

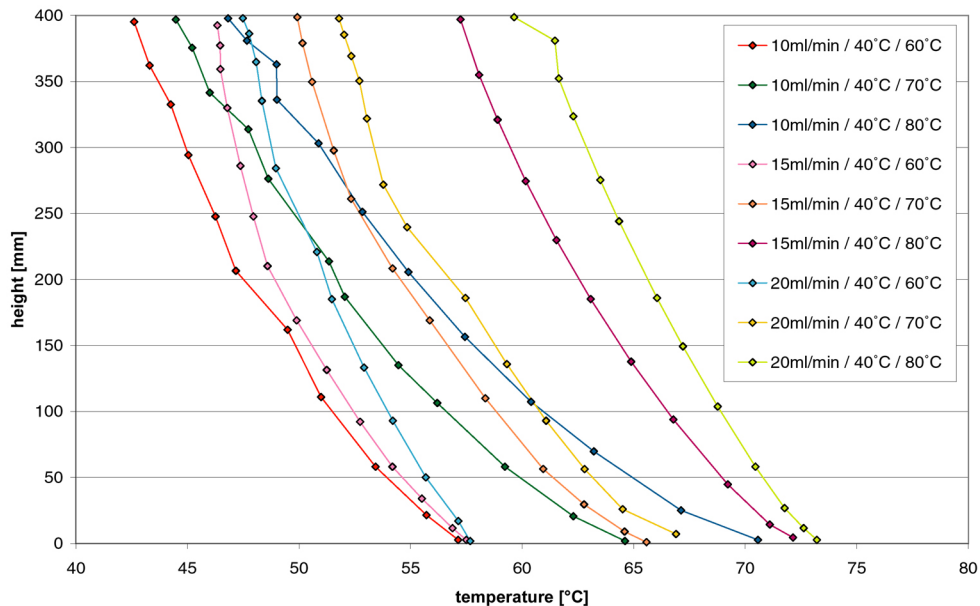


Figure 4.18: *Plume temperature profiles of the experiments of Set C. Displayed is the temperature of the plume core over the depth of the experimental tank, measured after the plume has reached the surface of the tank.*

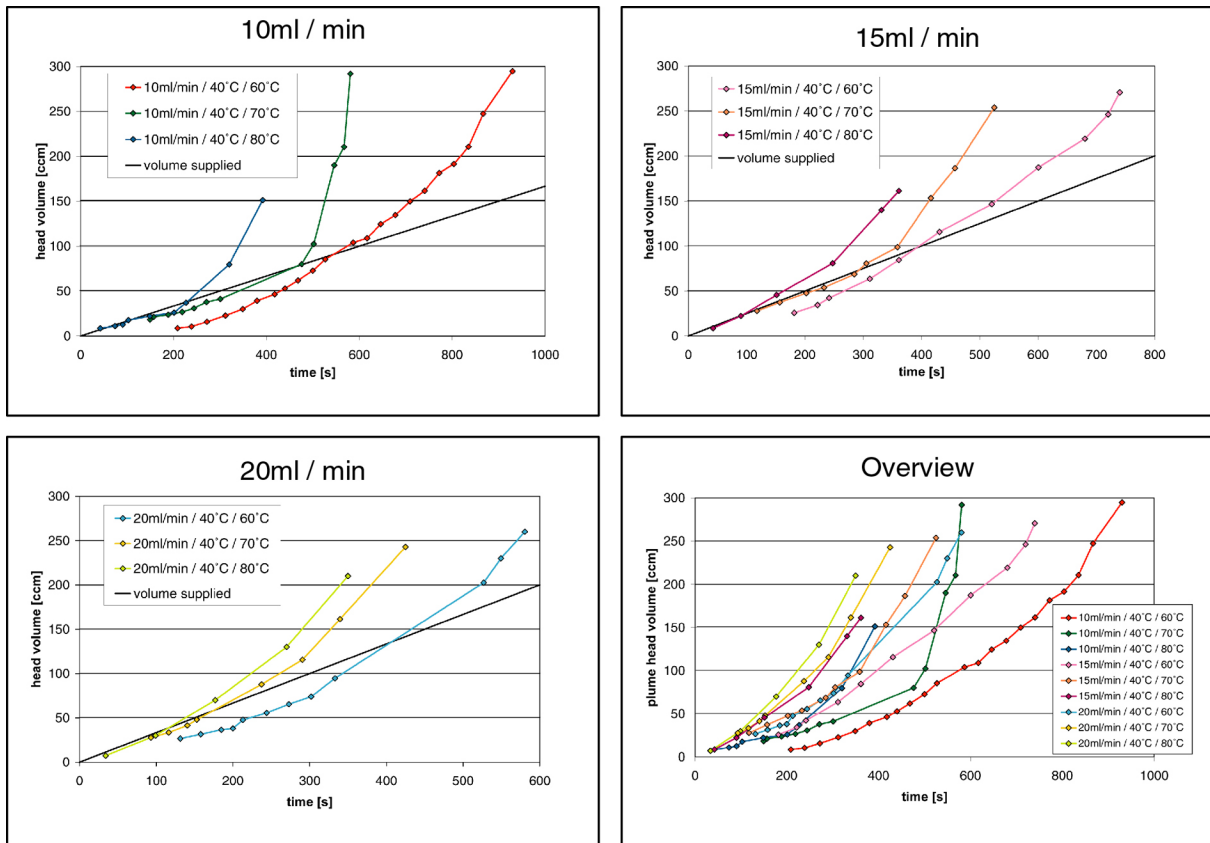


Figure 4.19: Plume head growth rates for the experiments of Set C.

temperatures of set B.

Measuring temperatures in the plume sheath region sheath, it is found that the higher plume core temperatures are also reflected in higher temperatures of the inner plume sheath. The region of the plume sheath closest to the plume core exhibits temperatures exceeding the tank temperature by up to 2.5°C . There is still a very steep drop in temperature between the plume core and plume sheath - while comparatively high temperatures can be registered within $\sim 8\text{mm}$ of the plume core, temperatures measured at double distance ($\sim 16\text{mm}$) hardly exceed the ambient tank temperature at all. Once again, the observed temperatures cannot sustain plume sheath ascent at the rate that is observed in the experiments. This, along with the velocity information gained on the plume sheath, lends more credibility to the notion that the plume sheath can be considered as acting in the manner of a laminar boundary layer surrounding the plume.

Figure 4.19 presents a comparison of the plume head growth rates with the respective injected volumes, and with each other. From comparing plume head growth at equal source temperature versus plume head growth at equal injection rate, it can safely be said that the peculiarities of plume head growth are more a function of plume core temperature than of injection rate - the graphs for plume head growth at 60°C display a very similar progression. As with the plume head growth rates of set B, there seems to be a specific point from which on the rate of growth changes from a gradually increasing growth rate to a constant, linear one. Comparing growth rates to injection rates, the large contribution of entrained plume sheath material to the volume of the plume head becomes evident.

4.3 Assessment, Summary and Proceedings

When critically examining the laboratory experiment data brought forward in this chapter, a couple of weaknesses can be identified. The source region temperatures and thus viscosity contrasts in the pure thermal source case are far below the aspired values, resulting in a temperature / viscosity contrast that is not as sharp as expected for the Earth's mantle. Likewise, the injection source experiments do not provide much more than one order of magnitude of viscosity contrast and add unwanted influence of the injection rate on the plume ascent velocity. Additionally, both approaches do not adequately reflect conditions as they are assumed for the lower mantle - notably a hot bottom boundary layer and nonhomogeneity of the experimental fluid (as e.g. implemented in the experimental setup of *Le Bars & Davaille* [2004] and *Kumagai & Kurita* [2000]). Experiments with whole bottom heating were conducted, but plume formation proved not to be easily limitable to one single center plume, so these experiments did not provide reasonable results.

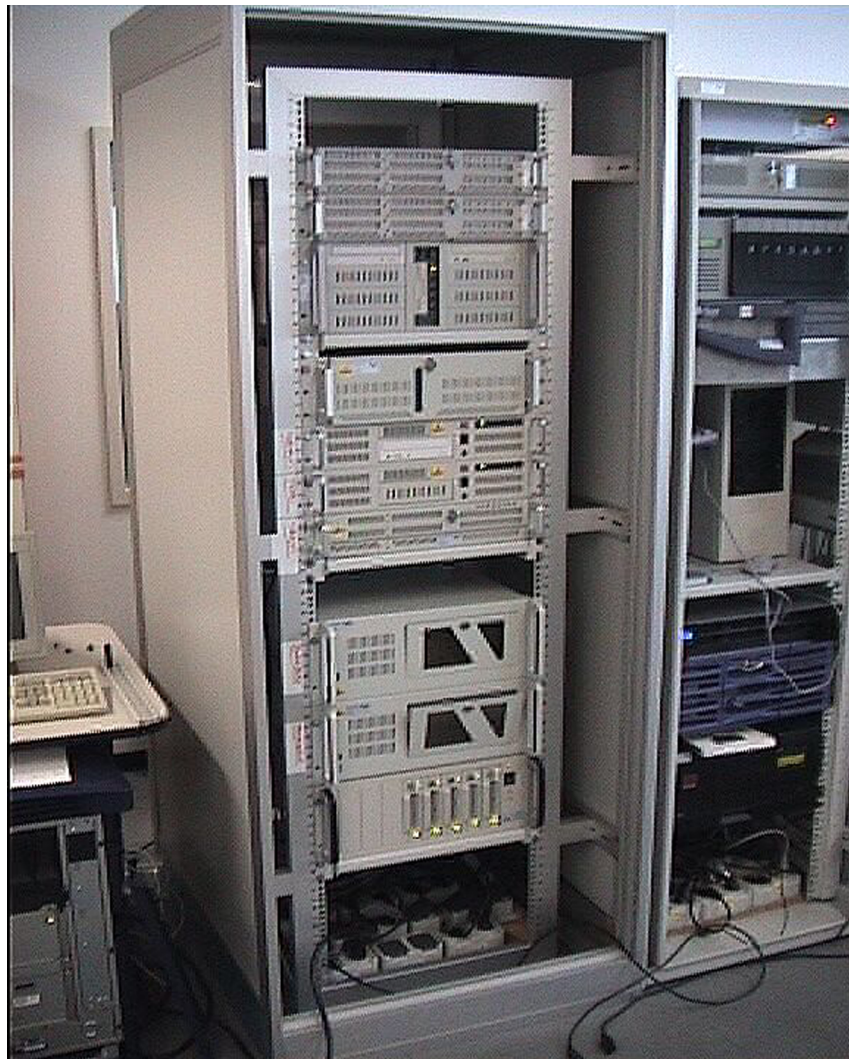
In support of the validity of the laboratory experiments presented here, the work of *Coulliette & Loper* [1995] and *Kumagai* [2002] should be brought up. Their studies show that ascent behavior and general structure of laboratory plumes are similar for viscosity ratios of up to 10^4 and more. Hence it follows that observations made for the viscosity/temperature ratios in the experiments at hand should also hold true for higher ratios. This means that the observations brought forward in this chapter are very much relevant and applicable, a fact that is also underlined by the results of the numerical experiments presented in the following chapters.

The laboratory experiments allude to the existence of a plume sheath that completely envelopes the classical plume region, or plume core, during ascent. The plume sheath is made up of material from the lowermost region of the experimental tank. All entrainment into the plume head has its origin in the plume sheath, and all entrainment of ambient material happens between plume sheath and surrounding material. The plume sheath itself is too cold to rise under its own thermal buoyancy, which suggests that it owes its rise to drag/pull of the fast ascending plume core material. The behaviour of the plume sheath during ascent is reminiscent of a laminar boundary layer.

The exact depth structure and sampling behaviour of the plume sheath, the exact origin of material entrained into the plume sheath and plume head, as well as detailed studies of temperature, velocities, mass flux and other properties, are subsequently investigated using numerical modelling, the results of which are presented in chapter 7.

Part Two

Numerical Modeling



Picture of the BEOWULF cluster 'Polynesia' used to run the lion's share of the numerical experiments. A total of 16 PIII processors spread over 8 nodes provides (almost) all the computing power necessary for the numerical work in this thesis.

Chapter 5

An Introduction to Numerical Modelling

With the advent of powerful computers, numerical studies of physical processes have become one of the most powerful and versatile tools available to researchers. Compared to laboratory experiments, numerical studies can cover a wide variety of scenarios and conditions that are impossible to implement in the laboratory, and can track specific physical properties precisely and almost effortlessly at any moment during the simulation run. Numerical simulation presents the researcher with the perfect sandbox that is almost completely customizable, observable and controllable, and changes in the initial setup of a numerical experiment are easy, fast and cheap. While designing and implementing a numerical code certainly is rather resource-intensive, actual maintenance and adaptation to the problem at hand is much faster and more easily done than for laboratory experiments.

The main drawback of numerical models is that they are limited by their model approach. Every numerical model represents a simplification of the real physical processes, and must be critically examined and tested against observed phenomena and analytical solutions because of this. Furthermore, implicit errors and numerical diffusion in solving the numerical equations are a direct result of numerical experiments being only able to provide a limited resolution, and thus cannot be completely eliminated. There are still many physical phenomena that numerical codes have serious problems to adequately handle, and for many phenomena, there simply do not exist relevant equations to describe the problem.

This chapter will give a brief overview of previous works in analytical studies and numerical modelling of mantle plumes and plume entrainment.

5.1 Previous Analytical and Numerical Studies of Plumes

There have been a number of analytic studies focused on finding a reasonably accurate interpretation of the basics of plume ascent and plume flow. The dynamics of plume ascent were examined in the early 80's by *Stacey & Loper* [1983], *Loper & Stacey* [1983] and *Loper* [1984], who, however, concluded that plumes have properties that are not widely accepted - in particular that plumes should be at most ≈ 10 km wide pipes in the lower mantle that should become even narrower as they rise through the upper mantle. Subsequent work by Sleep studied the effects of plumes on their presumed source D" region (*Sleep* [1987]) and the influence of plate tectonics on the initiation of plumes from the basal boundary layer

and their subsequent evolution (*Sleep [1992a]*). *Schubert et al. [1989]* used analytical and numerical methods to constrain the propagation of solitary waves in plume conduits, and pointed out the differences between a two-dimensional model and a fully three-dimensional approach. In the early 1990's, *Griffiths & Campbell [1990]* provided analytical models for their laboratory plumes that described ascent velocity and entrainment rates, which was later revised and expanded by *Coulliette & Loper [1995]*. Meanwhile, *Olson et al. [1993]* presented a comprehensive numerical and analytical study of the structure of axisymmetric mantle plumes. This work compared the results of then state-of-the-art computational plume models with simpler boundary-layer-theory-derived expressions from plume dynamics. A boundary layer model was constructed to estimate plume entrainment $f(z)$ as $f(z) = 1 - \exp\left(-\frac{4\pi\kappa(T_c - T_m)z}{\gamma Q}\right)$, where κ is the thermal conductivity, T_c and T_m are the central temperature of the plume and the distant mantle temperature, respectively, $\gamma = \ln\left(\frac{\eta_0}{\eta_c}\right)$, η_0 , η_c are the viscosities of the plume and mantle material, and Q is the plume heat flux. This result implies the following intuitive consequences - entrainment should increase with height in the rising plume and should be inversely proportional to the plume flux (i.e., strong plumes entrain proportionally less ambient material than do weak plumes). Perhaps the most complete pre-existing study of plume entrainment are the similarity solutions that were explored by *Hauri et al. [1994]*. These workers also attempted to quantify the efficiency of plume entrainment as a function of the upwelling plume flux. Their model assumes that the vertical buoyancy of the plume is pulling ambient mantle into the plume flow. *Phipps Morgan et al. [1995a]* presented a simple approach to assess the size of a hotspot swell generated by uplift of hot, deflected plume material. Lastly, *Korenaga [2005]* addresses how high-viscosity, high-radius plumes can penetrate a lower mantle whose rheology is dominated by the grain-size dependence of diffusion creep.

Numerical studies of plumes encompass a broad variety of starting models: *Liu et al. [1991]* presented two-dimensional models of the interaction of a deep mantle plume with the phase transition at 670km depth and showed how the phase boundary can pinch off the ascending plume head, offering an explanation for the observed episodicity of hot spot volcanism. This interaction was further elaborated on by *Kellogg [1991]*, who coupled the ability of a plume to cross the phase boundary to its buoyancy number $B = \frac{\Delta\rho_c}{\rho\alpha\Delta T}$, where $\Delta\rho_c$ is the density contrast due to compositional variation in the fluid, and concluded that the behaviour observed by *Liu et al. [1991]* only happens at $B \approx 1$. *Ribe & Christensen [1994]* used a 3D variable-viscosity convection code to model the interaction of a thermal plume with a moving plate to study what surface observables can tell about the structure of the underlying plume - this has been continued in *Ribe & Christensen [1999]*. *van Keken & Gable [1995]* examined the interaction of an ascending plume with a rheological boundary for 2D and 3D conditions, and found that pulsating behaviour similar to that pointed out by *Liu et al. [1991]* did only occur in the 2D models, thus further stressing the importance of fully 3D models in examining processes in the mantle. *Schubert et al. [1995]* also investigated the phase change at 660km in a 2D numerical model and found that the plume is heated by roughly 100K when passing through the endothermic phase change, but speculate that this heat might be lost again while passing through the exothermic phase change at 410km. *Albers & Christensen [1996]* focused on the structure of upwelling plumes and their thermal structure, and concluded that plumes with a buoyancy flux of less than $1000 \frac{kg}{s}$ do possibly not originate from the core-mantle boundary. *Nakakuki et al. [1997]* investigated the interaction of an ascending plume with transition zones under continental and oceanic lithosphere. *Thompson & Tackley [1998]* used a 2D model to constrain the point of transition from conventional plume to broad-scale

mega-plume. *Samuel & Farnetani* [2003] and *Farnetani & Samuel* [2003] investigated the consequences of a chemically denser D'' layer for plume structure and mantle convection, and conclude in *Farnetani & Samuel* [2005] that the head-tail structure of the conventional plume is just one of many possible plume shapes, and that compositional heterogeneities in the lowermost mantle favour the coexistence of a great variety of plume shapes and sizes. Lastly, *Lin & van Keken* [2005] present that the interaction of thermal and compositional buoyancy forces can cause secondary instabilities in the plume conduit that could possibly contribute to multiple episodes of large igneous provinces. It should be pointed out, however, that none of these studies go into the details of the plume entrainment processes in their models.

Few numerical studies have focused on plume entrainment. Those that do primarily cover the study of entrainment within the so-called plume head of a starting plume. *Farnetani & Richards* [1995] explored entrainment and the effects of melting of both entrained and deep plume material. They concluded that the plume would essentially only entrain deep mantle material, so that the geochemical consequences of entrainment were not fully reconciled by this model. However, their study explored only isoviscous or weakly temperature-dependent rheologies. Plume entrainment of a deep D'' boundary layer, as first noted by *Sleep* [1987], was explored by *Christensen & Hofmann* [1994]. *Kellogg & King* [1997] used a 2D spherical model to constrain the effects of different rheologies on the structure and composition of an upwelling plume. They agree with *Farnetani & Richards* [1995] in that in a constant viscosity model little entrainment occurs, but note that such a scenario is probably not appropriate for the mantle. *Kellogg et al.* [1999] have also invoked entrainment from a deep internal boundary layer as the origin of high ^3He hotspot basalts (see also *Hansen & Yuen* [2000]). *Farnetani et al.* [2002] use passive tracer particles in a 2D model to determine entrainment rates and find that the thermal boundary layer that the plume originates from is the region most effectively sampled, and that little entrainment into the ascending plume head occurs. They therefore conclude that the geochemically heterogeneous nature of mantle plumes is inherited at the plume source rather than being the result of entrainment and mixing of upper mantle material.

Less than a handful of studies have presented side-by-side and compared analogue modelling and numerical experiments. *Coulliette & Loper* [1995] conducted a series of laboratory experiments and compared these to numerical experiment using laboratory boundary conditions. *van Keken* [1997] compared laboratory experiments and numerical solutions by recalculating the experiments of *Griffiths & Campbell* [1990]. His solutions match the experimental observations of *Griffiths & Campbell* [1990] quite well, but he also shows that in the case where the plume rises from a thermal instability instead of being injected, the source for most of the entrained material is in the lower half of the system. This effect becomes even more pronounced if a stress dependent rheology is taken into account. Lastly, *Laudenbach & Christensen* [2001] compared the thermal plume structures of their laboratory experiments with that of numerical experiments using laboratory boundary conditions, but did not go into the implications of their experiments for mantle plumes at all.

Chapter 6

Numerical Methodology

To model the ascent of a plume through a highly viscous fluid, a three-dimensional model that solves for flow, temperature and compositional changes is implemented. The following chapter presents the derivation of the governing equations and their discretisation on a numerical grid. Furthermore, the equation solver, numerical advection scheme and limiting of timestep are discussed in brief. Lastly, the introduction of passive tracer particles into the numerical grid is presented.

6.1 Mathematical Treatment

When simulating a fluid, the first step is to consider the individual molecules of the fluid. Thus, the state of the entire system is fully defined through the spatial coordinates x and momentum p of all N particles. This opens up a six-dimensional phase space with the corresponding distribution function $f(x, p, t)$. Assuming a non-impact-free environment, the temporal evolution of the distribution function is given by the Liouville equation:

$$\frac{\partial f}{\partial t} = -v\nabla f + Stf . \quad (6.1)$$

Here, the term $v\nabla f$ stands for the change in the number of molecules in a specific time interval in a given volume of the phase space, caused by the free movement of molecules. The term Stf equals the change in the number of molecules within the phase space volume due to impacts within a given time interval, and is also called impact integral. When considering gains and losses during impact and assuming that the duration of an impact is small compared to the time between impacts, the impact integral can be formulated. The Liouville equation thus becomes the Boltzmann equation:

$$\frac{\partial f}{\partial t} + v\nabla f = \int \omega'(f'f'_1 - ff_1)dp_1dp'dp'_1 . \quad (6.2)$$

Here, $(f(x, p, t))$ is the distribution function of the impacting molecules, and $(f_1(x, p, t))$ the distribution function of impacted molecules. This equation defines the temporal evolution of the distribution function $(f(x, p, t))$. ω' stands for the probability of impacts going from $p, p_1 \rightarrow p', p'_1$ for all possible values of p_1, p', p_1 at constant p .

The exact solution of the Boltzmann equation within a manageable calculation time is only possible for a limited number of molecules. There are two methods used for solving the

Boltzmann equation approximately: The first does not follow individual molecules, but works with a limited number of particles that act as proxy for a larger number of molecules with equal properties. The second does not solve the one-particle-function in full detail, but instead solves for macroscopic values per volume element. The first method is used to great success for a variety of scenarios like e.g. the simulation of ideal gasses. Still, it is the second method that is obviously suited better for the task at hand.

To get the relevant equations for macroscopic values, first the moment equations have to be derived from the Boltzmann equation. In order to do so, the Boltzmann equation is multiplied with the mass m , impulse \vec{P} (separated into the three impulse components) and the kinetic energy E and integrated over the entire phase space. Thus, five equations are derived - one mass equation, three momentum equations and one energy equation. All in all, these have 14 variables - density ρ , energy e , three velocities v_z , v_x und v_y , six viscosity tensors τ_{ij} and three terms for the heat flux F_i .

Assuming a Newtonian fluid (that is, a fluid in which shear stress is linearly proportional to the viscosity gradient in the direction perpendicular to the plane of shear), we can express the viscosity tensors τ_{ij} as dependent on the dynamic viscosity η :

$$\tau_{ij} = \eta \left(\frac{\partial v_i}{\partial x_j} + \frac{\partial v_j}{\partial x_i} \right) + \lambda \delta_{ij} \nabla \cdot \vec{v}, \quad (6.3)$$

where $\delta_{i,j}$ is the Kronecker delta, λ is the second coefficient of viscosity, and $\nabla \cdot \vec{v}$ is the divergence.

Furthermore, it is assumed that the thermal conductivity is constant throughout the computational region. This leads to the Navier-Stokes equations¹.

6.2 Hydrodynamic Equations

We consider the Navier-Stokes equations in cartesian coordinates. Written out in full with a velocity vector given as $\vec{v} = (v_x, v_y, v_z)$, we get:

Continuity Equation:

$$\frac{\partial \rho}{\partial t} = -\rho \nabla \cdot \vec{v}, \quad (6.4)$$

Conservation of momentum:

$$\frac{\partial (\rho \vec{v})}{\partial t} + \rho \vec{v} \cdot \nabla \vec{v} = -\nabla P + \eta \nabla^2 \vec{v} + \mathcal{F}, \quad (6.5)$$

Conservation of energy:

$$\frac{\partial e}{\partial t} = -\vec{v} \cdot \nabla e + \nabla (\kappa \nabla T). \quad (6.6)$$

Here, ρ is the density, P is the pressure, \mathcal{F} is the body force, e is the entropy per unit mass, κ is the thermal diffusivity, and T is the temperature.

¹A full treatment on how the Navier-Stokes equations can be derived from the Boltzmann equation can be found in *Bouchut et al.* [2000]. Alternate derivations for the Navier-Stokes equations are presented e.g. in *Landau & Lifschitz* [1991] and *Batchelor* [2000].

Equation 6.5 can be put into dimensionless form using the definitions:

$$\begin{aligned}
x' &\equiv \frac{x}{L} \\
y' &\equiv \frac{y}{L} \\
z' &\equiv \frac{z}{L} \\
\vec{v}' &\equiv \frac{\vec{v}}{V} \\
P' &\equiv \frac{P}{\rho V^2} \\
\nabla' &\equiv \hat{x} \frac{\partial}{\partial x'} + \hat{y} \frac{\partial}{\partial y'} + \hat{z} \frac{\partial}{\partial z'} = L \nabla \\
t' &\equiv t \frac{V}{L} .
\end{aligned} \tag{6.7}$$

Here, V is the characteristic velocity, and L is the characteristic length scale. Thus, 6.5 is written as:

$$\frac{\partial (\rho V \vec{v}')}{\partial \left(\frac{L}{V} t' \right)} + \rho V \vec{v}' \cdot \frac{1}{L} \nabla' V \vec{v}' = -\frac{1}{L} \nabla' (\rho V^2 P') + \eta \frac{1}{L^2} \nabla'^2 (V \vec{v}') + \mathcal{F} . \tag{6.8}$$

In the Boussinesq approximation, variations in ρ are ignored, except insofar as they give rise to a buoyant body force. This also suggests that compressional phenomena can be neglected. For the problem at hand (the simulation of viscous flow under laboratory and mantle conditions), it can be safely assumed that for the Mach number M , $M \ll 1$, meaning that all flow is subsonic by a significant margin. Under these circumstances, the Bernoulli theorem

$$\frac{1}{2} \rho \vec{v}^2 + P = [const.] \tag{6.9}$$

is fully applicable. This results in $\nabla \rho = 0$, and in $\nabla \cdot \vec{v} = 0$ when considered along with the continuity equation 6.4, and effectively means that the flow can be treated as incompressible, and that the Boussinesq approximation can be applied.

Thus, assuming that $\rho = const.$, and multiplying both sides by $\frac{L}{(\rho V^2)}$, equation 6.8 becomes:

$$\frac{\partial \vec{v}'}{\partial t'} + \vec{v}' \cdot \nabla' \vec{v}' = -\nabla' P' + \frac{\eta}{LV\rho} \nabla'^2 \vec{v}' + \mathcal{F} . \tag{6.10}$$

Substituting \mathcal{F} with a term representing the buoyant body force, and using the definition of the Reynolds number as found in equation 2.4, we get:

$$\frac{\partial \vec{v}'}{\partial t'} + \vec{v}' \cdot \nabla' \vec{v}' = -\nabla' P' + \frac{1}{Re} \nabla'^2 \vec{v}' + \Delta \rho g . \tag{6.11}$$

For small Reynolds number, this can be simplified to:

$$\rho_0 \frac{\partial \vec{v}}{\partial t} + \nabla P = \eta \nabla^2 \vec{v} + \Delta \rho g , \tag{6.12}$$

which is also known as the Stokes equation.

For the purpose of our simulations, the density is assumed to depend on both temperature and composition of the fluid. For determining composition, we introduce the dimensionless compositional parameter D that represents the total amount of melt extraction, or 'depletion', in the mantle experiments, and is used to differentiate between rheologically different material. Thereby, the expression $\Delta \rho$ in equation 6.12 can be expressed as

$$\Delta \rho = \rho_0 - \rho(T, D) , \tag{6.13}$$

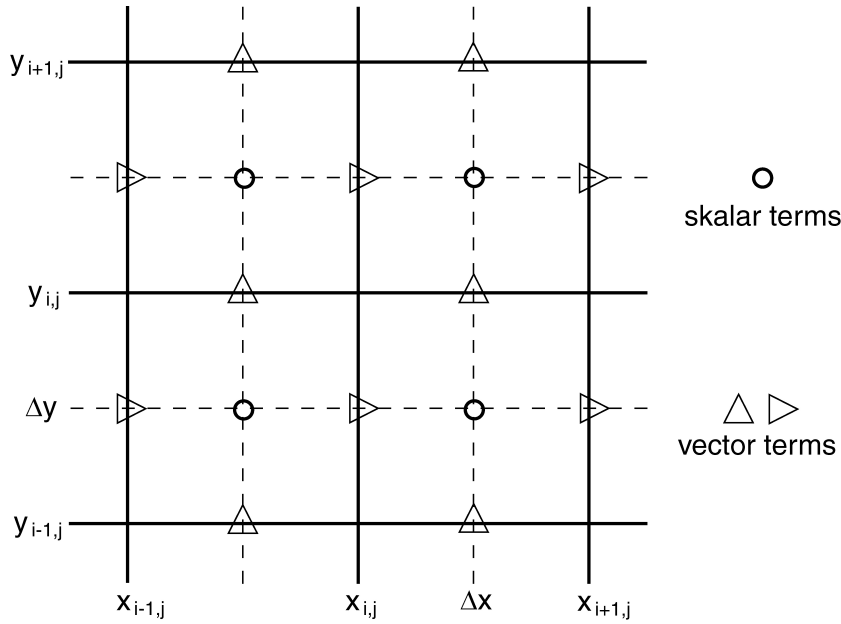


Figure 6.1: *2D-example of a staggered grid. The scalar terms are defined in the cell centres, the vector terms are defined on the cell edges.*

with

$$\rho(T, D) = \rho_0 (1 - \alpha T - \beta D) . \quad (6.14)$$

Here, ρ_0 is the reference density, ρ is the density, T is the temperature, D is the dimensionless depletion parameter, and the two constants α and β are the thermal expansion coefficient and the compositional buoyancy coefficient, respectively.

6.3 Numerical Methods

6.3.1 Discretisation

In the work presented here, the hydrodynamic equations are being solved through a finite difference approach. Essentially, this means that the differentials in equation 6.4, 6.6 and 6.12 are being replaced by the relevant differences. Formally, this is the equivalent of a Taylor expansion for the spatial coordinates, while only the leading terms are considered. This provides a second-order spatial dilineation.

For the discretization of the equations, a so-called 'staggered grid' is used. Here, all scalar terms like the pressure P or the density ρ are defined in the centres of the grid cells, while all vector terms like the momentum or the velocities are defined at the edges of the grid cells. This is illustrated in figure 6.1.

Using this approach suppresses spurious odd-even oscillatory solutions, and requires neither an artificial component to the viscosity nor extra numerical boundary conditions. In addition to this, all spatial differences are already centered, meaning that a vector that is determined through the differentiation of a scalar quantity is already defined between the two relevant scalars.

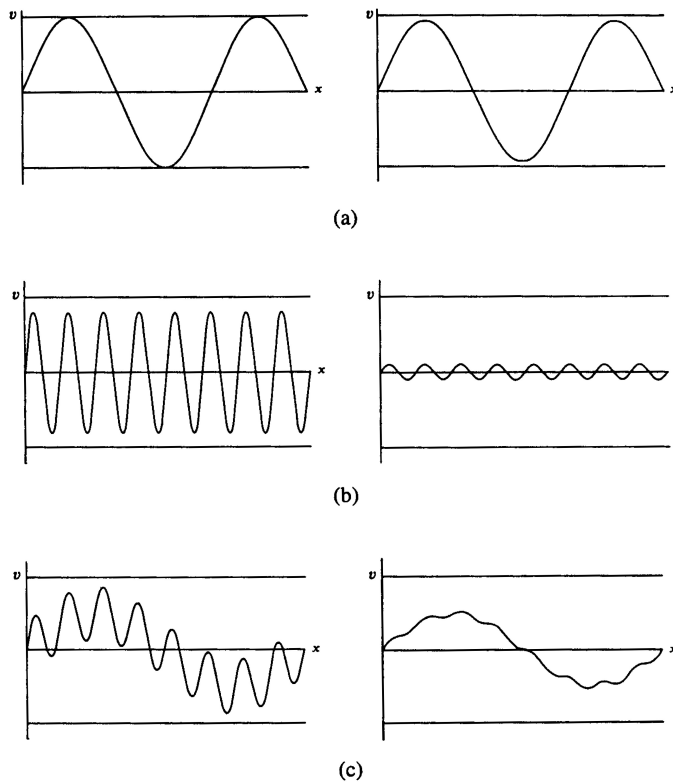


Figure 6.2: *Weighted Jacobi method with $\omega = \frac{2}{3}$ applied to a one-dimensional model problem with $n=64$ grid points and with an initial guess of (a) w_3 , (b) w_{16} and (c) $(w_2 + w_{16})/2$. The figures show the approximation after one iteration (left side) and after 10 iterations (right side). From Briggs [1987].*

6.3.2 Solving of the equations and Multigrid

Now that 6.4, 6.6 and 6.12 are discretised on a grid with N grid points in each direction and with $h = \frac{1}{N+1}$ as the discretisation parameter, the system can be written in the form

$$\mathbf{A}_h \vec{u} = \mathbf{f} , \quad (6.15)$$

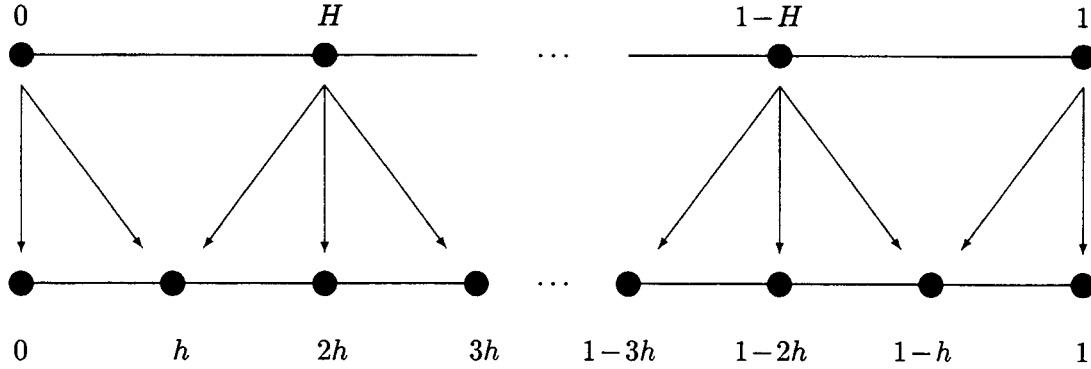
with \vec{u} being the solution function, \mathbf{f} being the given function with given boundary values φ , and \mathbf{A}_h being a $N^3 \times N^3$ matrix. \mathbf{A}_h is a sparse matrix and unsymmetrical, which makes finding an exact solution through direct methods like the Cholesky decomposition next to impossible. Therefore, and because of the large number of unknowns in the system, we use an iterative (or relaxation) method along the lines of

$$\mathbf{A} \vec{x} = \mathbf{f} , \quad (6.16)$$

with the right side \mathbf{f} being the given function, \mathbf{A} being a regular matrix, and \vec{x} being a set of successive approximations to the exact solution $\vec{u} = \mathbf{A}^{-1} \mathbf{f}$ determined through repeated processing of the calculation rule

$$\vec{x}_{m+1} = \phi(\vec{x}_m, \mathbf{f}) \quad (6.17)$$

for $m = 0, 1, \dots$ and a given starting vector \vec{x}_0 . Consistency and convergence of this approach is discussed at length in Meister [1999]. Common approaches to solve this system include standard splitting methods like the weighted Jacobi method or the Gauß-Seidel method. While these

Figure 6.3: 1D-example of a prolongation $\Omega_H \rightarrow \Omega_h$

regularly reach second-order or higher accuracy, they are often not computationally efficient. The reason for this lies in the algebraic error e of the approximation that is given by

$$\vec{e} = \vec{u} - \vec{x}_m . \quad (6.18)$$

Unfortunately, this error is just as inaccessible as the exact solution itself. Still, a computable measure of the accuracy of \vec{x}_m is given by the residual \vec{r} :

$$\vec{r} = f - \mathbf{A}\vec{x}_m , \quad (6.19)$$

which, put into 6.16 and using 6.18, gives us the residual equation

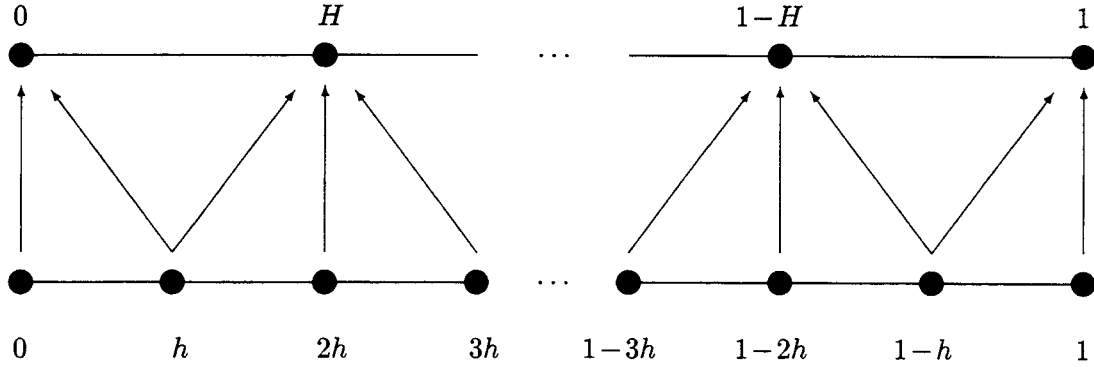
$$\mathbf{A}\vec{e} = \vec{r} . \quad (6.20)$$

When using Fourier modes as the components of the initial guess \vec{x}_0 , it can be shown (e.g. Briggs [1987]) that standard splitting methods are efficient in dampening the high-frequency component of the error \vec{e} , while the low-frequency error modes prove to be much more persistent. This is illustrated in figure 6.2. 'High frequency' here denotes modes with $k > \frac{N}{2}$ - the oscillatory modes - while 'low frequency' covers the spectrum below $\frac{N}{2}$ - the smooth modes. This behaviour of the error degrades the performance of the standard splitting methods.

To get a better performance and stronger convergence of the solution, the so-called Multigrid method is introduced for the iterative solver. This method is discussed at length in Hackbusch [1985] and Hackbusch & Trottenberg [1982], and shall be briefly presented here.

The basic idea behind the Multigrid method is that smooth, low-frequency modes on a fine grid can become more oscillatory, turning into high-frequency modes, on a coarser grid. This suggests that when relaxation begins to stall, signalling the predominance of smooth error modes, it is advisable to move to a coarser grid. There, the smooth error will appear more oscillatory, and relaxation will be much more efficient. Thus, coarse grids can be used to obtain better initial results for the next finer grid. Additionally, looking back at equation 6.16 and 6.20, we see that relaxation on the original equation 6.16 with an arbitrary initial guess is equivalent to relaxing on the residual equation 6.20 with the specific initial guess $\vec{e} = 0$. Thus, to improve on the initial approximation \vec{x}_m^h on the fine grid Ω^h , we can relax on the residual on a coarser grid Ω^{2h} to obtain an approximation of the error \vec{e}^{2h} , and then correct the initial approximation:

$$\vec{x}_{m+1}^h = \vec{x}_m^h + \vec{e}^{2h} . \quad (6.21)$$

Figure 6.4: 1D-example of a restriction $\Omega_h \rightarrow \Omega_H$

To transfer between the coarse grid and the fine grid, we consider the case in which the coarse grid has twice the grid spacing of the next finest grid, so $H = 2h$. This is nearly universal practice, since there is no advantage gained from having grid spacings with ratios other than two.

In one dimension, the interpolation, or prolongation, between a coarse grid and a fine grid can be expressed through the linear interpolation operator according to the rule $I_H^h \vec{x}^H = \vec{x}^h$, where

$$x^h(ih) = \begin{cases} x^H(jH) & i = 2j \\ \frac{1}{2} (x^H(jH) + x^H(jH + H)) & i = 2j + 1 \end{cases} . \quad (6.22)$$

This is illustrated in figure 6.3.

In the same vein, transfer from the fine grid to the coarse grid, termed 'restriction', can be expressed through $I_h^H \vec{x}^h = \vec{x}^H$, where

$$x^H(i) = \frac{1}{4} (x^h(2j - 1) + 2x^h(2j) + x^h(2j + 1)) . \quad (6.23)$$

This is illustrated in figure 6.4. For the three-dimensional case, the interpolation operators can be defined in a similar way. The issue of intergrid transfer is further discussed in [Brandt \[1984\]](#).

The Multigrid scheme can now be expressed in explicit terms. Written as a recursive algorithm, it is given as follows:

$$v^h \leftarrow V^h(v^h, f^h)$$

1. Relax ν_1 times on $A^h u^h = f^h$ with a given initial guess v^h .
2. If $\Omega^h =$ the coarsest grid, then go to step 4.
Else

$$\begin{aligned} f^{2h} &\leftarrow I_h^{2h} r^h \\ v^{2h} &\leftarrow 0 \\ v^{2h} &\leftarrow V^{2h}(v^{2h}, f^{2h}). \end{aligned}$$

3. Correct $v^h \leftarrow v^h + I_{2h}^h v^{2h}$.
4. Relax ν_2 times on $A^h u^h = f^h$ with the initial guess v^h .

Compared to standard splitting methods, this algorithm reduces computation time for a typical problem by up to four magnitudes, and reduces the number of iterations needed to find a solution by up to more than four magnitudes. For a comprehensive introduction to the Multigrid method, including convergence analysis and implementation, see *Briggs [1987]*.

6.3.3 Advection scheme

The physical properties within a cell are continuously changed through fluid flow. The problem in modelling this flow through advection is that while the transport velocities are defined on the edges of the grid cell in the staggered grid approach, the relevant source terms are defined in the cell centres. Thus, to determine e.g. the mass flux through a cell edge, the density has to be mapped on the cell edge. The easiest way to do this is to use a simple upwind solution, through which the average density within the cell is simply multiplied with the relevant transport velocity. Obviously, though, this method does provide inexact values, particularly for areas with a high density gradient. This results in the so-called numerical diffusion, where discontinuities are smoothed out in each iterative timestep until they disappear. To prevent this, this work uses a simple positive definite advection scheme as first presented by *Smolarkiewicz [1983]*. This scheme is an extension to the standard 'upstream' or 'monotonic transfer' schemes (e.g. *van Leer [1977]*), adding a corrective step to the scheme.

The equation to be solved is the continuity equation describing the advection of a nondiffusive quantity in a flow field. For simplicity, the problem is assumed to be one-dimensional in either x-, y- or z-direction. For the advection of a nondiffusive scalar quantity Ψ , the upstream advection scheme on a staggered grid can be written as:

$$\Psi_i^{N+1} = \Psi_i^N - \left\{ F \left(\Psi_i^N, \Psi_{i+1}^N, u_{i+\frac{1}{2}}^N \right) - F \left(\Psi_{i-1}^N, \Psi_i^N, u_{i-\frac{1}{2}}^N \right) \right\} \quad (6.24)$$

where

$$F(\Psi_i, \Psi_{i+1}, u) = [(u + |u|) \Psi_i + (u - |u|) \Psi_{i+1}] \frac{\Delta t}{2\Delta x} . \quad (6.25)$$

Here, Ψ_i^N is the value of Ψ at the i grid point for N time step, u is the velocity in x-direction, Δt and Δx are the time and space increments, and the fluxes F are defined at the same staggered points as the velocity values. This scheme is a first-order scheme in both space and time, and thus has strong implicit diffusion. The rate of the implicit diffusion may be easily estimated for the case of uniform flow ($u = \text{const.}$). Expanding Ψ_i^{N+1} , Ψ_{i+1}^N , Ψ_{i-1}^N in a second-order Taylor sum about the point (x_i, t^N) , equation 6.24 may be written as:

$$\left. \frac{\partial \Psi}{\partial t} \right|_i^N = - \left. \frac{\partial}{\partial x} (u\Psi) \right|_i^N + \left. \frac{\partial}{\partial x} \left[0.5 (|u| \Delta x - \Delta t u^2) \frac{\partial \Psi}{\partial x} \right] \right|_i^N . \quad (6.26)$$

From 6.26 it can be seen that 6.24 approximates with second-order accuracy the equation:

$$\frac{\partial \Psi}{\partial t} + \frac{\partial}{\partial x} (u\Psi) = \frac{\partial}{\partial x} \left(K_{impl} \frac{\partial \Psi}{\partial x} \right) , \quad (6.27)$$

where K_{impl} is the implicit diffusion defined as

$$K_{impl} = 0.5 \left(|u| \Delta x - \Delta t u^2 \right) . \quad (6.28)$$

As Δt and $\Delta x \rightarrow 0$, equation 6.27 approaches the continuity equation. Still, the implicit diffusion term is important for the stability of the advection scheme and cannot be simply subtracted. The intuitively obvious approach then is to make a regular advection step using equation 6.24 and then reverse the effect of the diffusion equation

$$\frac{\partial \Psi}{\partial t} = \frac{\partial}{\partial x} \left(K_{impl} \frac{\partial \Psi}{\partial x} \right) \quad (6.29)$$

in the next corrective step. The problem is that the diffusion process and the equation that describes it are irreversible. However, equation 6.29 can be written in the form

$$\frac{\partial \Psi}{\partial t} = - \frac{\partial}{\partial x} (u_d \Psi) , \quad (6.30)$$

where

$$u_d \equiv \begin{cases} - \frac{K_{impl}}{\Psi} \frac{\partial \Psi}{\partial x} & \Psi > 0 \\ 0 & \Psi = 0 \end{cases} . \quad (6.31)$$

Here, u_d is taken as the 'diffusion velocity'. Along this line, an 'antidiffusion velocity' is now defined as:

$$\tilde{u} = \begin{cases} -u_d & \Psi > 0 \\ 0 & \Psi = 0 \end{cases} . \quad (6.32)$$

Using this 'antidiffusion velocity', the reversal in time of the diffusion equation 6.29 may be simulated by the advection equation 6.30. Based on these concepts, the advection scheme can be summed up as following:

$$1) \Psi_i^* = \Psi_i^N - \left\{ F \left(\Psi_i^N, \Psi_{i+1}^N, u_{i+\frac{1}{2}}^N \right) - F \left(\Psi_{i-1}^N, \Psi_i^N, u_{i-\frac{1}{2}}^N \right) \right\} , \quad (6.33)$$

$$2) \Psi_i^{N+1} = \Psi_i^* - \left\{ F \left(\Psi_i^*, \Psi_{i+1}^*, \tilde{u}_{i+\frac{1}{2}} \right) - F \left(\Psi_{i-1}^*, \Psi_i^*, \tilde{u}_{i-\frac{1}{2}} \right) \right\} , \quad (6.34)$$

and

$$\tilde{u}_{i+\frac{1}{2}} = \frac{\left(|u_{i+\frac{1}{2}}| \Delta x - \Delta t u_{i+\frac{1}{2}}^2 \right) (\Psi_{i+1}^* - \Psi_i^*)}{\left(\Psi_i^* + \Psi_{i+1}^* + \epsilon \right) \Delta x} , \quad (6.35)$$

where F is defined as in equation 6.25, and ϵ is a small value, e.g. 10^{-15} , to ensure that $u = 0$ when $\Psi_{i+1}^* = \Psi_i^* = 0$. It is assumed that for all i , $\Psi_i^0 \geq 0$.

This is our new positive definite advection scheme with small implicit diffusion. It has a simple form that is computationally efficient. An analysis of the stability and consistency of this scheme is presented in *Smolarkiewicz [1983]*. The scheme is expanded to the multidimensional case and generalised in *Smolarkiewicz [1984]*, and its implementation, stability and general applicability is further discussed in *Smolarkiewicz [1991]* and *Smolarkiewicz & Margolin [1993]*.

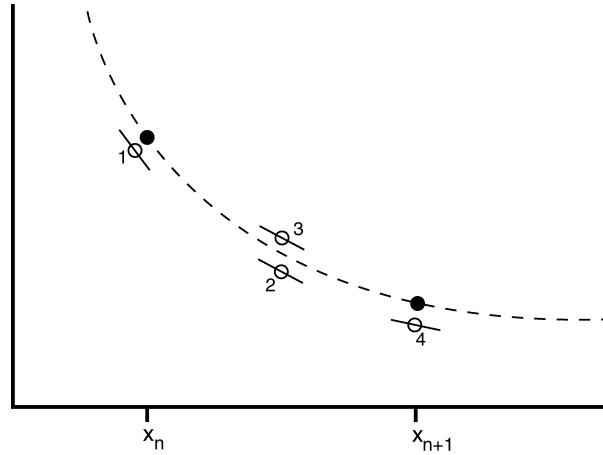


Figure 6.5: 1D-example of the fourth-order Runge Kutta method. In each step the derivative is evaluated four times: once at the initial point, twice at the trial midpoint, and once at the trial endpoint. From these derivatives, the final functional value is then calculated. From [Press et al \[1992\]](#).

6.3.4 Limiting of the timestep

The method of finite differences presented in the previous sections does not exactly reproduce the hydrodynamic equations, but does unavoidably produce numerical errors over the course of the calculations. Equations with nonlinear terms (like the hydrodynamical equations) are particularly sensitive to these errors - perturbations can grow exponentially. Thus, in addition to the increased precision of the multigrid algorithm, we use a von Neumann stability analysis ([Smarr \[1978\]](#)), which gives us the Courant-Friedrichs-Lewy criteria:

$$(|v| + c_s) \frac{\Delta t}{\Delta z} \leq 1. \quad (6.36)$$

For the known properties Δz , $|v|$, c_s we get a postulation to the timestep Δt :

$$\Delta t \leq \frac{\Delta z}{|v| + c_s}. \quad (6.37)$$

Here, Δt is the timestep, Δz is the length of a grid cell. The Courant-Friedrichs-Lewy criteria can be pictured in that during a time interval Δt , a perturbation can not propagate further than the length of a cell Δz . If that were possible, it would mean that the contributions of the 'overstepped' cells to the perturbation would be lost, since the program only updates all relevant values after the time Δt has passed. This, in turn, would result in artificial congestion phenomena, which in turn would cause Instabilities.

6.3.5 Tracer Particle implementation

The disadvantage of a grid-based hydrodynamics code is that it is impossible to track a specific volume of fluid within the computational region. To get around this problem, passive tracer particles are introduced. These particles do not influence the flow field, but can carry all kinds of information (e.g. starting position). To determine the particle flow speeds for all the particles within a grid cell, the velocities first have to be mapped on the centre of the grid cell. Then, velocity is weighted by the distance of the particle position relative to the centre of the grid

cell. The spatial displacement of a single tracer particle with the positional vector \vec{X}_{tp} during a timestep Δt can then be written as:

$$\frac{\partial \vec{X}_{tp}}{\partial t} = \vec{V}_{tp}(\vec{X}_{tp}, t) , \quad (6.38)$$

with $\vec{X}_{tp} = (x_{tp}, y_{tp}, z_{tp})$ and $\vec{V}_{tp} = (v_{x,tp}, v_{y,tp}, v_{z,tp})$. During a single time-step Δt , the tracer particle position is advanced from time 't' to time 't+ Δt ', corresponding with a change in the positional vector from \vec{X}_{tp}^n to \vec{X}_{tp}^{n+1} . The standard Euler method for this can be written as:

$$\vec{X}_{tp}^{n+1} = \vec{X}_{tp}^n + \vec{V}_{tp}^n \bullet \Delta t , \quad (6.39)$$

Written in general form for one dimension and simplified, we get:

$$x_{n+1} = x_n + hf(x_n, t_n) , \quad (6.40)$$

which advances a solution from t_n to $t_{n+1} \equiv t_n + h$. The formula is unsymmetrical: The solution is advanced through an interval h , but the formula uses derivative information only at the beginning of the interval. Thus, the step's error is only one power of h smaller than the corrective term $O(h^2)$. Essentially, this means that the Euler method is neither particularly accurate nor particularly stable. However, if we use equation 6.40 to take 'trial' steps over a number of midpoints before computing the 'real' step across the whole interval, we get a fourth-order Runge-Kutta formula (figure 6.5), as presented e.g. by *Abramowitz & Stegun [1972]*:

$$\begin{aligned} k_1 &= hf(x_n, t_n) \\ k_2 &= hf\left(x_n + \frac{k_1}{2}, t_n + \frac{h}{2}\right) \\ k_3 &= hf\left(x_n + \frac{k_2}{2}, t_n + \frac{h}{2}\right) \\ k_4 &= hf(x_n + k_3, t_n + h) \\ x_{n+1} &= x_n + \frac{k_1}{6} + \frac{k_2}{3} + \frac{k_3}{3} + \frac{k_4}{6} + O(h^5) \end{aligned} . \quad (6.41)$$

This gives us a reasonable accuracy of at least second order, while being computationally efficient. The specifics of implementation and accuracy of the fourth-order Runge Kutta method is discussed e.g. in *Press et al [1992]*.

Scalar quantities can be mapped effortlessly on the particles using a simple weighting algorithm, and can be updated at any point during the simulation run. Due to the passive nature of the particles, particle values are generally not mapped back onto the grid - for this, a more complicated weighting / mapping algorithm taking into account a number of additional factors (like the number of particles per grid cell, e.g.) would need to be implemented. A detailed discussion on the implementation of tracer particles can be found in e.g. *Brock et al. [1998]* and *Tackley & King [2003]*.

Chapter 7

Numerical Modelling of Lab Conditions

This chapter starts with a brief discussion of the boundary conditions specific to the modelling of laboratory point source and injection source experiments. The following sections then discuss the data derived from the numerical models and compare this data to the respective laboratory experiments. The results of detailed studies of temperature, velocities, mass flux and other properties are presented, with a special section dedicated to a closer look at the sampling of the plume source region. The chapter wraps up with a summary and assessment of the lab condition numerical modelling and leads on to the mantle condition models presented in the next chapter.

7.1 Initial Setup and Boundary Conditions

The size of the domain in the models at hand is $200\text{mm} \times 200\text{mm} \times 40\text{mm}$ in the x, y, and z direction, respectively. This domain is meshed by either $64 \times 64 \times 128$ grid cells, or by $128 \times 128 \times 256$ grid cells. Hence, the formal grid-point resolution is either 3.125mm or 1.5625mm, respectively. The physical parameters used in this set of models are chosen as to match the physical parameters of the syrup that are presented in appendix A.

The velocity boundary conditions are:

- closed (=no flow) boundaries in x-direction for the left and right walls, with no-slip boundaries for flow in y and z-direction.
- closed (=no flow) boundaries in y-direction for the front and back walls, with no-slip boundaries for flow in x and z-direction.
- closed (=no flow) boundary in z-direction for the surface boundary, with no-slip boundaries for flow in x and y-direction.

For the point source models, the bottom boundary is a closed (=no flow) boundary in z-direction, with no-slip boundaries for flow in x and y-direction.

In the injection models, the center of the bottom boundary is open for inflow in z-direction,

with a set inflow velocity of the form

$$v_{inflow} = v_0 + v_{inject} \exp\left(-\frac{(x - x_{center})^2 + (y - y_{center})^2}{r_{nozzle}^2}\right). \quad (7.1)$$

Here, v_{inject} is the injection velocity determined from the injection rates of section 4.2.2, and r_{nozzle} is the radius of the opening through which material is injected. To ensure mass balance, the fringe region of the bottom boundary is open for outflow in z-direction. The reason for this is thus: Continuously adjusting the total size of the computational region to reflect the rise in syrup level within the tank is both difficult to implement as well as computationally inefficient. Opening the top boundary for outflow would result in the plume simply passing through this boundary, neither slowing down, spreading out or forming a swell. Opening side boundaries, or even just parts of side boundaries, for outflow would potentially result in a disturbance of the general flow pattern. The flow at the edges of the bottom boundary is least relevant for this study, hence the decision to set the sides of the bottom boundary to allowing for material to escape. For flow in x and y-direction, the bottom boundary remains set to no-slip.

The boundary conditions for the temperature field are constant at the top, bottom and side walls ($T_{top}, T_{bottom}, T_{wall} = T_T$), with T_T set to the same values as the lab experiment tank temperatures presented in chapter 4. At the onset time of the simulation, the temperature is constant throughout the experimental tank at T_T .

In the point source models, the heating element is approximated through prescribing a gaussian temperature boundary condition of the form

$$T_{totbot} = T_{bottom} + T_{ps} \exp\left(-\frac{(x - x_{center})^2 + (y - y_{center})^2}{r_{ps}^2}\right), \quad (7.2)$$

centered on the center of the bottom of the computational grid. Here, T_{ps} is the point source temperature, with values reflecting those presented in section 4.1.2. The radius of the heating element is given by r_{ps} .

In the injection source models, the temperature of material flowing in through the bottom boundary is set to T_{inj} , with values reflecting those presented in section 4.2.2.

Fluid origins are tracked through more than six million passive tracer particles for the $64 \times 64 \times 128$ grid cells resolution, and upward of 50 million passive tracer particles for the $128 \times 128 \times 256$ grid cells resolution. Each tracer holds the information of initial starting position, with other quantities (like particle speed or temperature) mapped onto the tracers and updated during the simulation when required.

7.2 Point Source Runs

For the numerical modelling of point source thermally driven plumes, the laboratory experiments of set B presented in section 4.1.2.2 are recreated. The conditions of set B are shown in table 7.1.

Figure 7.1 presents a comparison between the temperature and ascent rates determined in the laboratory experiments and the temperature and ascent rates derived from the numerical models. Overall, the point source numerical models can very accurately reproduce the velocities and thermal evolution of the laboratory experiments. However, the plume head in the 30°C tank temperature models does not grow to as large a diameter as in the laboratory experiments,

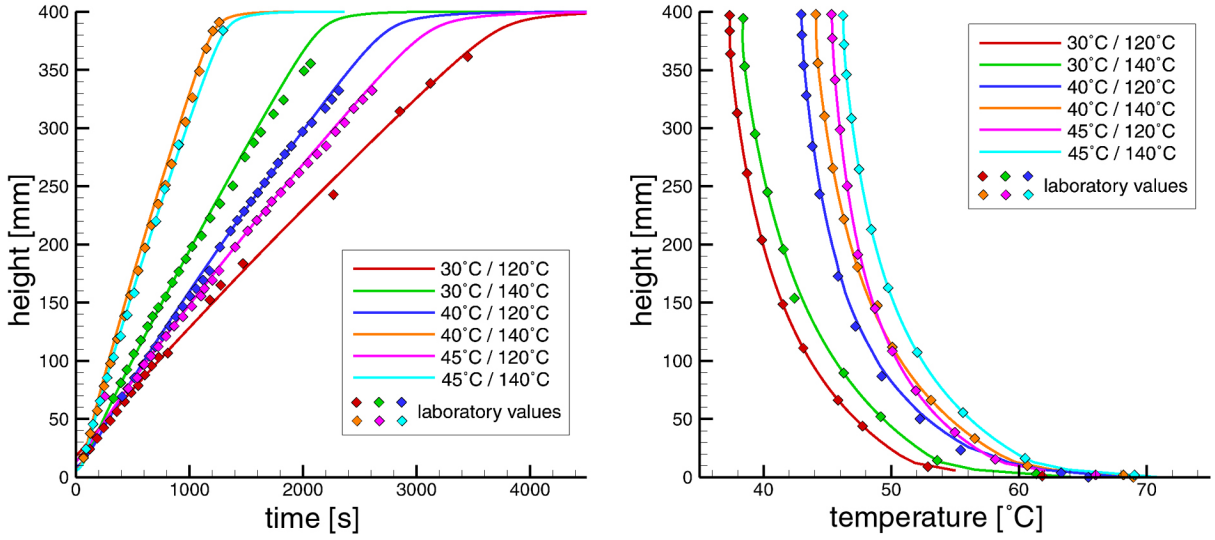


Figure 7.1: *Left: Comparison of the point source laboratory conditions numerical model ascent rates and the laboratory experiments data. Right: Comparison of the point source laboratory conditions numerical model temperature profiles and the laboratory experiments data.*

resulting in less influence from wall effects. This causes the numerical model to not suffer the same rate of slowdown in the upper half of the computational region that the laboratory experiments undergo.

Having thus established good agreement between laboratory and numerical data, and hence the applicability of the numerical models, the numerical models are now used to derive more information about the behaviour and physical characteristics of the laboratory plumes that is difficult to measure in laboratory experiments.

Figure 7.2 presents the thermal evolution of a numerical model with 40°C ambient temperature and 140°C point source temperature. It can be nicely seen how the source region material only absorbs a fraction of the bottom thermal perturbation before starting to rise, and how the material in the ascending plume cools significantly during ascent. The plume head exhibits a blunt dome-like shape, nicely reflecting the shape of the laboratory plume head. Furthermore, it seems as if the thermal pattern of the plume conduit reaches a quasi-steady state - temperatures in the plume tail remain relatively constant even long after the plume has been established. Temperatures in the offcenter regions of the plume head decrease significantly during plume ascent, with the outer regions of the plume head retaining a temperature anomaly of barely 1-2°C as the plume head approaches the surface.

To investigate the source heights of the plume and plume sheath material, the tracer particles

T_T	T_{ps}		T_T	T_{ps}		T_T	T_{ps}
30°C	120°C		40°C	120°C		45°C	120°C
30°C	140°C		40°C	140°C		45°C	140°C

Table 7.1: Overview of the various point source laboratory condition numerical models.

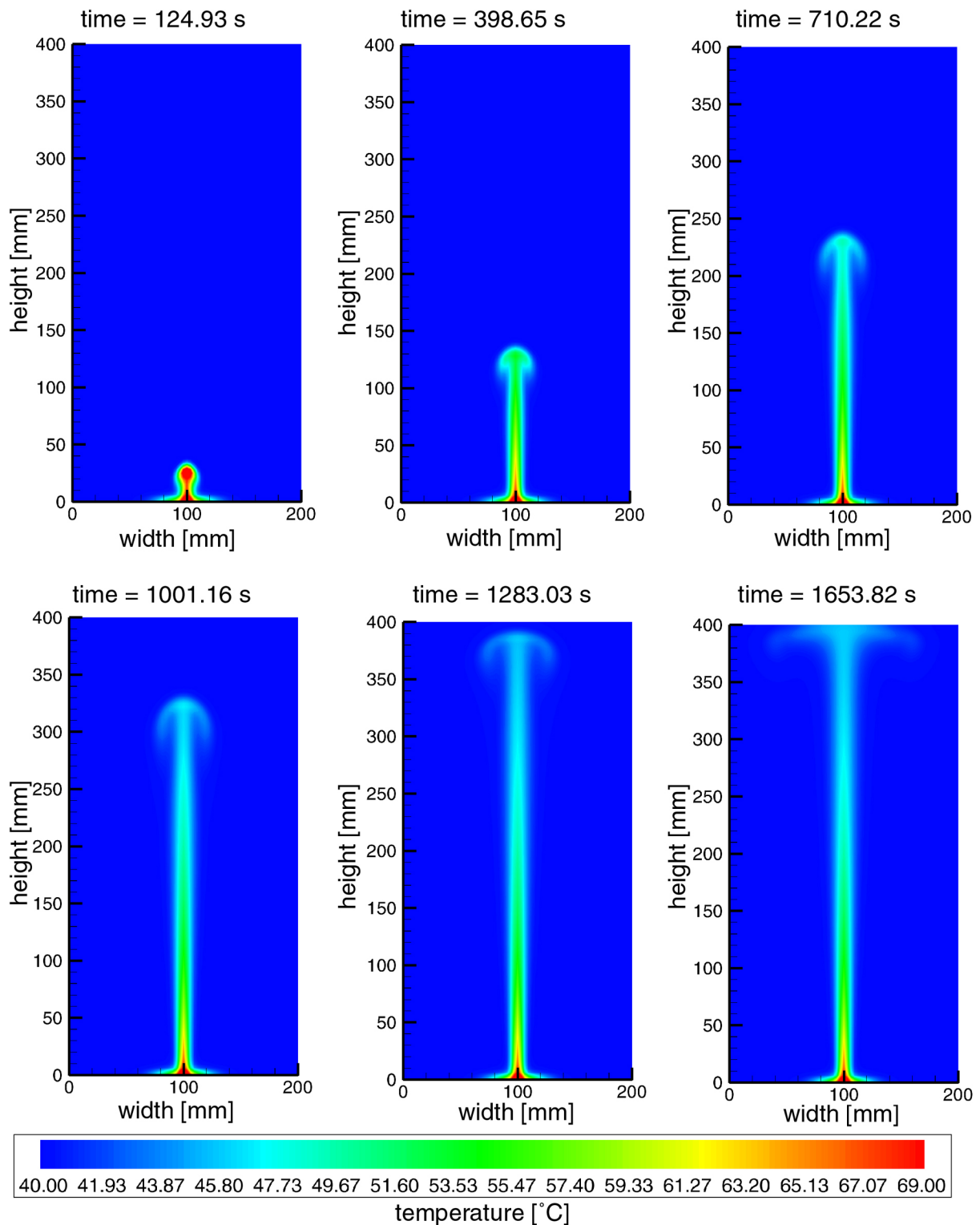


Figure 7.2: Thermal evolution of a point source laboratory conditions numerical model with 40°C ambient (tank) temperature and 140°C point source temperature.

used in the numerical model are colour-coded by starting height and plotted in figure 7.3. As seen from this sequence of figures, the plume sheath is formed at almost the same time as the

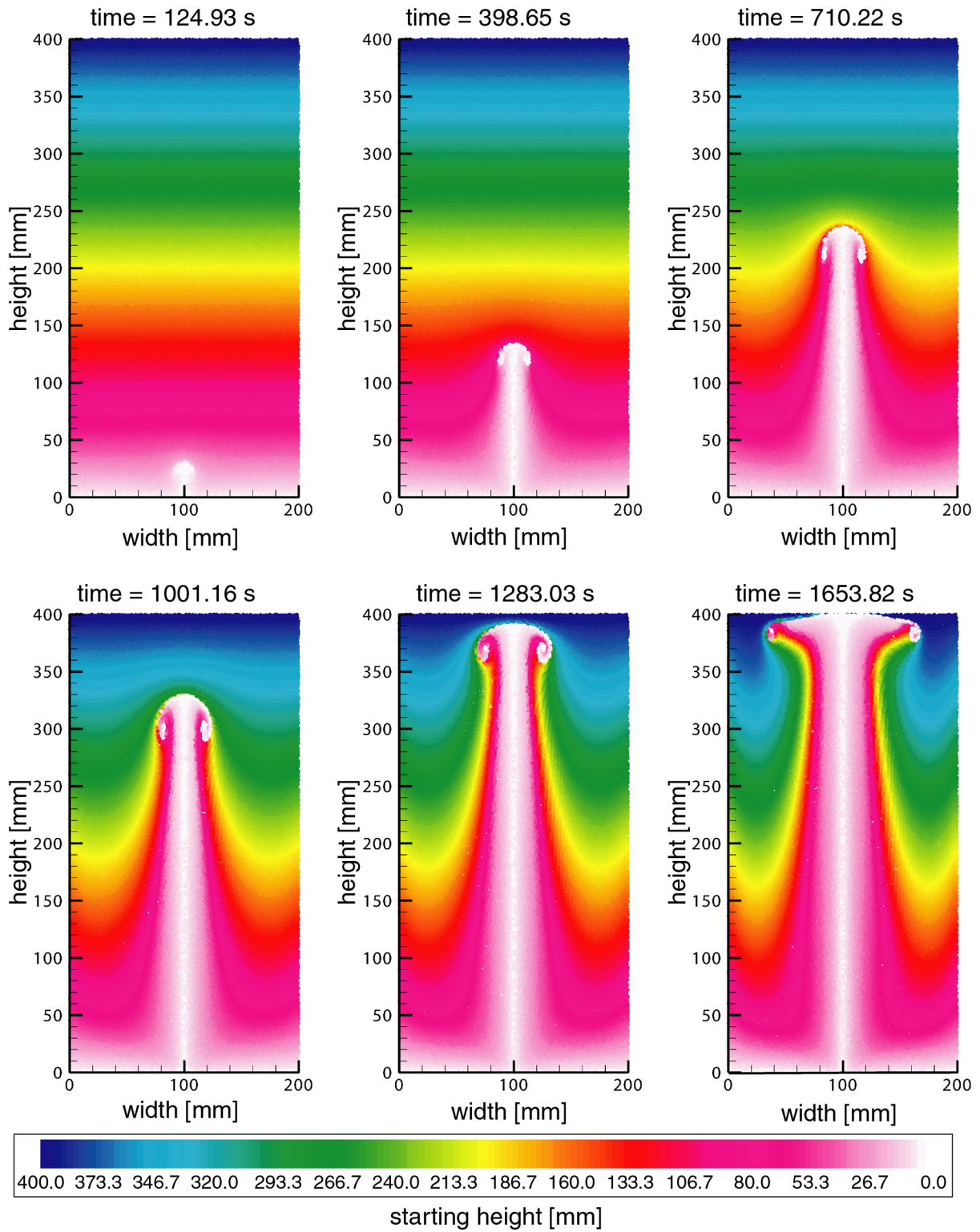


Figure 7.3: Material starting height sequence of a point source laboratory conditions numerical model with $40^{\circ}C$ ambient (tank) temperature and $140^{\circ}C$ point source temperature.

budding plume, with the material of the initial plume sheath coming from the deepest regions of the experimental region. This material is subsequently hoisted upwards in the wake of the

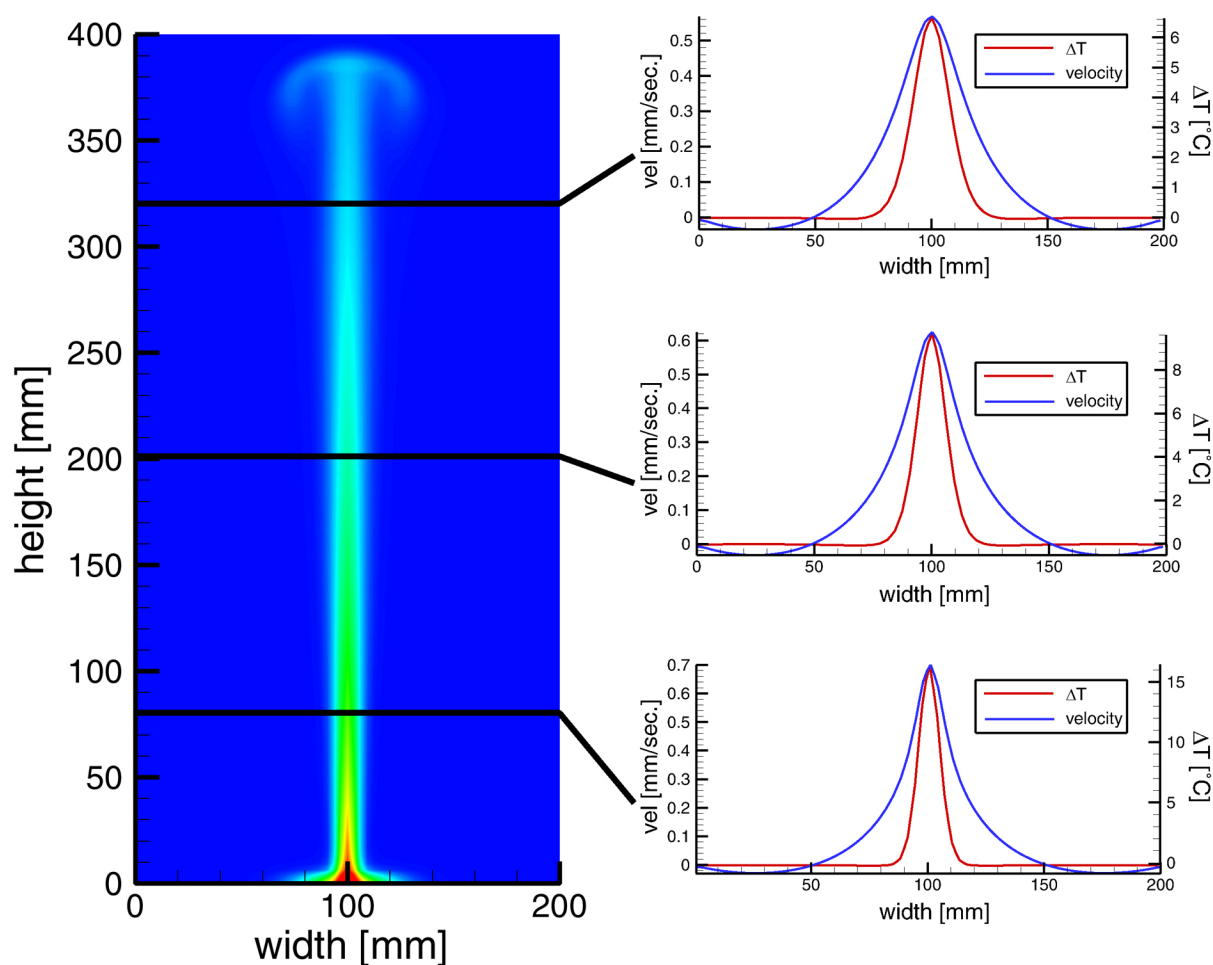


Figure 7.4: Horizontal cross-sections at 80mm, 200mm and 320mm height for a point source laboratory conditions numerical model with 40°C ambient (tank) temperature and 140°C point source temperature. Temperature and velocity profiles (pictures at right) reveal a partition in the plume sheath: a warm, inner plume sheath and a cold, outer plume sheath.

ascending plume head, forming a sheath of material around the plume with a width roughly corresponding to the diameter of the plume head. Some of the inner plume sheath is entrained into the plume head (see e.g. figure 7.3-1001.16s), where it is wound up around the 'doughnut' region of plume source material, and also provides some of the bulk of the plume head. Just like the plume forming a steady conduit once the plume head has reached the surface, the plume sheath establishes itself as a quasi-steady upwelling feature around the plume.

Investigating the temperatures and velocities of plume and plume sheath further (figure 7.4), it is found that a significant part of the plume sheath does not display a thermal anomaly at all. Obviously, the plume core does not strongly heat the enveloping plume sheath. Consequently, the plume sheath is to be further divided into an inner, heated ('warm') plume sheath that is in direct contact with the plume core, and an outer, cold plume sheath that rises as part of the large-scale flow induced by the buoyancy of the plume core. As the plume rises, more of the plume sheath is heated by conduction from the plume core, thus broadening the inner, warm plume sheath. However, the outer, cold plume sheath remains more or less constant in diameter.

The outer plume sheath is obviously not hot enough to sustain its own ascent. Rather, it

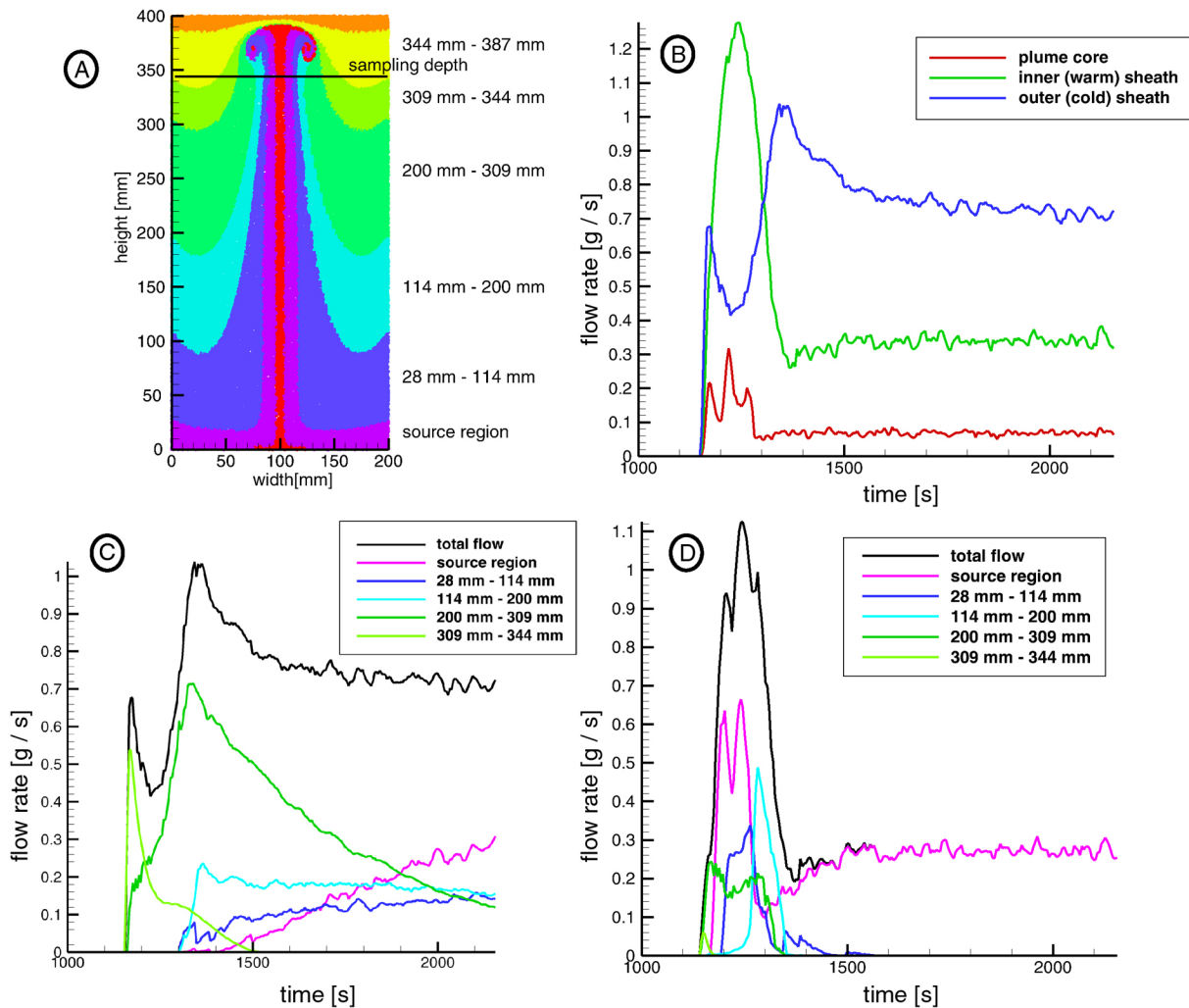


Figure 7.5: Flow rates for a point source laboratory conditions numerical model with 40°C ambient (tank) temperature and 14°C point source temperature: A) Overview on the distinct regions and sampling depth. B) Total plume flow, divided into core, inner sheath and outer sheath flow. C) Outer sheath flow, divided by origin of material. D) Inner sheath flow, divided by origin of material.

is being dragged upward in the slipstream of the ascending plume head. This also results in the viscosity of the outer plume sheath being roughly the same as the viscosity of the ambient material, thus greatly facilitating entrainment of ambient material.

The negative flow velocities on the sides of the velocity profiles in figure 7.4 are caused by the slow convective flow incited by the ascending plume and facilitated by the closed nature of the experimental region. This counter-flow can also be witnessed in the downgoing material in figure 7.3, and is representative of the flow behavior in the enclosed laboratory tank.

The entrainment characteristics of inner and outer plume sheath are further elaborated on in figure 7.5. Figure 7.5a presents the contribution of the different plume sections to the overall upward mass flux across a horizontal cross-section at 344mm height. The plume core and inner, warm plume sheath unsurprisingly dominate the passing through of the plume head (signified by the high flow rates), with the cool, outer plume sheath making up the majority of the plume conduit flow. All in all, up to fifteen times more material than found in the plume core is found

to be transported upwards in the plume sheath.

The composition of inner and outer plume sheath material is presented in figures 7.5c and 7.5d. The outer sheath is initially dominated by material from between 200mm and 309mm height as well as a smaller contribution from material originating between 309mm and 344mm height. This corresponds to the initial 'bow wave' of the plume head passing through the sampling region. Once the plume has been established, contributions from the upper regions drop dramatically. At the same time, contributions from the source region (0mm-28mm) to the outer plume sheath rise, which is indicative of the global, slow convective motion incited in the model region by the plume, which results in source region material being displaced and slowly driven towards the plume axis to be sampled into the plume. Meanwhile, the fraction of material from the lower regions (28mm - 200mm) remains relatively constant, hinting at a steady sampling of these regions. The inner plume sheath, by comparison, is fairly homogeneous in composition. During the passing of the plume head through the sampling region, there are minor contributions of entrained outer sheath material to the inner plume sheath, but once the plume head has passed through, the inner plume sheath is predominantly composed of source region material.

7.3 Pressure Runs

For the numerical modelling of injection source thermally driven plumes, the laboratory experiments of set C presented in section 4.2.2 are recreated. The conditions of set C are replicated in table 7.2 for ease of reference.

A critical look at figure 7.6 reveals that the fit between laboratory data and the injection source numerical models is still good, if not as good as the fit for the point source numerical models. Specifically, the injection source numerical model seems not to be able to faithfully reproduce the ascent rates at high ($=80^{\circ}\text{C}$) injection source temperature. This might not be entirely the fault of the numerical model, though - due to the rapid ascent rates and laboratory measurement method as well as the limited sample, the laboratory data itself might not be entirely representative in the 80°C injection temperature case. Still, comparing the rest of the laboratory and numerical data reveals a good fit between laboratory and mantle models.

The thermal evolution of a sample numerical model at 40°C ambient temperature, 70°C injection temperature and an injection rate of 20ml/min is presented in figure 7.7. As in the laboratory experiments, the thermal perturbation is much more pronounced in this set of models than in the point source models. The plume head is distinctly wedge-shaped, presumably because of the higher ascent rates of the injection case. Furthermore, the plume is much more

T_T	T_{inj}	inj. rate	T_T	T_{inj}	inj. rate	T_T	T_{inj}	inj. rate
40°C	60°C	$10 \frac{\text{ml}}{\text{min}}$	40°C	60°C	$15 \frac{\text{ml}}{\text{min}}$	40°C	60°C	$20 \frac{\text{ml}}{\text{min}}$
40°C	70°C	$10 \frac{\text{ml}}{\text{min}}$	40°C	70°C	$15 \frac{\text{ml}}{\text{min}}$	40°C	70°C	$20 \frac{\text{ml}}{\text{min}}$
40°C	80°C	$10 \frac{\text{ml}}{\text{min}}$	40°C	80°C	$15 \frac{\text{ml}}{\text{min}}$	40°C	80°C	$20 \frac{\text{ml}}{\text{min}}$

Table 7.2: Overview of the various injection source laboratory condition numerical models.

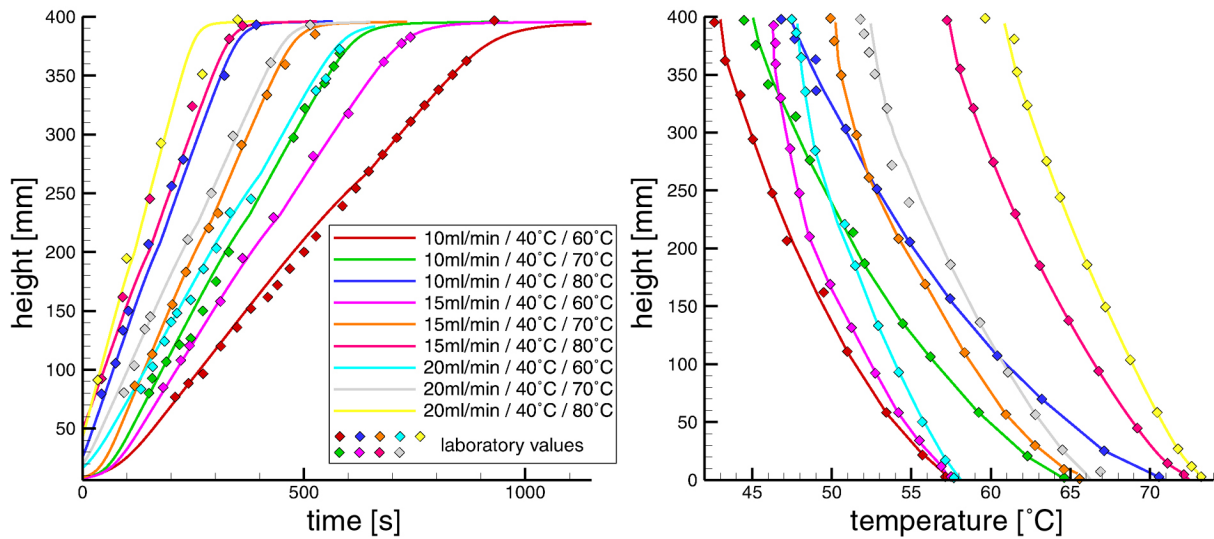


Figure 7.6: *Left: Comparison of the injection source laboratory conditions numerical model ascent rates and the laboratory experiments data. Right: Comparison of the injection source laboratory conditions numerical model temperature profiles and the laboratory experiments data. The figure legend in the left figure holds true for both figures.*

able to retain the initial thermal perturbation, and consequently is much hotter during the simulation than any point source model plume. This is particularly true of the plume head - while the plume head in the point source case is barely 1-2°C warmer than the surroundings at the time when the plume hits the surface, the plume head in the injection case remains a prominent thermal structure, with plume head temperatures exceeding the ambient temperature by around 10°C. Also, the plume tail is noticeably thicker. Still, the steady state behaviour of the plume conduit noticed in the point source models seems to hold true here as well - temperatures in the plume tail remain relatively constant even long after the plume has been established.

Looking at the source heights of the plume and plume sheath material in figure 7.8, it can be easily seen how the core upwelling of the plume is much broader than in the point source experiments. The formation of a plume sheath can be seen in this set of figures as well, however, there are a few remarkable differences to the point source experiments: First, the base of the plume sheath is much broader, which goes hand in hand with the observed broader plume core. Second, plume sheath material from the bottom of the experimental region is obviously flowing upwards much slower than the plume core is, resulting in the plume core continually replenishing the plume sheath with material of much shallower starting height. This is especially evident when comparing figure 7.8 at 483.39s and figure 7.3 at 1283.39s: In the point source case, there is a broad sheath of deep source material around the plume core, with comparatively thin layers of material from shallower origins at the outside of the plume sheath. Contrary to this, in the injection case the deep source layer is much thinner, mostly tapering off after roughly 200mm height, while at the same time material from shallower origins is dominant in the plume sheath.

The broadness and strength of the injection plume is further evidenced in the temperature and velocity diagrams of figure 7.9. Ascent velocities are up to twice as high as in the sample point source experiment in figure 7.4, with the temperature profiles hinting at a much hotter and much wider upwelling. Again, there is a definite distinction between inner, hot plume sheath and outer, cold plume sheath. While the plume inner plume sheath experienced some widening due to conductively heating its surroundings, this widening is not as expressed as in

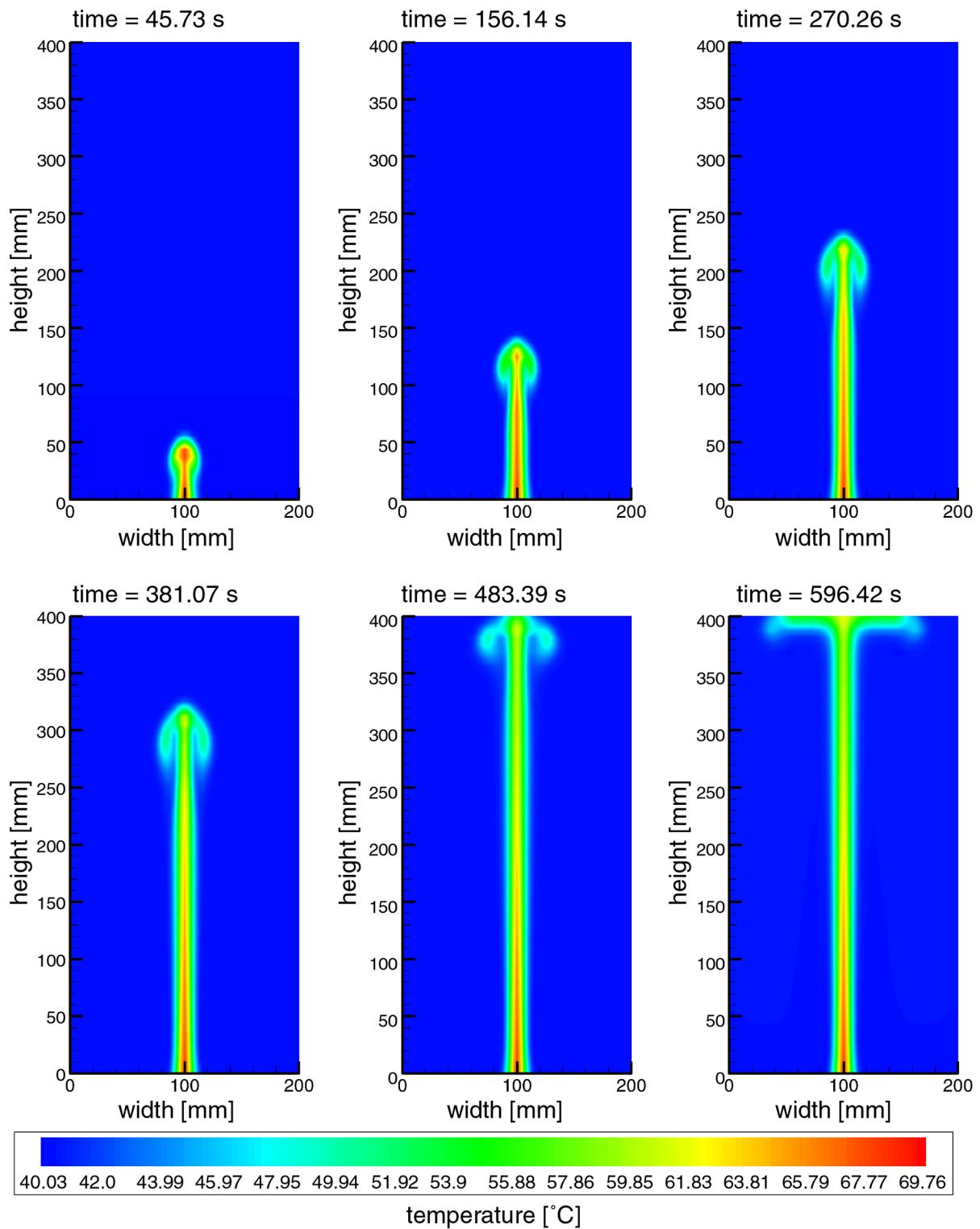


Figure 7.7: *Thermal evolution of a injection source laboratory conditions numerical model with 40°C ambient (tank) temperature, 70°C injection material temperature and an injection rate of $20\text{ml}/\text{min}$.*

the point source case - undoubtedly because of the much shorter ascent time, which is also the cause for the plume core being able to retain much more of the initial temperature perturbation.

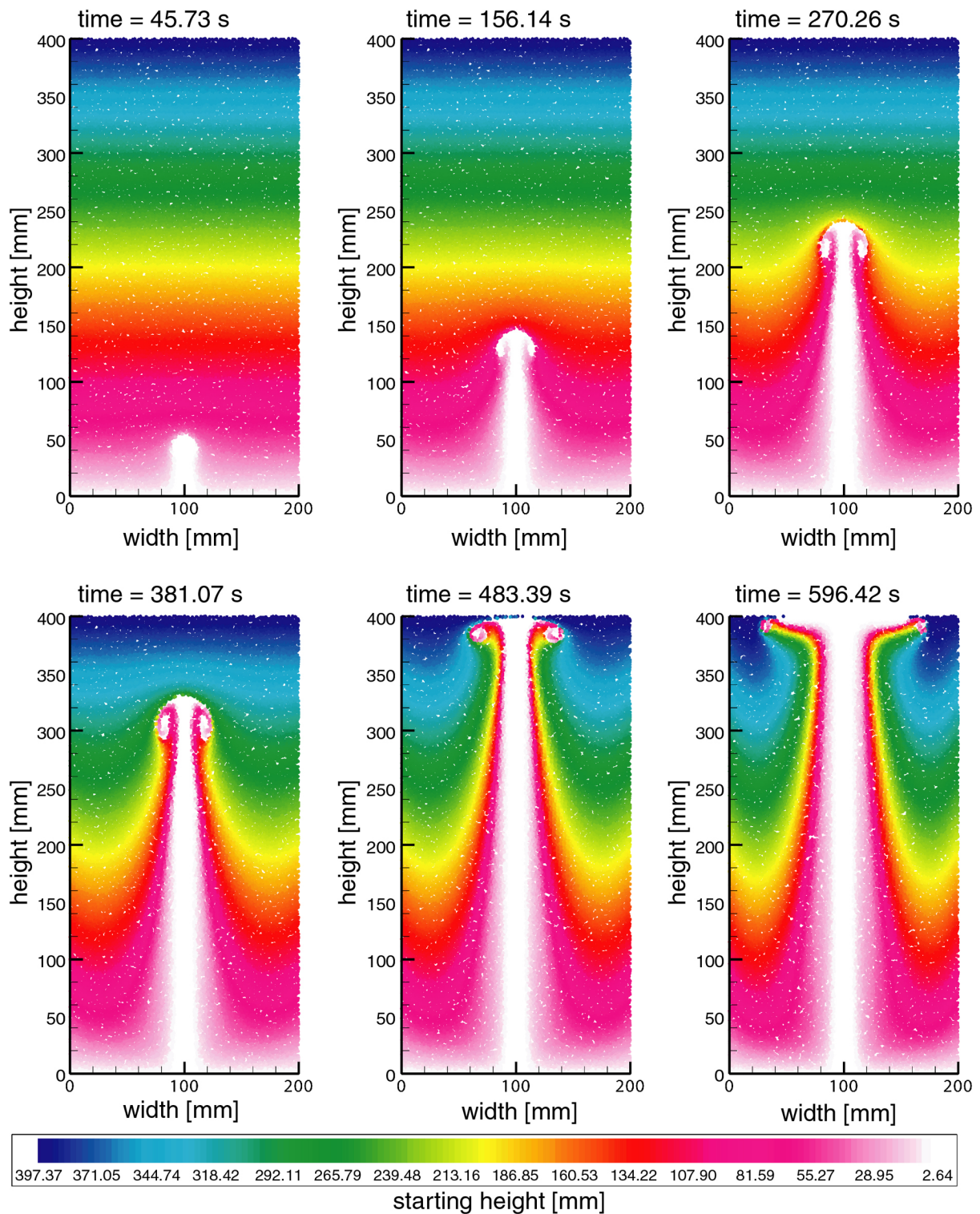


Figure 7.8: Material starting height sequence of a injection source laboratory conditions numerical model with 40°C ambient (tank) temperature, 70°C injection material temperature and an injection rate of $20\text{ml}/\text{min}$.

The cold plume sheath is about as broad as in the point source experiments, and changes little from bottom to top. Counter-flow at the sides is present, as also evidenced in figure 7.8, but

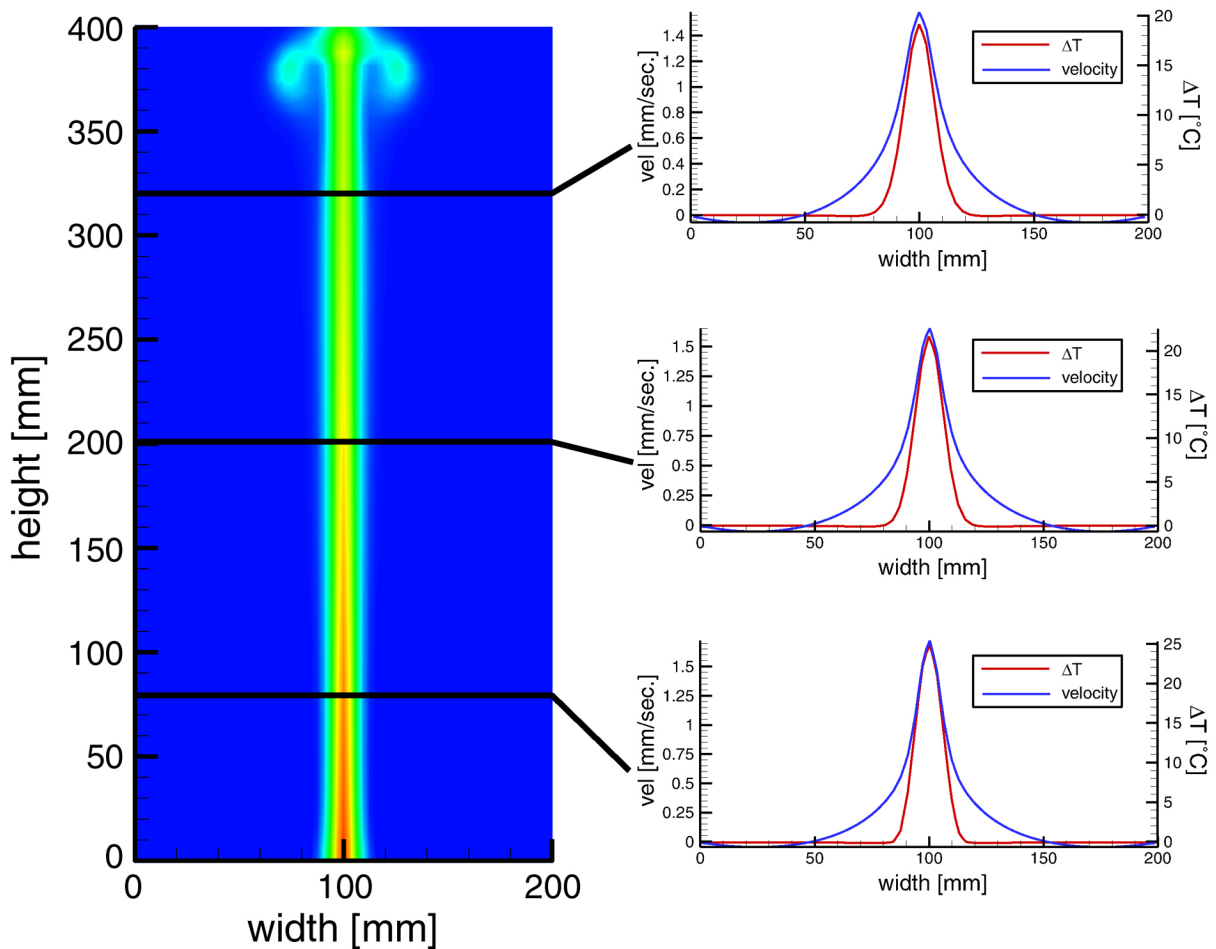


Figure 7.9: Horizontal cross-sections at 80mm, 200mm and 320mm height for a injection source laboratory conditions numerical model with 40°C ambient (tank) temperature, 70°C injection material temperature and an injection rate of 20ml/min. As with the point source models, temperature and velocity profiles (pictures at right) reveal a division into warm, inner plume sheath and cold, outer plume sheath.

downgoing velocities are not markedly higher than in the point source models.

The composition of inner and outer plume sheath as well as their contribution to the total plume flow are presented in figure 7.10. The higher plume core temperatures and faster plume ascent rate lead to a large contribution of plume core and particularly inner plume sheath material to the overall upward flow, with the inner plume sheath not only dominating during the time the plume head passes through the sampling region, but also afterwards. The ratio of plume core contribution to plume sheath contribution also goes down, with the sheath around the plume tail consisting of only about six times as much mass as the plume core.

The composition of the outer plume sheath does not differ greatly from the composition of the point source plume model sheath. Initially composed dominantly of material from above 200mm, this fraction of the outer plume sheath rapidly decreases, being replaced by slowly upwelling material from the broad 'base' of the plume sheath in the deep regions as well as by material from the source region. The inner plume sheath, however, retains an almost constant fraction of material from the 200mm-309mm and 309-344mm regions, while also displaying a very heterogeneous composition during the passing of the plume head through the sampling

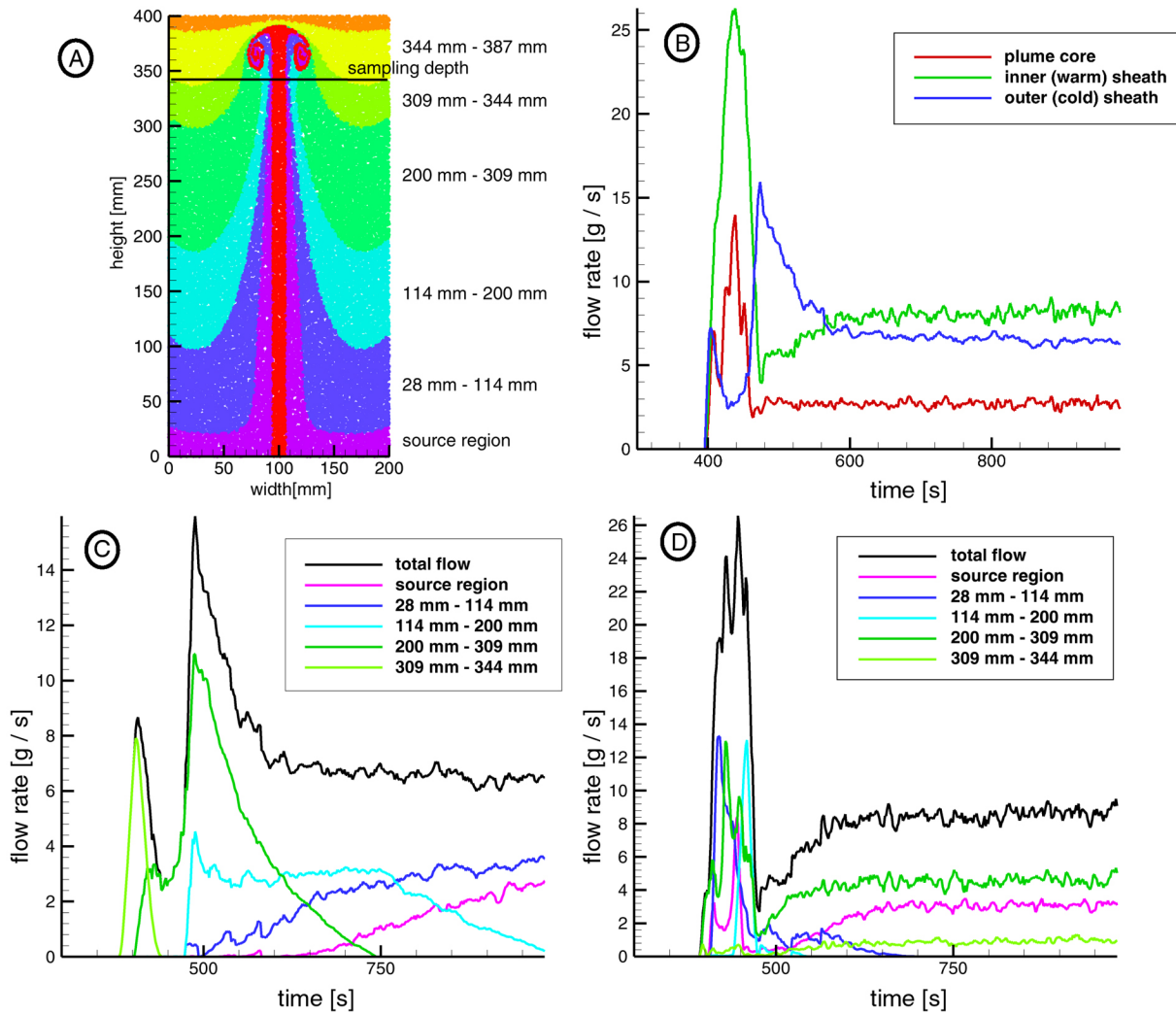


Figure 7.10: *Flow rates for a injection source laboratory conditions numerical model with 40°C ambient (tank) temperature, 70°C injection material temperature and an injection rate of 20ml/min: A) Overview on the distinct regions and sampling depth. B) Total plume flow, divided into core, inner sheath and outer sheath flow. C) Outer sheath flow, divided by origin of material. D) Inner sheath flow, divided by origin of material.*

region.

7.4 Sampling of the source layer

To study the sampling of the source region in detail, a number of numerical models using laboratory conditions are set up with only the deep plume source region holding tracer particles. These particles are subsequently colour-coded by their distance to the center of the thermal perturbation or inflow opening, respectively, with a distinct split in x-direction to distinguish between particles starting left of the plume and particles starting right of the plume.

The results of this is presented in figures 7.11 and 7.12. The lateral zonation of the plume source region is preserved as distinct vertical 'stripes' within the plume conduit, and is undistortedly reproduced in the plume swell as it spreads out under the surface. Lateral transport

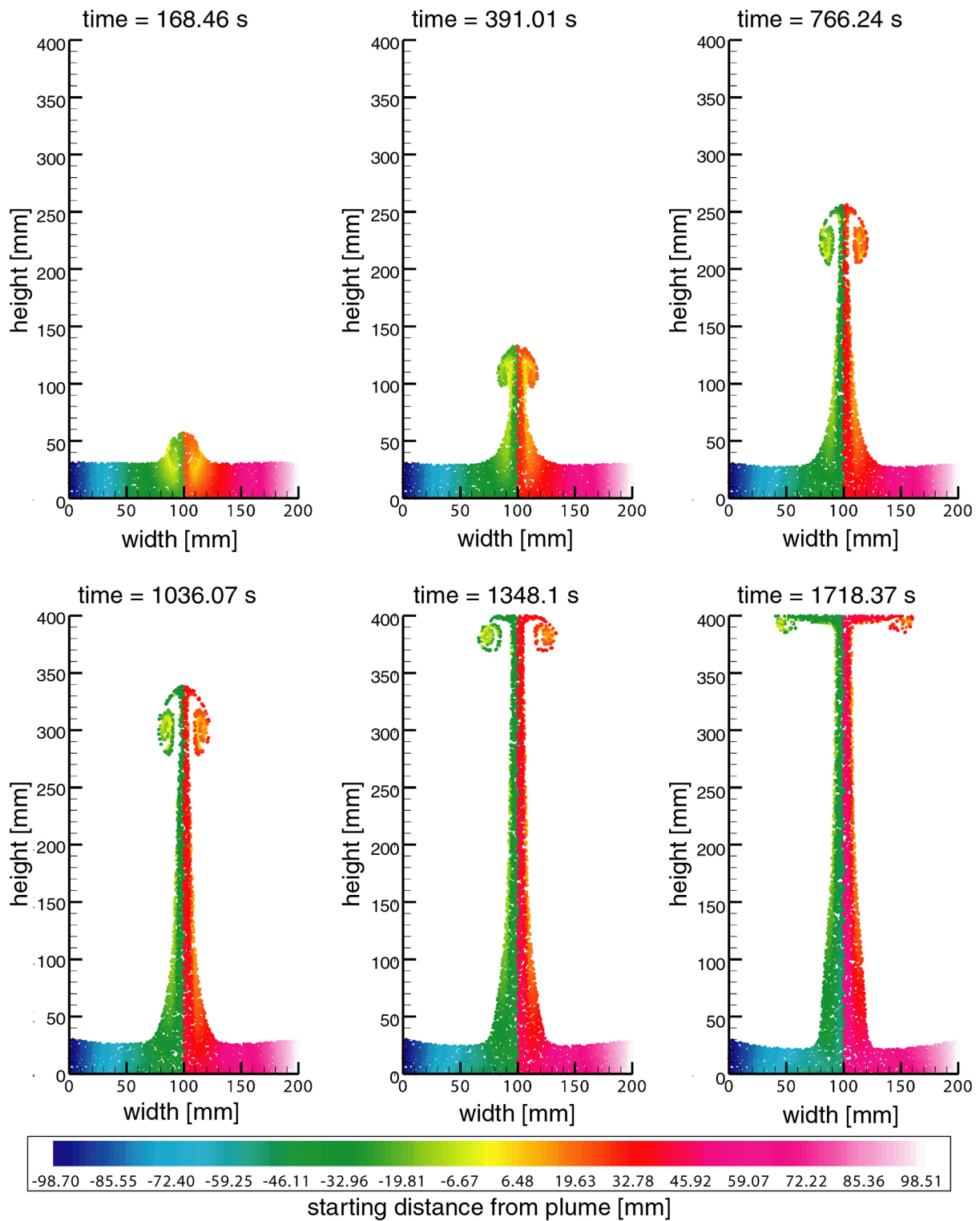


Figure 7.11: Sampling of the source layer a point source laboratory conditions numerical model with 40°C ambient (tank) temperature and 140°C point source temperature.

of material within the plume conduit is simply nonexistent, even after the plume source region and ambient material are seeded with small ($\sim 1\%$) density perturbations to facilitate turbulence and vorticity in the plume conduit. Simply put, what begins left of the plume axis remains left

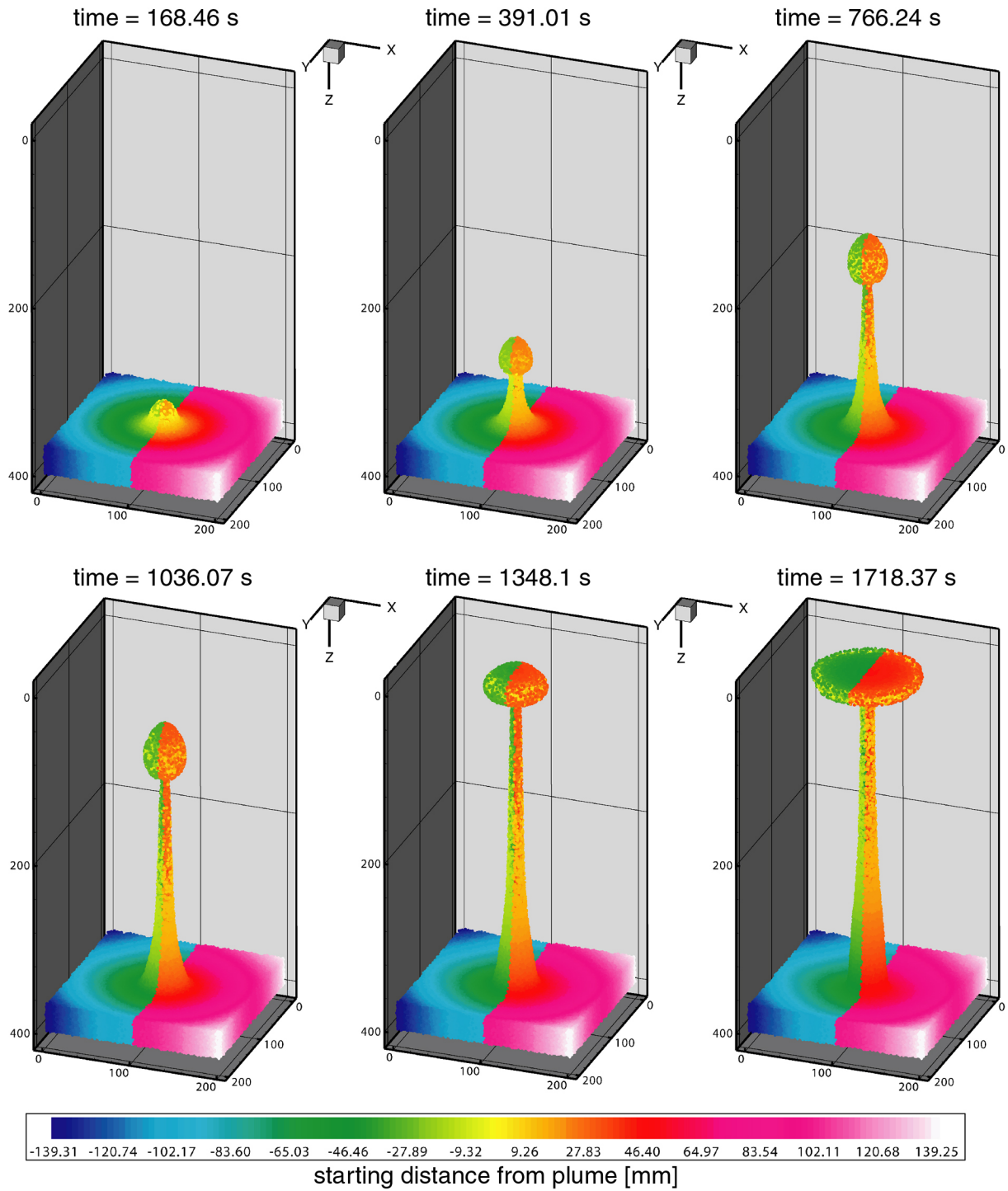


Figure 7.12: 3D plume evolution of a point source laboratory conditions numerical model with 40°C ambient (tank) temperature and 140°C point source temperature.

of the plume axis during ascent, and will spread to the left side of the plume axis during swell formation. This behaviour was tested for the full range of laboratory conditions outlined in sections 7.2 and 7.3 above, and was found to universally occur. This manifestly reproduces the plume flow behavior reported for the laboratory experiments of *Kerr & Mériaux* [2004], who observe this unshiftability of source region zonation even for plumes experiencing deformation

due to convective flow or shear from a moving top boundary.

It should be noted that figure 7.11 also nicely displays how plume core material is wound up in thin, delicate filaments around a 'doughnut' of source material in the plume core. This structure displays a distinct source progression, from material starting directly at the center axis of the upwelling plume making up the center 'doughnut' region to conduit material making up the outer 'curls' of the filament structure. This delicate buildup retains its general shape during plume ascent as well as for a short time after the plume has been established before finally collapsing against the surface boundary.

7.5 Assessment & Summary

Aside from questioning the resolution of the models presented in this chapter, it is the size of the computational region that raises the most concerns - namely whether the width of the computational region has been set to a large enough value to confidently rule out the influence of wall effects on the numerical models (this issue also applies to the width of the tank used in the laboratory experiments). To investigate this question, a number of experiments in which the width of the computational region was doubled while keeping the resolution value fixed were conducted. It was found that the behaviour of these double-wide numerical experiments did not substantially differ from the experiments presented in this chapter. Hence, the observations made in these models are very much relevant.

Regarding model resolution, it should be emphasised that the best resolution in the laboratory models presented here is one of $\sim 1.6\text{mm}$ - which compares favourably to most studies previously conducted in full 3D and is also on par with or exceeds the majority of previous 2D studies. Furthermore, it should be pointed out how distinctly well the filament structures of the ascending plume head are reproduced in the numerical models. The high level of detail in the filament structures highlights that the numerical resolution is adequate to resolve lab plume ascent and entrainment processes.

Reproducing the laboratory experiments presented in chapter 4 with numerical models not only supports the observations made in the laboratory experiments, but also serves as a test to validate and calibrate the fluid dynamics code the numerical models are based on. The presence of a plume sheath enveloping the ascending plume is confirmed, and the characteristics and behaviour of the plume sheath, like the partition of flow into an inner, warm plume sheath and an outer, cold plume sheath, are further constrained.

In the next chapter it will be investigated whether the experimental results of chapter 4 and the numerical results of this chapter also hold true for viscous flow in the Earth's mantle.

Chapter 8

Application to the Earth's Mantle

This chapter starts with a brief overview of the peculiarities of the Earth's mantle that have to be considered in the mantle models, and follows this up with a brief discussion on the boundary conditions common to the mantle simulations presented here. After that, four basic mantle models are introduced, and the results of the numerical simulations based on these models are presented and discussed in their respective sections. The chapter then wraps up with a discussion on the applicability of the models presented here, and leads on to the next chapter which will present a summary, discussion and outlook to this thesis.

8.1 The Earth's Mantle

Today's knowledge of the Earth's interior chiefly comes from compressional (P-wave) and shear (S-wave) waves that pass through the Earth in response to earthquakes. When hitting a discontinuity (caused by e.g. a change in pressure, temperature, composition or the amount of melt present), these waves are refracted and reflected, creating an abundance of seismic phases. From a seismological viewpoint, the interior of the Earth can be thought of as roughly spherical symmetric, and exhibiting three worldwide first-order discontinuities: the Mohorovičić discontinuity separating the crust from the mantle, the Gutenberg discontinuity separating the mantle from the outer core, and the boundary between the liquid outer core and the solid inner core. Focusing on the mantle, smaller velocity changes are found at ≤ 200 km, 410km and 660km depth, corresponding with the Lehmann discontinuity, the olivine to wadsleyite transformation, and the spinel to perovskite + magnesiowustite transformation, respectively. The 660km discontinuity is generally considered to separate the upper mantle and the lower mantle.

There are two boundary layers in the Earth that exhibit steep thermal gradients. The first is the lithosphere, which can be considered as a comparatively rigid upper boundary layer with conductive temperature gradient overlying a convecting adiabatic interior. The lower boundary of the lithosphere is defined to be an isotherm at approximately 1600K, denoting the threshold between rocks being sufficiently cool to behave rigidly and rocks being significantly hot to behave fluidly. The second is the D" layer overlying the core-mantle boundary, which is heated by conduction from the Earth's core, and which displays a complex seismological structure indicating temperature variations, compositional changes and mineralogical phase changes. Because of the high temperature and heterogeneous nature of D", it is commonly considered to be the source region where mantle plumes form. Between these two thermal boundary layers, the mantle convective system is reminiscent of the classical Rayleigh-Bénard

mantle density:	$\rho_m = 4000 \frac{kg}{m^3}$
mantle viscosity:	$\eta_m = 10^{21} Pa$
thermal expansion coefficient:	$\alpha = 2,0 \times 10^{-5} \frac{1}{K}$
thermal diffusivity:	$\kappa = 10^{-6} \frac{m^2}{s}$

Table 8.1: Physical parameters of the mantle models.

setup (see section 2.3.3).

Mantle convection is driven by a combination of three thermal processes: the aforementioned heating at the bottom by heat loss from the core, cooling from the top resulting in sinking of cool lithospheric slabs into the mantle, and heating by internal radioactive sources. Thermal structure and distribution in the mantle are still very much discussed. The same can be said about the mode of thermal convection in the mantle - some models present 'layered' convection as the explanation for the apparent compositional differences between the upper and lower mantle (with the line of demarcation between convective regions generally being the 660km discontinuity, although other models exist as well: see e.g. *Bercovici & Karato [2003]* for a summary on proposed mantle layers), while other models assume whole-mantle convection, pointing out that the negative Clapeyron slope of the spinel-perovskite transition does not significantly impede the sinking of slabs into the lower mantle or the rise of plumes into the upper mantle (e.g. *Davies [1995]*). In general, it can be said that the majority of geodynamic evidence today points towards the whole mantle convection of an intrinsically heterogeneous mantle (*Phipps Morgan [1998]*; *Phipps Morgan & Morgan [1999]*, *Ito & Mahoney [2005a,b]*).

The fluidlike behaviour of the mantle has been postulated by studies as early as the late 19th. century. It was established quantitatively by *Haskell [1935, 1936]*, who showed that the Earth's surface was still rebounding from the load of the ice during the last ice age. This so-called 'postglacial rebound' results from the fact that glacial growth and melting occur on sufficiently short time-scales so that dynamic effects are important in the adjustment of the mantle to the changing surface load. From the speed and velocities of uplift or subsidence, the viscosity of the mantle can be estimated (e.g. *Peltier [1989, 1996]*). The viscosity of the mantle is generally assumed to be on the order of 10^{21} Pa s, with a number of recent studies hinting at a more complex viscosity structure (e.g. *Griffiths & Richards [1989]*, *Richards [1991]*, *Kido & Yuen [2000]* and the studies mentioned below in their respective sections).

8.2 Numerical Modelling of Mantle Conditions

8.2.1 Initial Setup and Boundary Conditions

The size of the domain in the models at hand is $1450km \times 1450km \times 2900km$ in the x, y, and z direction, respectively. This domain is meshed by either $64 \times 64 \times 128$ grid cells, or by $128 \times 128 \times 256$ grid cells. Hence, the resolution is either 22,6km or 11,3km, respectively. The physical parameters used in this set of models can be found in table 8.1.

The velocity boundary conditions are:

- free slip boundaries on the front, back, left and right walls for flow in x, y and z-direction,

allowing for outflow and inflow of material.

- closed (=no flow) boundary for the surface boundary in z-direction, with no-slip boundaries for flow in x and y-direction.
- closed (=no flow) boundary for the bottom boundary in z-direction, with no-slip boundaries for flow in x and y-direction.

The boundary conditions for the potential temperature field are constant at the top ($T_{top} = 0^\circ\text{C}$) and bottom ($T_{bottom} = 1800^\circ\text{C}$), with reflective boundary conditions at the side walls. At the onset time of the simulation, the potential temperature is constant throughout the mantle at $T_{mant} = 1300^\circ\text{C}$, with a thermal boundary layer $\sim 80\text{km}$ thick at the top where the temperature decreases across as an error function (representing the lithosphere), and a thermal boundary layer $\sim 150\text{km}$ thick at the bottom where the temperature increases across as an error function (representing D^{''}). The thermal profile of the mantle is presented in figure 8.1. In order to trigger plume formation, a small perturbation ($T_{pert} \sim 3\% T_{bottom}$) is prescribed via a gaussian temperature boundary condition of the form

$$T_{totbot} = T_{bottom} + T_{pert} \exp\left(-\frac{(x - x_{center})^2 + (y - y_{center})^2}{r_{pert}^2}\right), \quad (8.1)$$

centered on the center of the bottom of the computational grid. Here, r_{pert} determines the width of the perturbation, and is set to $\sim 70\text{km}$.

Fluid origins are tracked through more than six million passive tracer particles for the $64 \times 64 \times 128$ grid cells resolution, and upward of 50 million passive tracer particles for the $128 \times 128 \times 256$ grid cells resolution. Each tracer holds the information of initial starting position, with other quantities (like particle speed or temperature) mapped onto the tracers and updated during the simulation when required.

Since the implementation of genuine phase transitions in the numerical model has not been met with success within the time frame of this thesis, the internal structure and buildup of the mantle is approximated by introducing a depth-dependent weighting function to the mantle viscosity. The following sections will present three different mantle viscosity models and their respective viscosity-depth functions. This weighting functions are applied to the computational domain at the start of the simulations as well as to every change in viscosity due to changes in temperature, composition or amount of melt present.

To get a first impression of the melting rates in the plume head, a very simple melting function taken from *Choblet & Parmentier* [2001] is implemented. Essentially, this melting model is based on a single solidus temperature given by:

$$T_{solidus} = T_{mant} + \left(\frac{dT}{dz}\right) z, \quad (8.2)$$

with the value for $(dT/dz) = 3.87^\circ\text{C km}^{-1}$ taken from *Choblet & Parmentier* [2001]. Melt produced by material exceeding this solidus temperature is reflected in the material depletion value (see section 6.2 for details), however the flow of melt is not treated in much detail in this model. It should be noted that this model is not intended to provide exact quantitative assessments on the amount of melt produced by the upwelling plume, but is rather meant to investigate whether the hottest, melt-producing regions of the plume head are composed solely of source region material (as suggested by *Farnetani et al.* [2002]) or whether entrained material is able to permeate the chief melting zone.

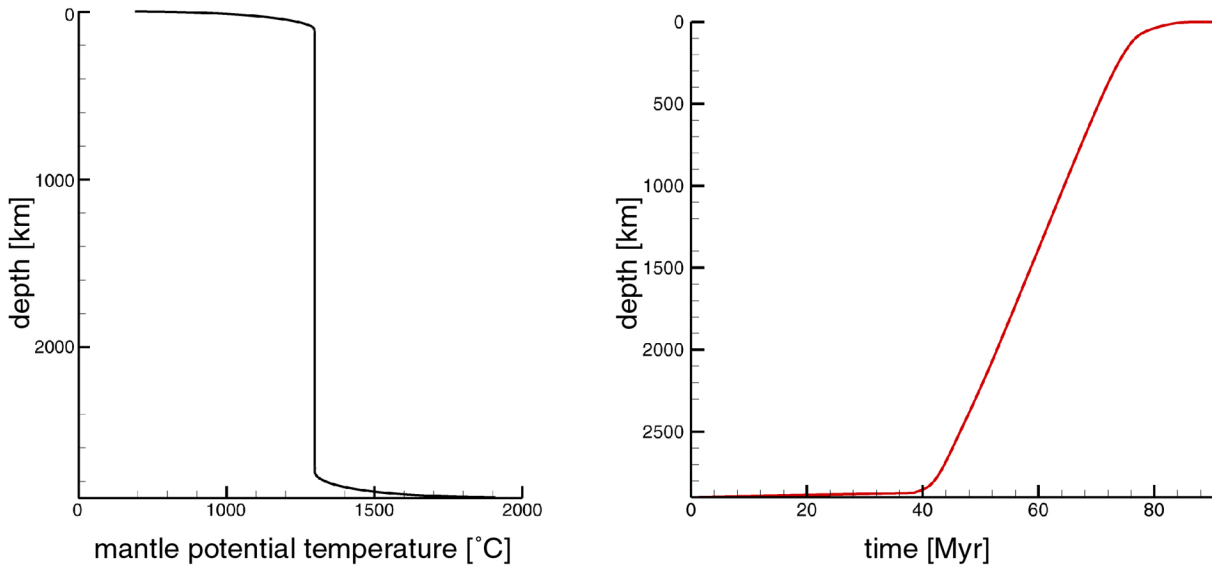


Figure 8.1: *Left: Temperature profile universal to the mantle models. Right: Ascent rate of the constant viscosity model.*

Lastly, in the experiments of section 8.3 plate motion and subsequent deflection of the plume is introduced. Plate motion is incited by prescribing a set velocity in x-direction to the surface boundary, as well as prescribing a fixed inflow velocity and outflow velocity over the depth of the lithosphere to the left and right boundaries. Below the lithosphere, the left and right side boundaries remain free slip, allowing for inflow and outflow of material.

8.2.2 The Constant Mantle Viscosity Model

The constant mantle viscosity setup most closely resembles the laboratory experimental and numerical setups, and is chosen for ease of comparison. Figure 8.2 shows the thermal evolution of a sample constant mantle viscosity experiment. It is immediately obvious that the ascending plume is much more able to retain the initial temperature perturbation compared with the laboratory experiments and laboratory conditions modelling. This is because of the thermal bottom boundary layer, which provides an ample source of pre-heated material to sustain plume ascent.

The plume itself rises relatively fast, with an initial period of ~ 40 Myr in which the temperature perturbation grows into a full-fledged plume, and another 40 Myr for the plume to traverse the mantle (see the plume ascent rate in figure 8.1). During ascent, the plume head exhibits a notable wedge-shaped deformation compared to the rather blunt heads of the point source laboratory experiments, while still maintaining the 'classic' mushroom head shape. This can presumably be attributed to the fast ascent, since similar deformation can also be observed in the injection source laboratory models (see section 7.3). The plume tail temperature remains relatively constant, while the offcenter regions of the plume head cool noticeably during ascent due to the entrainment of colder plume sheath material. The plume reaches the base of the lithosphere at ~ 80 Myr, with the plume head spreading out in reaction to the upper boundary. It should be noted that the hot center of the plume head is apparently strong enough to penetrate the cool, highly viscous lithosphere, while the outer, cooler regions of the plume head are spreading laterally just below the base of the lithosphere.

The bottom boundary layer, meanwhile, is far from stable. Small perturbations triggered

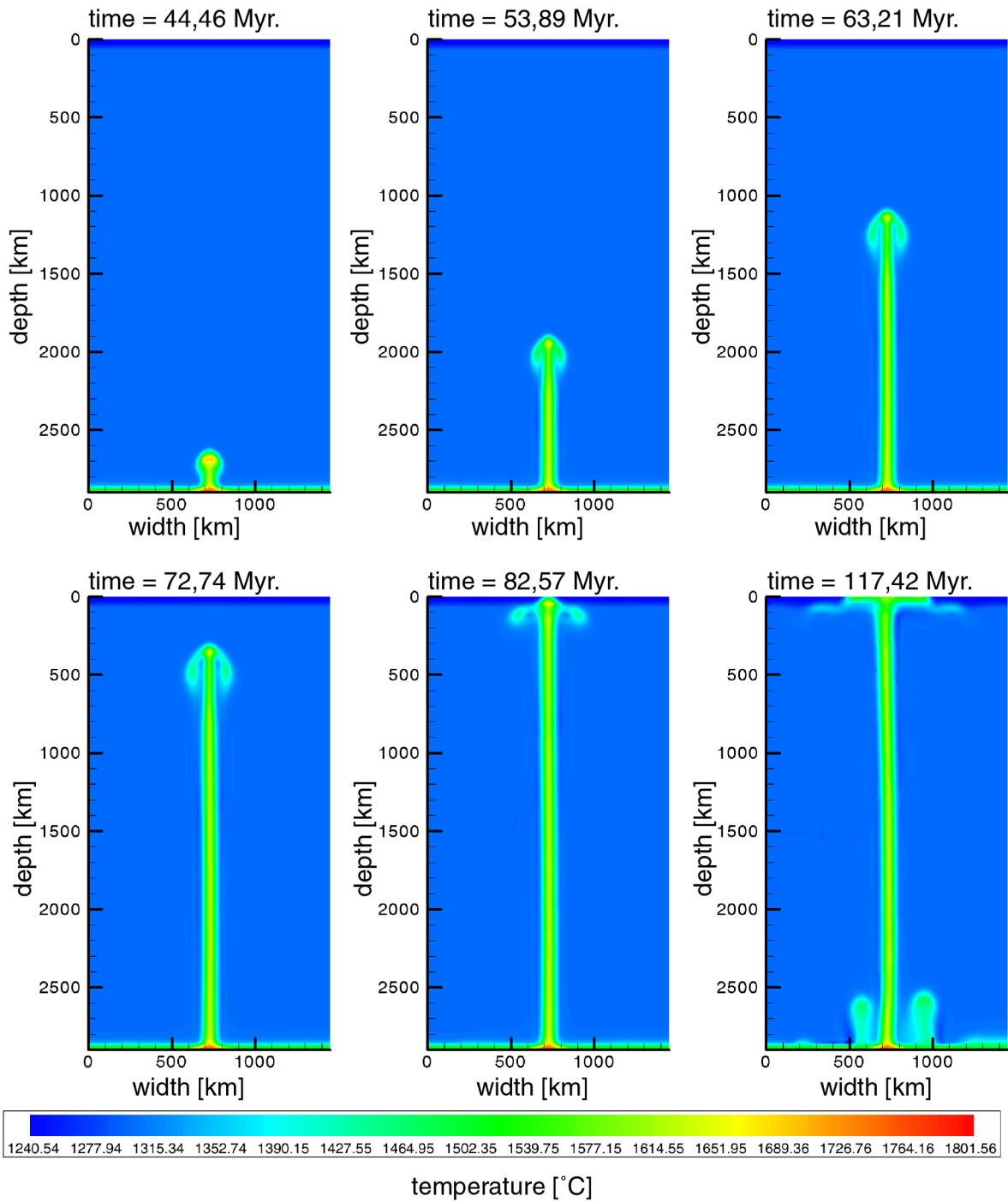


Figure 8.2: *Thermal evolution of the constant viscosity model.*

by the plume grow to form smaller, secondary plumes, as visible in the last frame of figure 8.2 (where two secondary plume have already begun to rise, while two more are starting to bulge and grow). These secondary plumes subsequently rise, massively disturbing and rupturing the plume tail and churning the bottom boundary layer even more. It is obvious that for plumes to remain fixed and stable over periods longer than ~ 30 Myr, there must be something stabilising the D'' layer and dampening the formation of smaller secondary plumes.

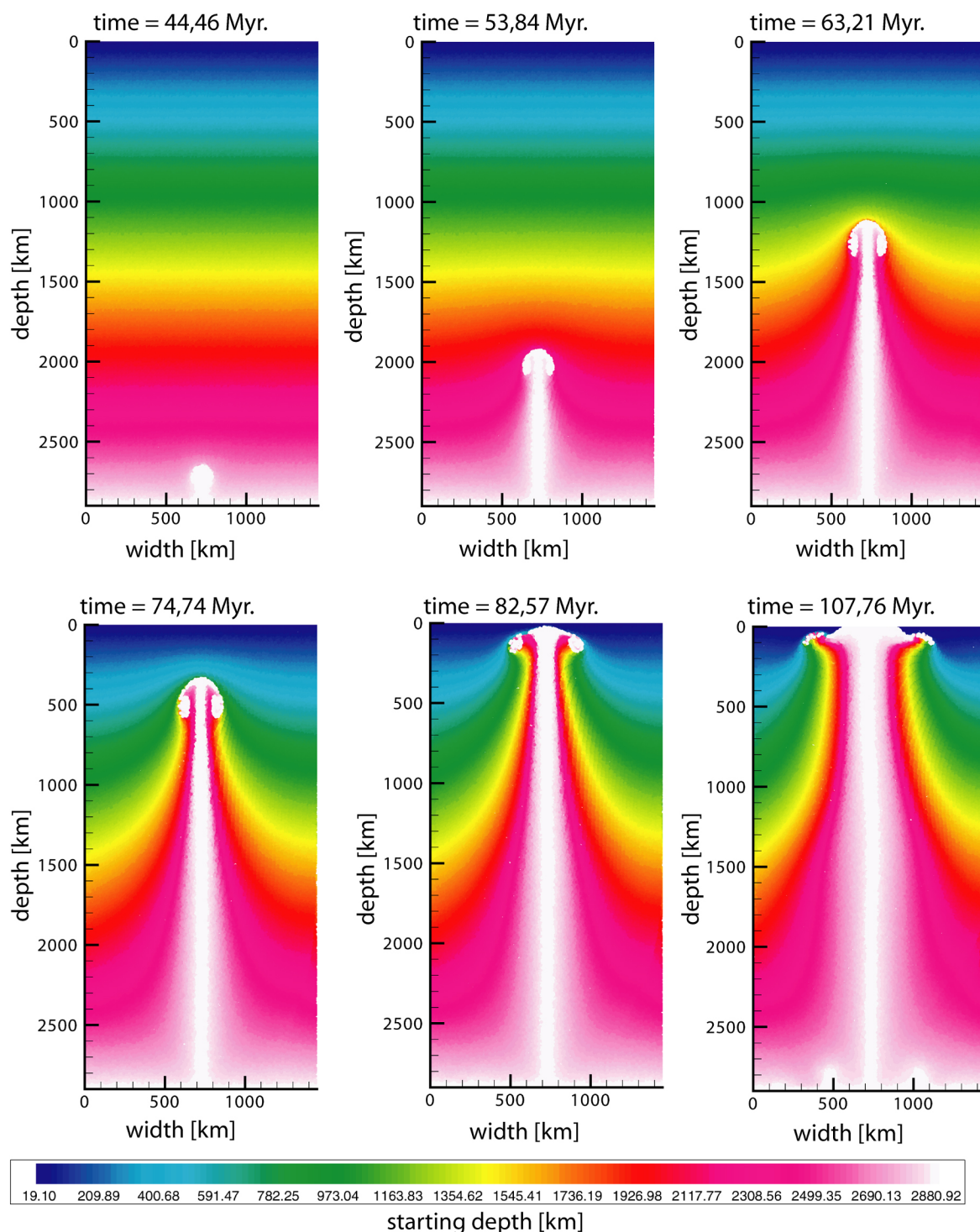


Figure 8.3: *Material starting depth sequence of the constant viscosity model.*

The entrainment characteristics of the plume are presented in figure 8.3. As observed in the laboratory experiments and laboratory condition models, the hot plume core is enveloped by a cold plume sheath rising in the wake of the plume head. The plume sheath here is as pronounced as in the laboratory models, consisting chiefly of deep source material directly overlying the D''

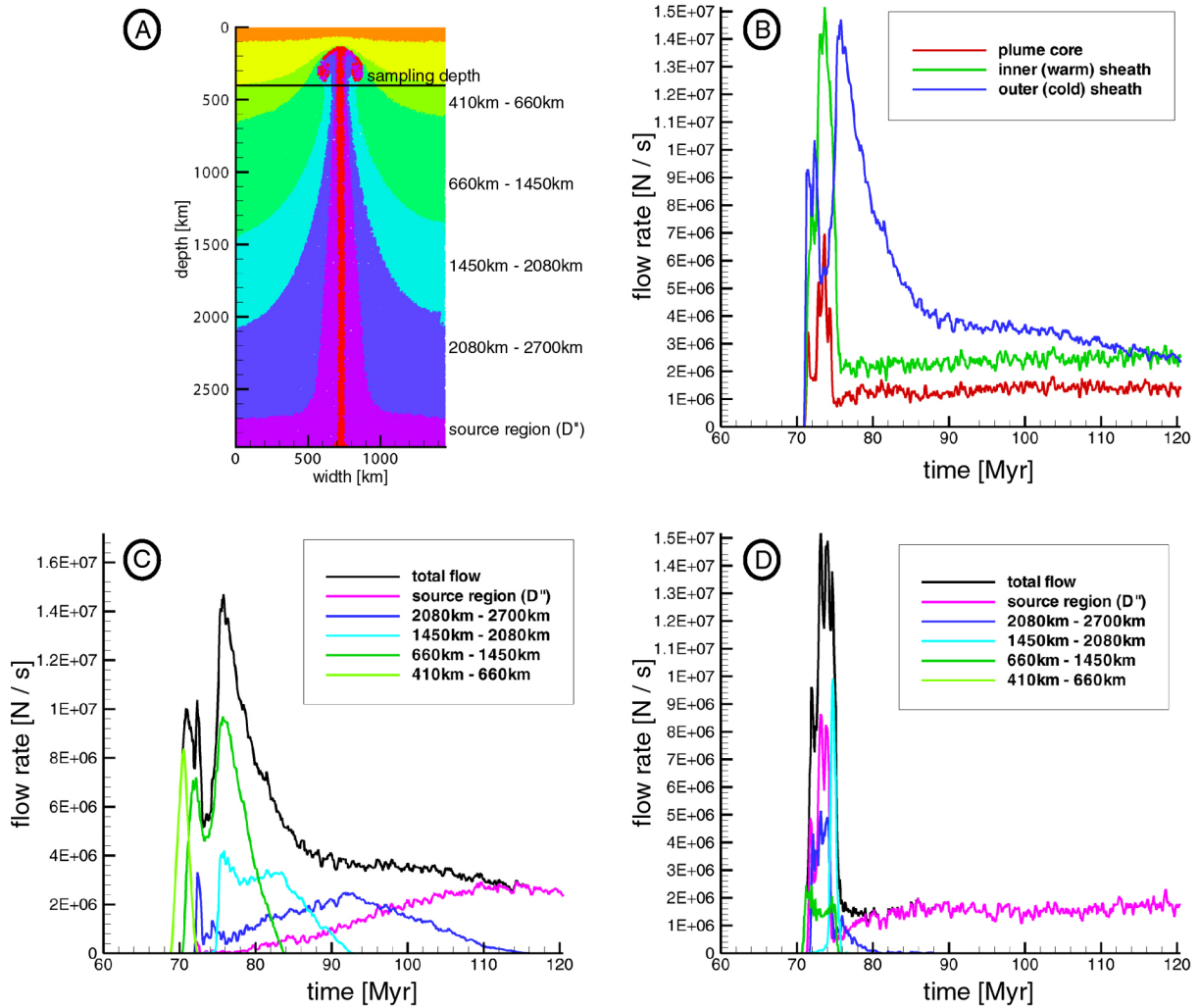


Figure 8.4: Flow rates of the constant viscosity model: A) Overview on the distinct mantle regions and sampling depth. B) Total plume flow, divided into core, inner sheath and outer sheath flow. C) Outer sheath flow, divided by origin of material. D) Inner sheath flow, divided by origin of material.

layer, but also entraining material from all through the mantle in the outer, cold portion of the plume sheath. Deep material from the inner plume sheath is also spiraled around a core of source material in the plume head. Once the plume has established itself, the sheath remains as a broad, slow, cool upwelling around the plume tail, while most of the initial cold deep material penetrating the lithosphere as part of the plume head is pushed downward and outward by subsequent hot plume tail material.

The plume sheath composition and share of overall plume flow is elaborated on in figure 8.4. Fluxes are given in N/s for ease of comparison with other studies, e.g. *Griffiths & Campbell [1990]*. Again, figure 8.4b presents how the plume sheath itself transports up to fifteen times as much material as the plume core. The initial flow is dominated by the plume core head and warm inner plume sheath, with flow rates for both dropping sharply after the plume head has passed through the sampling region. Flow from the core and inner sheath remains steady from then on, with the cold outer sheath slowly diminishing as the pull from the plume head abates.

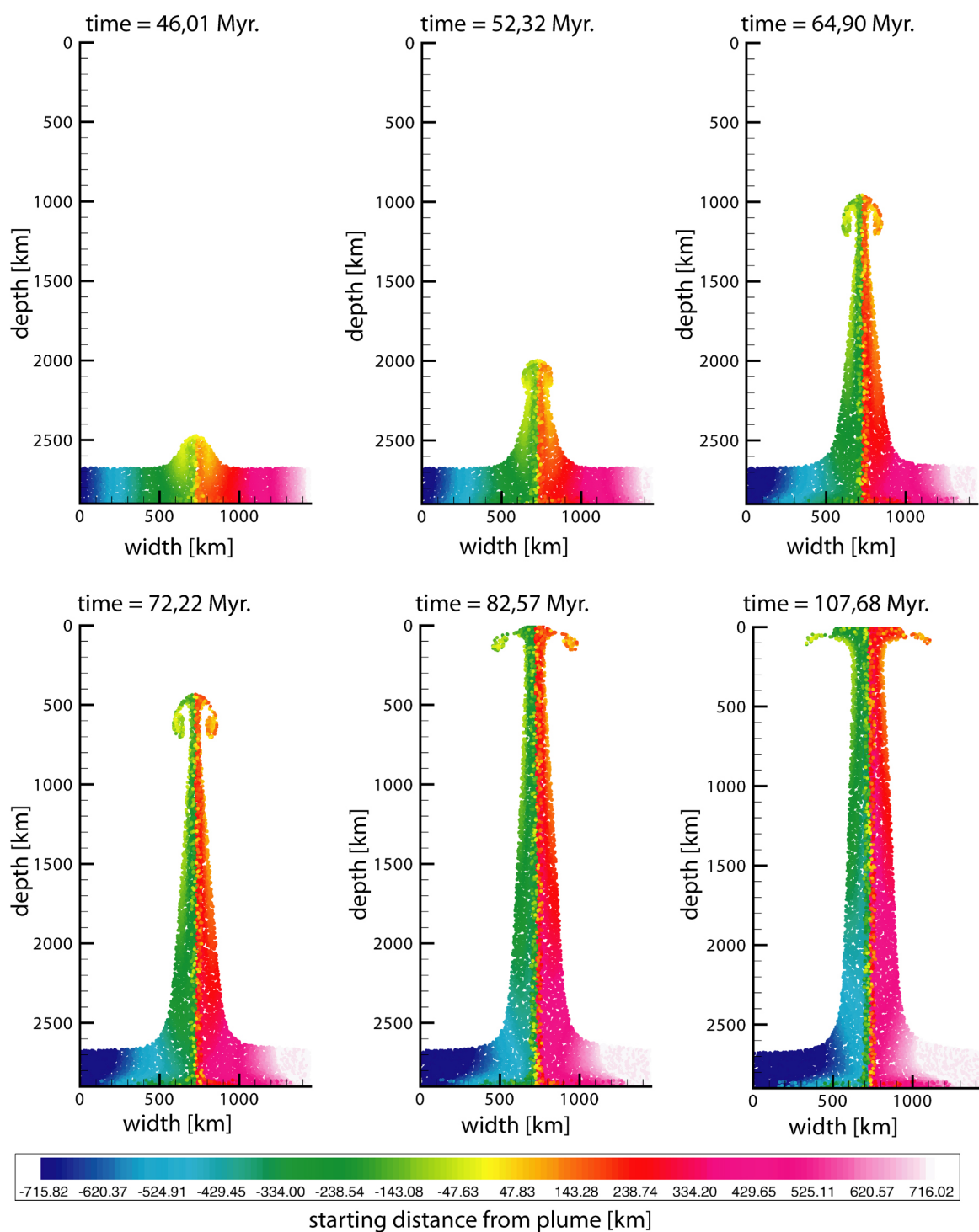


Figure 8.5: *Sampling of the source layer and D'' of the constant viscosity model.*

Unsurprisingly, this behavior is well reflected in the laboratory experiments and models.

Further looking in the material origins of inner and outer plume sheath reveals that the inner plume sheath is dominantly composed of source D'' material, with small amounts of lower mantle material entrained into the plume head or trailing the ascending plume head -

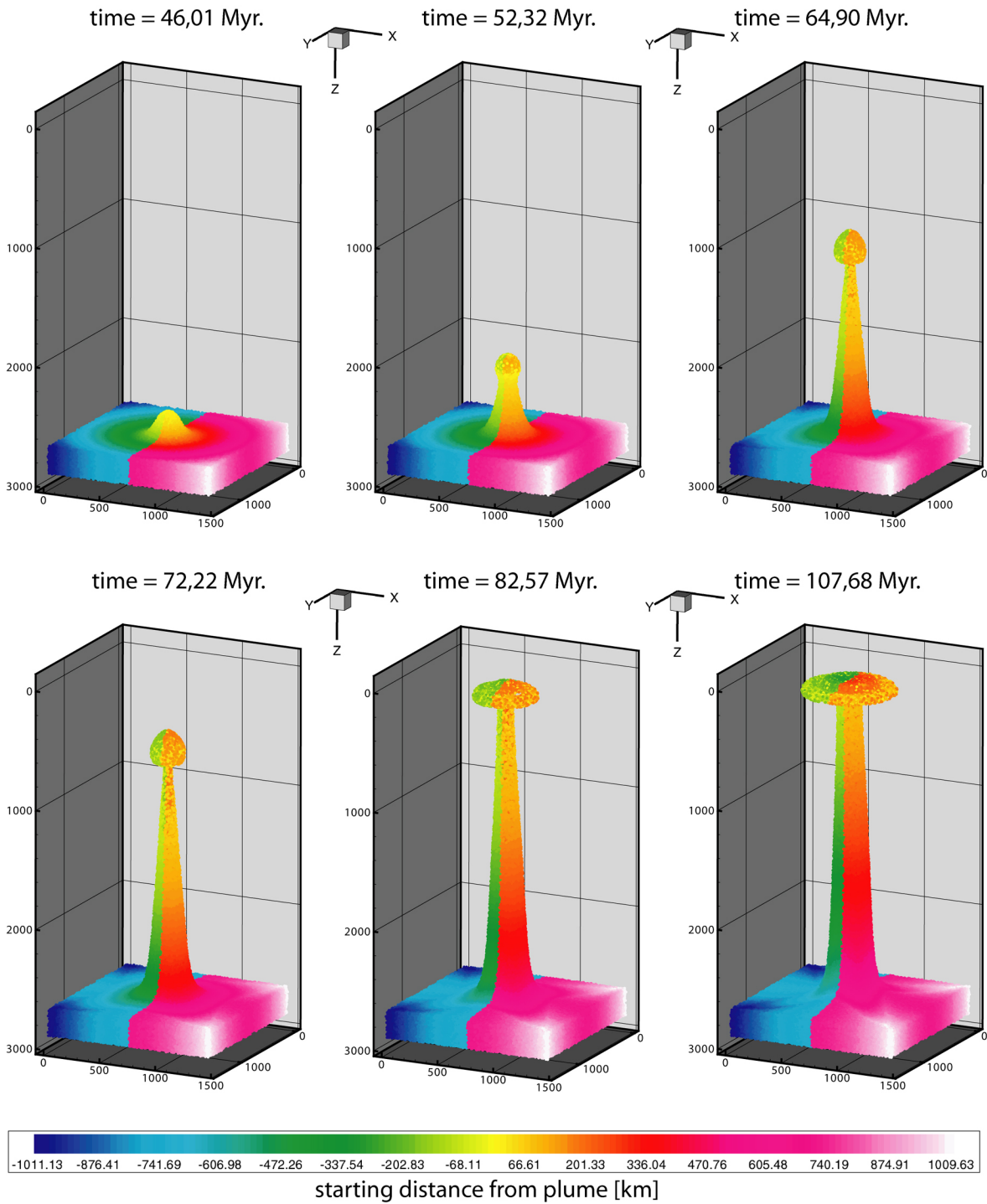


Figure 8.6: 3D plume evolution of the constant viscosity model.

this material has initially been entrained into the outer plume sheath and was subsequently transported inside. After the plume head has passed through the sampling region, the diversity of material in the inner plume sheath subsides, with the inner plume sheath enveloping the plume tail now solely consisting of source region material. The outer plume sheath is initially composed of a bow wave of upper mantle material, which is quickly replaced by predominant fractions of lower mantle and mid-mantle material in a bulk upwelling trailing the plume head.

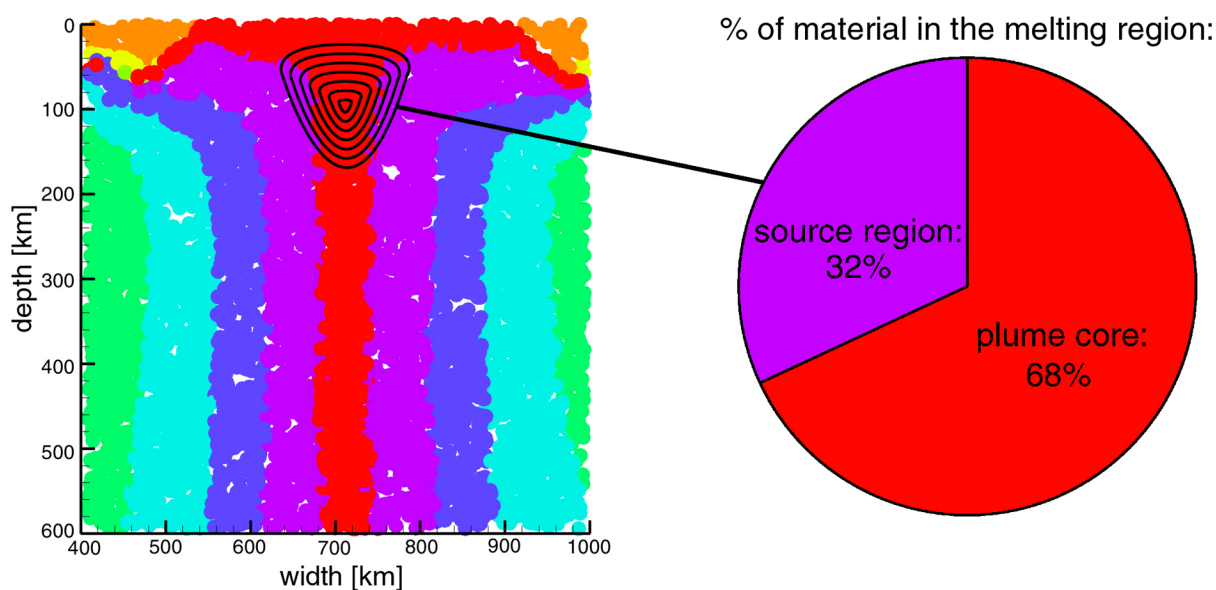


Figure 8.7: *Left: closeup on the plume head illustrating the melting region of the plume. Right: breakdown of the material origins for the melting region.*

Once the plume has established itself, the fraction of entrained material from the lower mantle regions drops to a low, near-constant rate, with source region material finally dominating the outer sheath flow as well.

The sampling of the source region is displayed in figure 8.5. As already evidenced in the laboratory models, material from each part of the plume source region undergoes 'streaking', stretching and thinning, with lateral zones being stretched into long filaments of material within the plume conduit. Once again, the absence of lateral transport, vorticity and mixing in the plume conduit catches the eye - as does the pronounced spiraling of material in the plume head, and the lossless reproduction of the source region zonation in the plume swell. This is also seen in figure 8.6, which clarifies the plume source division and also nicely shows the different stages in plume ascent, from local upwelling to plume head/plume tail differentiation to establishing as a constant conduit and plume swell. Once again, it can be seen that this model behaves remarkably similar to the laboratory experiments and models.

Lastly, the results of the simple melting model applied to these calculations can be seen in figure 8.7. Melting begins with the plume impinging on the base of the lithosphere, with melting rates averaging $\sim 0.039 \text{ km}^3/\text{yr}$. Melting is confined to the hot plume head center and subsequent plume tail, with most of the inner plume sheath displaced sideways before reaching the melting region and therefore remaining unmelted. Consequently, the melting region is dominated by plume core material, to wit material from the lower D'' directly heated by the bottom temperature perturbation. A significant fraction of non-core inner plume sheath material does enter the fringes of the melting region, however this material still has its origin in the plume source (D'') region, so is likely not distinct in composition from the plume core material.

8.2.3 The Mitrovica / Forte Viscosity Model

This model for mantle viscosity is presented in *Mitrovica & Forte [1997]*. It is based on data derived from long-wavelength free-air gravity harmonics associated with mantle convection as well as a large set of decay times estimated from postglacial uplift of a number of sites in North

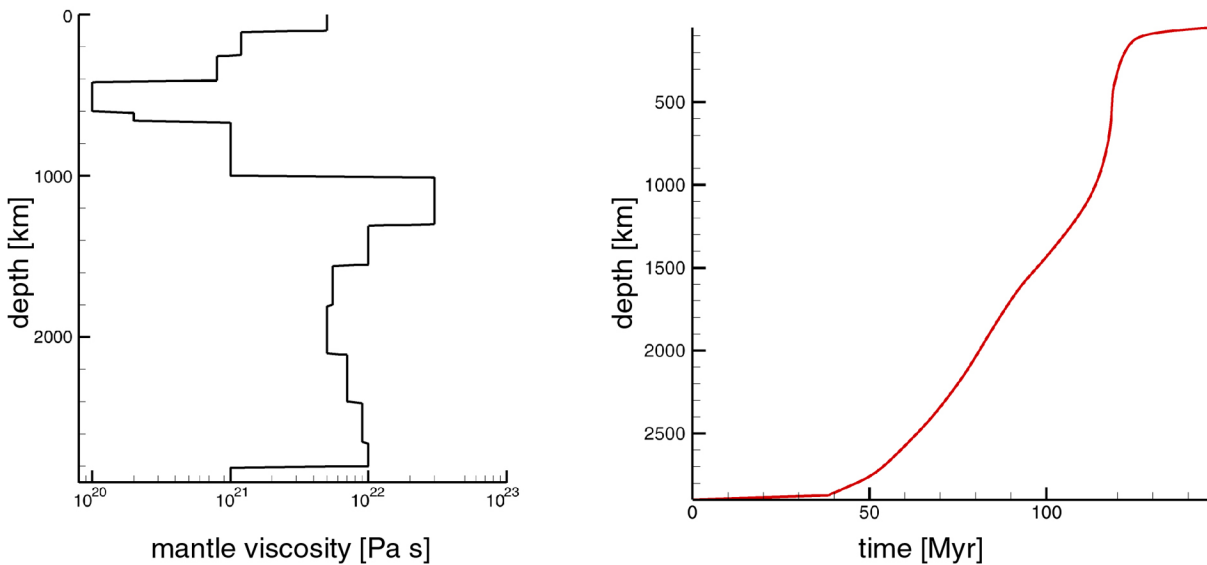


Figure 8.8: *Left: The Mitrovica & Forte [1997] viscosity profile. Right: Ascent rate of the Mitrovica / Forte viscosity model.*

America and northern Europe. The profile itself is characterised by a significant increase in viscosity with depth over more than two orders of magnitude, with a notably sharp drop over more than one order of magnitude at 1000km depth, and another sharp drop over almost one order of magnitude at 660km depth.

Figure 8.9 shows the thermal evolution of a sample Mitrovica / Forte viscosity experiment. While the thermal perturbation needs about as much time to grow into a starting plume as in the experiments with constant viscosity, the high-viscosity layer overlying the bottom thermal boundary layer significantly stalls the initiation of plume ascent. When the plume finally takes off, both its head and its tail are noticeably broader than in the constant viscosity models, and also noticeably hotter. This increase in core temperature comes from the fact that the deferred rise of the plume results in a longer stay in the area of influence of the temperature perturbation heating up overlying material. Plume ascent does not noticeably speed up in the region of slightly reduced viscosity between 2700km and 1500km depth. The increase in viscosity between 1500km and 1000km depth results in another noticeable increase in plume head width, with the plume head swelling to more than 400km in diameter. The sharp decrease in viscosity at 1000km depth results in the formation of a secondary plume from the slowly-rising plume head - material at the apex of the plume head and subsequent material from the plume tail / conduit cross the viscosity boundary first, forming a new, secondary plume and plume head, while the colder, slower material in the outer regions of the plume head remains 'trapped' in the high-viscosity layer.

The secondary plume rapidly ascends, tapping the reservoir of warm material in the trapped primary plume head to maintain its ascent, thereby literally 'draining' the primary plume head. The secondary plume tail, due to the abundance of material from both the plume head and plume conduit at this point, is not significantly thinner than the primary plume tail, and only noticeably thins on crossing the second sharp drop in viscosity at 660km depth. Plume ascent of the secondary plume is stalled once again when the secondary plume head hits the sharp viscosity increase at 410km depth, resulting once more in a significant bulging of the plume head. The plume tail, on account of the amount of material welling up through the low-viscosity zone, bulges even more, resulting in a most peculiar plume head/plume tail shape.

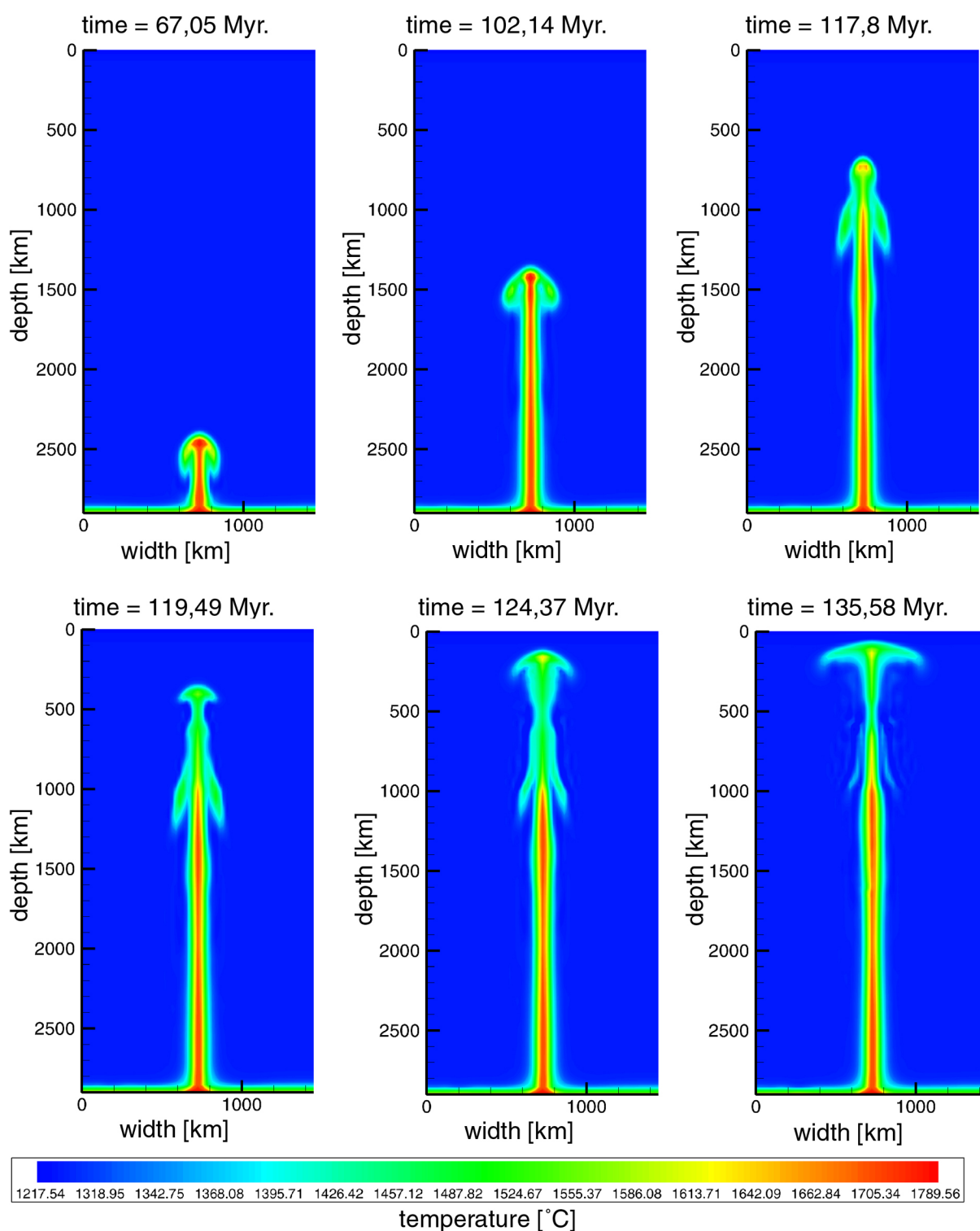


Figure 8.9: *Thermal evolution of the Mitrovica / Forte viscosity model.*

At the base of the lithosphere, the plume head spreads out even more, and along with the mass of plume tail material from the initial upwelling forms a distinctive crescent-shaped region below the lithosphere. The plume head is slow in penetrating the lithosphere because of the comparatively high lithospheric viscosity, meaning that the lithosphere is much more

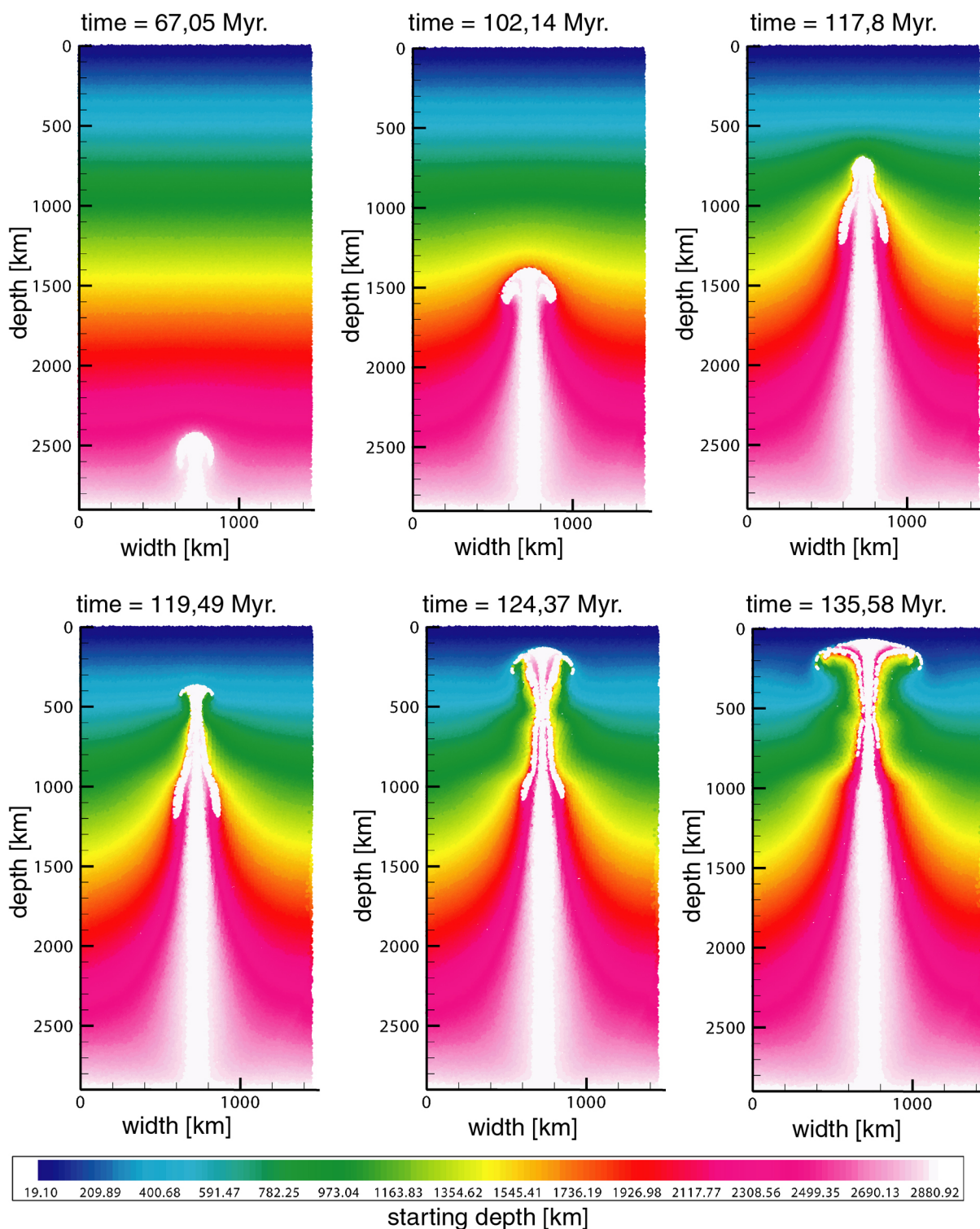


Figure 8.10: *Material starting depth sequence of the Mitrovica / Forte viscosity model.*

inert in being pushed away by the upwelling plume material. With the plume now being fully established, the primary plume head gets fully drained and dissolves, and the plume tail significantly thins down to less than 100km diameter in the low viscosity region. All in all, the plume needs ~ 80 Myr to traverse the mantle, of which ~ 20 Myr are attributed to lingering

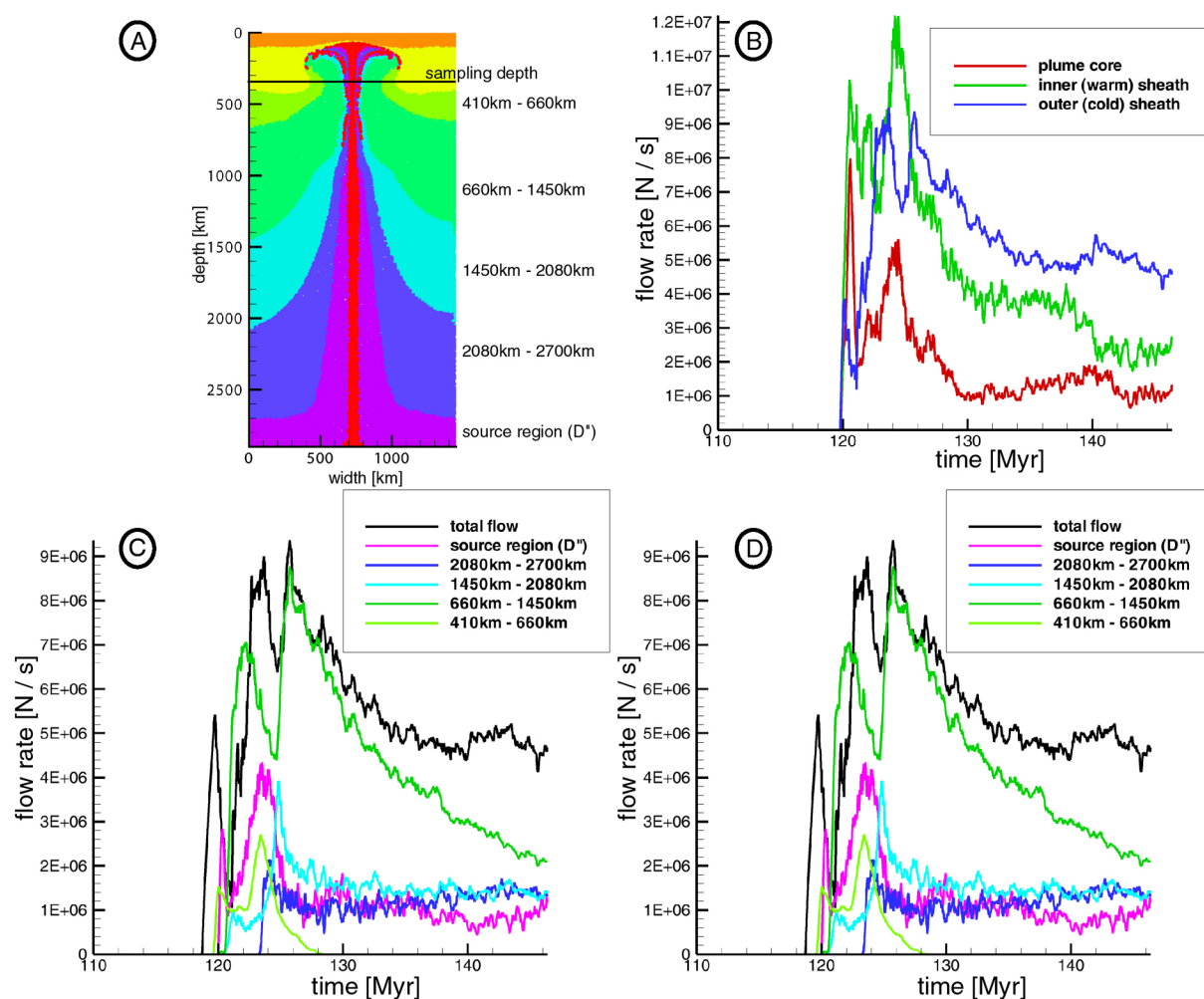


Figure 8.11: *Flow rates of the Mitrovica / Forte viscosity model: A) Overview on the distinct mantle regions and sampling depth. B) Total plume flow, divided into core, inner sheath and outer sheath flow. C) Outer sheath flow, divided by origin of material. D) Inner sheath flow, divided by origin of material.*

in the source region, building up enough buoyancy to penetrate the overlying high-viscosity region. This high-viscosity layer also acts as a stabiliser to the bottom thermal boundary layer, dampening the growth of secondary instabilities like those observed in the constant viscosity experiments.

Figure 8.10 presents the material source depths for the Mitrovica / Forte viscosity set of experiments. In the first half of the experiments (the upper row in figure 8.10), plume evolution is more or less as in the previous experiments and model, with a plume sheath of similar width to the plume head ascending along with the plume. With the formation of the secondary plume at the sharp viscosity decrease in 1000km depth, the development of the primary plume sheath is arrested, just like the primary plume head that gets 'stuck' in the high viscosity layer beneath 1000km depth. At the same time, the secondary plume forms a new, secondary plume sheath consisting of warm plume head material and ambient material from above the 1000km transition. The subsequent draining of the primary plume head has the interesting effect that most of the non-core warm plume sheath material entrained into the plume head

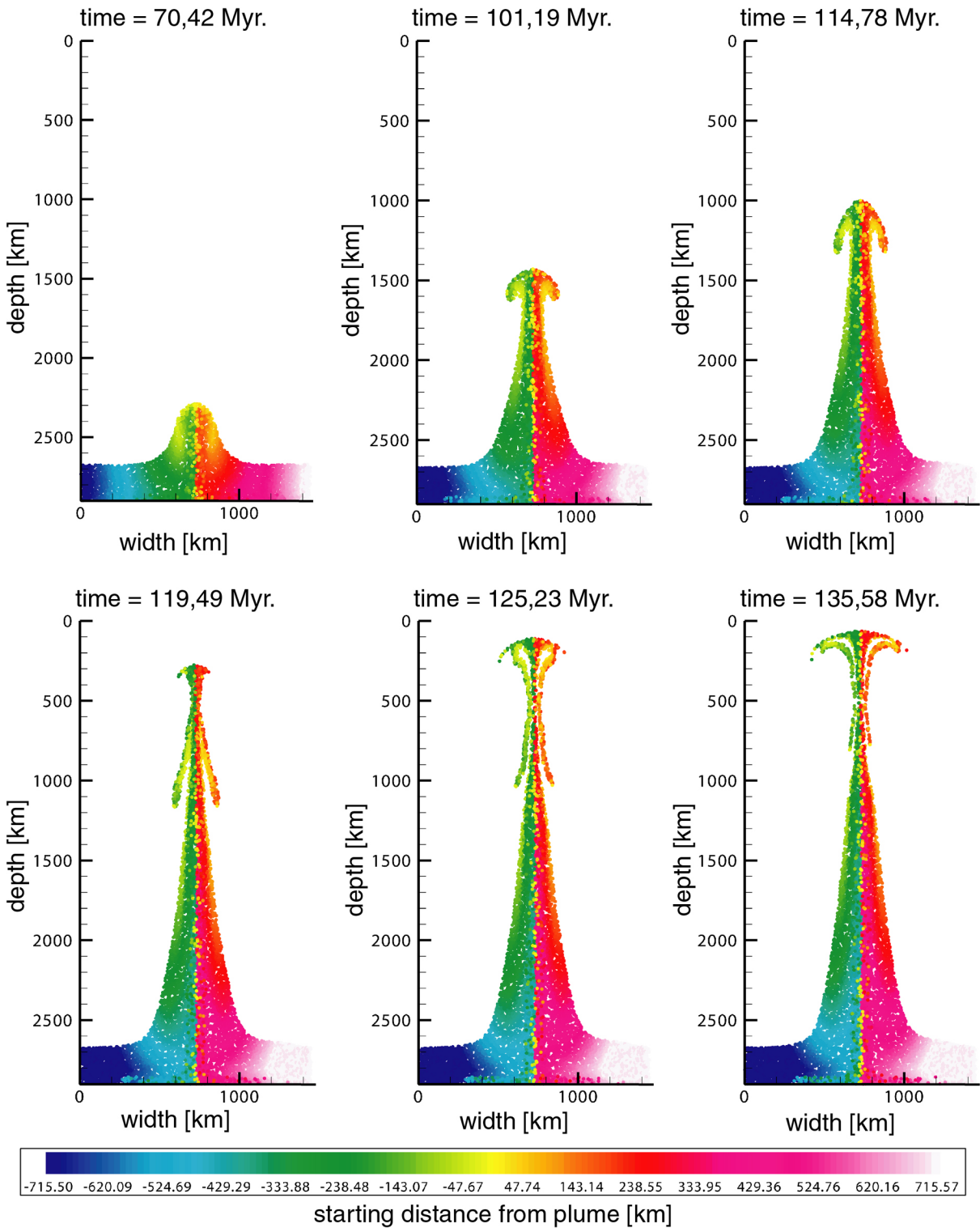


Figure 8.12: Sampling of the source layer and D'' of the Mitrovica / Forte viscosity model.

during early ascent is now literally 'sucked' into the secondary plume head, while at the same time remaining encased in a 'shell' of plume core material. Meanwhile outside of the complex secondary plume core structure, the secondary plume sheath proves to be very effective in establishing an upward flow primarily consisting of material from directly below the upper

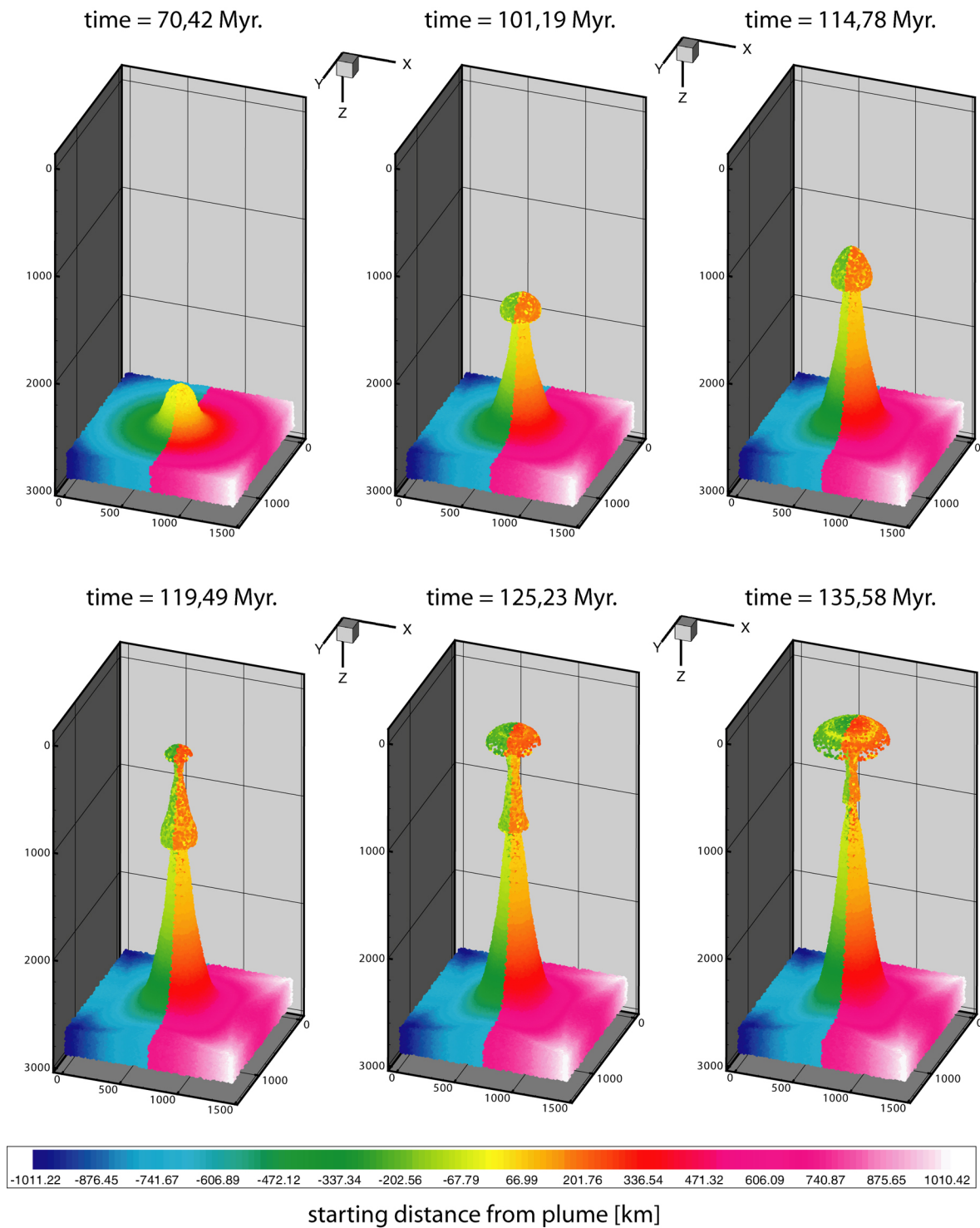


Figure 8.13: 3D plume evolution of the Mitrovica / Forte viscosity model.

mantle/lower mantle boundary. The primary plume sheath remains as a broad structure in the lower mantle, significantly constricted at the 1000km transition.

Flow rates and composition of the secondary plume sheath can be found in figure 8.11. The comparatively high ascent rates and narrow width of the plume sheath result in the outer cold sheath not nearly being as dominating as in the constant viscosity case as long as the

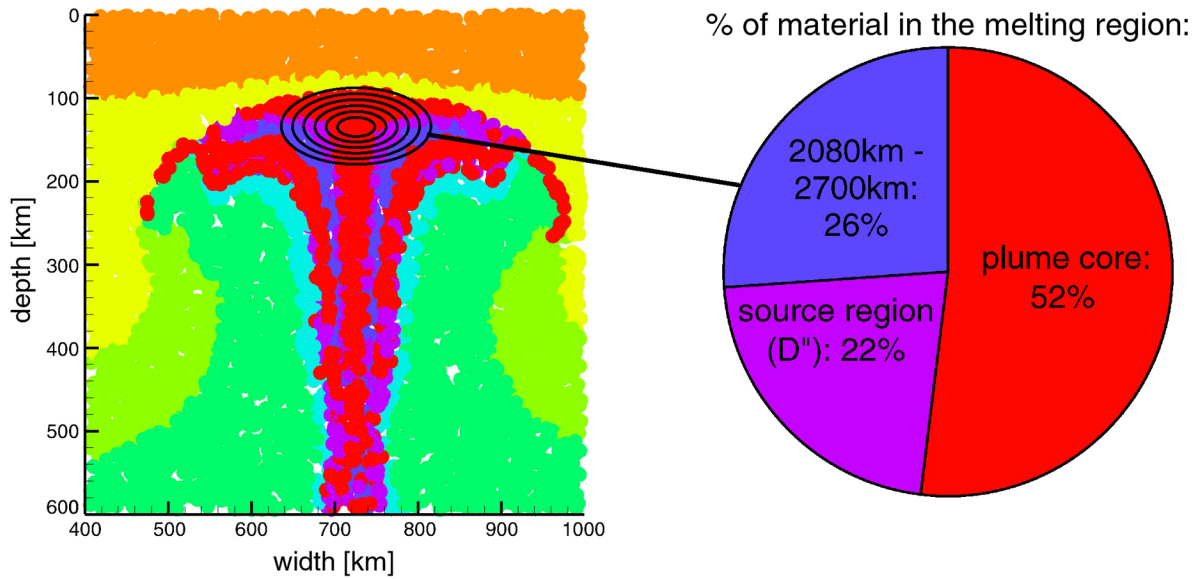


Figure 8.14: *Left: closeup on the plume head illustrating the melting region of the plume. Right: breakdown of the material origins for the melting region.*

secondary plume and sheath are still feeding on the warm material of the primary plume head. Once the primary plume head has dissolved, the fraction of flow attributed to the plume core and inner warm plume sheath drops noticeably, while the flow rate of the outer cold sheath remains relatively constant. As already observed in 8.10, the outer secondary plume sheath is dominated by material from just below the upper mantle/lower mantle transition, with a remarkable constant fraction of lower mantle material (the blue lines in figure 8.11c). The reason for this again lies with the sharp viscosity drop at 1000km, which results in the secondary sheath sampling the laterally zoned outer primary plume sheath at equal rates. The inner, warm sheath is, unsurprisingly, dominated by hot source region material, with a notable fraction of material from the upper mantle/lower mantle transition entrained when the secondary plume formed a new, secondary plume sheath. Inner sheath material upwelling after the plume has been fully established, however, once again displays a composition almost exclusively made up of source region and deep mantle material.

Zonation and source layer sampling of the the Mitrovica / Forte viscosity model plume is presented in figure 8.12 and figure 8.13. Despite the formation of a secondary plume and resulting massive deformation of the plume head, there is no evidence of lateral transport within the plume. As in the previous models, distinct zones in the source region are preserved as long 'streaks' in the plume. It should also be noted that due to the stalling of the primary plume head, forming of the secondary plume head and subsequent resampling of primary plume head material into the secondary plume head, the material closest to the plume axis (the yellow/orange material in figure 8.12 and figure 8.13) that in the constant viscosity experiments forms the outer rim of the unfurling plume head is, in this set of experiments, resampled along with the rest of the primary plume head and subsequently appears within the spreading plume head as a very prominent 'ring' of early plume material within material that has been sampled much later by the ascending primary plume.

The closeup of the plume head displayed in figure 8.14 illustrates the complex plume head structure exhibited by this set of experiments. Encased in an outer 'shell' of plume core material, source region and deep mantle material are overlying each other, being pulled into the hot,

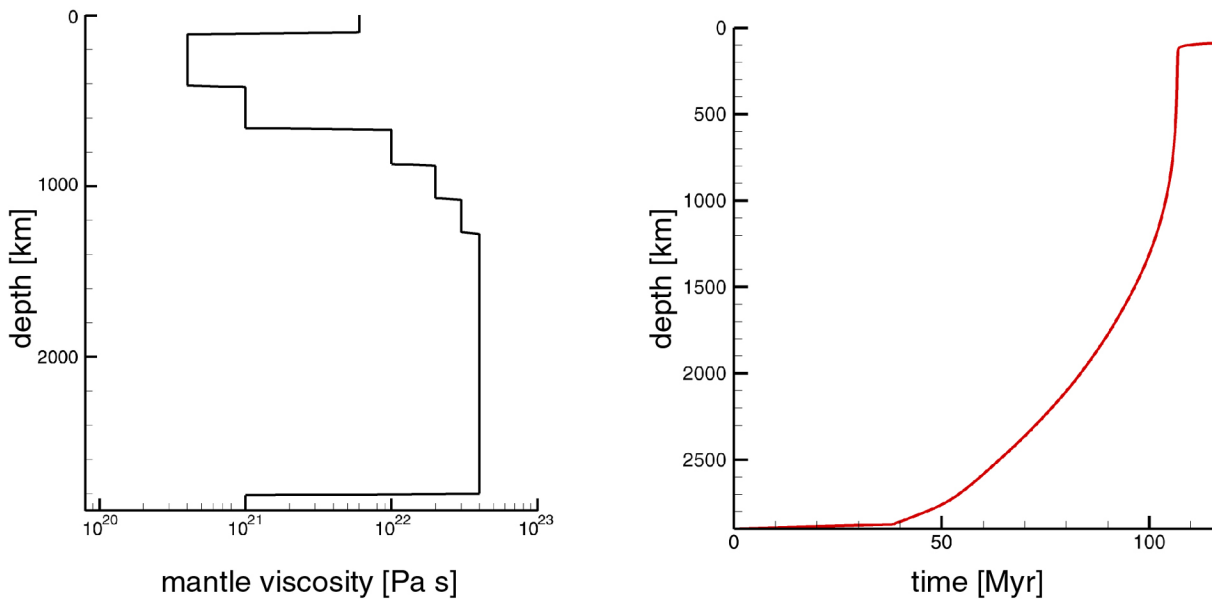


Figure 8.15: *Left: The Steinberger [2000] viscosity profile. Right: Ascent rate of the Steinberger viscosity model.*

melting plume head core. Melting rates in the plume head average $\sim 0.011 \text{ km}^3/\text{yr}$, with the origins of the melting material presented in figure 8.14. As a significant fraction of non-source, deep mantle material (mostly originating in the high viscosity zone overlying the source region) is now melting along with plume core and source region components, it can be speculated that the melts resulting from this will be more heterogeneous in composition than the melts produced in the constant viscosity model. It should also be noted that a higher amount of plume core material compared to the constant viscosity experiments is being displaced laterally without ever reaching the melting region of the plume.

8.2.4 The Steinberger Viscosity Model

This set of experiments uses the viscosity profile postulated by Steinberger [2000] as presented in figure 8.15. The viscosity profile itself is an amelioration to the viscosity profile originally put forth in Steinberger & O'Connell [1998], and takes into account inferences from postglacial rebound and geoid models as well as argumentation from dynamic modelling. It is characterised by a uniformly high viscosity for the lower mantle, with a gradual drop in viscosity between 1270km depth and 660km depth and a sharp drop in viscosity over more than one order of magnitude above 660km depth. A smaller, yet sharp decrease in viscosity at 410km depth and a steep rise in viscosity associated with the lithosphere finalises the profile.

The thermal evolution of a sample Steinberger viscosity model experiment is presented in figure 8.16. As in the Mitrovica / Forte models above, initial plume evolution is stunted by the overlying high viscosity region. The upcoming plume is noticeably broad and hot, remaining predominantly constant in width and temperature during ascent through the lower mantle. When reaching the point of diminishing viscosity at 1270km depth, the leading plume head starts to massively deform in order to sustain the rise in ascent speed, and forms a long, headless, diapiric finger. This ascent into the region above 1270km depth, and into the upper mantle above 660km depth in particular, happens on such a narrow time scale that the plume tail / conduit in the lower mantle remains almost completely unchanged. The plume impinges on the

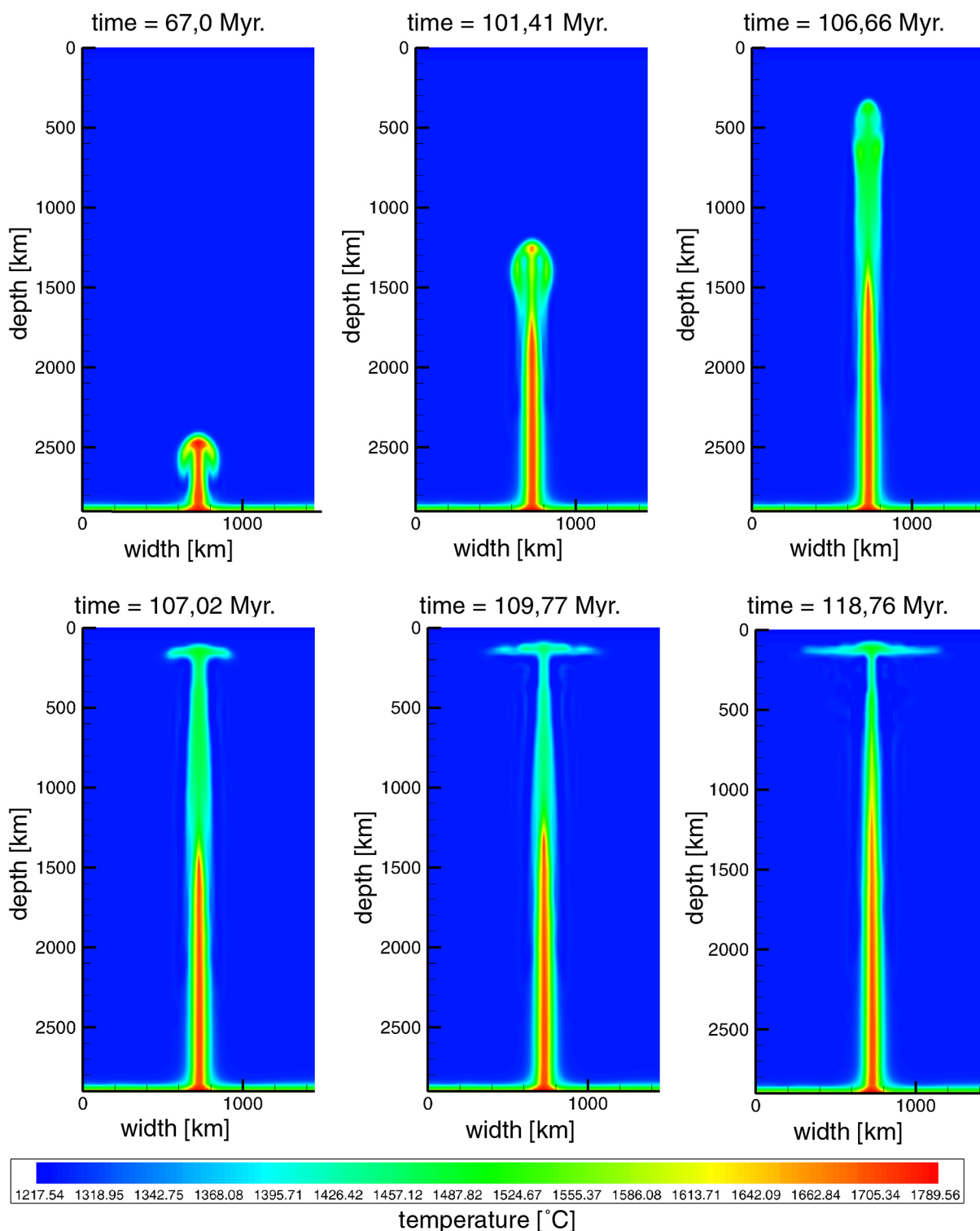


Figure 8.16: *Thermal evolution of the Steinberger viscosity model.*

base of the lithosphere at high upward velocity reminiscent of an impact, with the subsequent spreading out of plume material underneath the lithosphere more akin to the behaviour of a jet of fluid hitting a solid surface at speed than to the gradual widening of the plume head seen in previous models. The plume swell in this model remains remarkably thin and prone

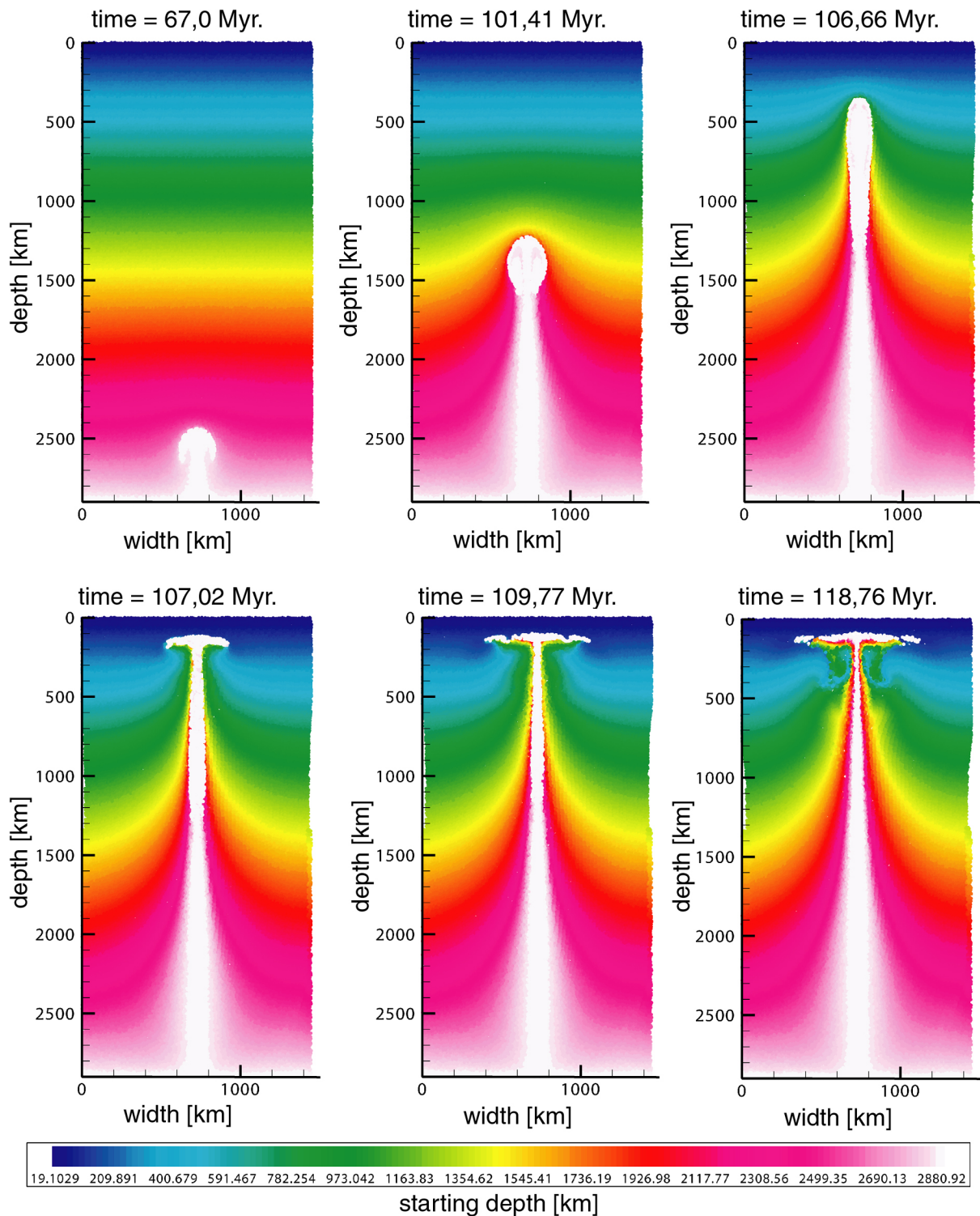


Figure 8.17: Material starting depth sequence of the Steinberger viscosity model.

to instabilities. The plume tail subsequently develops a pronounced conical or 'candle-like' shape, with a broad base and very narrow conduit in the low viscosity region. The plume needs ~ 60 Myr to traverse the mantle, of which ~ 20 Myr are spent on buildup in the source region, ~ 40 Myr are needed to traverse the lower mantle, and less than 1 Myr is needed to traverse the

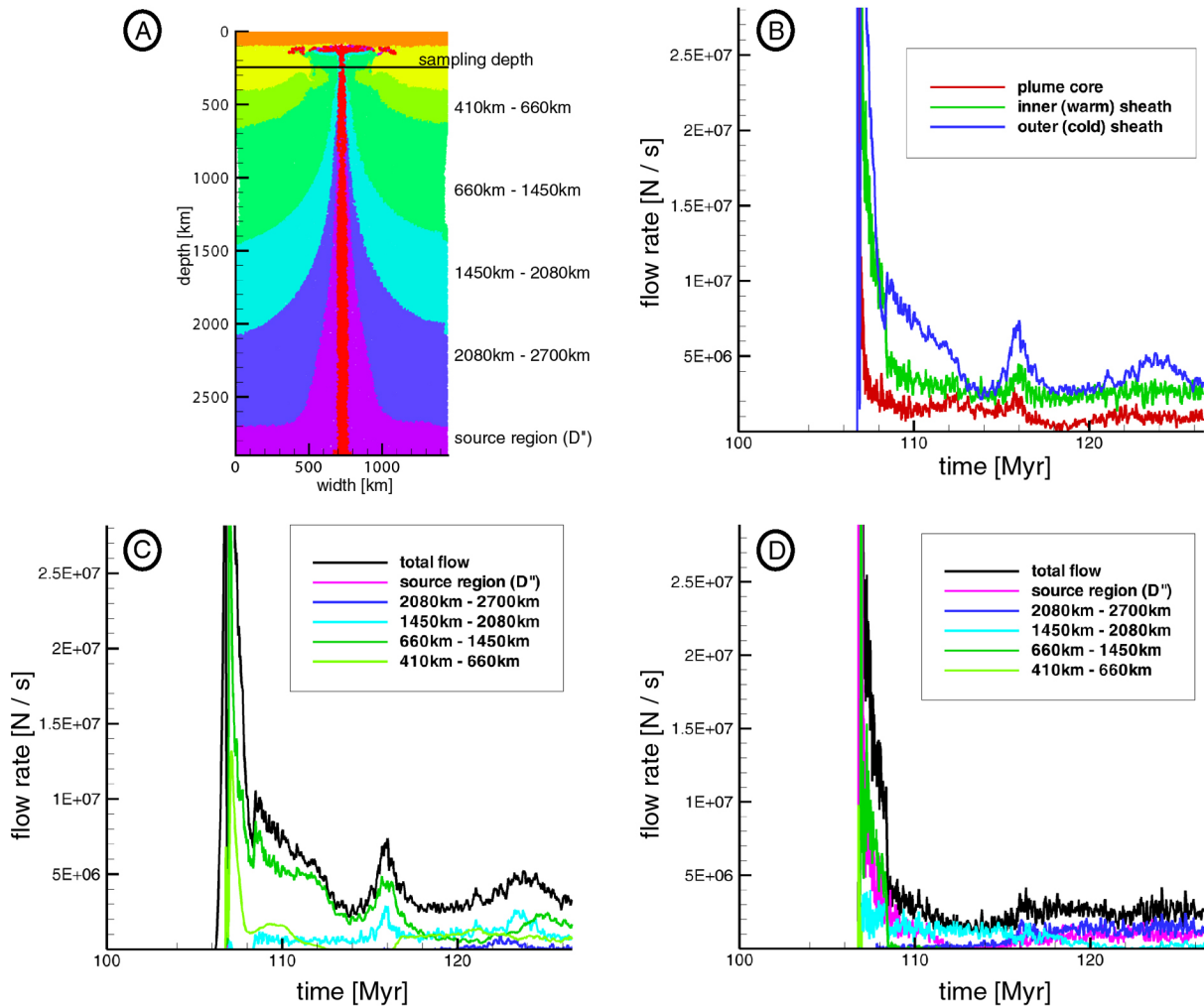


Figure 8.18: Flow rates of the Steinberger viscosity model: A) Overview on the distinct mantle regions and sampling depth. B) Total plume flow, divided into core, inner sheath and outer sheath flow. C) Outer sheath flow, divided by origin of material. D) Inner sheath flow, divided by origin of material.

upper mantle and fully establish the plume (figure 8.16).

Figure 8.17 pictures the material starting depth of the Steinberger model experiments. Plume ascent through the lower mantle and the forming of a plume sheath are mostly similar to the Mitrovica / Forte and Walzer et al. models, with the plume exhibiting a broad plume stem in the source region and consequently a broad plume tail and plume sheath in the lower mantle. It can also be clearly seen that the fast ascent through the upper mantle is exclusively sustained from the material of the voluminous lower mantle plume head, with very little material from below 1270km depth entering the upper mantle at this point. This also means that the diapiric upwelling is homogeneously composed solely of source region material. Consequently, the plume sheath of the fast diapiric upwelling is formed from material originating above 1270km depth, which is rapidly swept along by the swiftly rising plume. The fact this happens so fast that plume progression in the lower mantle is all but arrested is nicely seen in the pictures for 106.66Myr, 107.02Myr and 109.77Myr in which the lower part of the picture

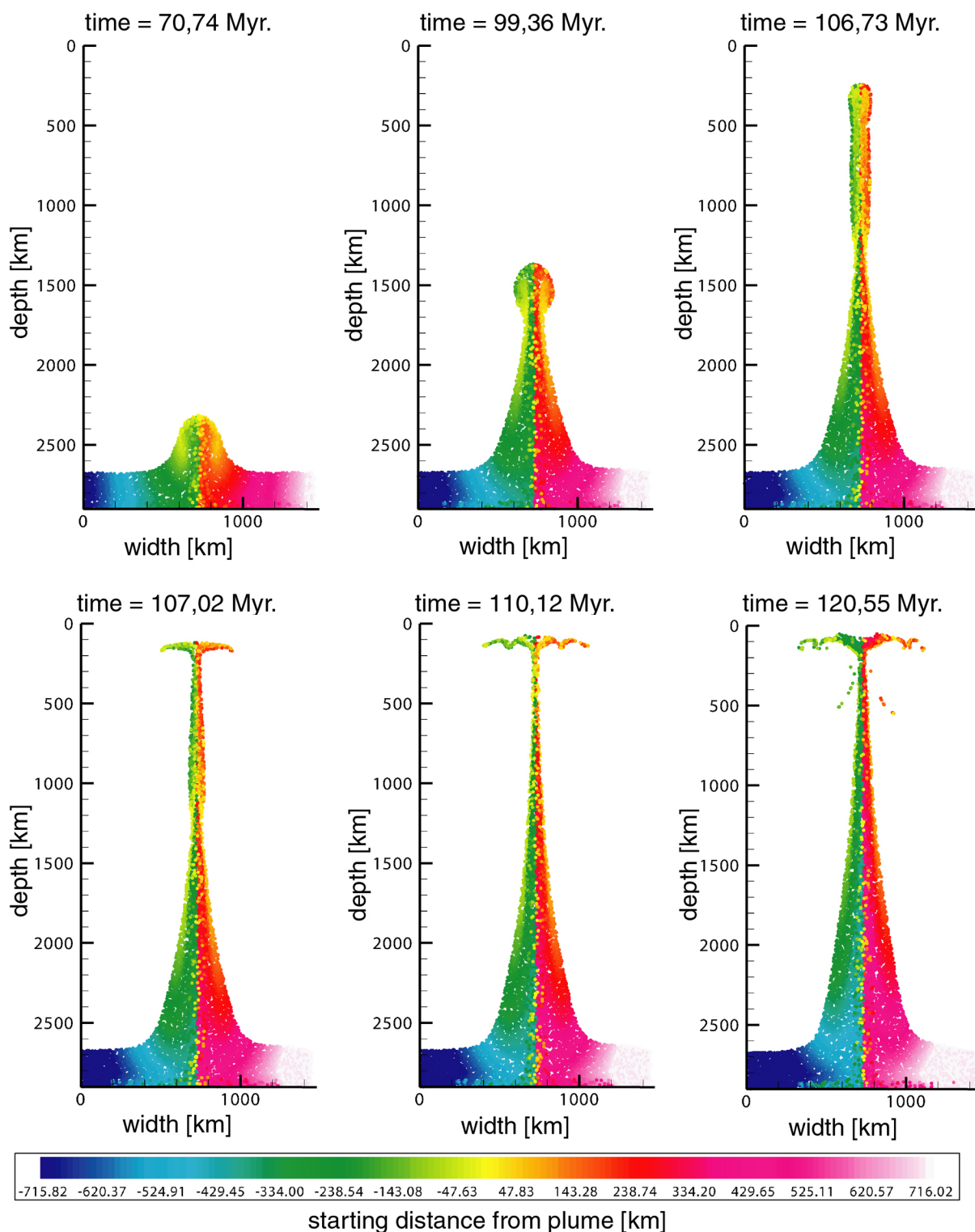


Figure 8.19: *Sampling of the source layer and D'' of the Steinberger viscosity model.*

changes very little, if at all. Only when the period of rapid ascent of the deformed plume head has passed does the plume remaining in the lower mantle develop further, reconnecting with the plume head material pooling at the base of the lithosphere.

Also, this set of experiments is the only set in which downwellings of upper mantle material

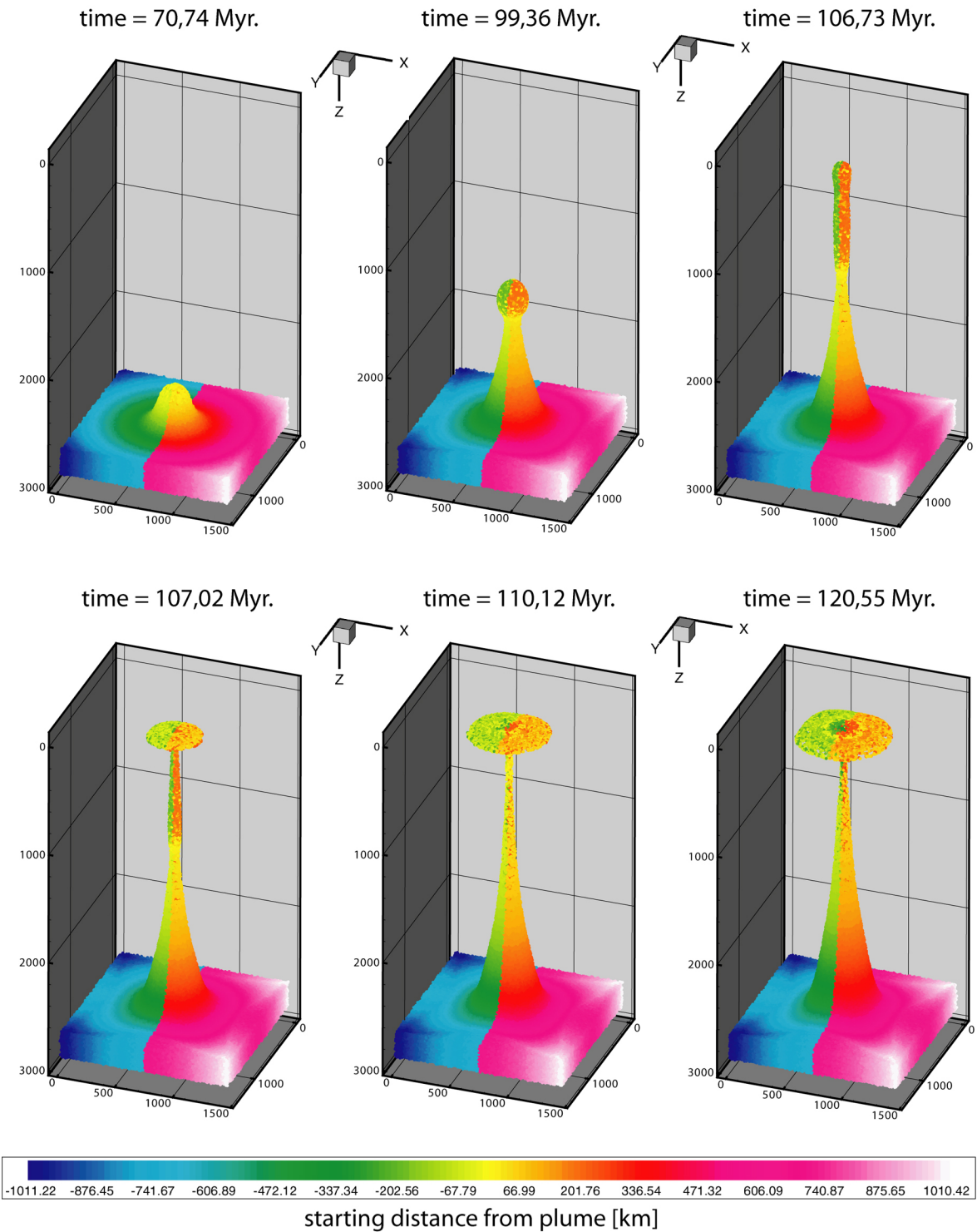


Figure 8.20: 3D plume evolution of the Steinberger viscosity model.

above the plume swell and in the outer plume sheath are observed. Some of these downwellings even penetrate the plume swell. This can be attributed to the plume head rising so explosively fast that overlying colder material can not completely be displaced, thus trapping cold, dense mantle material above the rising diapir. This material is subsequently displaced sideways along with the plume swell, and at that time, not being supported by the strong upward flow of

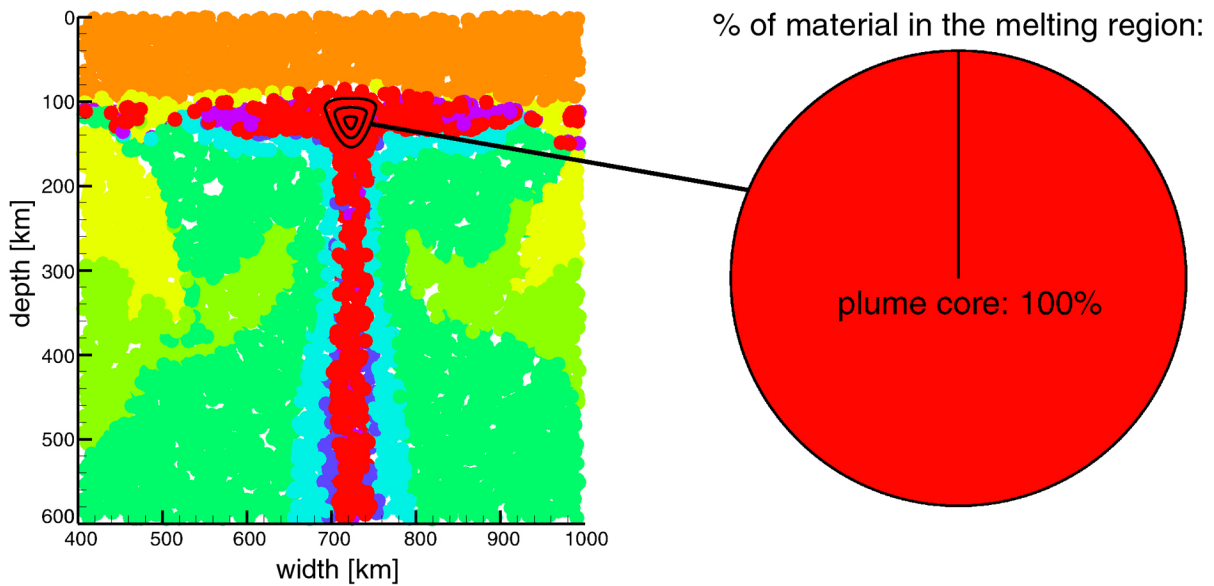


Figure 8.21: *Left: closeup on the plume head illustrating the melting region of the plume. Right: breakdown of the material origins for the melting region.*

the plume core anymore, starts to sink through the underlying warmer, lighter material of the plume swell. It is joined in descent by outer plume sheath material that is not supported in its ascent by the upwelling plume anymore, and forms a complex counterflow pattern around the 'bottleneck' of the plume tail above 660km depth.

This behaviour of the Steinberger model is also well reflected in the flow rates seen in figure 8.18. The initial passing of the fast diapiric upwelling created a massive upward flow, with flow rates dropping sharply after the plume has been established due to the small 'bottleneck' subsequently forming the plume conduit. There is another brief increase in upward flow once the plume sheath in the lower mantle fully reaches the 660km viscosity transition, forming a bottleneck of its own, and more or less constant flow afterwards, with total plume sheath flow only surpassing plume core flow by a factor of 8 or less.

The outer plume sheath is dominated by material from above 1270km and from the upper mantle, with a small but steady component originating directly from below 1450km, and a total absence of source region or deep mantle material in the outer sheath. The inner sheath displays initial components of upper mantle material and material originating above 1270km due to the direct contact and subsequent heating of this material by the plume core diapiric upwelling. Most remarkable here is how the inner plume sheath is almost entirely composed of material originating between 2080km depth and 1450km depth between 110Myr and 116Myr - the time during which the plume conduit reconnects with the plume head. Again, once the plume has become fully established inner plume sheath composition is dominated by source region and deep mantle material, with the same palpable small but steady fraction of material directly from below 1450km.

Looking at the way zones in the source layer are preserved during plume ascent (figure 8.19), the way material is zoned in the massively deformed diapiric upwelling penetrating the upper mantle catches the eye. Even more pronounced than in the Mitrova / Forte viscosity model experiments, the material starting the simulation closest to the plume axis (yellow/orange material) is being spiralled into the 'doughnut' region of the plume head during plume ascent through the lower mantle, and is then resampled into the core of the forming upwelling diapir

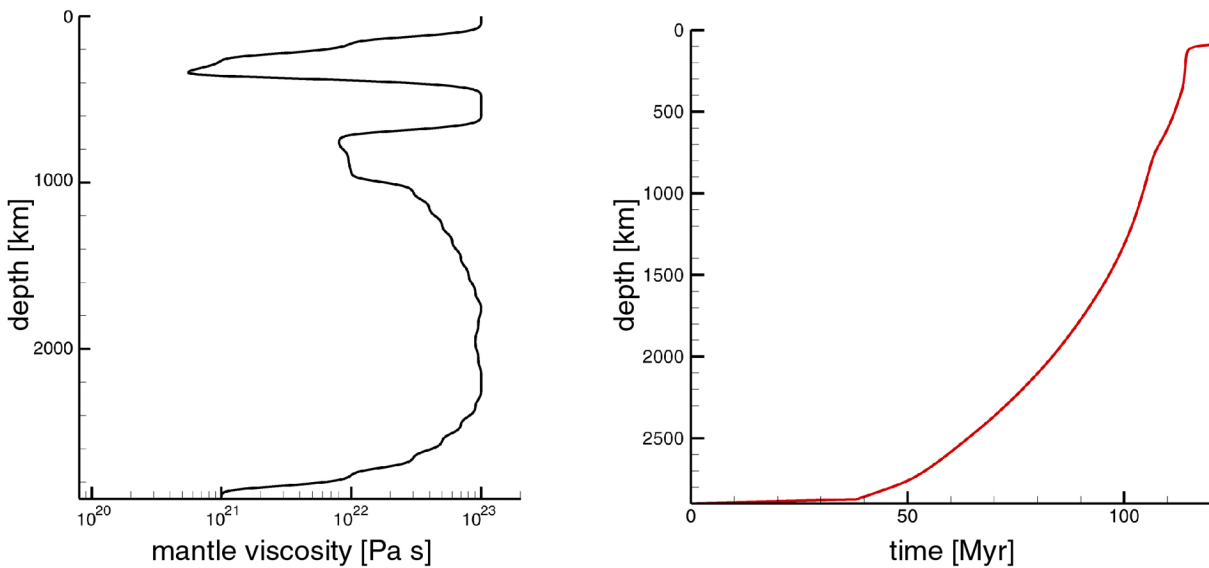


Figure 8.22: *Left: The modified Walzer et al. [2004] viscosity profile. Right: Ascent rate of the Walzer et al. viscosity model.*

at the viscosity transition. This results in a literal inversion of the inner plume zonation - where previously the outer layer of the plume had been formed by yellow/orange material with hotter red/green material forming the plume core, the red/green material suddenly supplies the outer 'shell' of the upwelling fast diapir while yellow/orange material dominates the core of the diapir. This inversion of plume structure is only reset once the plume tail has fully reconnected with the leading structure, re-establishing the plume conduit. The same process can be observed in figure 8.20, where the transition from regular plume to inverted diapiric upwelling is clearly visible in the picture at 106,73Myr, while the advent of the 'regular' plume tail is marked by a ring of yellow/orange material showing up in the plume head at 120,55 Myr.

The cold downwellings penetrating the plume swell, as already observed in figure 8.17, are found to entrain small amounts of plume source material. These downwellings do not cross the viscosity transition at 660km depth but remain in the upper mantle, stirring the region around the plume and mixing small fractions of deep source material into the upper mantle. Remarkably, even this process, along with the massive deformation exerted on the plume head / upwelling diapir, does not result in any noticeable lateral transport.

There is precious little melting going on in the plume 'head' of the Steinberger viscosity model experiments. The diapiric upwelling reaching the lithosphere, as evidenced by figure 8.16, is relatively cold, with an excess temperature of only $\sim 150^{\circ}\text{C}$. Therefore, average melting rates do not exceed $\sim 0.001 \text{ km}^3/\text{yr}$. Only after approximately 20Myr after the upwelling has first impinged on the base of the lithosphere, when the plume has been fully established and the plume tail has reconnected to the leading diapiric upwelling, does the plume head region heat up amply to produce more melts. As can be seen in figure 8.21, the melting region remains dominated by plume core material.

8.2.5 The Walzer et al. Viscosity Model

Contrary to the *Mitrovica & Forte [1997]* and *Steinberger [2000]* models for mantle viscosity, the *Walzer et al. [2004]* viscosity profile is not primarily based on postglacial rebound data, but on experimental and numerical constraints on the physical parameters and behaviour of

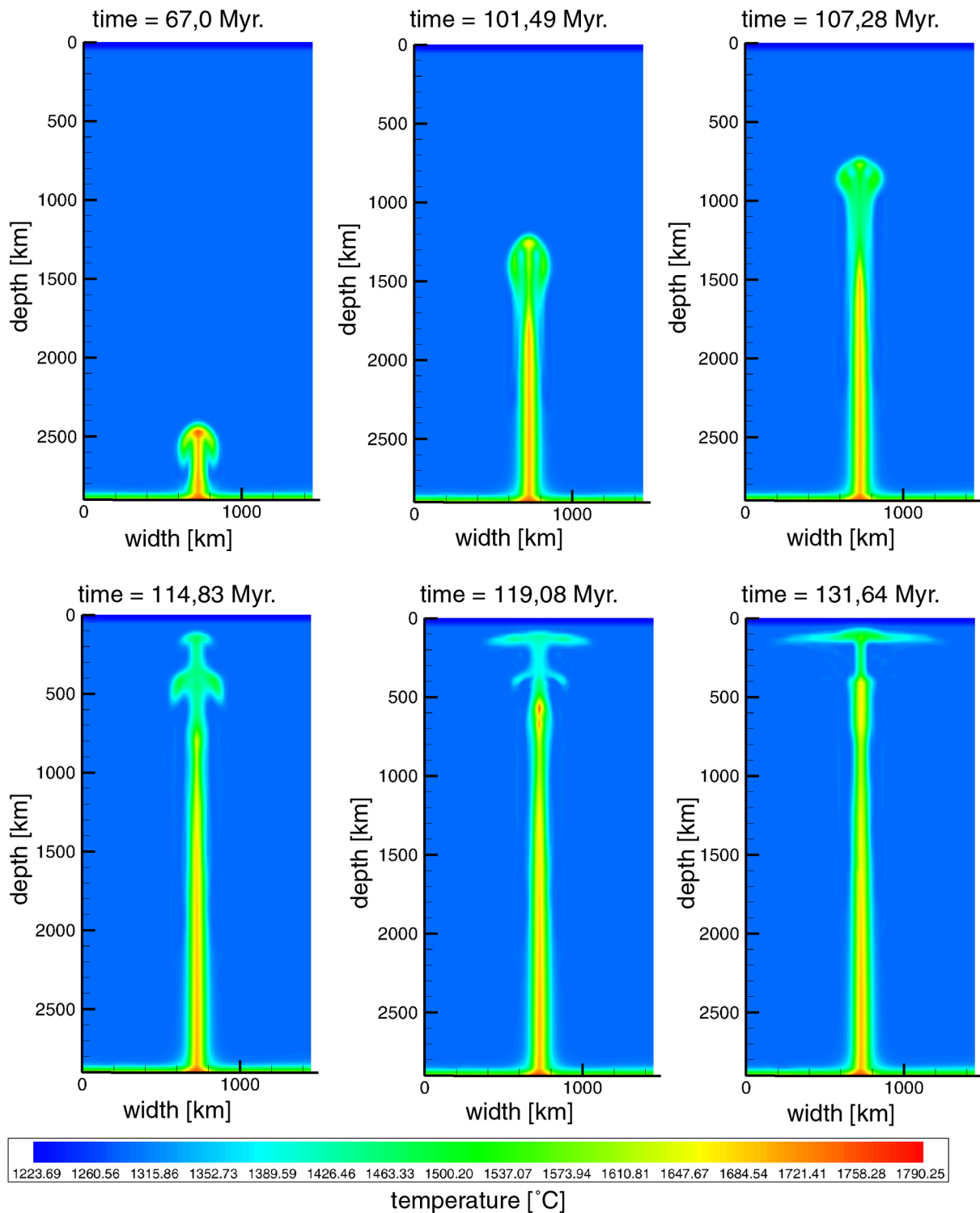


Figure 8.23: *Thermal evolution of the Walzer et al. viscosity model.*

different mineral phases occurring in the mantle. The original viscosity function, as presented in *Walzer et al. [2004]*, is characterised by astonishingly high viscosity values for the lower mantle (going up to 10^{25} Pa s). Since the code used for the numerical experiments presented in this thesis has a hard time handling viscosity contrasts of more than 3 orders of magnitude, and

in order to ensure comparability in the viscosity models presented here, the viscosity profile for the lower mantle has been modified for this study, with the viscosity in the lower mantle now going up to a maximum of 10^{23} Pa s. More importantly, the Walzer et al. viscosity profile is characterised by a high viscosity transition layer between 660km depth and 410km depth. The modified viscosity profile is presented in figure 8.22.

Figure 8.23 presents the thermal evolution of a sample Walzer et al. viscosity model experiment. As noticed in previous models with high deep mantle viscosity, plume ascent is distinctively slowed due to the high viscosity of the material overlying the source region, and the plume head is therefore considerably broad and hot. Due to the decreasing viscosity starting at approximately 1800km depth, the plume head starts to separate from the plume tail and (de)forms into a diapir-like upwelling. This process, as well as the rapid plume ascent above 1800km depth, is stopped when the plume nears the transition to high viscosity at 660km depth. The plume is slowed, and the lean, vertically elongated plume head/diapir-like upwelling forms back into a broad plume head feature in reaction to the viscosity step. The now restored plume head is significantly cooler and broader than it was during the passing through the lower mantle.

When hitting the transition to low viscosity at 410km depth, the plume head develops a secondary plume just as in the Mitrovica / Forte case. This secondary plume traverses the distance between the viscosity transition and the base of the lithosphere in 0.5Myr, being supplied by the 'trapped' primary plume head. Once the secondary plume has reached the lithosphere, hence establishing the plume, the trapped primary plume head is all but sucked dry by the secondary plume conduit, completely dissolving and vanishing as a structure in the transition zone over the period of ~ 10 Myr. For the overall ascent, the plume needs ~ 115 Myr.

The origins of plume and plume sheath material are elaborated on in figure 8.24. Of particular note in this set is the fact that despite deformation and rapid ascent of the plume head due to the diminishing viscosity above 1800km depth, the plume does not shed the plume sheath (as is happening in the Steinberger model experiments). Thus, the plume sheath remains almost undisturbed and comparable in size, shape and composition to the plume sheath of the constant viscosity experiments (compare figure 8.24 at 114.83Myr and figure 8.3 at 74.74Myr). This also ensues that when the secondary plume head starts tapping the primary plume head, it is not only sampling deep mantle material (as in the Mitrovica / Forte viscosity experiments), but also entrained material from the mid-mantle region around 1450km depth. As in the Mitrovica / Forte set of experiments, this results in a complex multiple-zoned structure of the secondary plume, with a significant amount of entrained inner and outer sheath material being 'encased' by a thin shell of hot plume core material.

Composition and flow rates of the secondary plume are presented in figure 8.25. As in the Steinberger viscosity experiments, there is a high initial flow dominated by plume core and inner (warm) plume sheath components that can be attributed to the rapidly ascending secondary plume head. This secondary plume head is mainly composed of material from the warm voluminous primary plume head and inner warm plume sheath. The plume core component of the overall flow is dropping equally sharp, with the inner plume sheath component sustaining comparatively high flow rates for another 5Myr due to the draining of warm material from the primary plume head. About 15Myr after the plume has first impinged on the base of the lithosphere a steady conduit has been established, with a combined inner and outer plume sheath flow exceeding the plume core flow by a factor of six.

The outer plume sheath of the secondary plume is initially dominated by material from above 1450km depth, with a significant fraction of upper mantle transition zone material. With

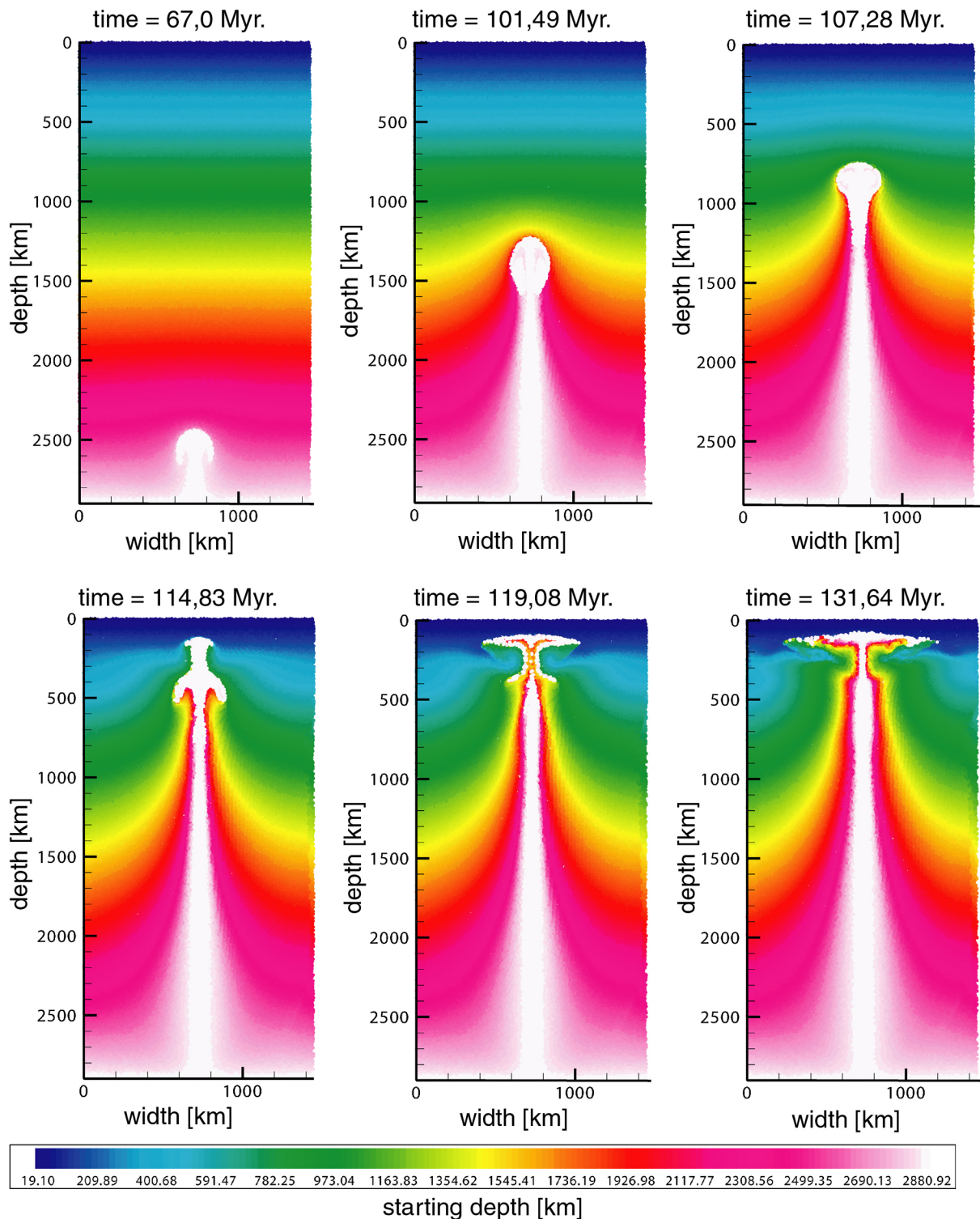


Figure 8.24: Material starting depth sequence of the Walzer et al. viscosity model.

increasing contribution from the primary plume conduit to the secondary plume sheath material, the outer plume sheath becomes more and more dominated by material from the mid- and deep mantle, with gradually decreasing contributions from material originating above 1450 km. The source region fraction of the outer plume sheath remains negligible for the most part. The inner

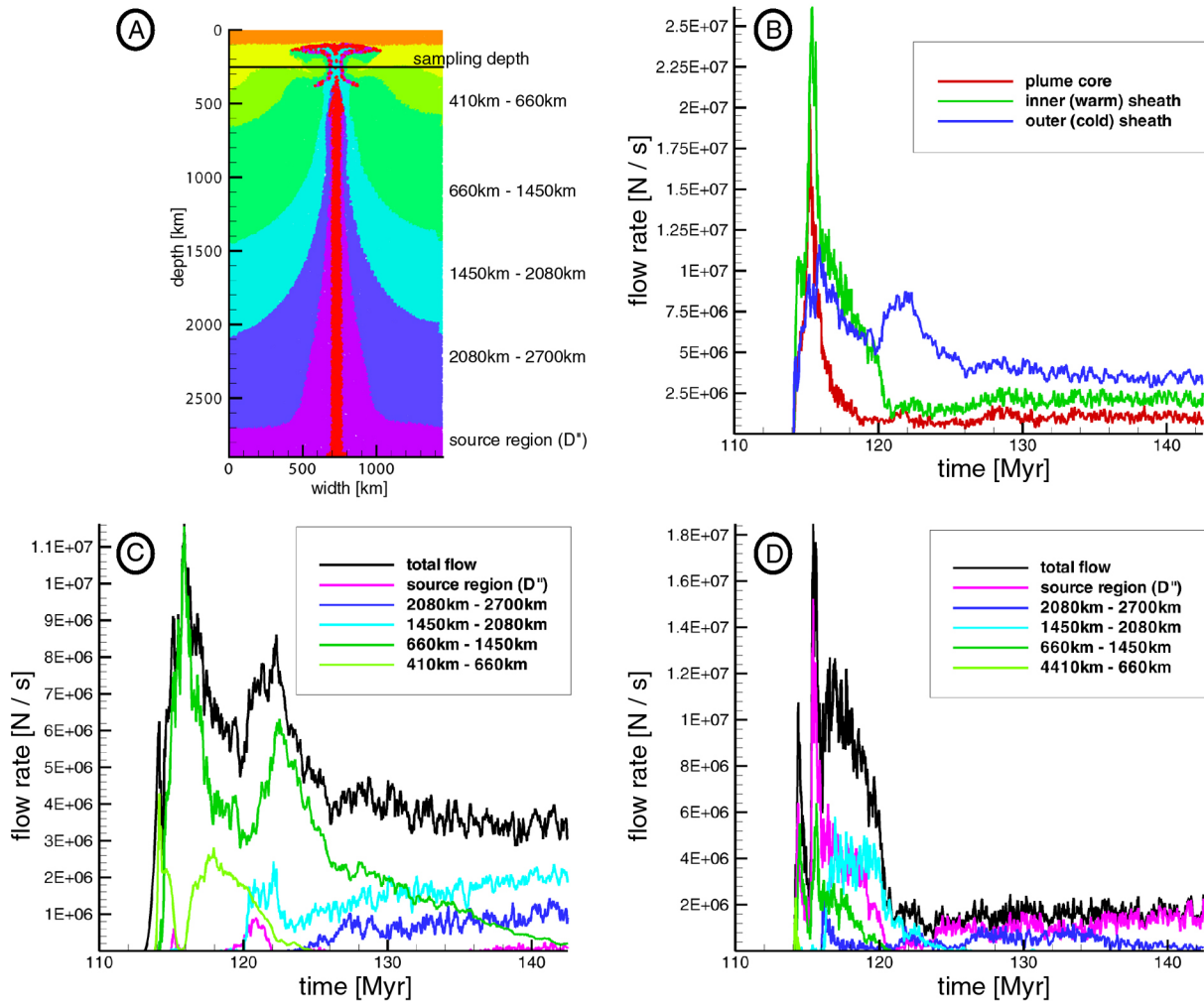


Figure 8.25: Flow rates of the Walzer et al. viscosity model: A) Overview on the distinct mantle regions and sampling depth. B) Total plume flow, divided into core, inner sheath and outer sheath flow. C) Outer sheath flow, divided by origin of material. D) Inner sheath flow, divided by origin of material.

plume sheath is initially characterised by a large fraction of material originating between 2080km depth and 1450km depth, the result of the secondary plume sampling the warm reservoir of the primary plume head. After a steady conduit has been established, the inner plume sheath solely consists of source region and deep mantle material.

Looking at the source layer sampling and zonation of the plume in figure 8.26, it can be seen that the composition of the plume head after it had been deformed by the rapid ascent due to decrease in viscosity above 1800km and re-formed in reaction to the high viscosity transition zone above 660km depth is highly complex: Essentially, the source material 'whorl' and resulting 'doughnut' region that were trailing the rapidly ascending plume head have been all but folded back into the plume head, encapsulating a significant volume of entrained inner plume sheath. This highly deformed structure serves as the source of the secondary plume, with the components to the secondary plume being thoroughly intermixed. Additionally, due to the sampling of the primary plume head, additional plume sheath material, primarily from the primary outer plume sheath, is being 'sucked' upwards and brought into the plume swell /

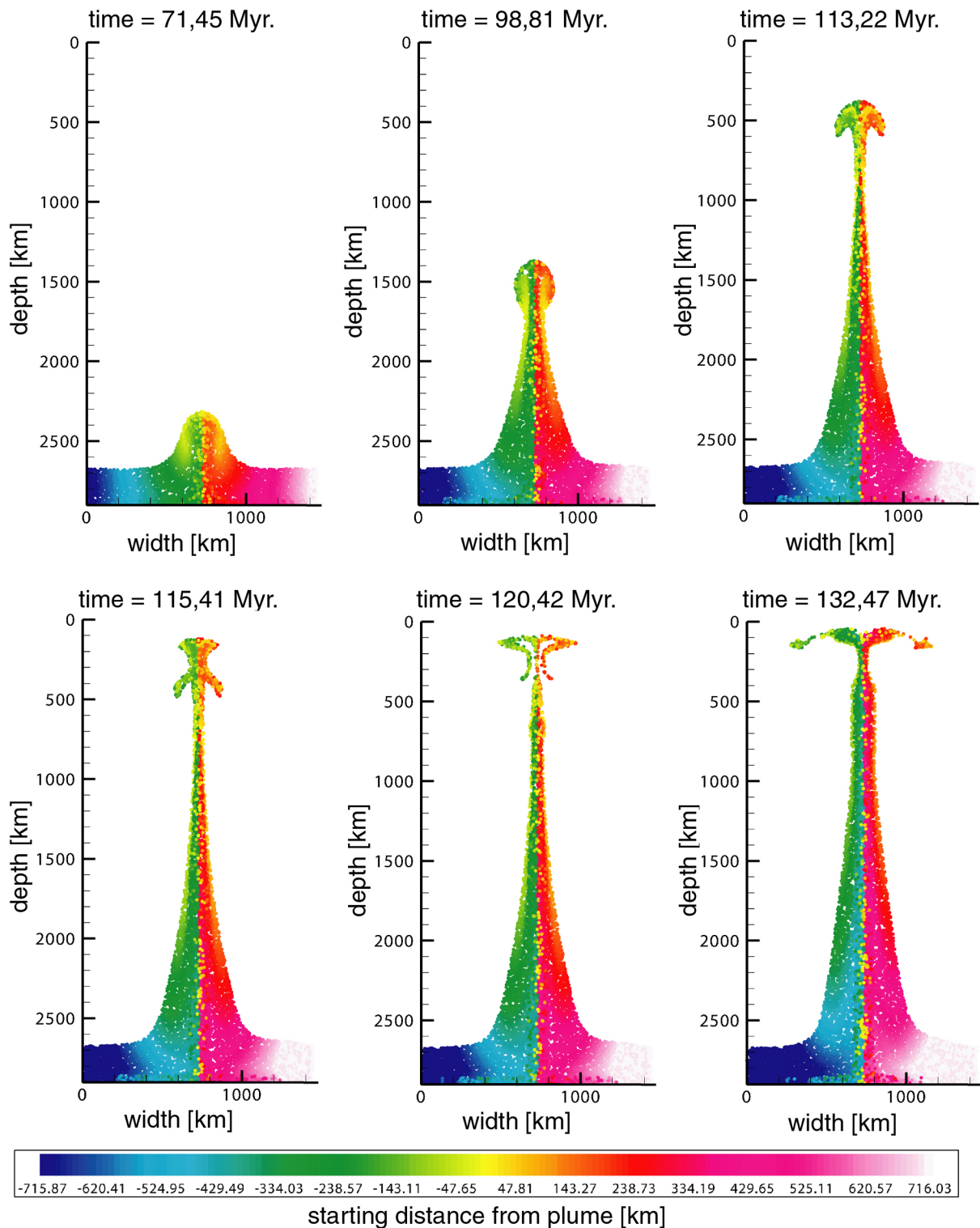


Figure 8.26: Sampling of the source layer and D'' of the Walzer et al. viscosity model.

melting region. Again, the 'ring' of yellow/orange material in figure 8.27 marks the reconnecting of the lower plume and plume sheath with the leading structure of the secondary plume head, and the 'establishing' of the plume as a steady conduit. No lateral transport within the plume is observable in either figure.

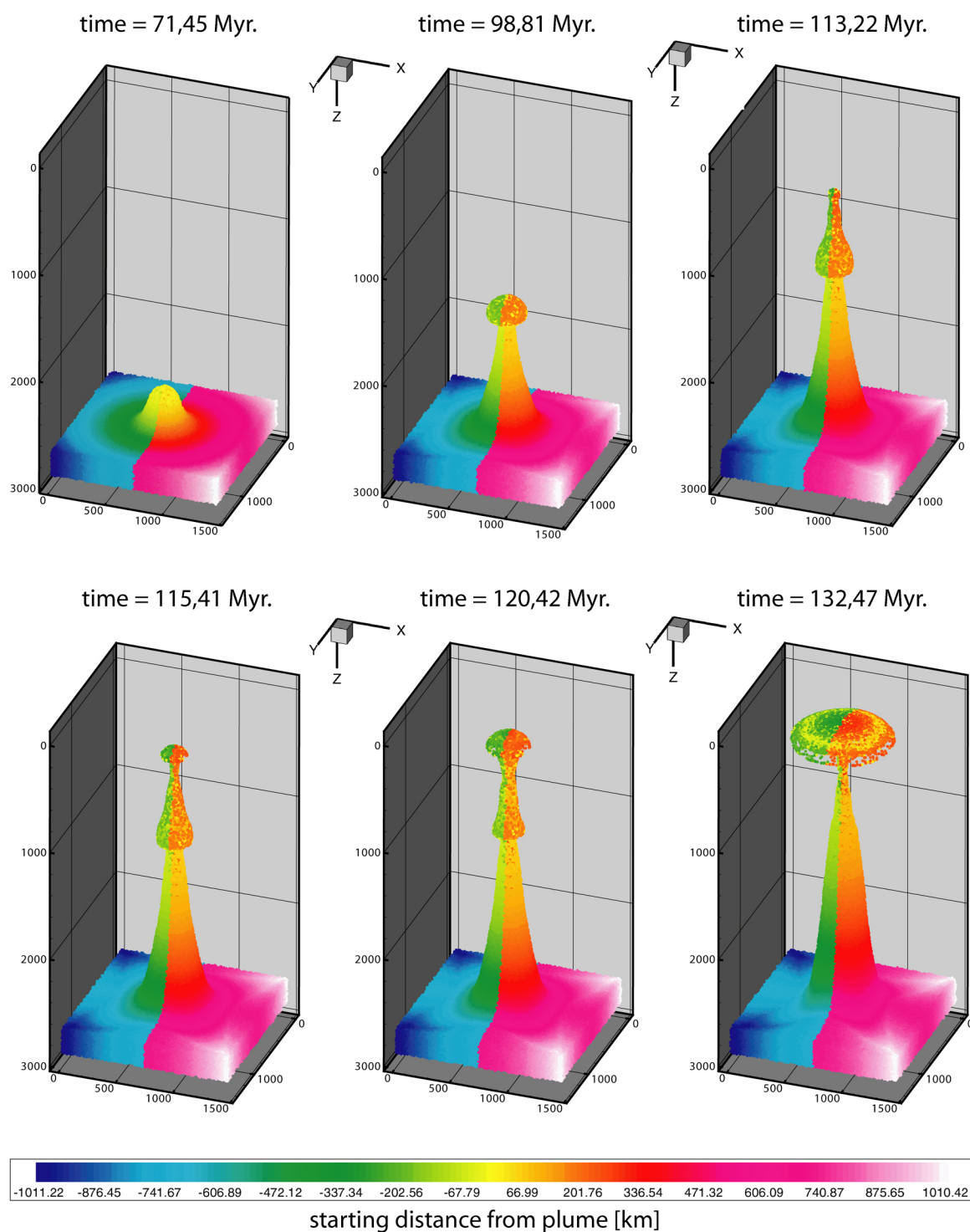


Figure 8.27: 3D plume evolution of the Walzer et al. viscosity model.

As a consequence of the multiple deformations and samplings of the plume head, the melting region of the Walzer et al. viscosity model experiments is the most heterogeneous in all the experiments presented here (figure 8.28). As in the Mitrovica / Forte experiments, the plume head displays a distinct vertical zonation, with primary sheath material from between 2080km depth and 1450km depth as well as a small fraction of material originating between 1450km and

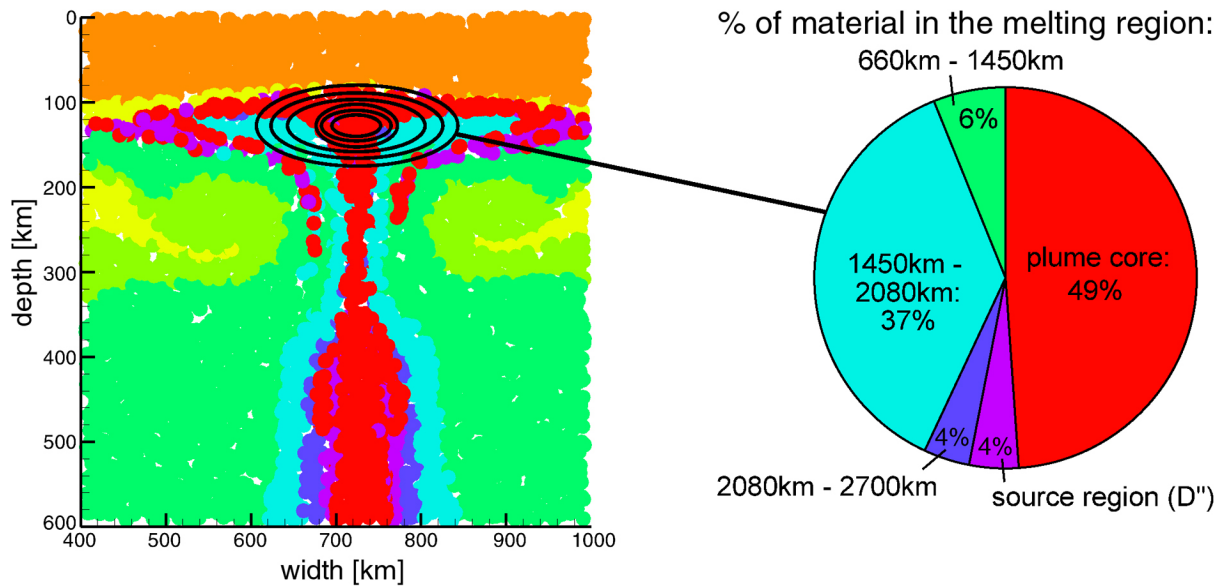


Figure 8.28: *Left: closeup on the plume head illustrating the melting region of the plume. Right: breakdown of the material origins for the melting region.*

660km depth being pulled into the hot, melting plume head core. Melting rates in the plume head average $\sim 0.021 \text{ km}^3/\text{yr}$. Again, the multitude of materials present in the primary melting region of the plume hints at a melting composition that is inherently heterogeneous, and that will display a multitude of characteristics representative of various deep mantle and mid-mantle sources.

8.3 Sampling of the Source Layer

To investigate how a distinct zonation of the plume source layer can affect the geochemical signature of plume swells and plume tracks, the plume source region is divided into three distinctly coloured sections, which are in turn distributed in six different alignments. To facilitate the formation of a plume track, a constant velocity of $\sim 9 \text{ cm/yr}$ is imposed on the lithospheric 'plate' of the model. Thus, the ascending plume will be laterally displaced in the direction of plate movement, forming not a pond-like swell but a long, elongated plume track. The results of this are pictured in figure 8.29: figure 8.29a gives an overview of the plume setup, with figures 8.29b-g presenting xy-cross-sections through the plume swell directly beneath the base of the lithosphere at $\sim 70 \text{ km}$ depth. All through figures 8.29b-g, the zonation of the source region is presented in a little box in the upper right corner, with the white dot marking the location of the thermal perturbation and plume root. The arrow denotes the direction of plate movement. All cross-sections are taken at $\sim 140 \text{ Myr}$, approximately 60 Myr after the plume has first impinged on the base of the lithosphere.

From figures 8.29b-g, it can be seen that different patterns of zonation in the source region result in distinct, unique zonation patterns in the plume swell and plume track. Considering that the results presented throughout this thesis strongly hint at the geochemical signature of the plume being predominantly defined by heterogeneities in the plume source region, this suggests that any observed distinct zonation in the plume, as e.g. exhibited by the 'horseshoe' pattern of the Galápagos islands and Cocos track (*Hoernle et al. [2000]*, *Werner et al. [2003]*), may be

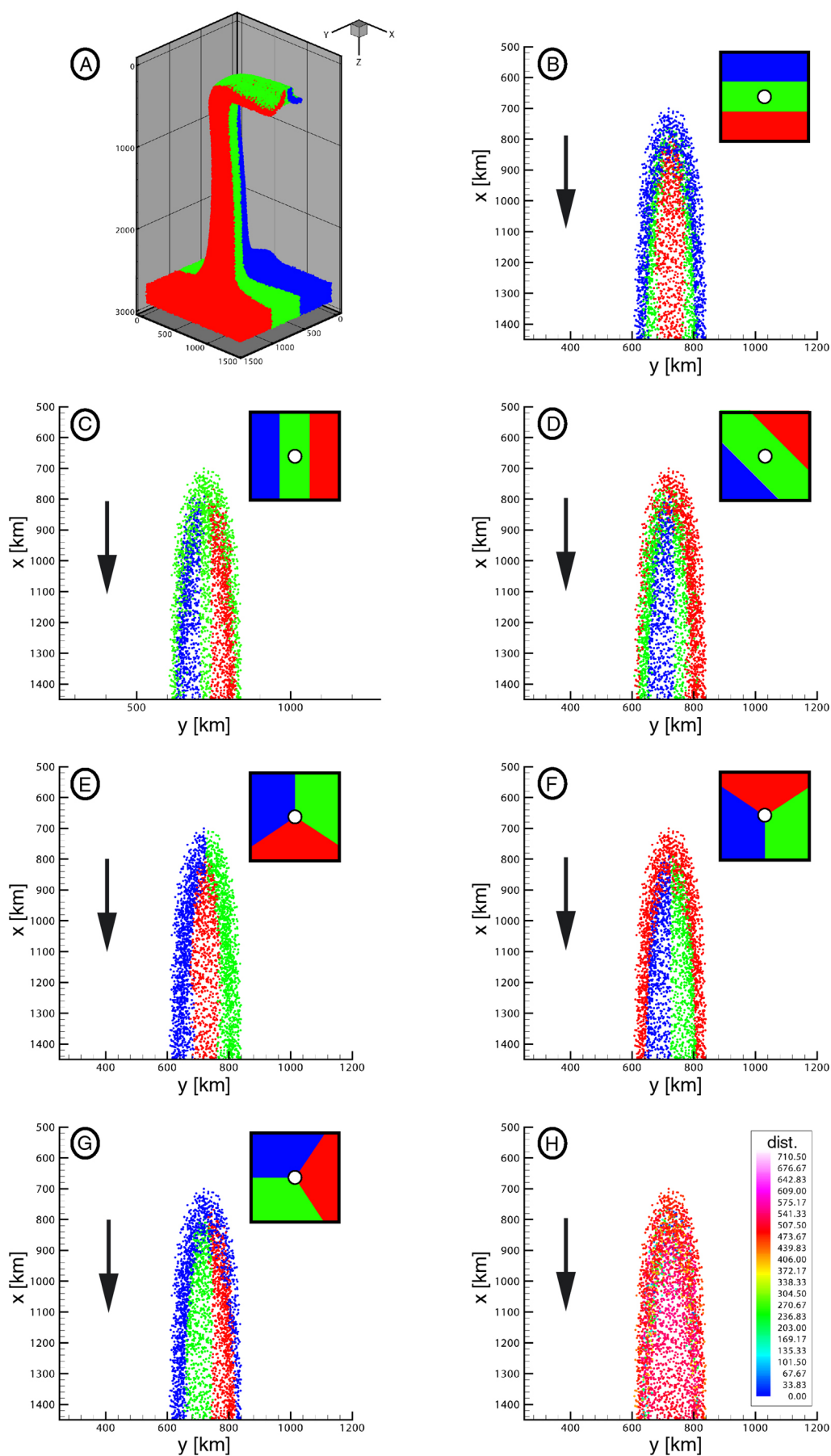


Figure 8.29: Sampling of distinct reservoirs in the plume source region.

an indicator of the distribution of heterogeneities in the plume source region. For example, in the case of Galápagos the pattern observed is most reminiscent of figure 8.29e, meaning that the source region of the Galápagos plume may likely be composed of three distinct zones of discrete composition (blue, green, red) arranged at roughly 60° angles.

Figure 8.29h presents the starting distance from the plume root/plume axis (the white dots in figures 8.29b-g) of material in the plume swell at ~140Myr. As can be seen, the majority of material in the plume swell at ~140Myr originates no further than 500km-600km from the center axis of the plume, meaning that distinct zones in the plume source region that are no more than 500km-600km across can provide a constant zonation of the plume for at least 60Myr. This observation also holds true for experiments with different depth-dependent mantle viscosity functions, like those presented in the above sections of this chapter.

8.4 Assessment and Summary

Critically examining the numerical models presented in this chapter, it is seen that the biggest flaw in the models lies with the fact that trying to implement the physical processes of mantle phase changes has not been met with success. For example, it can be questioned if the cool, non-buoyant outer plume sheath material would really cross phase transitions as easily as it does in these models. Other than that, treating the mantle as a Newtonian fluid and using the Boussinesq approximation might be seen as overly simplifying. In addition to this, the melting rates brought forward seem uncharacteristically low. Lastly, there remains the almost obligatory question of grid resolution, and if it is sufficiently resolving the physical processes of the models to produce confidential results.

Addressing the last issue first, the best resolution in the models presented here is one of 11.3km for the mantle models - which compares favourably to most studies previously conducted in full 3D, and is also on par with or exceeds the majority of 2D studies. Still, it must be conceded that the numerical mantle models of this thesis do not seem to reproduce the delicate plume head filament structures in much detail.

In evaluating the simplifications made in the mantle model, the works of *Nakakuki et al.* [1997], *Marquart & Schmeling* [2000]; *Marquart et al.* [2000] and *Farnetani et al.* [2002] should be referenced. Comparing these studies, which use more detailed and sophisticated models of the mantle, with the models presented in this chapter, it can be seen that the method of approximating phase changes through sharp viscosity interfaces results in model behavior that is at least qualitatively similar to more sophisticated models incorporating a more realistic treatment of phase changes. The last two studies in particular display deep mantle, sheath-like upwellings crossing the negative Clapeyron slope phase boundary at 660km depth alongside the plume.

The low melting rates are the logical consequence of the very simplified melting model utilised for this study, and are neither meant as nor serve as a quantitative indicator of actual melt production. A more sophisticated melting model would incorporate multi-component, Eclogite and 'plum' melting (e.g. *Condie* [2001] and *Phipps Morgan* [2001]), the effects of pressure-release melting through cracks in the overlying lithosphere, secondary melting in the plume tail (e.g. *Ribe & Christensen* [1999]) and the effect of water on the melting behaviour of the mantle plume (*Bercovici & Karato* [2003]). Still, the determined melting rates are well in the realm of realistic values for a single-component, ultramafic source, so that the current melting model serves as a solid base for further study.

All in all, it can safely be said that the necessary simplifications in the mantle models presented in this chapter do not invalidate the results derived from these models.

Based on the results presented in this chapter, a plume sheath can be considered to form around a budding plume in the mantle, and to follow the plume throughout its ascent through the mantle. Interaction with viscosity and/or phase changes may dramatically change the shape, composition and behaviour of both plume and plume sheath. Models with a high viscosity zone in the upper mantle or at the top of the lower mantle (the *Mitrovica & Forte* [1997] and *Walzer et al.* [2004] viscosity profiles) seem to best reflect observations of plume shape and plume temperature in the upper mantle, and both exhibit a very complex zonation and intermixing of reservoirs in the plume heads, providing ample explanation for the geochemical diversity of hot spot basalts. No evidence of lateral transport within the ascending plume and plume sheath have been found, leading to the conclusion that any spatial anomalies in composition and/or geochemical signature found in hot spot melts and basalts may mirror zonation and location of heterogeneities in the plume source region.

Chapter 9

Summary, Discussion and Outlook

The goal of this work was to study the dynamics of plume entrainment, focussing on the origin of entrained material, the specifics of source layer sampling, and the effects of mantle discontinuities on entrainment rates.

9.1 Summary of the Experimental and Numerical Work

The analogue laboratory experiments presented in Chapter 4 indicate that the plume model proposed by *Griffiths & Campbell [1990]* is lacking in an important feature: a sheath of mostly unheated material enveloping the core thermal plume structure and rising along with the plume. The plume sheath is chiefly made up from material of the lowermost plume source region. All entrainment into the plume head has its origin in the plume sheath, and all entrainment of ambient material happens between plume sheath and surrounding material. However, it is still possible for ambient material to eventually end up in the plume head, by way of being entrained into the sheath first and the sheath/ambient material mix being entrained into the plume head later. Yet only a very small fraction of ambient material is transported into the plume head this way. The plume sheath itself is too viscous and too cold to rise under its own thermal buoyancy, which suggests that it owes its rise to drag/pull of the fast ascending plume core material. Extensive testing with a variety of source and ambient temperatures as well as two inherently different experimental setups (pure thermal source vs. injection source) proves that the plume sheath is a solid phenomenon, not a by-effect of one specific set of experimental conditions.

The reason this phenomenon has been missed by *Griffiths & Campbell [1990]* and other researchers lies in the experimental setup and focus. More specifically, most prior experiments solely marked and followed the behaviour of the plume core material and did not investigate in detail the behaviour of the plume's surroundings. The existence of this plume sheath, and the observation that it, contrary to previous models of plume ascent and entrainment, prevents the large-scale entrainment of ambient material into the plume head, leads to the conclusion that any heterogeneity of the plume head is predominantly inherited at the source region rather than being the result of entrainment of ambient material during plume ascent.

Moreover, the apparent similarities between the (source-unmarked) diapiric ascent of experimental set A and the (source-marked) plume core + plume sheath ascent of experimental set B provide ground for speculation that an intricate internal structure, as displayed by the *Griffiths & Campbell [1990]* and the experiments of set B, might also be found within the blunt,

diapir-like upwellings recently reported by e.g. *Le Bars & Davaille [2004]* and *Farnetani & Samuel [2005]*, in the latter case meaning that the diversity in plume shapes and populations that the authors imply might, in fact, not be all that broad as it appears from their study.

Investigating the plume sheath model inferred from the laboratory experiments via numerical modelling, it is found that the numerical models readily reproduce plume sheath behaviour in the ascending plume. Namely, numerical experiments prominently exhibit blunt, diapiric uprisings that can be differentiated into a hot plume core, similar in shape and dimensions to the intricate source-marked structure in the laboratory experiments, a warm inner plume sheath comprised of source region material heated up by the hot plume core, and a cold outer sheath predominantly consisting of source region material, but containing material entrained all through the experimental region. The notion that the sheath, because of its low temperature, lacks the buoyancy to sustain ascent on its own is confirmed, which implies that the sheath is, at least to a considerable degree, hoisted up by the ascended plume head.

Focusing on the plume core, and how it samples the source region, it is observed that there is little to no vorticity within the ascending plume core, and hence no lateral transport of material found within. Rather, distinct spatial regions within the deep plume source region are preserved as distinct vertical stripes, and subsequently form distinct regions in the plume head. This is especially true when the plume head spreads out in reaction to a surface boundary. Likewise, distinct source-depths being entrained into the plume sheath during plume ascent are preserved as vertical stripes in the plume sheath.

Numerical models for mantle conditions start out with the case of an isoviscous mantle, with a hot boundary layer at the core-mantle boundary and a cold boundary layer representing the lithosphere. This setup most closely resembles the laboratory experiments and laboratory condition models, and displays all of the phenomena already noted for these experiments. Once again a clear distinction in plume core, inner 'warm' plume sheath and outer 'cold' plume sheath can be made, and lack of lateral transport and vertical zonation of plume core and plume sheath are observed under these conditions as well. It must be noted that, due to the plume sampling the hot bottom boundary layer, the plume is able to retain much more of its initial temperature perturbation, leading to excessive heat of the sub-lithospheric plume head and plume stem of $\sim 200^{\circ}\text{C} - 300^{\circ}\text{C}$ - which is in good agreement with recent data derived from olivine liquid equilibria (e.g. *Putirka [2005]*).

Introducing depth-dependent viscosity does dramatically change the dynamics of plume ascent and plume dynamics. Three different viscosity profiles taken from *Mitrovica & Forte [1997]*, *Steinberger [2000]* and *Walzer et al. [2004]* are introduced to the numerical model and their effects on model behaviour are tested. Essentially, high viscosity zones result in significantly stalled plume ascent as well as a broad plume head and resulting broad plume sheath. Low viscosity zones result in strong deformation and elongation of the plume head up to the point where the plume head is, in shape and diameter, practically indistinguishable from the plume tail. Also, the plume sheath is considerably thinned in low viscosity zones, to the point of partial or total separation from the leading plume head. Sharp interfaces from low viscosity to high viscosity result in behaviour similar to hitting the surface boundary - notably spreading out and widening of the plume head. Sharp interfaces from high to low result in the formation of secondary plumes from the plume head. These secondary plumes subsequently form an entirely new plume sheath from the low viscosity ambient material above the interface in the process. This particular phenomenon results in parts of the primary plume head already forming the secondary plume while other parts of the primary plume head remain trapped in the high viscosity zone. As a consequence, the secondary plume literally 'sucks dry' the primary

plume head and plume sheath, resulting in a remarkably complex compositional structure of the secondary plume: A plume sheath surrounding an outer shell of hot source region material, which in turn envelopes a cylinder of entrained warm lower mantle material, that itself surrounds a hot plume core. The plume head structure is equally intricate, with a shell of plume core material encasing a horizontally-zoned 'filling' of entrained material.

It should be noted that despite all the deformations exerted on the ascending plume and plume sheath through changes and jumps in viscosity, there remains little to no lateral transport to be found in either plume sheath or plume core. Rather, distinct reservoirs in the plume source region remain distinct even after entrainment, deformation and transport to the surface.

Again, the reason these phenomena have been missed by previous numerical studies lies with the fact that these studies focused more on the broader dynamics and flow behaviour of mantle convection and plume ascent and did not follow the origins of material in the flow field. In the few studies that do (e.g. *Farnetani et al. [2002]*), there are a number of hints at the existence of a plume sheath in the data they present that are, however, not followed up. For example, *Farnetani et al. [2002]* present in their study a huge volume of lower mantle material underlying their plume head at 200km depth - that is even exceeding their plume head in diameter - but make no mention how it got there.

Applying a simple melting model to the numerical calculations, it is seen that only part of the plume head hitting the base of the lithosphere melts - most of the material brought up by plume flow remains unmelted and spreads horizontally under the lithosphere. The part of the plume head that actually melts is predominantly composed of plume core material, having its origin in the core-mantle boundary. However, deformation of the plume head during plume ascent may result in deep source and mid-source material being entrained into the plume head and ending up in the melting portion of the plume head, thus adding to the heterogeneity of the plume head melts.

Lastly, the effects of plume deflection by a moving plate is investigated. For a number of distinct source region zonations, it is investigated how the bending and deformation exerted on a plume through interaction with a top moving plate is affecting their spatial distribution within the plume. Not only are spatial zonations retained as distinct zones of the plume track, but the arrangements of these zones exhibit characteristic patterns, thus potentially allowing for the drawing of conclusions on the composition and layout of the source region from the zonation of the plume track.

9.2 Implications for Plume Ascent and Plume Entrainment

From these collected observations, it is now possible to form a model of plume ascent and entrainment in the mantle. It is obvious that parts of the well-established interpretation of plume head and plume tail dynamics need to be revised and expanded. Specifically, the plume model that is proposed by this thesis predicates that the geochemical interpretation of heterogeneities in flood basalts and hotspot volcanism reflecting the entrainment-induced mixing of a small amount of deep material with a much larger amount of shallower material is inaccurate. From the results presented in this thesis, the processes of plume ascent and plume entrainment present themselves thus:

- The plume emerges from a thermal instability in a thermal boundary layer that is compositionally heterogeneous, and that exhibits distinct compositional zonation in the plume

source region. These distinct zones might stem from subducted slabs overlying the core-mantle boundary (e.g. *Tan et al. [2002]*), 'piles' of primitive material (e.g. *Hansen & Yuen [2000]*) or mantle 'plums' (*Phipp's Morgan & Morgan [1999]*).

- The plume subsequently starts to rise in the mantle while primarily sampling the lowermost, hottest region of the boundary layer to sustain itself during plume ascent. This material is referred to as the 'plume core' in this thesis, and follows the classical plume model in flow and behaviour, i.e. the formation of a distinct plume head and plume tail, the 'jolleying' of plume core material in the outer and lower parts of the 'mushroom cap' of the plume head, and the 'doughnut'-shaped region of plume core material running like a ring around the plume tail.
- In the wake of the ascending plume head, a sheath of material enveloping the budding plume tail forms and rises. This sheath is primarily made up of deep material, sampling the plume source region and overlying D" layer. Compositional heterogeneities are preserved when sampled, and form distinct vertical 'stripes' within the plume. This part of the plume sheath retains some of the thermal anomaly characteristic of its thermal boundary layer source and can be considered warmer than the ambient mantle it is passing through - yet it is generally too cold to fully sustain its own ascent. It is referred to as the 'inner plume sheath' in this thesis.
- In reaction to the rising plume, material from the upper D" and lower mantle is also displaced and induced to ascend along with the rising plume. This material forms an outer, predominantly 'cold' (meaning 'not heated above ambient mantle temperature' in this context) sheath around the 'hot' plume core and 'warm' inner plume sheath. This part of the plume sheath owes its ascent fully to the pull and drag of the ascending plume and plume head, and consequently exhibits rising velocities that are up to one order of magnitude smaller than those of the plume core. This part of the plume sheath is prone to entraining mantle material that it passes through. As with the inner sheath, heterogeneities (originating e.g. from further mantle 'plums') sampled by this sheath during formation or ascent persist as distinct zones within the plume sheath.
- Variations in viscosity and/or phase transitions within the mantle disturb and deform the ascending plume core + plume sheath, and can in some cases cause the partial or complete separation of the plume sheath from the plume core, and subsequent buildup of a new plume sheath layer from mid-mantle and upper mantle sources. The majority of mantle models favour at least one sharp viscosity change (from lower highly viscous material to upper less viscous material) in the mantle, mostly coinciding with the 660km or 410km phase change. Such an interface would be associated with a complex deformation and zoning of the plume head, incorporating material from the 'warm' inner plume sheath into the newly-formed secondary plume head and plume tail, and the formation of a new plume sheath predominantly made up of upper mantle material.
- The plume head reaches the base of the lithosphere, where part of the plume head melts. The melting region predominantly consists of plume core material - however, in a 'zoned' plume head resulting from interaction with a viscosity/phase change, lower mantle material entrained into the plume head can persist in the melting region for approximately 10-20 Myr before succeeding plume core material dominates the melting region. Unmelted material is displaced laterally beneath the lithosphere, forming a plume swell in the direction of plate movement. Barring disruption from mantle convection flow, the plume

will form a steady plume sheath + plume core system, exhibiting a distinct horizontal zonation of its components and further zonation due to heterogeneities inherited during plume source sampling and plume ascent.

These conclusions lend strong support to recent data from the Iceland hotspot and Reykjanes Ridge, where *Kempton et al.* [2000] and in particular *Murton et al.* [2002] attribute the geochemically distinct zones in the Iceland-Reykjanes Ridge system to the presence of at least two geochemically distinct plume sheaths in addition to a heterogeneous main plume core, with the 'inner' sheath originating in the lower mantle and the 'outer' sheath originating at the 660km discontinuity. According to them, the Iceland plume core comprises a heterogeneous mixture of an enriched component E₁ (characterised by high ³He/⁴He, high ⁸⁷Sr/⁸⁶Sr, low ¹⁴³Nd/¹⁴⁴Nd, positive ΔNb, and rich in trace elements) and a depleted component (characterised by high ³He/⁴He, high ⁸⁷Sr/⁸⁶Sr, low ¹⁴³Nd/¹⁴⁴Nd, positive ΔNb, and poor in trace elements). The inner (lower mantle source) plume sheath comprises a mixture of E₁ and a depleted component (characterised by high ³He/⁴He, high ⁸⁷Sr/⁸⁶Sr, low ¹⁴³Nd/¹⁴⁴Nd, negative ΔNb, poor in trace elements) distinct from the plume core depleted component. During ascent, the plume entrains a sheath of 'MORB-like' material with a high εHf signature that has been infused with lower-mantle helium, and displaying only intermediate ¹⁴³Nd/¹⁴⁴Nd, thus making it compositionally distinct from actual MORB. This structure is well-reflected in the distinct source regions of the plume core, inner plume sheath and outer plume sheath of this thesis.

Furthermore, support is lend to the seismological observations of *Montelli et al.* [2004a,b], who point out that most of the plumes they find seem to be surprisingly large in diameter. In the mantle models of this study, plume core + inner ('warm') plume sheath regularly reach diameters of 200km and more, while the proper plume core seldom grows larger than 100km in diameter. Thus, it can be concluded that the large thermal structures they see in the lower and upper mantle are, in fact, not only the plume core but the plume core and inner plume sheath.

Strong support is given to the notion brought forward by *Farnetani et al.* [2002] and other studies that the geochemical signature of hotspot basalts is primarily inherited in the plume source and lower mantle - the necessary amount of plume-ascent-linked entrainment simply does not take place during the ascent of a buoyant plume under lab and computational conditions for the composition of the plume head and plume tail to be dominated by material not coming from the plume source region. Instead, the chemical composition of flood basalts and hotspot volcanism is most likely reflecting the melting of an intrinsically heterogeneous mantle, with hotspot volcanism reflecting lower degrees of selective melt extraction from the more enriched, lower-solidus components within the source, while flood basalts reflect higher degrees of melting of the same heterogeneous source (*Phipps Morgan & Morgan* [1999]). In this conceptual model, plume entrainment is mostly irrelevant to the composition of the plume head and plume tail since the mantle between 400km - 2900km depth can have a uniformly heterogeneous plum-pudding composition, with local variations between hotspots reflecting local variations in mantle heterogeneity caused by regional nonuniformity in the stirring and mixing of the mantle. In fact, entraining of a cold plume sheath and subsequent stripping of the sheath at a mantle discontinuity might be considered as another process to facilitate mantle mixing, mantle heterogeneity and the formation of mantle 'plums'.

Lastly, the observed longevity of distinct spatial regions within the plume source region, and their transformation from lateral source heterogeneity to vertical 'stripe' zonation in the ascending plume and back to lateral heterogeneity in the spreading plume head and plume swell support the suggestions of *Hoernle et al.* [2000] and *Werner et al.* [2003] for the Galápagos

hotspot that geochemical zonation of the plume source region is little affected by stirring and lateral transport during plume ascent, thus preserving lateral spatial variations in the chemistry of hotspot basalts for ~ 40 Myr. and longer.

9.3 Outlook

This study has postulated the existence of a plume sheath enveloping the mantle plume during ascent, and has offered the results of extensive laboratory and numerical experimentation to support this notion. The plume sheath model does not only reconcile laboratory and numerical models of ascending plumes (see e.g. *Farnetani et al.* [2002] and their criticism on the *Griffiths & Campbell* [1990] plume model), but provides ample support and explanation for a number of phenomena observed in this thesis and in a variety of other studies (see section 9.2 above).

Further constraints on the dynamics and implication of the plume sheath model can be acquired through laboratory studies employing an improved, more effective heating element and conducting a parameter study broader than the one presented in this thesis, while still keeping focus on plume and plume sheath behaviour. In addition to this, laboratory studies implementing a hot bottom boundary layer as the plume source, while also implementing nonhomogeneity of the experimental fluid, will certainly produce more valuable and interesting data as well as more support for the model presented in this thesis.

Improving the resolution of the numerical models is always desirable and should be possible through pure technical means: At the time of writing this thesis, the BEOWULF cluster acquired at the start of this study is already obsolete, and is being upgraded with up-to-date components, almost doubling its system memory and computational power. The use of advanced computational methods (like weighted computational grids or an adaptive mesh refinement scheme) should also improve model resolution and increase general model effectiveness. Further numerical studies of the plume and plume sheath will implement a more detailed and sophisticated model of the mantle, incorporating e.g. compositional differences and stress and strain rates, as well as a more detailed melting model. This will shed more light on the minutiae of plume sheath behaviour, e.g. the interaction with prominent phase changes in the mantle, and will also allow for a more detailed breakdown and quantification of the contribution of multiple-zoned plume head components to the overall melt signature. Lastly, investigating the details of plume-lithosphere interaction, and in particular the details of plume-ridge and plume sheath-ridge interaction, will provide additional insights into the complex dynamical behaviour associated with these processes.

Appendix A

Properties of the Glucose Syrup used in the laboratory experiments

The syrup used in the experiments is of the brand 'Cerestar C*Sweet 01444', produced by the company Cerestar. The following data is courtesy of Cerestar Deutschland:

Dextrose equivalent (DE)		40.5
Dry substance	%	79.5
Refractive index at 20°C		1.496
pH		5.3
Recommended storage temperature		55°C
Carbohydrate composition:		
Dextrose		15.0
Maltose		15.0
Maltotriose		13.5
Polysaccharides		56.5
Density at 20°C	min.	1.417 g/ml
	max.	1.424 g/ml
Viscosity (mPa.s)	30°C	61.000
	40°C	17.000
	50°C	6100
	60°C	2900

Table A.1: Manufacturer's data for the Cerestar C*Sweet 01444 syrup.

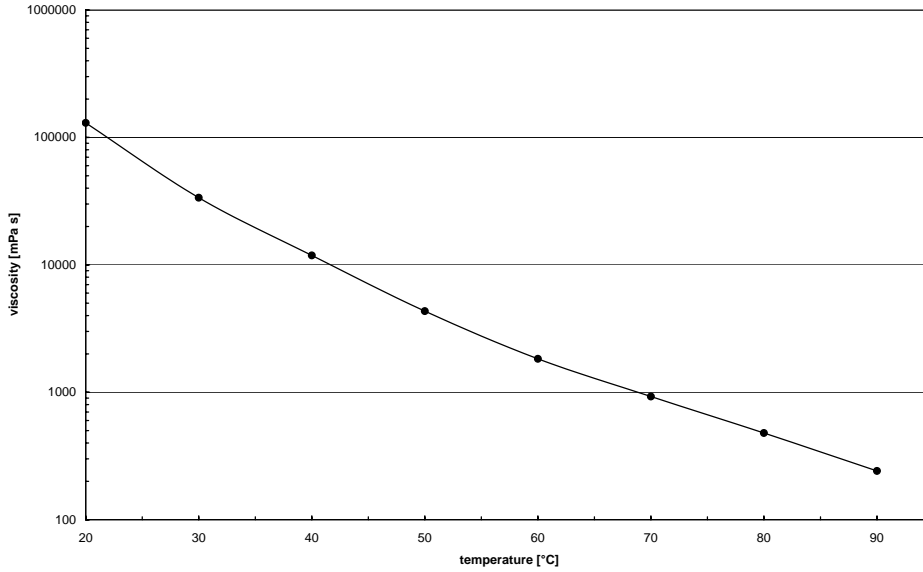


Figure A.1: *Temperature dependency of the viscosity of the syrup.*

The syrup itself is described as a purified and concentrated glucose syrup with high polysaccharide content obtained from starch by enzymatic conversion. It's usual application lies with confectionary products such as hard candy and fillings. It is clear with a slight yellowish tint, and has a distinctive, slightly acidic smell.

Due to inappropriate decanting and storage, the syrup was free to absorb ambient moisture from the air for a period of about ten days. This resulted in decreasing the viscosity of the syrup, so that the viscosity curve of the syrup had to be re-determined. This has been done using a tube velocimeter. The resulting viscosity curve has first been presented by *Hasenclever [2004]* and was expanded in range for this study. The viscosity curve was not expanded to temperatures exceeding 90°C because there was legitimate concern that using the viscosimeter with the silicone oil would either damage the viscosimeter or at least overcome the sealing and contaminate the syrup sample. The extended viscosity curve can be seen in figure A.1. From this, an exponential law for the temperature-dependent viscosity can be expressed as:

$$\eta(T) = \eta_0 e^{34\left(\frac{T_0}{T} - 1\right)}. \quad (\text{A.1})$$

Thus, between 20°C and 100°C, the viscosity of the syrup varies over roughly four magnitudes. As it has already been mentioned in section 3.3, storing the syrup at temperatures below the recommended storage temperature results in a certain 'aging' effect - the combination of polysaccharine molecules to even longer sugar chains. This, in turn, results in a change in viscosity by up to a factor of 1.5. These long polysaccharides can be destroyed by heating up the syrup to at least the recommended storage temperature, and keeping it at that temperature for at least 24h.

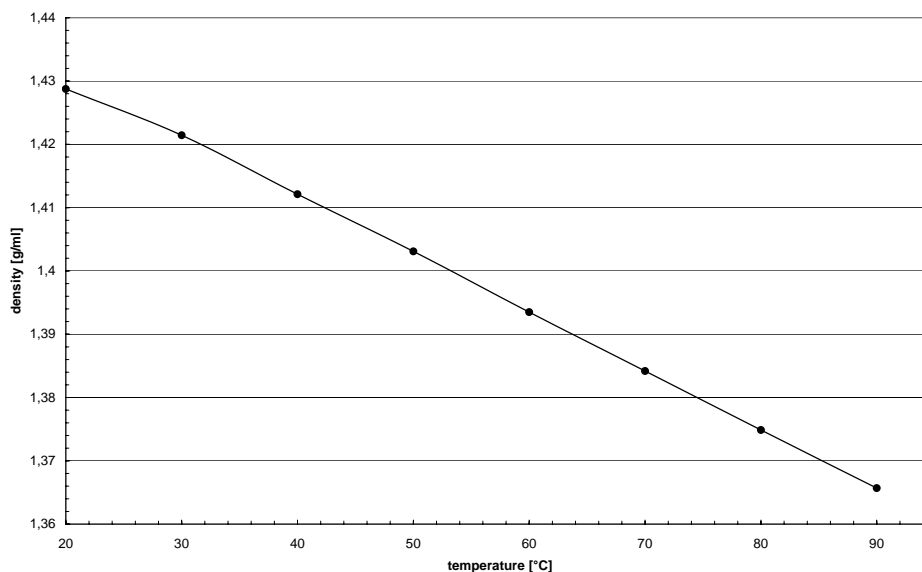


Figure A.2: *Temperature dependency of the density of the syrup.*

The density curve of the syrup can be seen in figure A.2. The density data shows a good fit to the manufacturer's data.

Table A.2 lists further attributes of the syrup. The thermal expansion coefficient is determined through the density measurements, the heat capacity, thermal diffusivity and thermal conductivity are values taken from literature (e.g. *Stöcker [1992]*).

thermal expansion coefficient:	$\alpha \approx 6,0 \times 10^{-4} \frac{1}{K}$
heat capacity:	$c_p \approx 3000 \frac{J}{kgK}$
thermal diffusivity:	$\kappa \approx 0,07 \frac{cm^2}{s}$
thermal conductivity:	$\lambda \approx 0.37 \frac{W}{mK}$

Table A.2: Further attributes of the syrup.

Lastly, the issue of caramelisation shall be addressed briefly. In some of the experiments presented in chapter 4, temperatures in the source region go up to 140°C. Over the course of multiple experiments, a significant change in the colour of the syrup can be observed - the yellowish tint is replaced by a darker, brownish tint. This is the result of the partial caramelisation of the sugars in the syrup.

Basically, caramelisation is the process of the non-enzymatic oxidation of sugar. The actual process is a complex, poorly understood reaction involving hundreds of intermediates, and is the object of extensive ongoing research. In general, caramelisation occurs in a purely sugary environment, while the better-known Maillard reaction is what's happening when making homemade caramels and candies out of sugar and cream: the reaction between amino acids and reducing sugar under heat.

The typical caramelisation temperatures of the bulk of sugars native to the syrup are in the range of 180°C and above. A layman's guess would thus be that the perceivable browning of the syrup comes from either partial caramelisation of the maltose and maltotriose contents, or from caramelisation of small amounts of lesser sugars (like fructose) that form from decay/breakup products of the larger polysaccharides formed through our inadequate storage and broken up through heating of the syrup. Either way, this perceived caramelisation of the syrup does not necessarily implicate an increase in viscosity: since the bulk contribution to the viscosity comes from the long polysaccharide chains of the syrup, the intramolecular bonding and isomerisation between the lesser sugars that is part of the caramelisation process should be a negligible contribution to the overall viscosity.

For further reading on sugar chemistry, and on food chemistry in general, see *Belitz et al.* [2004].

Appendix B

Laboratory Inventory

The following lists all of the appliances used for the laboratory experiments and their technical specifications:

The main experimental tank was built to specification by Adolf Richter Stahl Metalle Kunststoffe GmbH, Kiel. A sketch of the tank configuration and dimensions is presented in figure B.1, with further details of the tank configuration presented in chapter 3, figure 3.1.

The injection tank was built to specification by TuTech TUHH Technologie GmbH, Hamburg. A sketch of the tank configuration is presented in figure B.2.

The heating element was built to specification by TuTech TUHH Technologie GmbH, Hamburg, and modified in the IFM-Geomar workshop. Configuration and dimensions of the heating element are presented in chapter 4, figure 4.1.

The injection apparatus consists of a hydraulic cylinder built by the workshop of the Institut für Geophysik der Universität Hamburg, and an Iselautomation LF4 linear unit driven by an Iselautomation MV 120 servo motor. This setup is controlled through a Iselautomation CVD 1-SPS programmable controlling unit. Technical data sheets for the Iselautomation

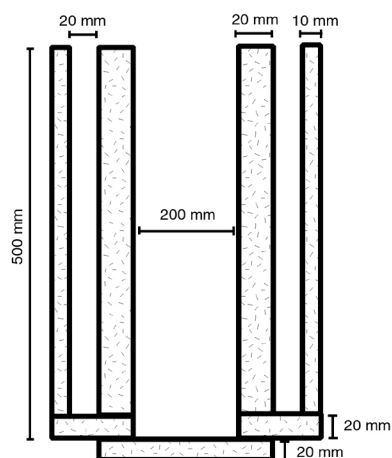


Figure B.1: *Assembly and measurements of the experimental tank.*

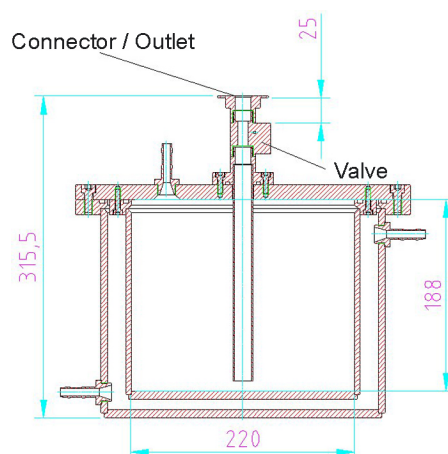


Figure B.2: *Assembly and measurements of the injection tank.*

components are freely available on the internet at <http://www.iselautomation.net/> .

The hydraulic fluid used in the injection apparatus is simple motor oil. The specific brand is Shell Helix Super 10W-40. It has been tested extensively, and has proven to not intermix with the glucose syrup used in the experiments for a number of temperatures, and over long time spans.

Temperature control and feed of heated water to the different parts of the experiment is handled by two Haake C35 thermal baths with Haake F6 thermostats. The bath fluid used in the temperature range below 100°C is simply distilled water (allowing for cheap and easily replaceable silicone tubing), while in the temperature range above 100°C Haake SIL180 silicone oil is used. Due to the silicone oil dissolving the standard silicone tubing, a more complicated supply/drain setup incorporating teflon tubing and special valve and link pieces

Temperature range:	-35°C - 200°C
Bath dimension:	150mm x 220mm x 140mm
Temp. const.:	0.01°C
Pumpage:	
Pressure side:	20 l/min with 300mbar
Suction side:	15 l/min with 210mbar
Cooling capacity:	
20°C	0.40 kW
0°C	0.30 kW
-20°C	0.15 kW

Table B.1: Manufacturer's data for the Haake C35 - F6 thermal bath combo.

Chemical Characteristic:	(oil of) polydimethylsiloxane (α -(trimethylsilyl)- ω -(trimethylsilyloxy) polydimethylsiloxane)
Fire point:	>225°C
Flash point:	170°C
Temperature range:	-40°C - 200°C
Viscosity at 20°C:	11.0 mPas
Density at 20°C:	0.93 $\frac{kg}{l}$
Spec. heat capacity:	1.51 $\frac{kJ}{kgK}$
Colour:	transparent
Reacts with:	Silicone

Table B.2: Manufacturer's data for the SIL180 silicone oil.

is required for the above-100°C experiments.

The technical data of the heating bath/thermostat combo is listed in table B.1. The specifics of the silicone oil are listed in table B.2.

Two different varieties of hollow glass spheres are used as tracer particles in this thesis. The first batch of hollow glass spheres is of unknown manufacturer, with a diameter of 100

CCD Sensor:	Monochrome 1/2" Hyper HAD IT progressive scan CCD
Sensing area:	6.4mm (h) \times 4.8mm (v)
Cell size:	8.3 \times 8.3 μ m
Resolution (horizontal):	600 TV lines
Resolution (vertical):	575 TV lines
Sensitivity:	0.8 lux, F1.4
S/N ratio:	\geq 56 db (AGC off, Gamma 1)
Video 1 / Video 2 interlaced:	1 frame 1/25sec.
Operating temperature:	-5°C to +45°C
Power:	12V DC \pm 10%. 0.5 Amp.
Lens Mount:	C-mount

Table B.3: Manufacturer's data for the Progressive Scan CV-M10 camera.

Format:	Mini-DV PAL
Sensor:	0.8 Mpixels 1/4"
Sensitivity:	5 lux (0 lux at night shot setting)
Optical Zoom:	x 10
Digital Zoom:	x 40
Focal length equiv.:	f 1.7-2.2 / 3.3-33mm (equiv 42-420mm)
Lens Diameter:	30mm
Exposure mode:	auto
White balance:	auto

Table B.4: Manufacturer's data for the Sony DCR-PC2E camera.

μm , identical to the tracer particles used by *Laudenbach* [2001] and courtesy of the Institute of Geosciences of the Georg August Universität zu Göttingen. The second batch of hollow glass particles is manufactured by DanTec Dynamics A/S, Skovlunde/Denmark under the product code HGS-10, with a diameter of 10 μm , a density of 1.1 g/cm^3 and a refractive index of 1.52, and are made of borosilicate glass.

The CCD camera used for particle tracking is a Progressive Scan CV-M10. It is operated along with a Pentax PENT H1212B-TH objective with a focal length of 12mm. The technical data of the CCD camera is listed in table B.3. The camera is mounted on a telescope mount that allows for effortlessly changing the height of the field of view of the camera.

The particle tracking equipment is based on a COIM IC-P-2M framegrabber card with COIM AM-VS add-on module, supplied by Stemmer Imaging GmbH, Purchheim. It is operated with the Heurisko Workspace digital image processing software, with the main applet based on the program used by *Hering* [1996] and extensively modified in-house by Malte Vöge, who also provided additional programming work in the run-up to this project.

Additional video data is captured by video camera and digitised via firewire card. Images are processed with ULEAD Video Studio. The technical data of the video camera is presented in table B.4.

Bibliography

- Abbott, D.H., Isley, A.E., Extraterrestrial influences on mantle plume activity, *Earth Planet. Sci. Lett.*, Vol. 205, No. 1-2, 53-62, 2002
- Abouchami, W., Hofmann, A.W., Galer, S.J.G., Frey, F.A., Eisele, J., Feigenson, M., Lead isotopes reveal bilateral asymmetry and vertical continuity in the Hawaiian mantle plume, *Nature*, Vol. 434, 851-856, 2005
- Abramovitz, M., Stegun, I.A. (eds.), *Handbook of Mathematical Functions with Formulas, Graphs and Mathematical Tables*, 9th Printing, New York: Dover, 896-897, 1972
- Adrian, R.J., Particle-Imaging Techniques for Experimental Fluid Mechanics, *Ann. Rev. Fluid Mech.*, Vol. 23, 261-394, 1991
- Albers, M., Christensen, U.R., The excess temperature of plumes rising from the core-mantle boundary, *Geophys. Res. Lett.*, Vol. 23, No. 24, 3567-3570, 1996
- Anderson, D.L., The edges of the mantle, in Gurnis, M., Wyssession, M.E., Knittle, E., Buffet, B.A. (eds.), *The Core-Mantle Boundary Region*, Geodynamics Series 28, Am. Geophys. U., Washington D.C., 255-271, 1996
- Anderson, D.L., The thermal state of the upper mantle: no role for mantle plumes, *Geophys. Res. Lett.*, Vol. 27, 3623-3626, 2000
- Ansari, A., Morris, S., The effects of a strongly temperature-dependent viscosity on Stoke's drag law: experiments and theory, *J. Fluid. Mech.*, Vol. 159, 459-476, 1985
- Backus, G., Parker, R., Constable, C., *Foundations of Geomagnetism*, Cambridge University Press, Cambridge, 1996
- Batchelor, G.K., *An Introduction to Fluid Dynamics*, 19th Printing, Cambridge University Press, Cambridge, 2000
- Belitz, H.D., Grosch, W. Schieberle, P., *Food Chemistry*, 3rd Edition, Springer Publishing, Berlin, 2004
- Belmonte, A., Tilgner, A., Libchaber, A., Temperature and velocity boundary layers in turbulent convection, *Phys. Rev. E*, Vol. 50, No. 1, 269-279, 1994
- Bercovici, D., Mahoney, J., Double Flood Basalts and Plume Head Separation at the 660-Kilometer Discontinuity, *Science*, Vol. 266, 1367-1369, 1994
- Bercovici, D., Kelly, A., The non-linear initiation of diapirs and plume heads, *Phys. Earth Planet. Int.*, Vol. 101, 119-130, 1997

- Bercovici, D., Karato, S.-I., Whole-mantle convection and the transition-zone water filter, *Nature*, Vol. 425, 39-44, 2003
- Bouchut, F., Golse, F., Pulvirenti, M., *Kinetic Equations and Asymptotic Theory*, Series in Applied Mathematics (Paris), 4. Gauthier-Villars, Éditions Scientifiques et Médicales, Elsevier, Paris, 2000
- Brandt, A., *Multigrid Techniques: 1984 Guide with Applications to Fluid Dynamics*, GMD-Studien Nr. 85, Gesellschaft für Mathematik und Datenverarbeitung, St. Augustin, Bonn, 1984
- Briggs, W.L., *A Multigrid Tutorial*, Society for Industrial and Applied Mathematics, Philadelphia, 1987
- Brock, J.S., Painter, J.W., Kothe, D.B., Tracer-Particle Advection: Algorithm Components and Implementation Methods, *LANL Report LA-UR-98-5659*, 1998
- Campbell, I.H., Griffiths, R.W., Implications of mantle plume structure for the evolution of flood basalts, *Earth Planet. Sci. Lett.*, Vol. 99, 79-93, 1990
- Chandrasekhar, S., *Hydrodynamic and Hydromagnetic Stability*, Oxford University Press, London, 1961
- Choblet, G., Parmentier, E.M., Mantle upwelling and melting beneath slow spreading centers: effects of a variable rheology and melt productivity, *Earth. Planet. Sci. Lett.*, Vol. 184, 589-604, 2001
- Christensen, U.R., Hofmann, A.W., Segregation of subducted oceanic crust in the convecting mantle, *J. Geophys. Res.*, Vol. 99, No. B10, 19867-19884, 1994
- Class, C., Goldstein, S.L., Evolution of helium isotopes in the Earth's mantle, *Nature*, Vol. 436, 1107-1112, 2005
- Class, C., Goldstein, S.L., Stute, M., Kurz, M.D., Schlosser, P., Grand Comore Island: A well-constrained "low $^3\text{He}/^4\text{He}$ " mantle plume, *Earth Planet. Sci. Lett.*, Vol. 233, 391-409, 2005
- Condie, K.C., *Mantle Plumes and Their Record in Earth History*, Cambridge University Press, New York, 2001
- Coolen, M.C.J., Kieft, R.N., Rindt, C.C.M., van Steenhoven, A.A., Application of 2-D LIF temperature measurements in water using a ND:YAG laser, *Experiments in Fluids*, Vol. 27, 420-426, 1999
- Coulliette, D.L., Loper, D.E., Experimental, numerical and analytical models of mantle starting plumes, *Phys. Earth Planet. Int.*, Vol. 92, 143-167, 1995
- Courtillot, V.E., Jaupart, C., Manighetti, I., Tapponnier, P., Besse, J., On causal links between flood basalts and continental breakup, *Earth Planet. Sci. Lett.*, Vol. 166, No. 3-4, 177-195, 1999
- Courtillot, V.E., Davaille, A., Besse, J., Stock, J., Three distinct types of hotspots in the Earth's mantle, *Earth Planet. Sci. Lett.*, Vol. 205, No. 3-4, 295-308, 2003

- Cross, W., An occurrence of trachyte on the island of Hawaii, *J. Geol.*, Vol. 12, 510-523, 1904
- Dana, J.D., *United States exploring expedition during the years 1838, 1839, 1840, 1841, 1842*, G.P. Putnam's, New York, 1849
- Dahlen, F.A., Hung, S-H., Nolet, G., Fréchet kernels for finite-frequency traveltimes - I. Theory, *Geophys. J. Int.*, Vol. 141, 157-174, 2000
- Davaille, A., Jaupart, C., Transient high Rayleigh number thermal convection with large viscosity variations, *J. Fluid. Mech.*, Vol. 253, 141-166, 1993
- Davaille, A., Jaupart, C., Onset of thermal convection in fluids with temperature-dependent viscosity: Application to the oceanic mantle, *J. Geophys. Res.*, Vol. 99, No. B10, 19853-19866, 1994
- Davaille, A., Simultaneous generation of hotspots and superswells by convection in a heterogeneous planetary mantle, *Nature*, Vol. 402, 756-760, 1999
- Davaille, A., Vatteville, J., On the transient nature of mantle plumes, *Geophys. Res. Lett.*, Vol. 32, No. 14, L14309, 2005
- Davaille, A., Imaging isotherms in viscous fluids, submitted to *Exper. in Fluids*, 2005, in review
- Davies, G.F., Mantle plumes, mantle stirring and hotspot chemistry, *Earth Planet. Sci. Lett.*, Vol. 99, 94-109, 1990
- Davies, G.F., Penetration of plates and plumes through the mantle transition zone, *Earth Planet. Sci. Lett.*, Vol. 133, 507-516, 1995
- Dietz, R.S., Continent and Ocean Basin Evolution by Spreading of the Sea Floor, *Nature*, Vol. 190, 854-857, 1961
- Dixon, E.T., Honda, M., McDougall, I., Campbell, I.H., Sigurdsson, I., Preservation of near-solar neon isotopic ratios in Icelandic basalts, *Earth Planet. Sci. Lett.*, Vol. 180, 309-324, 2000
- Duncan, R.A., Richards, M.A., Hotspots, mantle plumes, and true polar wander, *Rev. Geophys.*, Vol. 29, 31-50, 1991
- Elkins-Tanton, L.T., Hager, B.H., Giant meteoroid impacts can cause volcanism, *Earth Planet. Sci. Lett.*, Vol. 239, No. 3-4, 219-232, 2005
- Ellsworth, W.L., Koyanagi, R.Y., Three-dimensional crust and mantle structure of Kilauea volcano, Hawaii, *J. Geophys. Res.*, Vol. 82, 5379-5394, 1977
- Engel, A.E.J., Engel, C.G., Havens, R.G., Chemical characteristics of oceanic basalts and the upper mantle, *Geol. Soc. Amer. Bullet.*, Vol. 75, No. 7, 719-734, 1965
- Ernst, R.E., Buchan, K.L., Campbell, I.H., Frontiers in Large Igneous Province research, *Lithos*, Vol. 79, 271-297, 2005
- Farley, K.A., Craig, H., Mantle Plumes and Mantle Sources, *Science*, Vol. 258, 821-822, 1992
- Farnetani, C.G., Richards, M.A., Thermal entrainment and melting in mantle plumes, *Earth Planet. Sci. Lett.*, Vol. 136, 251-267, 1995

- Farnetani, C.G., Legras, B., Tackley, P.J., Mixing and deformation in mantle plumes, *Earth Planet. Sci. Lett.*, Vol. 196, 1-15, 2002
- Farnetani, C.G., Samuel, H., Lagrangian structures and stirring in the Earth's mantle, *Earth Planet. Sci. Lett.*, Vol. 206, 335-348, 2003
- Farnetani, C.G., Samuel, H., Beyond the thermal plume paradigm, *Geophys. Res. Lett.*, Vol. 32, L07311, 2005
- Fitton, J.G., Saunders, A.D., Norry, M.J., Hardarson, B.S., Taylor, R.N., Thermal and chemical structure of the Iceland plume, *Earth Planet. Sci. Lett.*, Vol. 153, 197-208, 1997
- Fitton, J.G., Saunders, A.D., Kempton, P.D., Hardarson, B.S., Does depleted mantle form an intrinsic part of the Iceland plume?, *G-cubed*, Vol. 4, No. 3, 2003
- Garnero, E.J., Heterogeneity of the lowermost mantle, *Annu. Rev. Earth Planet. Sci.*, Vol. 28, 509-537, 2000
- Gonnermann, H.M., Jellinek, A.M., Richards, M.A., Manga, M., Modulation of mantle plumes and heat flow at the core mantle boundary by plate-scale flow: results from laboratory experiments, *Earth Planet. Sci. Lett.*, Vol. 226, 53-67, 2004
- Graham, D.W., Humphris, S.E., Jenkins, W.J., Kurz, M.D., Helium isotope geochemistry of some volcanic rocks from Saint Helena, *Earth Planet. Sci. Lett.*, Vol. 110, 121-131, 1992
- Graham, D.W., Christie, D.M., Harpp, K.S., Lupton, J.E., Mantle Plume Helium in Submarine Basalts from the Galápagos Platform, *Science*, Vol. 262, 2023-2026, 1993
- Graham, D.W., Larsen, L.M., Hanan, B.B., Storey, M., Pedersen, A.K., Lupton, J.E., Helium isotope composition of the early Iceland mantle plume inferred from the Tertiary picrites of West Greenland, *Earth Planet. Sci. Lett.*, Vol. 160, 241-255, 1998
- Griffiths, R.W., Thermals in extremely viscous fluids, including the effects of temperature-dependent viscosity, *J. Fluid. Mech.*, Vol. 166, 115-138, 1986a
- Griffiths, R.W., Particle motions induced by spherical convective elements in Stokes flow, *J. Fluid. Mech.*, Vol. 166, 139-159, 1986b
- Griffiths, R.W., The differing effects of compositional and thermal buoyancies on the evolution of mantle diapirs, *Phys. Earth Planet. Int.*, Vol. 43, 261-273, 1986c
- Griffiths, R.W., Dynamics of mantle thermals with constant buoyancy or anomalous internal heating, *Earth Planet. Sci. Lett.*, Vol. 78, 435-446, 1986d
- Griffiths, R.W., Richards, M.A., The Adjustment of Mantle Plumes to Changes in Plate Motion, *Geophys. Res. Lett.*, Vol. 16, No. 5, 437-440, 1989
- Griffiths, R.W., Campbell, I.H., Stirring and structure in mantle starting plumes, *Earth Planet. Sci. Lett.*, Vol. 99, 66-78, 1990
- Griffiths, R.W., Entrainment and stirring in viscous plumes, *Phys. Fluids A*, Vol. 3, No. 5, 1233-1242, 1991

- Griffiths, R.W., Campbell, I.H., Interaction of Mantle Plume Heads With the Earth's Surface and Onset of Small-Scale Convection, *J. Geophys. Res.*, Vol. 96, No. B11, 18,295-18,310, 1991
- Grossmann, S., Lohse, D., Scaling in thermal convection: A unifying theory, *J. Fluid. Mech.*, Vol. 407, 27-56, 2000
- Hackbusch, W., *Multigrid Methods and Applications*, Springer-Verlag, Berlin, 1985
- Hackbusch, W., Trottenberg, U., *Multigrid Methods*, Vol. 960, Lecture Notes in Mathematics, Springer-Verlag, Berlin, 1982
- Hagstrum, J.T., Antipodal hotspots and bipolar catastrophes: Were oceanic large-body impacts the cause?, *Earth Planet. Sci. Lett.*, Vol. 236, No. 1-2, 13-27, 2005
- Hamblin, J.D., The Navy's 'Sophisticated' Pursuit of Science - Undersea Warfare, the Limits of Internationalism, and the Utility of Basic Research, 1945-1956, *Isis*, Vol. 93, 1-27, 2002
- Hanan, B.B., Schilling, J-G., The dynamic evolution of the Iceland mantle plume: the lead isotope perspective, *Earth Planet. Sci. Lett.*, Vol. 151, 43-60, 1997
- Hanan, B.B., Blichert-Toft, J., Kingsley, R., Schilling, J-G., Depleted Iceland mantle plume geochemical signature: Artifact of multicomponent mixing?, *G-cubed*, Vol. 1, No. 1, 2000
- Hansen, U., Yuen, D., Extended boussinesq thermal-chemical convection with moving heat sources and variable viscosity, *Earth Planet. Sci. Lett.*, Vol. 176, 401-411, 2000
- Hart, S.R., Hauri, E.H., Whitehead, J.A., Oschmann, L.A., Mantle Plumes and Entrainment: Isotopic Evidence, *Science*, Vol. 256, 517-520, 1992
- Hasenclever, J., *Implications of a weak and buoyant asthenosphere for entrainment and mantle flow at a subduction zone*, Diploma thesis, Christian-Albrechts-Universität zu Kiel, Kiel, 2004
- Haskell, N.A., The motion of a fluid under surface load 1., *Physics*, Vol. 6, 265-269, 1935
- Haskell, N.A., The motion of a fluid under surface load 2., *Physics*, Vol. 7, 56-61, 1935
- Hauri, E.H., Whitehead, J.A., Hart, S.R., Fluid dynamics and geochemical aspects of entrainment in mantle plumes, *J. Geophys. Res.*, Vol. 99, No. B12, 24275-24300, 1994
- Hauri, E.H., Lassiter, J.C., DePaolo, D.J., Osmium isotope systematics of drilled lavas from Mauna Loa, Hawaii, *J. Geophys. Res.*, Vol. 101, No. B5, 11793-11806, 1996
- Hering, F., *Lagrangesche Untersuchungen des Strömungsfeldes unterhalb der wellenbewegten Wasseroberfläche mittels Bildfolgenanalyse*, Ph.D. thesis, Ruprecht-Karls-Universität zu Heidelberg, Heidelberg, 1996
- Hering, F., Leue, C., Wierzimok, D., Jähne, B., Particle tracking velocimetry beneath water waves. Part I: visualisation and tracking algorithms, *Experiments in Fluids*, Vol. 23, No. 6, 472-482, 1997
- Hering, F., Leue, C., Wierzimok, D., Jähne, B., Particle tracking velocimetry beneath water waves. Part II: Water waves, *Experiments in Fluids*, Vol. 24, No. 1, 10-16, 1998

- Hess, H.H., History of ocean basins, in Engel, A.E.J., James, H.L., Leonard, B.F. (eds.) *Petrologic Studies: a Volume in Honor of A.F. Buddington*, 559-620, Geol. Soc. Am., New York, 1962
- Hinze, J.O., *Turbulence*, McGraw-Hill, New York, 1995
- Hoernle, K., Werner, R., Phipps Morgan, J., Garbe-Schönberg, D., Bryce, J., Mrazek, J., Existence of complex spatial zonation in the Galápagos plume for at least 14 m.y., *Geology*, Vol. 28, No. 5, 435-438, 2000
- Hofmann, A.W., White, W.M., Mantle plumes from ancient oceanic crust, *Earth Planet. Sci. Lett.*, Vol. 57, 421-436, 1982
- Hofmann, A.W., Mantle geochemistry: the message from oceanic volcanism, *Nature*, Vol. 385, 219-229, 1997
- Holden, J.C., Vogt, P.R., Graphic Solutions to Problems of Plumacy, *EOS Trans. AGU*, Vol. 56, 573-580, 1977
- Hung, S-H., Dahlen, F.A., Nolet, G., Fréchet kernels for finite-frequency traveltimes - II. Examples, *Geophys. J. Int.*, Vol. 141, 175-1203, 2000
- Ito, G., Mahoney, J.J., Flow and melting of a heterogeneous mantle: 1. Method and importance to the geochemistry of ocean island and mid-ocean ridge basalts, *Earth Planet. Sci. Lett.*, Vol. 230, 29-46, 2005a
- Ito, G., Mahoney, J.J., Flow and melting of a heterogeneous mantle: 2. Implications for a chemically nonlayered mantle, *Earth Planet. Sci. Lett.*, Vol. 230, 47-63, 2005b
- Jähne, B., *Digital Image Processing: Concepts, Algorithms and Scientific Applications*, 6th Ed. revised & expanded, Springer Publishing, Berlin, 2005
- Jellinek, A.M., Manga, M., The influence of a chemical boundary layer on the fixity, spacing and lifetime of mantle plumes, *Nature*, Vol. 418, 760-763, 2002
- Kaminski, E., Jaupart, C., Laminar starting plumes in high-Prandtl-number fluids, *J. Fluid. Mech.*, Vol. 478, 287-298, 2003
- van Keken, P.E., Gable, C.W., The interaction of a plume with a rheological boundary: A comparison between two- and three-dimensional models, *J. Geophys. Res.*, Vol. 100, No. B10, 20291-20302, 1995
- van Keken, P.E., Evolution of starting mantle plumes: a comparison between numerical and laboratory models, *Earth Planet. Sci. Lett.*, Vol. 148, 1-11, 1997
- Kellogg, L.H., Interaction of Plumes with a Compositional Boundary at 670km, *Geophys. Res. Lett.*, Vol. 18, No. 5, 865-868, 1991
- Kellogg, L.H., King, S.D., The effect of temperature dependent viscosity on the structure of new plumes in the mantle: Results of a finite element model in a spherical, axisymmetric shell, *Earth Planet. Sci. Lett.*, Vol. 148, 13-26, 1997
- Kellogg, L.H., Hager, B.H., van der Hilst, R.D., Compositional stratification in the deep mantle, *Science*, Vol. 283, 1881-1884, 1999

- Kempton, P.D., Fitton, J.G., Saunders, A.D., Nowell, G.M., Taylor, R.N., Hardarson, B.S., Pearson, G., The Iceland plume in space and time: a Sr-Nd-Pb-Hf study of the North Atlantic rifted margin, *Earth Planet. Sci. Lett.*, Vol. 177, 255-271, 2000
- Kerr, R.C., Mériaux, C., Structure and dynamics of sheared mantle plumes, *G-cubed*, Vol. 5, No. 12, 2004
- Kido, M., Yuen, D.A., The role played by a low viscosity zone under a 660-km discontinuity in regional mantle layering, *Earth Planet. Sci. Lett.*, Vol. 181, 573-583, 2000
- Kincaid, C., Ito, G., Gable, C., Laboratory investigation of the interaction of off-axis mantle plumes and spreading centres, *Nature*, Vol. 376, 758-761, 1995
- King, S.D., Anderson, D.L., An alternate mechanism of flood basalt volcanism, *Earth Planet. Sci. Lett.*, Vol. 136, 269-279, 1995
- King, S.D., Anderson, D.L., Edge-driven convection, *Earth Planet. Sci. Lett.*, Vol. 160, 289-296, 1998
- Korenaga, J., Firm mantle plumes and the nature of the core-mantle boundary region, *Earth Planet. Sci. Lett.*, Vol. 232, 29-37, 2005
- Krishnamurti, R., On the transition to turbulent convection 2. The transition to time-dependent flow, *J. Fluid Mech.*, Vol. 42, 309-320, 1970
- Kumagai, I., Kurita, K., On the fate of mantle plumes at density interfaces, *Earth Planet. Sci. Lett.*, Vol. 179, 63-71, 2000
- Kumagai, I., On the anatomy of mantle plumes: effects of the viscosity ratio on entrainment and stirring, *Earth Planet. Sci. Lett.*, Vol. 198, 211-224, 2002
- Kumagai, I., Yaganisawa, T., Kurita, K., Importance of Entrainment in Plume Dynamics, poster presentation at the EGU/AGU 2003 spring meeting, Nice, poster-ID GD2-1TU1P-0020, *Geophys. Res. Abstracts*, Vol. 5, EAE03-A-05393, 2003
- Landau, L.D., Lifschitz, E.M., *Lehrbuch der Theoretischen Physik, Band VI: Hydrodynamik*, 5. Auflage, Akademie Verlag GmbH, Berlin, 1991
- Laske, G., Phipps Morgan, J., Orcutt, J.A., First results from the Hawaiian SWELL pilot experiment, *Geophys. Res. Lett.*, Vol. 26, No. 22, 3397-3400, 1999
- Lassiter, J.C., Hauri, E.H., Osmium-isotope variations in Hawaiian lavas: evidence for recycled oceanic crust in the Hawaiian plume, *Earth Planet. Sci. Lett.*, Vol. 164, 483-496, 1998
- Laudenbach, N., *Experimentelle und numerische Untersuchungen zur Ausbreitung von Volumenstörungen in thermischen Plumes*, Ph.D. thesis, Georg August Universität zu Göttingen, Göttingen, 2001
- Laudenbach, N., Christensen, U.R., An optical method for measuring temperature in laboratory models of mantle plumes, *Geophys. J. Int.*, Vol. 145, 528-534, 2001
- Le Bars, M., Davaille, A., Whole layer convection in a heterogeneous planetary mantle, *J. Geophys. Res.*, Vol. 109, No. B03403, 2004

- van Leer, B., Towards the ultimate conservative difference scheme: III - Upstream-centered finite difference schemes for ideal compressible fluid, *J. Comp. Phys.*, Vol. 23, 276-285, 1977
- Li, X., Kind, R., Priestley, K., Sobolev, S.V., Tilmann, F., Yuan, X., Weber, M., Mapping the Hawaiian plume conduit with converted seismic waves, *Nature*, Vol. 405, 938-941, 2000
- Lin, S.-C., van Keken, P.E., Multiple volcanic episodes of flood basalts caused by thermochemical mantle plumes, *Nature*, Vol. 436, 250-252, 2005
- Liu, M. Yuen, D.A., Zhao, W., Honda, S., Development of Diapiric Structures in the Upper Mantle Due to Phase Transitions, *Science*, Vol. 252, 1836-1839, 1991
- Loper, D.E., Stacey, F.D., The dynamical and thermal structure of deep mantle plumes, *Phys. Earth Planet. Int.*, Vol. 33, 304-317, 1983
- Loper, D.E., The dynamical structure of D" and deep plumes in a non-newtonian mantle, *Phys. Earth Planet. Int.*, Vol. 34, 57-67, 1984
- Loper, D.E., Mantle Plumes, *Tectonophysics*, Vol. 187, 373-384, 1991
- Lyn, D.A., Einav, S., Rodi, W., Park, J.H., Laser Doppler velocimetry study of ensemble-averaged characteristics of the turbulent near wake of a square cylinder, *J. Fluid. Mech.*, Vol. 304, 285-319, 1995
- Malamud, B.D., Turcotte, D.L., How many plumes are there?, *Earth Planet. Sci. Lett.*, Vol. 174, No. 1-2, 113-124, 1999
- Marquart, G., Schmeling, H., Interaction of small mantle plumes with the spinel-perovskite phase boundary: implications for chemical mixing, *Earth Planet. Sci. Lett.*, Vol. 177, No. 1-2, 241-254, 2000
- Marquart, G., Schmeling, H., Ito, G., Schott, B., Conditions for plumes to penetrate the mantle phase boundaries, *J. Geophys. Res.*, Vol. 105, No. B3, 5679-5693, 2000
- McKenzie, D.P., Parker, R.L., The north Pacific: An example of tectonics on a sphere, *Nature*, Vol. 216, 1276-1280, 1967
- Meister, A., *Numerik linearer Gleichungssysteme*, Friedr. Vieweg & Sohn Verlagsgesellschaft, Braunschweig/Wiesbaden, 1999
- Merzkirch, W., *Flow Visualization*, Second Edition, Academic Press Inc., London, 1987
- Mitrovica, J.X., Forte, A.M., Radial profile of mantle viscosity: Results from the joint inversion of convection and postglacial rebound observables, *J. Geophys. Res.*, Vol. 102, No. B2, 2751-2769, 1997
- Montelli, R., Nolet, G., Dahlen, F.A., Masters, G., Engdahl, R.E., Hung, S.-H., Finite-Frequency Tomography Reveals a Variety of Plumes in the Mantle, *Science*, Vol. 303, 338-343, 2004
- Montelli, R., Nolet, G., Masters, G., Dahlen, F.A., Hung, S.-H., Global P and PP traveltime tomography: rays versus waves, *Geophys. J. Int.*, Vol. 158, 637-654, 2004
- Moreira, M., Breddam, K., Curtice, J., Kurz, M.D., Solar neon in the Icelandic mantle: new evidence for an undegassed lower mantle, *Earth Planet. Sci. Lett.*, Vol. 185, 15-23, 2001

- Morgan, W.J., Rises, trenches, great faults and crustal blocks, *J. Geophys. Res.*, Vol. 73, 1959-1982, 1968
- Morgan, W.J., Convection plumes in the lower mantle, *Nature*, Vol. 230, 42-43, 1971
- Morgan, W.J., Deep mantle convection plumes and plate motions, *Am. Assoc. Petrol. Geol. Bullet.*, Vol. 56, 203-213, 1972a
- Morgan, W.J., Plate motions and deep mantle convection plumes, *Geol. Soc. Am. Mem.*, Vol. 132, 7-22, 1972b
- Morgan, W.J., Rises, Trenches, Great Faults and Crustal Blocks, *Tectonophysics*, Vol. 187, No. 1-3, 6-22, 1991
- Moses, E., Zocchi, G., Libchaber, A., An experimental study of laminar plumes, *J. Fluid. Mech.*, Vol. 251, 581-601, 1993
- Murton, B.J., Taylor, R.N., Thirlwall, M.F., Plume-Ridge Interaction: a Geochemical Perspective from the Reykjanes Ridge, *J. Petrol.*, Vol. 43, No. 11, 1987-2012, 2002
- Nakakuki, T., Yuen, D.A., Honda, S., The interaction of plumes with the transition zone under continents and oceans, *Eart Planet. Sci. Lett.*, Vol. 146, 379-391, 1997
- Neavel, K.E., Johnson, A.M., Entrainment in compositionally buoyant plumes, *Tectonophysics*, Vol. 200, 1-15, 1991
- Nimmo, A.H., Pele's Journey to Hawai'i: An Analysis of the Myths, *Pacific Studies*, Vol. 11, No. 1, 1-42, 1987
- Niu, Y., O'Hara, M.J., Origin of ocean island basalts: A new perspective from petrology, geochemistry, and mineral physics considerations, *J. Geophys. Res.*, Vol. 108, No. B4, doi:10.1029/2002JB002048, 2003
- Olson, P., Singer, H., Creeping Plumes, *J. Fluid. Mech.*, Vol. 158, 511-531, 1985
- Olson, P., Nam, I.S., Formation of Seafloor Swells by Mantle Plumes, *J. Geophys. Res.*, Vol. 91, No. B7, 7181-7191, 1986
- Olson, P., Hot spots, swells and mantle plumes, in Ryan, M.P. (ed.) *Magma Transport and Storage*, John Wiley & Sons Ltd., 1990
- Olson, P., Schubert, G., Anderson, C., Structure of axisymmetric mantle plumes, *J. Geophys. Res.*, Vol. 98, 6829-6844, 1993
- Peltier, W.R., Mantle Viscosity, in Peltier, W.R. (ed.), *Mantle Convection - Plate Tectonics and Global Dynamics*, The Fluid Mechanics of Astrophysics and Geophysics Volume 4, Gordon and Breach Science Publishers, Montreux, Switzerland, 1989
- Peltier, W.R., Mantle Viscosity and Ice-Age Ice Sheet Topography, *Science*, Vol. 273, 1359-1364, 1996
- Phipps Morgan, J., Morgan, W.J., Price, E., Hotspot melting generates both hotspot volcanism and a hotspot swell?, *J Geophys. Res.*, Vol. 100, No. B5, 8045-8062, 1995a

- Phipps Morgan, J., Morgan, W.J., Zhang, Y-S., Smith, W.H.F., Observational hints for a plume-fed, suboceanic asthenosphere and its role in mantle convection, *J. Geophys. Res.*, Vol. 100, No. B7, 12753-12767, 1995b
- Phipps Morgan, J., Thermal and rare gas evolution of the mantle, *Chem. Geol.*, Vol. 145, 431-445, 1998
- Phipps Morgan, J., Morgan, W.J., Two-stage melting and the geochemical evolution of the mantle: a recipe for mantle plum-pudding, *Earth Planet. Sci. Lett.*, Vol. 170, No. 4, 215-239, 1999
- Phipps Morgan, J., Thermodynamics of pressure release melting of a veined plum pudding mantle, *G-cubed*, Vol. 2, 2001
- Le Pichon, X., Sea-floor spreading and continental drift, *J. Geophys. Res.*, Vol. 73, 3661-3697, 1968
- Le Pichon, X., Introduction to the publication of the extended outline of Jason Morgan's April 17, 1967 American Geophysical Union Paper on "Rises, Trenches, Great Faults and Crustal Blocks", *Tectonophysics*, Vol. 187, No. 1-3, 1-5, 1991
- Press, W.H., Teukolsky, S.A., Vetterling, W.T., Flannery, B.P., *Numerical Recipes in Fortran: The Art of Scientific Computing*, Second Edition, Cambridge University Press, 1992
- Putirka, K.D., Mantle potential temperatures at Hawaii, Iceland, and the mid-ocean ridge system, as inferred from olivine phenocrysts: Evidence for thermally driven mantle plumes, *G-cubed*, Vol. 6, No. 5, 2005
- Ribe, N.M., Christensen, U.R., Three-dimensional modeling of plume-lithosphere interaction, *J. Geophys. Res.*, Vol. 99, No. B1, 669-682, 1994
- Ribe, N.M., Christensen, U.R., The dynamical origin of Hawaiian volcanism, *Earth Planet. Sci. Lett.*, Vol. 171, 517-531, 1999
- Richards, M.A., Griffiths, R.W., Thermal entrainment by deflected mantle plumes, *Nature*, Vol. 342, 900-902, 1989
- Richards, M.A., Duncan, R.A., Courtillot, V.E., Flood Basalts and Hot-Spot Tracks: Plume Heads and Tails, *Science*, Vol. 246, 103-107, 1989
- Richards, M.A., Hotspots and the case for a high viscosity lower mantle, in Sabadini, R., Lambeck, K., Boschi, E. (eds.), *Glacial Isostasy, Sea Level and Mantle Rheology*, NATO ASI Ser. C, Vol. 334, 571-587, Kluwer Academic Publishing, USA, 1991
- Rost, S., Garnero, E.J., Williams, Q., Manga, M., Seismological constraints on a possible plume root at the core-mantle boundary, *Nature*, Vol. 435, 666-669, 2005
- Sakakibara, J., Adrian, R.J., Whole field measurements of temperature in water using two-colour laser induced fluorescence, *Experiments in Fluids*, Vol. 26, 7-15, 1999
- Samuel, H., Farnetani, C.G., Thermochemical convection and helium concentrations in mantle plumes, *Earth Planet. Sci. Lett.*, Vol. 207, 39-56, 2003

- Schlee, S., *On Almost Any Wind: The Saga of the Oceanographic Research Vessel 'Atlantis'*, Cornell University Press, Ithaca N.Y., 1978
- Schubert, G., Olson, P., Anderson, C., Goldman, P., Solitary Waves in Mantle Plumes, *J. Geophys. Res.*, Vol. 94, No. B7, 9523-9532, 1989
- Schubert, G., Anderson, C., Goldman, P., Mantle plume interaction with an endothermic phase change, *J. Geophys. Res.*, Vol. 100, No. B5, 8245-8256, 1995
- Selig, F., A Theoretical Prediction of Salt Dome Patterns, *Geophysics*, Vol. 30, 633-643, 1965
- Seuntjens, H.J., Kieft, R.N., Rindt, C.C.M., van Steenhoven, A.A., 2D temperature measurements in the wake of a heated cylinder using LIF, *Experiments in Fluids*, Vol. 31, 588-595, 2001
- Shen, Y., Solomon, S.C., Bjarnason, I.T., Wolfe, C.J., Seismic evidence for a lower-mantle origin of the Iceland plume, *Nature*, Vol. 395, 62-65, 1998
- Shu, F.H., *Gas Dynamics*, University Science Books, Mill Valley, 1992
- Singer, H., *Heat transport by steady state plumes with strongly temperature-dependent viscosity*, Ph.D. thesis, John Hopkins University, Baltimore Md., 1986
- Sleep, N.H., Tapping of magmas from ubiquitous mantle heterogeneities: An alternative to mantle plumes?, *J. Geophys. Res.*, Vol. 89, 9980-9990, 1984
- Sleep, N.H., An analytical model for a mantle plume fed by a boundary layer, *Geophys. J. R. astron. Soc.*, Vol. 90, 119-128, 1987
- Sleep, N.H., Hotspots and Mantle Plumes: Some Phenomenology, *J. Geophys. Res.*, Vol. 95, No. B5, 6715-6736, 1990
- Sleep, N.H., Time Dependence of Mantle Plumes: Some Simple Theory, *J. Geophys. Res.*, Vol. 97, No. B13, 20007-20019, 1992a
- Sleep, N.H., Hotspot Volcanism and Mantle Plumes, *Annu. Rev. Earth Planet. Sci.*, Vol. 20, 19-43, 1992b
- Sleep, N.H., Ridge-crossing mantle plumes and gaps in tracks, *G-cubed*, Vol. 3, No. 12, 2002
- Smarr, L., in L. Smarr (ed.) *Sources of Gravitational Radiation*, 139-160, Cambridge University Press, Cambridge, 1983
- Smolarkiewicz, P.K., A Simple Positive Definite Advection Scheme with Small Implicit Diffusion, *Monthly Weather Review*, Vol. 111, No. 3, 479-486, 1983
- Smolarkiewicz, P.K., A Fully Multidimensional Positive Definite Advection Transport Algorithm with Small Implicit Diffusion, *J. Comp. Phys*, Vol. 54, 325-362, 1984
- Smolarkiewicz, P.K., On Forward-in-Time Differencing for Fluids, *Monthly Weather Review*, Vol. 119, No. 10, 2505-2509, 1991
- Smolarkiewicz, P.K., Margolin, L.G., On Forward-in-Time Differencing for Fluids: Extension to a Curvilinear Framework, *Monthly Weather Review*, Vol. 121, No. 6, 1847-1859, 1993

- Somatov, V.S., Scaling of temperature- and stress-dependent viscosity convection, *Phys. Fluids*, Vol. 7, No. 2, 266-274, 1995
- Stacey, F.D., Loper, D.E., The thermal boundary layer interpretation of D'' and its role as a plume source, *Phys. Earth Planet. Int.*, Vol. 33, 45-55, 1983
- Stein, C., Schmalzl, J., Hansen, U., The effect of rheological parameters on plate behaviour in a self-consistent model of mantle convection, *Phys. Earth Planet. Int.*, Vol. 142, 225-255, 2004
- Steinberger, B., O'Connell, R.J., Advection of plumes in mantle flow: implications for hotspot motion, mantle viscosity and plume distribution, *Geophys. J. Int.*, Vol. 132, 412-434, 1998
- Steinberger, B., Plumes in a convecting mantle: Models and observations for individual hotspots, *J. Geophys. Res.*, Vol. 105, No. B5, 11127-11152, 2000
- Stöcker, H. (ed.), *Taschenbuch der Physik*, Second Edition, Verlag Harry Deutsch, Frankfurt am Main, 1994
- Tackley, P.J., King, S.D., Testing the tracer ratio method for modeling active compositional fields in mantle convection simulations, *G-cubed*, Vol. 4, No. 4, 2003
- Takahashi, E., Nakajima, K., Wright, T.L., Origin of the Columbia River basalts: melting model of a heterogeneous plume head, *Earth Planet. Sci. Lett.*, Vol. 162, No. 1, 63-80, 1998
- Tan, E., Gurnis, M., Han, L., Slabs in the lower mantle and their modulation of plume formation, *G-cubed*, Vol. 3, No. 11, 2002
- Thompson, P.F., Tackley, P.J., Generation of mega-plumes from the core-mantle boundary in a compressible mantle with temperature-dependent viscosity, *Geophys. Res. Lett.*, Vol. 25, No. 11, 1999-2002, 1998
- Toussaint, G., Burov, E., Avouac, J-P., Tectonic evolution of a continental collision zone: A thermomechanical numerical model, *Tectonics*, Vol. 23, TC6003, 2004
- Tozer, D.C., Thermal Plumes in the Earth's Mantle, *Nature*, Vol. 244, 398-400, 1973
- Voulgaris, G., Trowbridge, J.H., Evaluation of the Acoustic Doppler Velocimeter for Turbulence Measurements, *J. Atmos. Ocean. Tech.*, Vol. 15, No. 1, 272-289, 1998
- Wadati, K., On the activity of deep-focus earthquakes in the Japan Islands and neighbourhood, *Geophys. Mag.*, Vol. 8, 305-325, 1935
- Walzer, U., Hendel, R., Baumgardner, J., The effects of a variation of the radial viscosity profile on mantle evolution, *Tectonophysics*, Vol. 384, 55-90, 2004
- Wegener, A. *Die Entstehung der Kontinente und Ozeane*, reprint of the 1st Edition, revised and expanded with handwritten notes and letters by A. Wegener, Alfred-Wegener-Institut für Polar- und Meeresforschung, Bremerhaven, 2005
- Werner, R., Hoernle, K., Barckhausen, U., Hauff, F., Geodynamic evolution of the Galápagos hot spot system (Central East Pacific) over the past 20 m.y.: Constraints from morphology, geochemistry, and magnetic anomalies, *G-cubed*, Vol. 4, No. 12, 2003

- White, R.S., McKenzie, D., Magmatism at Rift Zones: The Generation of Volcanic Continental Margins and Flood Basalts, *J. Geophys. Res.*, Vol. 94, No. B6, 7685-7729, 1989
- White, R.S., McKenzie, D., Mantle plumes and flood basalts, *J. Geophys. Res.*, Vol. 100, No. B9, 17543-17585, 1995
- Whitehead, J.A., Luther, D.S., Dynamics of Laboratory Diapir and Plume Models, *J. Geophys. Res.*, Vol. 80, No. 5, 705-717, 1975
- Whitehead, J.A., Helfrich, K.R., Wave transport of deep mantle material, *Nature*, Vol. 336, 59-61, 1988
- Wilson, J.T., A possible origin of the Hawaiian islands, *Can. J. Phys.*, Vol. 41, 863-870, 1963a
- Wilson, J.T., Evidence from islands on the spreading of ocean floors, *Nature*, Vol. 197, 536-538, 1963b
- Wilson, J.T., Evidence from ocean islands suggesting movement in the Earth, *Philos. Trans. R. Soc. London*, Series A, Vol. 258, 145-165, 1965
- Wolfe, C.J., Bjarnason, I.T., VanDecar, J.C., Solomon, S.C., Seismic structure of the Iceland mantle plume, *Nature*, Vol. 385, 245-247, 1997
- Yuen, D.A., Peltier, W.R., Mantle plumes and the thermal stability of the D" layer, *Geophys. Res. Lett.*, Vol. 7, 625-628, 1980

Acknowledgments

I would like to thank Jason Phipps Morgan for taking an astrophysicist under his wings and introducing me to the wide world of geosciences. I am grateful for the many chances he offered me to attend national and international courses, workshops, meetings and conferences, as well as for offering me the chance to spend some time abroad as part of my Ph.D. work. I also thank him for his unwavering patience and support everytime I went off on one of my wild tangents - I'm afraid that there are really no 'plume spokes' after all, Jason...

I owe much to the support and encouragement offered by Matthias Hort. He introduced me to the intricacies and trappings of analogue laboratory modelling, and without his virulent enthusiasm and his unfaltering optimism in the face of ruptured tanks, spilled syrup, broken instruments, fried computers, wiped data and all the other large and small catastrophes common to everyday lab work, I would possibly have quit in the first year.

Kaj Hoernle agreed to act as the co-referee for this thesis on very short notice. For this, as well as for introducing me to the geochemical peculiarities of the Galápagos hotspot and Cocos track, I would like to offer my heartfelt thanks.

I would like to thank Marc Parmentier for inviting me to Brown University, and for allowing and coaching me to fold, distort and mutilate his fluid dynamics code to my needs. In the same vein, I would also like to thank the staff of the Brown University department of Geological Sciences for welcoming a stranger and making him feel at home.

Ernst Flüh reached out a helping hand, providing critically-needed repair funds at a time when an important part of my laboratory apparatus broke down. Without his help, continuing the laboratory experiments might have been held up for months, and I would like to thank him for that.

Peter Linke unhesitatingly offered to lend me his video camera at times when our own camera was held hostage somewhere around the globe, and wasn't even too mad when I returned it late. Many thanks!

Arnim Berhorst and Lars Planert have been great office-mates, suffering the company of my own grumpy self without too much eye-rolling and mockery, patiently listening to my rants about complications in the lab or my inability to find this or that bug in the code, and generally being fun to share an office with.

I'd also like to thank the past and present staff of the FB4 for providing a stimulating and enjoyable working environment, and for always being eager to discuss their work and answer questions. Special mention should be made of Ingo Grevemeyer, who read through the very early buds of this thesis and whose constructive and encouraging comments tremendously helped me in overcoming 'thesis inertia', Martina Nöske, for conspiring with me to ambush Jason whenever he was in his office and for always being helpful and forthcoming, Jörg Geldmacher for taking the time to introduce me to and discuss a number of interesting papers on Iceland, and Michiko Yamamoto and Guillermo Booth Rea for simply being wonderful people and fun to be around.

Claudia Bartels, my future wife, has supported me every step of the way - both morally and, in the last few hectic weeks of writing this thesis, also with her considerable Photoshop and Illustrator skills. Without you, Claudia, all of this might never have come to pass, and you must allow me to tell you how ardently I admire and love you.

Many thanks go out to Markus Hirt and Arne Stademann, who have been great friends for all these years since we first started studying at Kiel University. Your tales of humour and woe about life as a Ph.D. student in your respective departments have greatly helped me keeping things in perspective.

Paul Knaus has mercilessly culled grammatical and spelling errors from this thesis, and has made me aware of the fact that my English sways wildly from BE to AE and back again. My thanks for this, and I can assure anyone that any errors still in this text were put in after Paul was done with it.

Heike Herden has been an island of calm and understanding during the frenzied rush to get this thesis finished in time, and I would like to thank her for that.

Last but not least I would like to thank my parents for their support and encouragement, and for not asking that question dreaded by every Ph.D. student ('when are you finally going to graduate?') too often...

Curriculum Vitae

Frank Cord Lohmann
geboren am 14. August 1974
in Hamburg
Staatsangehörigkeit: Deutsch

Schulbildung:

- Sachsenwaldschule Gymnasium Reinbek Sep. 1985 - Juni 1994
- Abitur Juni 1994

Studium:

- Grundstudium an der Christian-Albrechts-Universität zu Kiel (CAU) Okt. 1994 - 1996
- Vordiplom der Physik Nov. 1996
- Hauptstudium an der Christian-Albrechts-Universität zu Kiel (CAU) Okt. 1996 - Feb. 1999
- Diplom-Hauptprüfungen Feb. 1999 - März 1999
- Diplomarbeit am Institut für Theoretische Physik und Astrophysik, Abt. Astrophysik, zum Thema "Ram Pressure Stripping an Galaxien in Galaxienhaufen" unter Betreuung von Prof. Dr. Gerhard Hensler April 1999 - Juli 2000
- Diplomzeugnis der CAU Kiel im Fach Physik, Gesamturteil: Gut Sep. 2000
- Promotion zum Thema "Entrainment Processes during Plume Ascent" am Leibniz-Institut für Meereswissenschaften IFM/GEOMAR (ursprünglich GEOMAR) unter Betreuung von Prof. Dr. Jason Phipps Morgan seit März 2001

Erklärung

Hiermit erkläre ich, dass die von mir für das Promotionsverfahren vorgelegte Abhandlung "Entrainment Processes during Plume Ascent" von mir in Inhalt und Form unter Anleitung von Prof. Dr. J. Phipps Morgan und nur unter Zuhilfenahme der angegebenen Hilfsmittel angefertigt wurde. Diese Dissertationsschrift wurde noch nicht an anderer Stelle ganz oder zum Teil im Rahmen eines Prüfungsverfahrens vorgelegt.

Kiel, den 16. Dezember 2005

Frank Cord Lohmann